Universiteit
Antwerpen
Faculty of Science , Physics Department

Search for production of hidden particles in proton-proton collisions with the CMS experiment at the Large Hadron Collider (LHC) using displaced non-prompt lepton

---

Thesis submitted
To obtain the degree of Doctor of Science in physics
At the University of Antwerp
To be defended
By

Mohamed Darwish

Supervisors:
Prof. Dr. Albert De Roeck
Prof. Dr. Nick Van Remortel

Antwerp, 2022

Abstract

This thesis project conducts a search for a new type of particle using the data of the CMS experiment at the Large Hadron Collider at CERN, in Geneva, Switzerland. The data have been collected in 2016, 2017 and 2018, before the long shutdown started. The new particle is a so called Heavy Neutral Lepton (HNL), a potential new family member of the Standard Model neutrino.

Along with the known left-handed neutrinos that interact with the W and Z particles, the νMSM model postulates the existence of three right-handed neutrinos with a small mass, labelled as N_1 (a light stable dark matter candidate particle), N_2 and N_3, the latter two being potentially long-lived particles. The existence of these particles would restore the symmetry in the standard model such that all left handed particles have a right handed partner. The νMSM model, when realized in Nature could e.g. explain the existence of Dark Matter in the Universe, the baryon asymmetry after the Big Bang and the non-zero observed neutrino masses. The exact values of the masses and couplings of these new particles are unknown but in a large part of the preferred theory phase space the N_1 is much lighter than a GeV while N_2 and N_3 can be in the GeV to tens of GeV range, and can be searched for at the LHC.

The thesis contains a summary of the theoretical framework of the SM and νMSM extension, along with a comprehensive description of the CMS experiment at the LHC accelerator complex. This thesis focuses on the search for long lived Heavy Neutral Leptons, both as possible right-handed Dirac or Majorana neutrinos, and is conducted using final states that contain two charged leptons (electrons or muons), jets and displaced vertices. These particles can be produced in proton-proton collisions at the LHC in decays of the produced W and Z bosons through mixing with the standard model neutrinos. Their lifetimes depend on the mass and on the strength of the coupling with standard model neutrinos. For low masses and small mixing parameters, the decay length can be sufficiently large to produce a detectable secondary vertex.

No excess in the collision data is observed with respect to the predicted standard model backgrounds in the searches for all channels, and hence a statistical interpretation of the results is performed to set upper limits in the production cross sections on the νMSM particles. These limits extend in the region beyond previously derived results.

Abstract

Dit doctoraatsproject beschrijft een speurtocht naar een totaal nieuw mogelijk fundamenteel deeltje en gebruikt daarvoor de gegevens die geregistreerd werden met het CMS experiment bij de Large Hadron Collider (LHC), een proton-proton collider in CERN, Geneve, Zwitserland. De gegevens werden gedurende de zogenaamde Run-2 van de LHC in 2016, 2017 en 2018 geregistreerd met proton-proton botsingen bij een botsingsenergie van 13 Tera-electron volt. Het gezochte nieuwe deeltje is een zogenaamd zwaar neutraal lepton (Heavy Neutral Lepton; HNL) dat potentieel tot dezelfde familie behoort als het welgekende Standard Model neutrino deeltje.

Samen met de gekende links-handige neutrinos die interageren met het zware W en Z boson, postuleert het νMSM model het bestaan van drie extra rechts-handige neutrinos met relatief lage massa waarden, die en geëtikeerd zijn als N_1 –dat mogelijk een kandidaat is voor een light stabiel deeltje dat donkere materie kan verklaren–, N_2 en N_3, en deze twee laatste zouden metastabiele deeltjes zijn met, voor een onstabiel fundamenteel deeltje, een potentiele lange leeftijd. Het bestaan van deze deeltjes zou de symmetrie tussen links- en rechtshandige deeltjes kunnen herstellen in het Standard Model. Bovendien kan het νMSM model, als dat inderdaad gerealiseerd is in de natuur, buiten het bestaan van de donkere materie ook de materie-antimaterie asymmetrie die we waarnemen in het heelal, en de eveneens experimenteel geobserveerde zeer kleine, maar definitief verschillend van nul, massa waarden van de neutrinos te verklaren. De exacte waarden van de massas en interaktie koppelingen van deze nieuwe deeltjes zijn niet bekend, maar in een groot gedeelte van de theoretische parameter ruimte is het N_1 deeltje veel lighter in massa dan een GeV, terwijl het N_2 en N_3 deeltje een massa waarde tussen een GeV tot tientallen GeV kan bedragen. Deze laatste deeltjes kunnen geproduceerd en geobserveerd worden bij de LHC

Dit doctoraatswerk geeft eerst een theoretische inleiding tot het Standard Model en de uitbreiding daarvan naar het νMSM model, samen met een uitgebreide beschrijving van het CMS experiment en het versnellingscomplex van de LHC. De hoofdfocus van het proefwerk is de zoektocht naar HNL deeltjes met een lange leeftijd, voor neutrinos met zowel Dirac als Majorana eigenshappen, en geconcentreerd op verval-eindtoestanden die gekenmerkt zijn door de aanwezigheid van twee geladen leptonen (muonen of elektronen), jets en een expliciete observeerbare verval-vertex. Zulke deeltjes kunnen geproduceerd worden in proton-proton botsingen bij de LHC in vervallen van W en Z bosonen. Deze vervallen zijn een bron van Standard Model neutrinos bij de LHC en deze neutrinos kunnen door mixing in de experimenten tevoorschijn komen als HNLs. De leeftijd van deze deeltjes, alvorens ze vervallen, hangt af van de grootte van de mixing parameters van neutrinos met HNLs en van de massa van deze HNLs. Voor lage massa waarden en kleine mixing is de verval lengte groot genoeg opdat een detecteerbare verval-vertex kan worden gemeten.

Na een zoektocht in de CMS data waarbij verschillende nieuwe analyse methoden worden voorgesteld en toegepast, en die uitgevoerd worden op de data in een zogenaamde blinde analyse, blijkt de data uiteindelijk geen signaal van HNL deeltjes te bevatten. De resultaten zijn volledig consistent met de verwachte hoeveelheid achtergrond botsingen. De resultaten worden daarom vervolgens voorgesteld als bovenlimieten voor de produktie werkzame doorsnede van deze potentieel nieuwe deeltjes. De limieten zijn de op dit moment beste resultaten in de zoektocht naar Zware Neutrale Leptonen.

Acknowledgement

First of all, I would like to thank ***ALLAH*** for helping me to stay on the right track and showed me the way to proceed. I couldn't go further without this help.

I would like to express my gratitude to my supervisor, ***Prof. Dr. Albert De Roeck***, for the patient guidance, continuous encouragement and valuable advice he has provided throughout my time as his student. I have been extremely lucky to have a supervisor who cared so much about my work, and who responded to my questions and queries so promptly.

I wish also, to represent my appreciation to ***Prof. Dr. Nasser El-Maghraby***, for all you have done, which I will never forget. I truly appreciate you and your time you spent helping me in many occasions. Thank you very much for your support.

High appreciation and deep thanks are due to ***Prof. Dr. Marco Pieri*** for his dedicated support, guidance, continuously provided encouragement and was always willing and enthusiastic to assist in any way he could throughout the research project

High appreciation and deep thanks are due to my friend, ***Baraa Khamis***, who have always been a major source of support when things would get a bit discouraging.

Finally, my deep and sincere gratitude to my family for their continuous and unparalleled love, help and support. I am grateful to my sisters for always being there for me as a friend. I am forever indebted to my mother for giving me the opportunities and experiences that have made me who I am.

Contents

Introduction

The discovery of neutrino oscillations, a mixing between several neutrino flavours in flight, has provided experimental proof that Standard Model (SM) neutrinos have masses. Constraints on the neutrino masses have been established from a number of different experimental results, including results from cosmology [1, 2], as well as direct measurements such as experiments that look at the decay of tritium [3]. These results indicate that the neutrino masses are extremely smaller compared to the other SM particles, and suggest that the model used for mass generation of elementary particles can be extended to assess these new observations.

The smallness of the observed neutrino masses could be explained introducing new heavy states N, also called heavy neutral leptons (HNLs), with right-handed chirality [4, 5]. The existence of HNLs would give rise to a gauge mass term $m_\nu \sim y_\nu^2 v^2/M_N$, where y_ν is a Yukawa coupling and v is the Higgs vacuum expectation value (vev) in the SM, through a $see - saw$ mechanism [6].

Beyond the gauge mass term, HNLs may also help understand several other problems in cosmology and high energy physics. For example a stable HNL may be a possible candidate for dark matter, while any heavy partner might help explain the matter-antimatter asymmetry of the early universe as a second and third generation of heavy neutrinos would increase the amount of CP-violation [7, 8].

Searches for HNLs have been conducted by several experiments exploring a mass range from few keV to several hundred GeV [9]. Figure 1 shows the current limits on the HNL mixing parameters with three lepton families (denoted as $|V_{Nl}|^2$) and their masses (M_N), as well as the projected sensitivity that can be achieved in planned future facilities.

HNLs are singlets in each gauge group of the SM, this implies that they can't interact

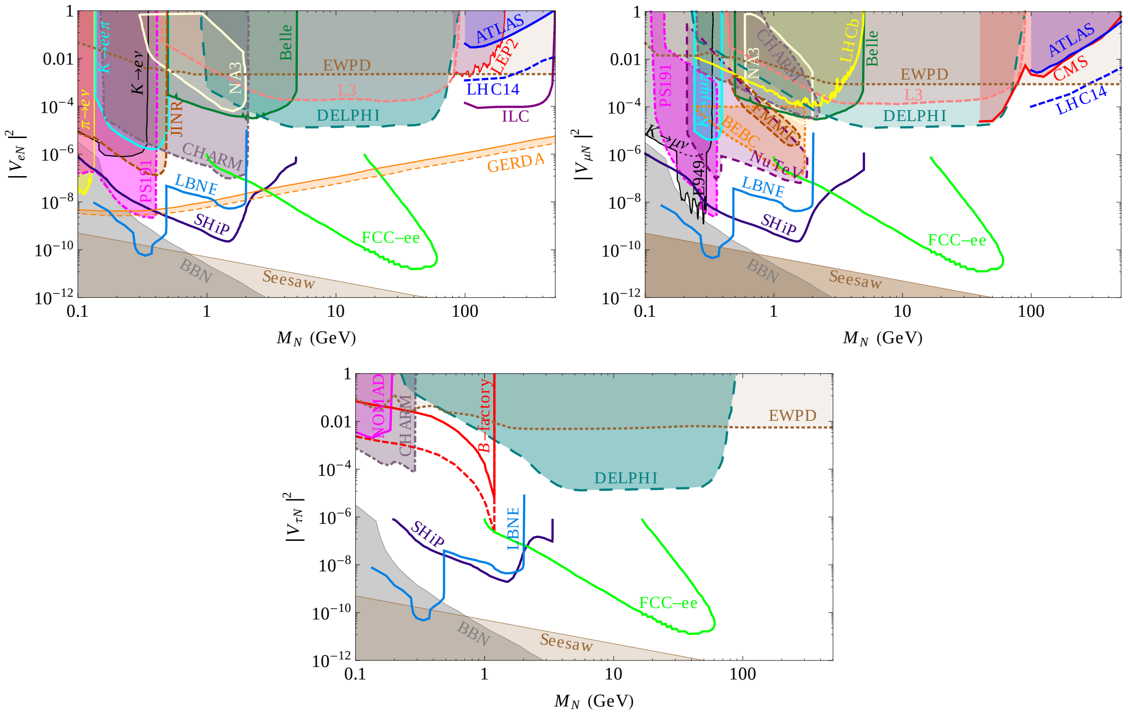

Figure 1: Current limits on the HNL masses and their couplings to the three lepton families, and projected sensitivity achievable in planned future facilities [9].

with the SM particle through the electroweak nor the strong interaction. They can however mix with the SM neutrinos and the mixing can be exploited to search for such states at the LHC. The search described hereafter will probe the direct production of HNLs in the decays of W bosons, where the SM neutrino oscillates into a HNL, and the HNL afterwards decay into a W boson and a charged lepton. In this analysis hadronic decays of W boson are considered, leading to a final state composed by two leptons and two quarks (which will fragment into hadrons or lead to jets).

Also, since neutrinos are electrically neutral, they can be the same as their antiparticles. That is, the Mjorana [10] fermions, which do not have a charge like the lepton, so does not conserve lepton number for case-weak interactions containing neutrinos. Alternatively, Dirac fermions, neutrinos, and anti-neutrinos will be distinguished from each other and neutrinos will carry lepton number, hence lepton number will to be conserved. Therefore, it is important to determine whether neutrinos are Dirac or Majorana fermions to solve the origin of neutrino mass.

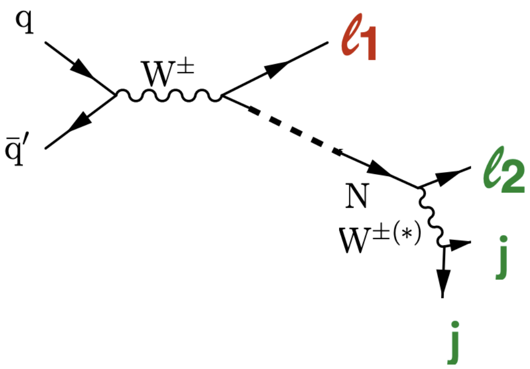

Figure 2: Typical diagrams for the production of a HNL at the LHC (N) through its mixing with a SM neutrino, leading to a final state with two charged leptons and two jets.

A Feynman diagram of the process considered is shown in Figure 2. In case the HNL is a Majorana particle, ℓ_1 and ℓ_2 will have the same chirality, lepton-number violation (LNV) decay , but in case HNL is a Dirac particle, ℓ_1 and ℓ_2 will have opposite chirality, lepton number conservation (LNC) decay. This can be understood as follows: for W decays at rest frame the N and ℓ_1 will have different chirality. So in the case where N is Majorana, the neutrino and anti-neutrino are indistinguishable, so N can have the same chirality as ℓ_1, and hence N can decay to ℓ_2 having the same chirality as ℓ_1 and in that case the lepton number will be violated. The opposite scenario will be the case where N is Dirac, so the neutrino and anti-neutrino are distinguished, so N will decay into ℓ_2 with opposite chirality as the one of ℓ_1, and in that case the lepton number is conserved. A LNV decay can lead to final states with no opposite-sign, same-flavour lepton pairs (no-OSSF), such as $e^{\pm}e^{\pm}q\bar{q}'$ or $\mu^{\pm}\mu^{\pm}q\bar{q}'$. Such final states have relatively low SM background rates, providing a characterizing signature for the performed HNL search.

The HNL can couple exclusively to a single lepton-neutrino family or to multiple families through mixing with the SM neutrinos for which the coupling is governed by the mixing angle V_{lN}, where l is the flavor of the SM neutrino and N is the right-handed neutrino. In the former case, only one of $|V_{Ne}|^2$, $|V_{N\mu}|^2$, or $|V_{N\tau}|^2$ is nonzero and ℓ_1 and ℓ_2 always belong to the same lepton generation, conserving the lepton flavour (LFC). In the latter case instead, at least two of $|V_{Ne}|^2$, $|V_{N\mu}|^2$, and $|V_{N\tau}|^2$ are nonzero at the same time and the lepton flavour can be violated (LFV). In this search, both LFC and LFV cases are considered.

The lifetime of a HNL is inverse proportional to M_N and $|V_{Nl}|^2$: ($\tau_N \propto M^{-5}|V_{Ml}|^{-2}$) [11]. This practically implies that HNLs with masses below about 20 GeV can have long lifetimes. If the N has a long lifetime, its decay products emerge from a secondary vertex, spatially displaced with respect to the primary vertex of the process, and is thus distinguishable from it.

The production rates of HNLs depend on their mass M_N and on the squared mixing parameter $|V_{Nl}|^2$. The final results of this analysis will be presented as a function of both M_N and $|V_{Nl}|^2$, for each flavour l separately.

There have been several searches for HNLs in CMS, ATLAS and LHCb. The CMS experiment reported on a search for HNLs using events with two same-sign leptons and at least one jet is searched for using data collected during 2016 in proton-proton collisions at a center-of-mass energy of 13 TeV and corresponding to an integrated luminosity of 35.9 fb^{-1} [12]. The results have been interpreted as limits on $|V_{Ne}|^2$, $|V_{N\mu}|^2$ and, $|V_{Ne}V^*_{N\mu}|^2/(|V_{Ne}|^2 + |V_{N\mu}|^2)$. The upper limits obtained are reported in Figure 3. These limits are the most restrictive direct limits for heavy Majorana neutrino masses above 430 GeV.

The ATLAS experiment reported on a search for HNLs using events with three charged leptons [13] using PP collision data corresponding to integrated luminosities of 32.9 to 36.1 fb^{-1}. The observations are consistent with background predictions and the research results are presented as exclusion limit in the HNL coupling strength versus the mass plane in the range 4.5-10 GeV in a model that assumes a single HNL mixing with either muon or electron neutrinos.

The LHCb experiment recently reported on a search for HNLs using events with two leptons and two jets [14] using a data set corresponds to an integrated luminosity of approximately 3.0 fb^{-1} of proton-proton collision data at centre of mass energies of 7 and 8 TeV collected with the LHCb experiment. Both same sign and opposite sign muons in the final state are considered. Data are found to be consistent with the expected background. Upper limits on the coupling of a heavy neutrino with a Standard Model neutrino are set at 95% confidence level in the heavy neutrino mass range from 5 to 50 GeV/c^2. These are of the order of 10^{-3} for lepton number conserving decays and of the order of 10^{-4} for lepton-number-violating heavy neutrino decays.

The analysis strategy we follow in this thesis has as main objective to extend the

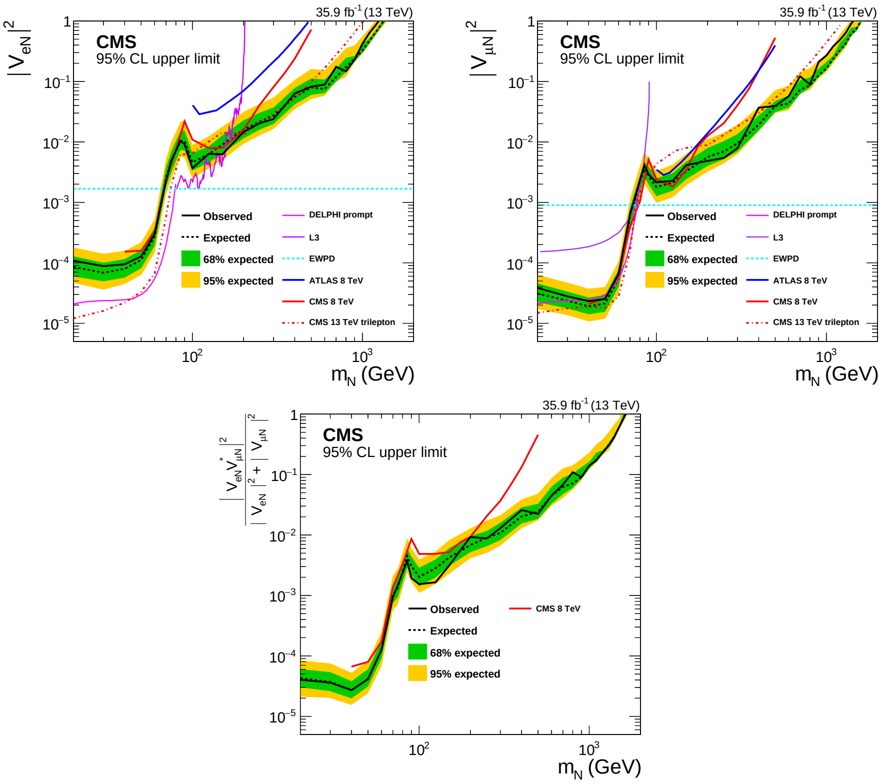

Figure 3: Exclusion region at 95% CL in the $|V_{Ne}|^2$ (top-left), $|V_{N\mu}|^2$ (top-right) and, $|V_{Ne}V^*_{N\mu}|^2/(|V_{N\mu}|^2 + |V_{Ne}|^2)$ (bottom) vs. m_N plane [12].

sensitivity to low HNL masses and mixing parameters, namely HNL masses below about 20 GeV. To achieve this goal, identification of leptons has been optimized for leptons produced in the decay of long-lived HNLs. Secondary vertex reconstruction has been improved starting from the CMS Inclusive Vertex Finder (IVF) algorithm, optimized for the specific physics case. Machine Learning (ML) techniques have been developed to enhance the purity of the secondary vertex selected.

The search uses the full run2 data set with an integrated luminosity of 137 fb^{-1}, and the major backgrounds are estimated using a data-driven technique.

The thesis is structured as follows. Chapter 1 provides a brief presentation of the Standard Model and examines the properties of νMSM. The parameter restrictions that are important for the scope of the study are presented and the signal channel, the associated cross section and the implementation of the right-handed neutrino in the SM process are addressed. The considered HNL masses, as well as their decay lengths and mixing angles with the SM neutrino, are described. The LHC and the

CMS detector are introduced in Chapter 2, and trigger and data acquisition in CMS are discussed in Chapter 3. In Chapter 4, the applied data and MC samples are discussed, as well as the basic principles for determining the research procedure and the selection requirements, which are used in the search for displaced HNL signal events. Chapter 5 is devoted to the optimal requirements for the signal region, which are determined by optimizing the expected discovery significance and the background estimation method, followed by the data-driven model that is created, and control regions that are specified to test the model's stability. Chapter 6 focuses on the systematic uncertainties related to the fake rate method and physics objects used in the analysis. Finally, the statistical techniques along with the expected sensitivity to the mixing angle and the results are presented in Chapter 7 .

I did a full analysis of the search for HNL through the di-lepton channel and all the results in chapters 4 to 7 are my results. This work was part of a team effort on the search for HNL particles so that there was a constant dialogue and cross-checking process within the team. My decisive contributions to the analysis are consistent with conducting a detailed study on the final state kinematics of the signal, especially on the effect of the displaced vertex, as well as the design and development of a method to reconstruct the displaced vertex, based on an Inclusive Vertex Finder algorithm, a variant of the CMS standard b-quark tagging. Furthermore I initiated the idea of using machine learning techniques to most efficiently suppress the background of Standard Model processes. I also generated a significant part of the HNL MC signal samples for better training and testing in ML processes, leading to better upper limits of the HNL signal. Finally, I contributed to writing the internal CMS note, detailing the analysis and presenting it to the CMS collaboration, as well as writing a paper draft to be published later in 2022.

In a large experiment like CMS, we also have duties to contribute to the general service and running of the experiment. I participated in the CMS data taking process in 2018 by taking many experimental shifts in the control room as the HLT DOC (Expert Detector On Call). I broke the record for the number of shifts performed by one person in one year, and as a result, I was awarded the 2018 CMS Achievement Award through the HLT group. In 2019 I became the HLT Monte Carlo contact where I was responsible for generating the Monte Carlo samples for the HLT group for trigger studies. I also got a position as request manager convener in the PPD (Physics Performance Dataset) group. In 2020, I was invited to join the CMS global shift organization team, a subgroup of run coordination. The main responsibilities of the group is to train CMS people to be technical shifters and shift leaders, as well as the organization of shifts and coverage of missing shifts when necessary, and be part of the CMS virtual visit team and train CMS guides.

Chapter 1

Theoretical Motivations

The experimental evidence for neutrino oscillations motivates extensions of the Standard Model. The neutrino flavor oscillations have been observed in experiments reported in [15, 16, 17, 18, 19] and these observations indicate that neutrinos have mass. The neutrinos in the Standard Model are only produced in left-handed states, so an extension is needed, like the Neutrino Minimal Standard Model (νMSM), by adding three heavy right-handed Majorana neutrinos to the SM, heavy neutral leptons (HNL). In this chapter, two main sections are presented. In the first section, a general overview of the Standard Model of particle physics is described. This is followed by a description of the electroweak and strong interactions, along with the breaking of the electroweak symmetry. Part 2 gives a brief introduction to the theory behind νMSM with an emphasis on the term neutrino mass and the see-saw mechanism. Finally, the limitations of the free parameters of νMSM, which were set by the Byond Standard Model (BSM) phenomenon observations, are studied. In conclusion, the important characteristics of the νMSM model that can be studied in the LHC are shown.

1.1 The Standard Model of Particle Physics

The modern approach to fundamental particles is based upon the Standard Model theory (SM), developed in the 1970's with the works of Brout, Englert, Higgs, Glashow, Weinberg, and others [20, 21, 22, 23, 24, 25, 26]. The SM is a quantum field theory that describes the three fundamental forces of nature (the electromagnetic, the weak, and the strong) and their interactions with elementary particles. The SM has been extremely successful in describing nature as we know it, as verified by many experiments. The final piece of the theory, the Higgs Boson, was discovered recently in the joint efforts at the Large Hadron Collider in 2012, which makes the SM an important milestone in elementary particle physics. However, this grand theory has its own limitations and issues, one of which is that gravitational interaction is not included as the SM lacks a description of gravity, which renders the theory only able to describe three out of four fundamental interactions.

The discussion about SM mostly follows the references [27, 28, 29]. According to SM, all particle content can be divided into three groups: leptons, quarks, and mediators (bosons). The content and properties of SM particles are summarized in Figure 1.1. SM is a quantum gauge field theory based on the symmetries of the

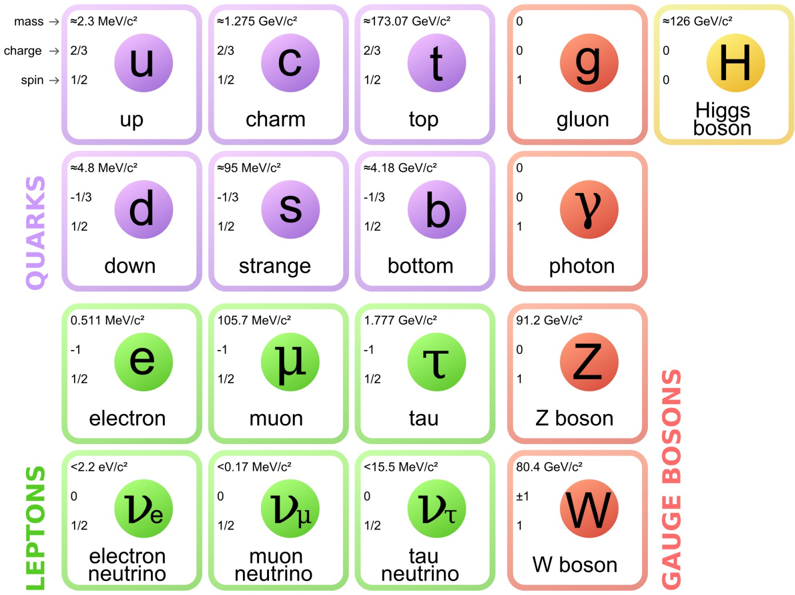

Figure 1.1: The elementary particles of the Standard Model [30].

unitary product group. U(1) × SU(3) × SU(2). The particle content in SM, which describes pretty much all known elementary particles, is basically divided into two categories: fermions and gauge bosons. Fermions form matter, and gauge bosons are force carriers that mediate particle interactions. Fermions and bosons also fall into subcategories based on the characteristics of the particles.

Fermions are particles with half an integer spin, according to Fermi-Dirac statistics.

Depending on the interactions in which they participate, they are further divided into leptons and quarks. Leptons do not participate in strong reactions; they only interact through electroweak interactions.

Three generations of leptons have been observed, consisting of three different flavors. The lepton generations are composed of three types of leptons, including the electron (e), the muon (μ), the tau (τ), and three neutrinos, which are the electron neutrino (ν_e), the muon neutrino (ν_{mu}), and the tau neutrino (ν_{tau}). One particle (e, μ, or τ) carries an integer charge of -1, while the other (neutrinos ν_e, ν_μ,ν_τ) is electrically neutral. The quark generations consist of up (u), charm (c), and the top (t) quarks, which are referred to as "up-type" quarks, down (d), strange (s), and bottom quarks (b), which are called the "down-type". Quarks have fractional charges of -1/3, or +2/3. Leptons and quarks carry a 1/2 spin and can be described by the positive energy solutions of the Dirac equation:

$$(i\gamma^\mu \partial_\mu - m)\psi = 0 \tag{1.1}$$

where γ^μ denotes gamma matrices and "m" is the fermion mass. The particles of each generation differ according to their mass, and the particles in the previous generations are lighter than the particles corresponding to the next generations. For every lepton and quark, there is an antiparticle (denoted by a bar above the particle symbol) that has the same spin and mass. Anti-leptons and anti-quarks are described by negative energy solutions of Eq. 1.1, which takes on a physical meaning when interpreted as particles with positive energy propagating backwards in time [31]. Solutions to ψ from Eq.1.1 they are four components of spinous called "Dirac spinors." Besides spin and mass, Standard Model fermions are distinguished by their gauge charges. They define their coupling to the gauge bosons, which arise from the assumption of symmetry on a local gauge scale. Gauge bosons, or simply "bosons" with a spin integer number 1, are force carriers that mediate strong, weak, and electromagnetic interactions. Photons mediate the electromagnetic interaction and are massless. The W^+ W^-, and Z bosons mediate the weak interaction and are massive. $W^\pm$ carry an electric charge of +1 and -1 and couples with the electromagnetic interaction. These three bosons and a photon are electroweak mediators, outlined in Section 1.1.1. There are eight types of gluons (dependent on color charge) that mediate strong interactions, as described in Section ref 1.1.3. Finally, there is a boson called the Higgs boson with a spin of 0 that is responsible for breaking the electroweak symmetry. Despite gluons and photons, why do elementary particles have mass?However, for the electroweak gauge bosons to have masses, the electroweak symmetry must be broken. This is explained by a mechanism of spontaneous symmetry breaking, as described in Section 1.1.2.

1.1.1 Electroweak Interaction

The weak interaction was observed for the first time in certain types of radioactive β decays. It is the only interaction that can change the flavor of the particles. Leptons and quarks can interact weakly. Neutrinos can only interact via weak interaction. The interaction is mediated by three measured massive bosons: W ($W^{\pm}$) and Z bosons (Z 0). Figure 1.2 shows the basic vertices for the weak interaction. The Z boson can be coupled with two fermions of the same flavor, while the W boson can be coupled with two different flavors of fermions. Moreover, both bosons can interact with each other. Since W bosons are electrically charged, they can also couple with photons. The weak interaction only operates over very short distances in the range of 10^{-18}m, because the Z and W bosons have large masses, around 91 GeV and 80 GeV [32], respectively. Glashow [21], Salam [23], and Weinberg [22] unified the description of the weak force with the electromagnetic force to obtain the electroweak (EW) force described by a $SU(2)_L \times U(1)_Y$ gauge symmetry: a unification of the weak interactions' SU(2) symmetry with the U(1) symmetry of QED. One of the difficulties was developing a theory capable of providing masses for the $W^{\pm}$ and Z gauge bosons while keeping the Lagrangian gauge invariant locally. There are a number of other phenomena that must be included in the electroweak theory: fermion flavor change, parity, and CP violation. Here is some history of electroweak standardization, leading to a solution that gives mass to vector scaling bosons-the Higgs mechanism.

1.1.2 Electroweak Symmetry Breaking

The BEH (Brout, Englert, and Higgs) mechanism, a method for spontaneous electroweak symmetry breaking proposed by Brout, Englert, and Higgs (1966), can generate masses of W $^{\pm}$ and Z bosons. In this model, an additional scalar field is introduced in the Lagrangian, with invariant potentials under the transformations of

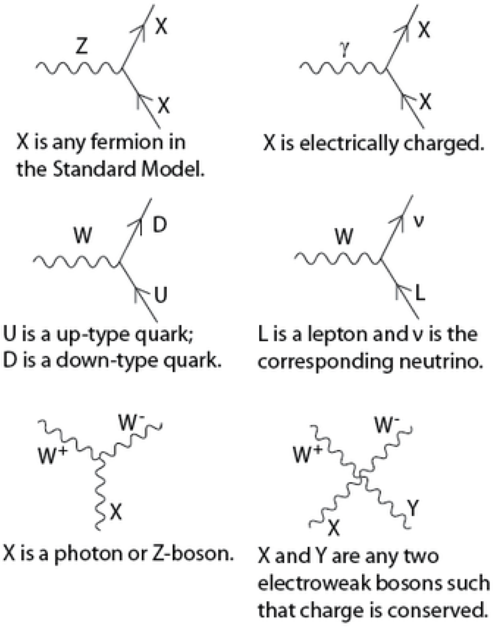

Figure 1.2: The Fundamental vertices of the weak interaction [33].

$SU(2)_L \times U(1)_Y$, and with non-zero ground state energy. Weinberg [22] and Salam [23] expanded on Glashow's work by introducing the idea of automatically breaking positional symmetries in electroweak theory to form the Glashow-Weinberg-Salam (GWS) model. Essentially, in the Standard Model, the Higgs mechanism breaks the $SU(2)_L \times U(1)_Y$, electroweak symmetry, giving mass to the vector bosons in the process, while keeping the U(1) symmetry of QED intact and remaining a local gauge invariant.

1.1.3 Strong Interaction

Quantum chromodynamics (QCD) is the quantum field theory of a strong interaction that binds neutrons and protons into an atomic nucleus. The strong interaction has a short range in the range of 10^{-15}m, the size of a proton. It is mediated by a massless boson called a gluon (g), which acts on particles with color charges. There are three such charges that are denoted by red, green, and blue (r, g, and b). The corresponding anti-colors are indicated by $\bar{r}, \bar{g}$, and $\bar{b}$. Quarks are the only fermions that carry a color charge. The basic process for a strong interaction is the process in which a quark emits or absorbs a gluon: q → q + g. Gluons carry color and anti-color, thus interacting with each other. There are eight types of gluons and, in Figure 1.3 displays the strong interaction's standard vertices. A charge of color is surrounded by a "sea" of virtual quarks and gluons. At shorter distances, corresponding to higher energies, the observed charge decreases until only charge is seen. The phenomenon that the strength of the interaction weakens with increasing energy and decreasing distance is referred to as asymptotic freedom. The observed charge increases with distance, which results in a strong attraction between two distant charges. At a great distance, the potential energy between two quarks is large enough to form a real pair of quarks and antiquarks out of space. This process is known as fragmentation or hadronisation. Two separate quarks always hadronise into colorless particles. Observed in nature are only colorless binding states, which is referred to as "color confinement."

The strong interaction binds the quarks into composite states called hadrons. Baryons are made of three quarks with a spin of either 1/2 or 3/2. Their antiparticles are made of antiquarks. Mesons consist of a quark and an antiquark. They are particles that spin 0 or 1. As a result, mesons are similar to bosons and baryons are similar to fermions, but they are coup as the particles in the composite.

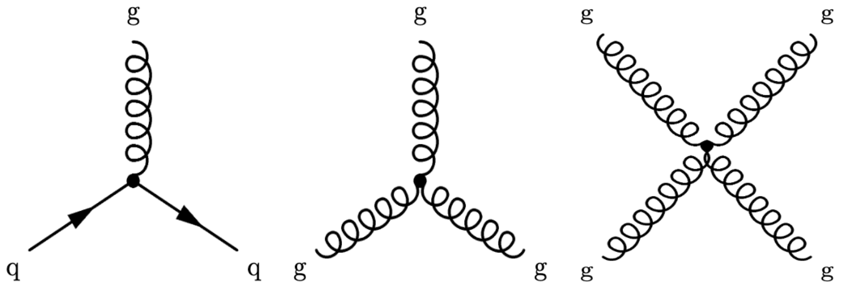

Figure 1.3: The Fundamental vertices of the strong interaction [33].

1.1.4 Chirality and Helicity

Chirality can be defined in a simple definition as the "handedness" of a particle. The particle's handedness can be defined by the spin of the particle and the direction indicated by the spin vector using a right-or left-hand system. Chirality is most often used to define a helicity, which is the projection of a spin vector onto the momentum vector. When a particle with right-handed chirality spins in the same direction as its momentum vector, the particle is said to have "positive" helicity. If the same particle has the same spin direction and momentum vector but is in a left-handed system, the spin vector will point in the opposite direction of the momentum vector, resulting in ”negative” helicity as shown in Figure 1.4. It should be noted, though, that chirality is not the same as helicity. Helicity is dependent on the angle between the spin vector and the momentum vector, the particle’s spin, the system’s handedness, and the reference frame used. Chirality, on the other hand, is the particle’s handedness and, as such, is not frame dependent [34]. Chirality is usually assumed to be conserved, just like other symmetries. This ensures that a right-handed particle and a left-handed particle are distinguishable. The complexities of chirality, on the other hand, stem from the fact that mass introduces a way to break this symmetry. As a result, for massless particles, chirality equals helicity, but symmetry will break for particles with mass, allowing right-handed and left-handed particles to be distinguished. Moreover, particles like quarks and leptons (electrons, muons, and tau) have both left-handed and right-handed versions of their matter and antimatter partners. However, as far as we can tell, neutrinos are just left-handed. This raises the question of where all the right-handed neutrinos and left-handed anti-neutrinos are, given that neutrinos have mass (as we’ll see in the next section). If right-handed neutrinos existed, they would be very different from the left-handed neutrinos we are familiar with. Perhaps they are much heavier, or do not interact via the weak force but instead interact only via gravity (so-called sterile neutrinos mixing). In particular, right neutrinos are in principle good candidates for sterile neutrinos, for which there are some experimental hints [35], but they have not yet been discovered through different experiments.

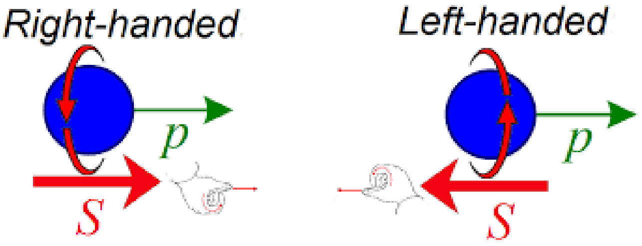

Figure 1.4: The left figure shows an object moving to the right (with momentum p represented by the green arrow) and spinning in the same direction as its movement: it has right-handed helicity. The figure on the right shows an object that is also moving to the right (green arrow) but spinning in the opposite direction: it has a left-handed helicity [34].

1.2 The Neutrino Minimal Standard Model (νMSM).

Over the past decade, our understanding of neutrinos has changed dramatically. After decades of confusion, it is now proven that neutrinos change their flavor after propagating a finite distance. The transition probability depends on the energy of the neutrino, the distance between the neutrino source and the neutrino detector, and, in some cases, the medium through which the neutrinos propagate. While the neutrino data revealed new properties of the lepton (neutrino mass-squared differences and leptonic mixing angles), there are still many "known unknowns" that must be revealed through next-generation neutrino experiments. In the next section, we'll discuss the fact that neutrinos have mass.

1.2.1 Neutrino Masses

Regarding neutrino masses and how they compare to the rest of the Standard Model particles, neutrino masses are very small, but not zero. Figure 1.5 depicts the masses of all typical fermions, including neutrinos. Two remarks stand out immediately. First, the mass of a neutrino is at least six orders of magnitude less than the mass of an electron. The mass of the electron itself is actually more than 100 times smaller than the mass of the muon and small compared to the weak scale, at around 100 GeV. Second, to the best of our knowledge, there is a "gap" between the largest allowed neutrino mass and the electron mass, in contrast to the fact that a new mass is encountered every order of magnitude in the charged-fermion part of the mass-space. We don't know why the neutrino masses are so small or why there is a large gap between the neutrino and the charged fermion masses. However, we suspect that this may be nature's way of telling us that the masses of neutrinos are "different". This suspicion is only amplified by the fact that the neutrinos may be Majorana fermions.

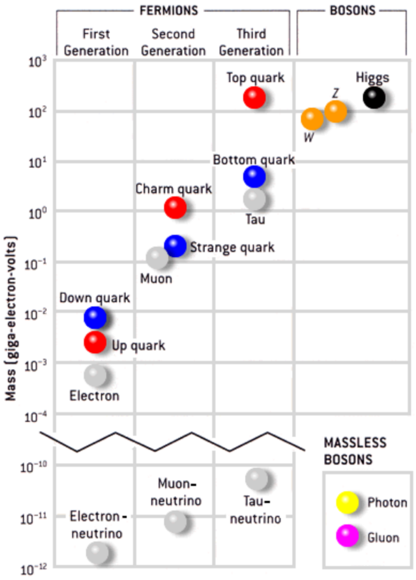

Figure 1.5: Particles in the standard model with mass map [36].

1.2.2 Modification to the Standard Model

As mentioned above, the observation of neutrino masses and neutrino oscillations in neutrino experiments [37] clearly shows that the SM is not a complete theory. The presence of dark matter, dark energy, and baryon asymmetry observations in the universe are phenomena observed in particle physics, astrophysics, and cosmology that SM cannot explain. By extending the SM by three gauge-singlet neutrinos with masses smaller than the electroweak scale, it is possible to achieve a theory that can predict the observed BSM phenomena. These neutrinos are referred to as singlets or sterile because they do not have strong, weak, or electromagnetic charges and therefore do not interact with gauge bosons. In order to theoretically describe measurements of neutrino oscillations, it is not sufficient to simply create a mass term for neutrinos. The model should also take into account the very small size of the neutrino's mass, so it is imperative that the right-hand neutrinos have majorana properties, thus allowing a see-saw mechanism to explain the size of the neutrino's mass (see section 1.2.4).

The theory candidate is called νMSM, and it is a strongly motivated and popular theory due to its apparent applicability to describing neutrino flavor oscillations, the simplicity of the SM extension, and its ability to explain the observed BSM phenomena without introducing a new energy scale. When the SM is extended using the right neutrino fields, the mass terms are generated. The basis of νMSM is studied in the next section, where the focus will be on the different fermion fields that represent solutions to the Dirac equation and the method for constructing mass terms.

1.2.3 Dirac and Majorana Fields

In order to describe the effect of extending SM with right-hand neutrinos, some basic properties of SM are first introduced. So, as we discussed in the SM section, the SM is a relativistic formulation of quantum mechanics in which the Dirac equation Eq. 1.1 is used to describe basic fermions. The solution to the Dirac Eq.1.1 can be expressed as the Dirac, Weyl, and Majorana field. The Dirac field is an unconstrained solution to the Dirac equation represented by a four-component spinor, whereas the Weyl and Majorana fermions are simpler solutions. The massive leptons and all quarks are represented by the Dirac fields, while massless neutrinos are represented by the Weyl field. In SM, the Majorana field does not change under charge conjugation, so Majorana particles are their own antiparticles. Therefore, there are no Majorana fields in the SM because it might break the gauge invariance of the SM. The dynamics of fermion fields are governed by a Lagrangian density, which for Dirac fields is:

$$LD = i\bar{\Psi}\gamma^{\mu}\partial_{\mu}\Psi - m\bar{\Psi}\Psi \tag{1.2}$$

where the first and second terms represent the kinetic and potential energy density of the field, respectively. The field $\bar{\Psi}$ refers to the Dirac point adjacent to the specified field as follows: $\bar{\Psi} = \Psi^{\dagger}\gamma^{0}$. The variable "m" is the mass of the massive fermion field, which is a function of Yukawa's coupling with the Higgs field [38]. For Weyl and Majorana fields, the Lagrangian can be simplified. First, Weyl fermions are massless particles described by a two-component spinor. The Dirac field can be expressed in terms of the Weyl field:

$$\Psi = PL\Psi + PR\Psi = \psi_L + \psi_R \tag{1.3}$$

where PL and PR are the left and right chiral projection operators and L and R are the left-handed and right-handed Weyl fields. So, Dirac Lagrange's Eq.1.1 is written in terms of two Weyl fields:

$$LD = i\bar{\psi}_L\gamma^{\mu}\partial_{\mu}\psi_L + i\bar{\psi}_R\gamma^{\mu}\partial_{\mu}\psi_R - m(\bar{\psi}_R\psi_L + \bar{\psi}_L\psi_R) \tag{1.4}$$

which indicates that Dirac Lagrange can be written using only one Weyl field to describe a massless Weyl fermion with two degrees of freedom. In SM, the neutrino is described as a two-component Weyl fermion which violates parity invariance but preserves Lorentz's invariance [39]. When adding the right neutrino field, the above Dirac Lagrangian Eq. 1.4 is divided into two parts by agreement with SM and one by BSM:

$$L_{SM} = i\bar{\psi}_L \gamma^\mu \partial_\mu \psi_L \tag{1.5}$$

$$L_{BSM} = i\bar{\psi}_R \gamma^\mu \partial_\mu \psi_R - m(\bar{\psi}_R \psi_L + \bar{\psi}_L \psi_R) \tag{1.6}$$

This indicates that the right-handed field is necessary to generate the Dirac mass term via the Yukawa interaction. The sum of the SM and BSM equations above is identical to Lagrange's kinetic and potential terms for any of the other massive fermions in SM when the Dirac spinor is expanded to the left and right hand components. This is not sufficient to explain why the mass of SM neutrinos is smaller than 2 eV while the mass of an electron is 511 keV by comparison. To explain the smallness, it is necessary to introduce the majorana properties of the right neutrino. This is possible because right-handed neutrinos convert into singlets under SM gauge transformations, so any term that includes only right-handed neutrinos can be added without breaking the gauge invariance of the SM. The Majorana fermion is a fermion which is its own anti-particle:

$$\chi = \chi^c \tag{1.7}$$

Where χ is used to describe Majorana's field, and χ^c is the charge conjugate of the field corresponding to the antiparticle of χ. The term "Majorana Mass in Lagrangian" can be expressed as:

$$L_{BSM} = 1/2 m_R (\bar{\chi}^c \chi + \bar{\chi} \chi^c) \tag{1.8}$$

Now, three additional BSM terms will be introduced in SM for νMSM: A kinetic term for right-hand neutrinos, the term Dirac mass, which uses the Yukawa interaction between the active SM neutrinos and the sterile BSM neutrinos, and finally the Majorana mass term for BSM neutrinos. In the simplified case of having only one active neutrino denoted as ψ_L and one sterile neutrino χ, the Lagrangian BSM density is:

$$L_{BSM} = i\bar{\chi}\gamma^\mu \partial_\mu \chi - m_D(\bar{\chi}\psi_L + \bar{\psi}_L \chi) - 1/2 m_R (\bar{\chi}^c \chi + \bar{\chi}\chi^c) \tag{1.9}$$

In the next section, the general expression for which more than one sterile fermion field is added, then the principles behind the see-saw mechanism [40] will be presented.

1.2.4 The see-saw mechanism

In the previous section, it was explained that a mass term for a neutrino field could be created by introducing a right-handed neutrino field with Majorana properties [41]. A more general form of the BSM part derived from Lagrangian density is now being studied. When adding N right-handed neutrinos, the complete Lagrangian density has the form [42]:

$$L = L_{SM} + i\bar{N}_I\gamma^\mu\partial_\mu N_I - (\lambda_{\alpha I}\bar{L}_\alpha N_I\bar{H} - 1/2M_I\bar{N}_I^c N_I + h.c.) \tag{1.10}$$

Because the Higgs boson has a non-zero vacuum expectation value, the Dirac M$_D$ masses are defined by Yukawa coupling and the Higgs vev ⟨H⟩. In the case that three right-handed neutrinos are added to the SM, a 6 × 6 neutrino mass matrix in the Lagrangian is presented. It represents 3 masses of active SM neutrinos in the three generations e, μ, and $\tau/3$, and 3 masses of the right new neutrinos. The terms of the Majorana/Dirac mass were created as cited by [43]:

$$-1/2(\bar{\nu}_L\bar{\nu}_R^c)\begin{pmatrix} 0 & M_D^T \\ M_D & M \end{pmatrix}\begin{pmatrix} \nu_L^c \\ \nu_R \end{pmatrix} + h.c. \tag{1.11}$$

Where M$_D$ is the 3 × 3 matrix of Dirac masses and the M a 3 × 3 matrix of Majorana masses for right-handed neutrinos. By diagonalizing the mass matrix, the physical state of a system can be found. At the limit where the Majorana M$_I$ mass are much larger than the Dirac M$_D$ mass, the see-saw mechanism results in nearly pure right handed neutrinos with heavy Majorana masses [44].

$$m_{\nu I}^{RH} = M_I \tag{1.12}$$

and to 3 almost pure left-handed neutrinos with light Majorana masses

$$m_\nu^{LH} = -M_D^T M^{-1} M_D \tag{1.13}$$

The SM neutrino masses are thus suppressed by the M^{-1} factor, which explains the small observed neutrino masses. In order to theoretically describe the observed neutrino oscillations, this could be sufficient to introduce two right-handed neutrinos into the SM. But in order to also obtain a dark matter candidate between sterile neutrinos, it is necessary to insert three right-handed neutrinos [42]. Moreover, if three right-handed neutrinos are inserted, the neutrino sector follows the observed symmetry of the charged quarks and leptons, where each lepton or left quark has a right counterpart. When introducing three right-handed neutrinos, 18 free parameters appear: 3 majorana masses, 3 Dirac masses, 6 mixing angles between sterile and active neutrinos, and 6 CP violation phases [42]. These free parameters are discussed in the next section.

1.2.5 The νMSM Features.

The νMSM is defined as an extension of the SM by three sterile neutrinos represented in the right-hand fields in which the 18 free parameters were adjusted to explain all confirmed BSM phenomena. Hence, the model is required, for example, to provide a mechanism that could generate the baryon asymmetry observed in the universe and provide a dark matter candidate. The observed neutrino oscillations also define limits for possible mixing angles between active neutrinos and sterile neutrinos based on the observed mixing angles of the active neutrinos [43]. All of these model limitations are examined in [42]. It is evident here that νMSM indeed has the potential to explain all of the observed BSM phenomena. Based on the findings in [42], some limitations to model parameters relevant to this analysis are presented briefly.

The three sterile neutrinos are classified as N_1, N_2 and N_3. As mentioned above, νMSM should provide a dark matter candidate. The lightest sterile neutrino, referred to as the N_1, has a very weak coupling to the active neutrinos. Sterile neutrinos are therefore commonplace in models with "dark" or "hidden" sectors. This includes many models of dark matter, even though in these models the coupling is often taken to be negligibly small. In fact, the only direct re-normalizable coupling that an SM singlet fermion can have with the SM is a coupling to the operator $(i\sigma^2 H^\star)L^\alpha$. This type of operator is therefore also called the "neutrino portal" [45]. The analysis presented in this thesis will focus on N_2 and N_3.

The limitations on the mass of the additional sterile neutrinos are determined by generating the desired baryon asymmetry: N_2 and N_3 neutrinos should have a mass in the range of 150 MeV to 100 GeV and should be degenerate ($\Delta M_{2,3}$ << $M_{2,3}$). Moreover, the lifetime of the neutrinos must be less than 0.1 seconds. This limitation was set in order not to influence the predictions of the Big Bang's nucleosynthesis [42].

Sterile neutrinos can only be observed indirectly by mixing them with active neutrinos. Therefore, the possibility of detecting sterile neutrinos depends greatly on the coupling strength between the active neutrinos and the new sterile neutrinos. Mixing is characterized by coupling strength: $V_{\alpha I}$, where $\alpha = e, \mu, \tau$ represent active neutrino generation, and I is a sterile neutrino index. In [42], the Yukawa coupling strength between active and sterile neutrinos is discussed. It was found that the coupling of N_2 and N_3 with active neutrinos should be nearly identical: $V_{\alpha 2} \approx V_{\alpha 3}$. Moreover, the $V_{\alpha I}$ coupling was found to be highly dependent on the mass hierarchy of the active neutrinos. For different scenarios, a sterile neutrino can have a stronger coupling by generating e, μ, τ or active neutrinos. The production mechanism and experimental signature of sterile $N_{2,3}$ neutrinos will be discussed in the next section.

1.2.6 The Heavy Neutral Lepton (HNL) Production and Cross Section

By searching for sterile neutrinos, the search is carried out in the decay channel of the sterile neutrino. In this analysis, the coupling between the sterile neutrino and the SM neutrino was examined. The sterile neutrinos were taken in νMSM, for which N_2 and N_3 were indicated in the previous section. They will also be referred to as Heavy Neutral Leptons (HNL). Due to their likely degraded mass and coupling strength with active neutrinos, the two sterile neutrinos will be denoted as one and termed HNL or simply N. The coupling strength between HNL and the active muon neutrino is V_μ, while V_e is indicated for the electron, and both are used to determine the production rate of the sterile neutrino channel. In this section, the signal channel covered in this analysis is presented.

HNL cross section

The Feynman diagram of the signal channel used in this study is shown in Figure 1.6. The SM neutrino, which will mix with the sterile neutrino, is created by its coupling to an on-shell W-boson, which is a gauge boson of the weak force: W $\rightarrow l + \nu_l$. Because of its majorana properties, the sterile neutrino can interact with the SM neutrino ν_l via the Higgs field and mix back into an anti-particle with an opposite lepton number, denoted by $\bar{\nu}_l$. As a result of this weak interaction, the SM neutrino decays: $\nu_l \rightarrow l + W^* \rightarrow llq\bar{q}^{'}$ The total cross section for the signal region channel is denoted $\sigma(pp \rightarrow llq\bar{q}^{'})$, where pp refers to the two colliding protons and it can be expressed as:

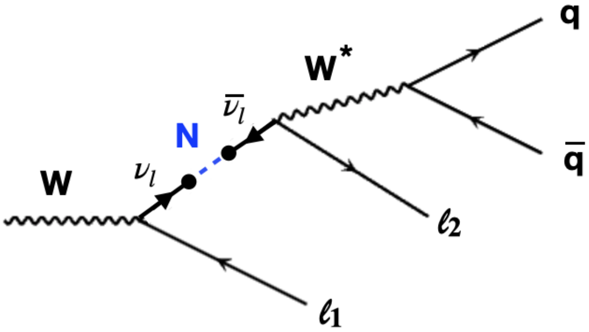

Figure 1.6: Feynman diagram for the production of a heavy neutrino via mixing with a neutrino from the decay of a W boson and semi-leptonic decay of the heavy neutrino to one lepton and two quarks.

$$\sigma(pp \rightarrow llq\bar{q}^{'}) = \sigma(pp \rightarrow W) \cdot Br(W \rightarrow lN) \cdot Br(N \rightarrow lq\bar{q}^{'}) \tag{1.14}$$

Where the two branching ratios rely on the predictions made by the νMSM and are thereby not known. In order to evaluate the branching ratio leading to the BSM sterile neutrino production, the two free parameters describing the HNL mass point M$_N$ and the mixing angle, V_{lN}, are applied: [46].

$$Br(W \rightarrow lN) = Br(W \rightarrow l\nu_l) \cdot |V_{lN}|^2 \cdot (1 - \frac{M_N^2}{M_W^2})^2(1 + \frac{M_N^2}{2M_W^2}). \tag{1.15}$$

The branching ratio for the HNL decay is determined by the process partial decay width and the HNL's total decay width:

$$Br(N \rightarrow lq\bar{q}^{'}) = \frac{\Gamma(N \rightarrow lq\bar{q}^{'})}{\Gamma} \tag{1.16}$$

The total decay width Γ is the sum of all partial decay widths of HNL :

$$\Gamma = \sum_i \Gamma_i(M_N, |V_{lN}|^2) \tag{1.17}$$

To evaluate the branching ratio of the HNL decay, all partial decay widths for the HNL in their dependence on M_N and $|V_{lN}|^2$ must be calculated. This is done in [11] for the partial decay widths of both charged-current and neutral-current weak interactions. The cross-section in equation 1.14 is determined as the function of two free parameters M_N and $|V_{lN}|^2$, given branching ratios for HNL production and the HNL decay in Eq.1.15 and Eq.1.16.

This now describes the relationship between $|V_{lN}|^2$, M_N and cτ. The proper decay length cτ_N is an important variable in this search for HNLs since it specifies the displacement of the HNL vertex from the hard scattering event, where the W is produced. The proper decay length is connected to the total decay width of the HNL:

$$\tau_N = \frac{1}{\Gamma_N} \tag{1.18}$$

As a result, the total decay width can be calculated as a function of the above-mentioned variables M_N and $|V_{lN}|^2$. Moreover, the mixing angle for given M_N and cτ_N can be determined accordingly and the cross section can be determined using the expressions in equations 1.14 and 1.15 given M_N and $|V_{lN}|^2$. Finally, the product of the cross section $\sigma(pp \rightarrow llq\bar{q}^{'})$ scaled by the integrated luminosity giving the number of expected signal events:

$$N_{events} = \sigma(pp \rightarrow llq\bar{q}^{'}) \int L dt \tag{1.19}$$

From the above, we can conclude that as the mixing angle increases, so does the cross section of the signal, and hence the number of expected signal events. Therefore, higher luminosity would generally allow the analysis to exploit lower mixing angles. However, for a constant HNL mass point, the proper decay length increases as the mixing angle decreases, affecting the analysis's efficiency (see Figure 1.7). The dataset used corresponds to an integrated luminosity of 137 fb^{-1} and the considered HNL masses are M_N= 1, 2, 3,... to 15 GeV, as explained in the following section.

HNL production

The N production and decay process is simulated using the leading order (LO) event generator MADGRAPH5 MC@NLO in the strong coupling constant α_S. The model parameters used for signal generation are described in [47], which was made available in Universal FeynRules Output (a universal format used to describe the particle physics models designed to be readable by many event generators) UFO by [48, 49]. This model extends the SM by introducing 3 right-handed neutrinos, which are singlets under the SM gauge symmetry. The user can specify the mass and the mixing parameters of the HNLs. The width Γ_N is automatically determined by the generator, and the mean lifetime is used to derive the HNL lifetime in each simulated event, according to a distribution of decay probability :

$$\frac{dN(t)}{dt} = \frac{1}{\tau_N} e^{\frac{-t}{\tau_N}} \tag{1.20}$$

Where τ_N is the proper lifetime, measured in the HNL rest frame. Figure 1.7 shows the inverse proportional relation of the decay length and the mixing angle $|V_{lN}|^2$ for the HNL at given mass M_N.

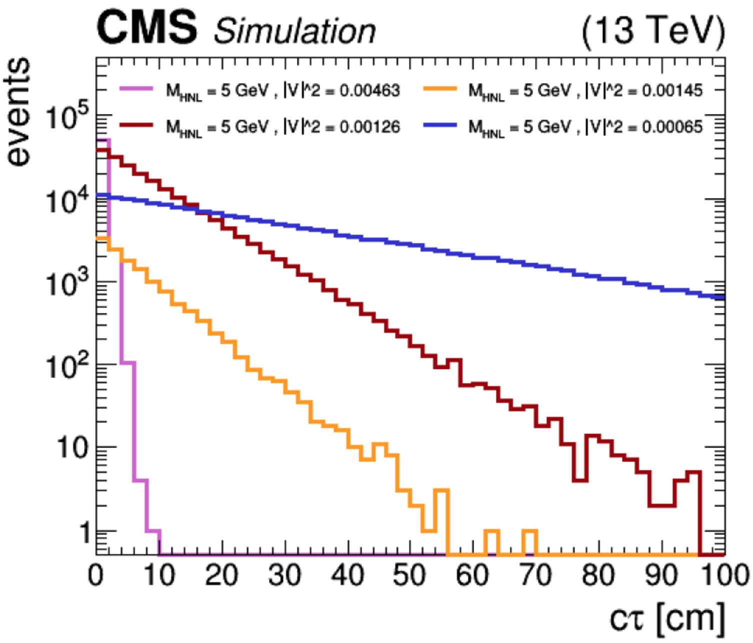

Figure 1.7: The decay length $c\tau$ distribution for the HNL at mass $M_N = 5$ GeV for various mixing angle $|V_{lN}|^2$.

For our signal samples, we have 3 different configurations for the mixing matrices in order to probe different flavor combinations and mixing parameters, typically in a range $|V_{Nl}|^2 = 0.9 - 10^{-10}$. We only consider the cases where HNLs of masses M$_N$ = 1–15 GeV, and does not couple to the τ lepton generation.

$$V_{lN} = \begin{pmatrix} V_{eN1} & V_{eN2} & V_{eN3} \\ V_{\mu N1} & V_{\mu N2} & V_{\mu N3} \\ V_{\tau N1} & V_{\tau N2} & V_{\tau N3} \end{pmatrix}$$

For the $\mu\mu$ channel, where both leptons in final state are muons, $|V_{\mu N1}|^2$ is in the range of $0.9 - 10^{-10}$, whereas for the ee channel, $|V_{eN1}|^2$ is in the range of $0.9 - 10^{-10}$, and finally, for eμ and μe channels, $|V_{eN1}|^2 = |V_{\mu N1}|^2$ is in the range of $0.9 - 10^{-10}$. The rest of the parameters in the mixing matrix that are not specified are set to 0.0. A challenge we have in this analysis is to study the behaviour of HNLs with the same mass in a wide range of $|V_{Nl}|^2$ values, since the cross-section of HNL production is not only determined by the M_N and $|V_{Nl}|^2$ values, but also depends on the mean lifetime and, thus its kinematics, acceptance, and reconstruction efficiency. Therefore, rescaling the cross-section is not sufficient to reproduce the behaviour of other HNLs of the same mass and different $|V_{Nl}|^2$. Instead, we use a re-weighting strategy based on the HNL lifetime per event for this reason, which correctly accounts for all the differences in kinematics and acceptance. First, we found that the HNL decay kinematics is independent of the mean lifetime τ_N and determined by the mass of the HNL M$_N$, its momentum $p_N = \beta\gamma M_N$, and its decay length. Therefore, we can reproduce the kinematic distributions of any other HNL with same mass and different mean lifetime τ_1 by simply re-weighting each event with proper decay time t by the ratio of probabilities to obtain a lifetime of t for mean lifetimes τ_0 and τ_1, given a simulated HNL sample of mass M_N and mean lifetime τ_0:

$$W(t) = \frac{dN_1(t)/dt}{dN_0(t)/dt} = \frac{\tau_0}{\tau_1} exp[-t(\frac{1}{\tau_0} - \frac{1}{\tau_1})] \tag{1.21}$$

Note that $\frac{\tau_0}{\tau_1} = \frac{|V_{Nl1}|^2}{|V_{Nl0}|^2}$, therefore this method allows us to move along the $|V_{Nl}|^2$ axis of the (M_N, $|V_{Nl}|^2$) plane.

To conclude, the search presented in this thesis is optimized for displaced HNL decays with an HNL mass in the range of 1–15 GeV. It follows a similar strategy and uses the same dataset of 137 fb^{-1} of pp collisions at $\sqrt{s}$= 13 TeV collected between 2016 and 2018 as in [50], in an orthogonal event selection. A special reconstruction of the secondary vertex and the associated charged lepton and jets is used. Using dedicated machine-learning techniques, an event selection with an enhanced sensitivity to signal-like signatures is implemented. Background contributions from SM processes are estimated from control samples in the data. In the interpretation of the results, both LFC and LFV decays are considered, and limits are determined for simplified scenarios with one HNL generation with either pure electron-or muon-neutrino couplings, or with mixed couplings to both electron-and muon-neutrinos.

Chapter 2

The Large Hadron Collider and The CMS Experiment

The Large Hadron Collider (LHC) at CERN is the largest and most powerful particle accelerator ever built. High-energy proton collisions provide a picture of the conditions present in the Universe immediately after the Big Bang and an opportunity to probe elementary particles and their interactions on an unprecedented energy scale. The primary goals for the LHC are to test and verify the Standard Model of particle physics, in particular the study of the Higgs boson, and to find any hints of new physics. The Compact Muon Solenoid (CMS) is one of two general-purpose particle detectors at the LHC that measure the results of proton collisions. The amount of data produced from these collisions is very large, and significant computational power and storage are required to process the data. This is handled by a trigger system consisting of multiple levels of hardware, software, and a multi-tiered distributed computing system.This chapter gives a brief description of the LHC in Section 2.1, followed by a full description of CMS in Section 2.2, where the four main parts of the CMS detector are described in detail.

2.1 The Large Hadron Collider

The LHC is located on the border between Switzerland and France near Geneva and was built and operated by the European Organization for Nuclear Research (CERN).

It occupies a tunnel with a circumference of 26.7 km and a depth of 50 to 175 meters underground, which was originally built for the Large Electron Positron (LEP) collider. The machine is capable of delivering particle collisions to four equipped interaction points along its circumference and does so at unprecedented energy and rate. The LHC is designed to be able to accelerate both protons and heavy ions such as oxygen, lead, and xenon. The nominal design energy of each proton beam is 7 TeV, and the nominal instantaneous luminosity of collisions is 2.5 x 10^{34} cm^{-2} s^{-1}.

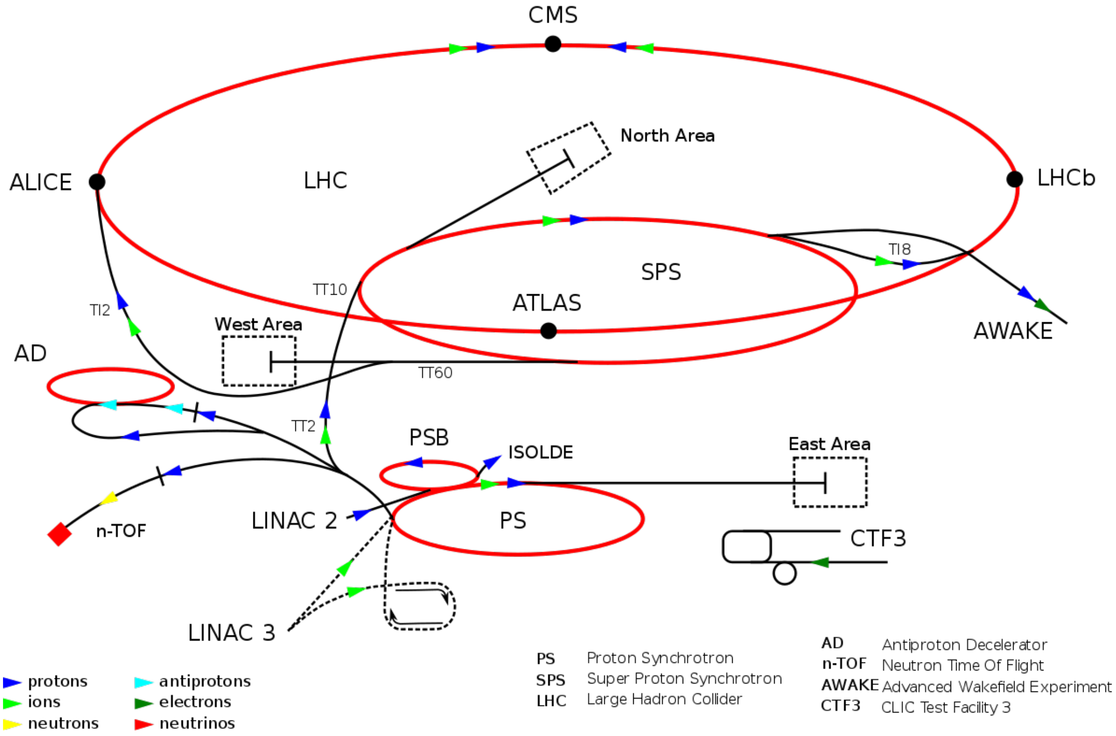

Figure 2.1: CERN Accelerator Complex. Protons that collided at the Large Hadron Collider(LHC) are accelerated by Linear Accelerator 2 (LINAC2) before passing through the Booster, the Proton Synchrotron (PS) and Super-ProtonSynchrotron (SPS) before being injected into the Large Hadron Collider (LHC). Acceleration facilities that support other CERN experimental activities can also be seen [51].

The accelerator is filled with proton bunches from its injection chain, which consists of several accelerators available at CERN, shown in Figure 2.1. The protons used in the LHC are extracted from compressed hydrogen gas by stripping electrons from the atoms through a strong electrostatic field. The resulting protons are injected into LINAC 2, where they are accelerated to 50 MeV. Those are subsequently passed to the PS Booster, PS and SPS storage rings, each of which increases the proton's kinetic energy until they are injected into the LHC when travelling at 450 GeV [52].

The LHC's two beam pipes accelerate protons or heavy ions in opposing directions. A large number of superconducting magnets of various types are installed along the beam pipes to control the paths of the proton beams. A total of 1232 dipole magnets are used to bend the path of the proton beams to follow a circular path. Made of NbTi, superconducting dipole magnets operate at 1.9K and can generate a magnetic field of up to 8.3T. The LHC also has a large number of quadruple magnets to focus the beams before they collide with the detectors.

At each LHC-instrumented interaction point (IP), opposing proton beams can be brought into collision using focused quadrupole magnets. The rates of interaction between the protons in the two beams depend significantly on the luminosity and kinetic properties of the colliding beams. The instantaneous luminosity of two colliding beams with Gaussian profiles can be written as:

$$L = \frac{N_b^2 n_b f_{rev} \gamma_r}{4\pi \epsilon_n \beta^*} F \tag{2.1}$$

where N_b is the number of particles per bunch, n_b is the number of bunches per beam, f_{rev} is the revolution frequency, ϵ_n is the normalized transverse beam emittance, β^* is the beta function at the collision point, which measures the beam focalization and is corrected by the relativistic gamma factor γ_r ($\equiv$ E/m), and F is the geometric luminosity reduction factor due to the crossing angle at the interaction point. Instantaneous luminosity, and thus the rates of interaction between the beams, depends on the geometry of the luminous region from which the interactions between the beams arise, which in itself depends on the angle of crossing between two beams of particles. In nominal operation, the beam optics maintains its configuration throughout the period of stable collisions until the luminosity is significantly decreased and the beams are dumped so that another fill for the LHC can be prepared. Knowing the kinematic properties of the proton beams, including their energy and luminosity, one can use predictions from QCD [54] to estimate the expected interaction rates and the resulting number of collisions as a function of both energy and luminosity. Those can be compared with theoretical predictions of production cross-sections of various processes of interest in order to estimate production yields and event rates. Figure 2.2 a) shows the integrated luminosity delivered by the LHC and the frac-

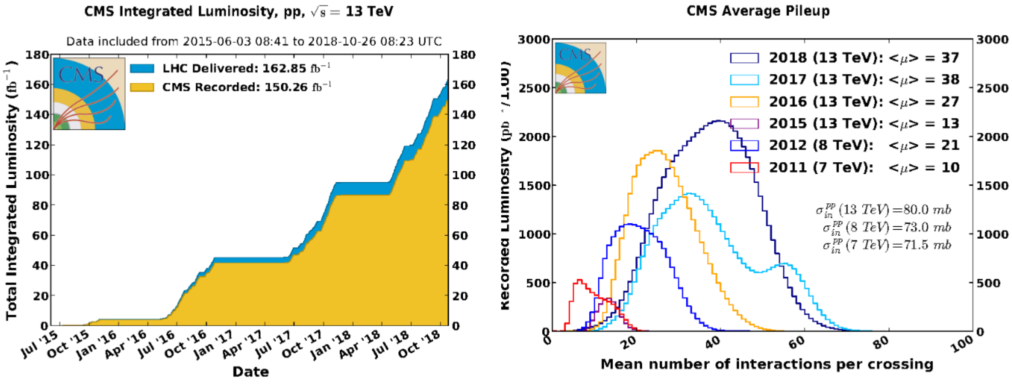

(a)

(b)

Figure 2.2: A) The integrated luminosity delevired by the LHC and recorded by CMS during run2 data taking between 2015 and 2018, where high efficiency in taking data can be observed. B) Average pileup distribution of each bunch crossing in a collision recorded by CMS. The bimodal pileup distribution in 2017 indicates the distribution of the pileup before and after the luminosity level was introduced [53].

tion of it that was successfully recorded by CMS over the run2 data taking period between 2015 and 2018. Figure 2.2 b) shows the distribution of the average pileup (number of PP collisions per bunch crossing) for each year of data taking for runs 1 and 2, where a steady increase in pileup can be seen up to 2017, when luminosity levelling was introduced.

With knowledge of the kinematic properties of the proton beams, including their energy and luminosity, one can use predictions from QCD [54] to estimate the expected interaction rates and the resulting number of collisions as a function of both energy and luminosity. Those can be compared with theoretical predictions of production cross-sections of various processes of interest in order to estimate production yields and event rates. Figure 2.2 on the left shows the integrated luminosity delivered by the LHC and the fraction of it that was successfully recorded by CMS over the run2 data taking period between 2015 and 2018. Figure 2.2 on the right shows the distribution of the average pileup (number of PP collisions per bunch crossing) for each year of data taking for runs 1 and 2, where a steady increase in pileup can be seen up to 2017, when luminosity levelling was introduced.

2.2 The Compact Muon Solenoid Detector

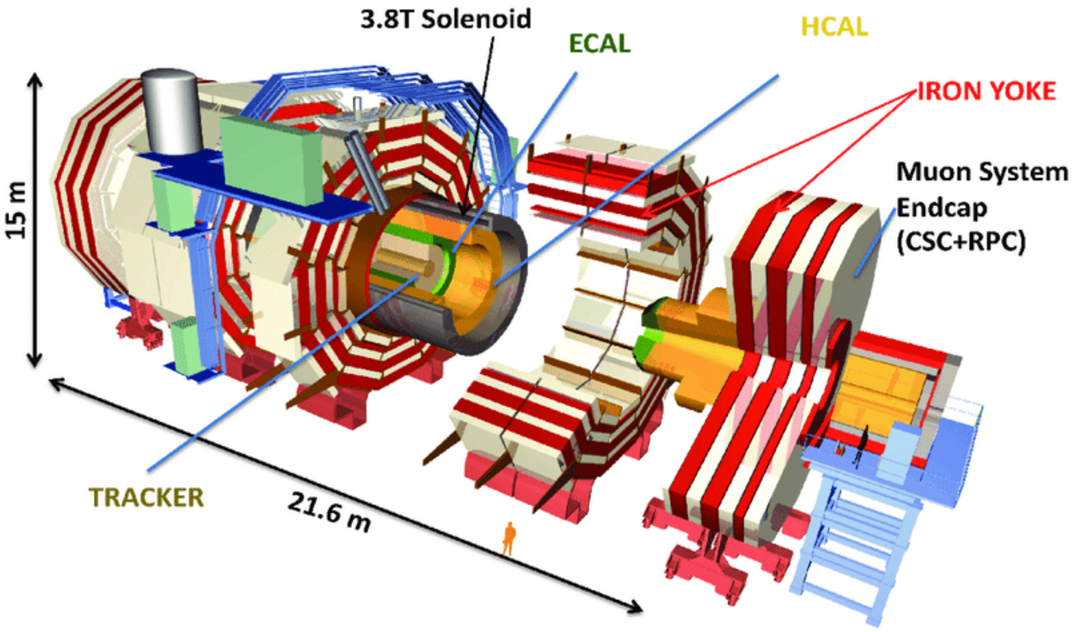

Figure 2.3: Schematic view of the CMS detector [55].

The CMS detector [56] is a general-purpose particle detector installed at interaction point 5 of the LHC. It features a superconducting solenoid capable of delivering a uniform coaxial magnetic field of 3.8 Tesla at a length of 12.5 meters and a free bore radius of 3.5 meters. A compact design is made possible thanks to a strong magnetic field; the tracker detector, electromagnetic calorimeter (ECAL), and hadron calorimeter (HCAL) are all installed inside the solenoid, thus minimizing energy losses due to particle interactions in front of the calorimeters. Outside the solenoid is the iron return yoke of the magnet, interlaced with layers of muon detector. The detector is 15 meters high, 21.6 meters long, and weighs a total of 14,000 tons. A schematic view of the CMS detector and its components is shown in Figure 2.3. The CMS detector uses a coordinate system as shown in Figure 2.4. It is oriented such that the x-axis points to the center of the LHC ring, the y-axis is pointing vertically upwards, and the z-axis is in the direction of the opposite proton beam, anti-clockwise, when looking at the LHC from above. The origin is centred at the nominal collision point within the experiment. The azimuthal angle, ϕ, is measured from the x-axis in the (x, y) plane. The polar angle θ is measured with respect to the z-axis in the plane (r, z), where r is the radial coordinate in the plane (x, y). The pseudo-rapidity eta is defined as $-ln\ tan(\frac{\theta}{2})$.

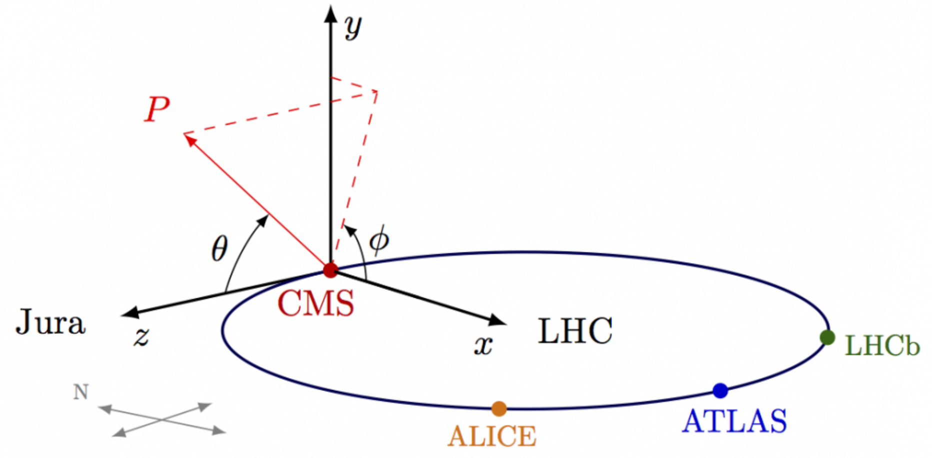

Figure 2.4: An illustration of the CMS coordinate system [57].

2.2.1 Tracker

The internal tracker is the innermost layer of CMS, and it is designed to observe the trajectories of charged particles with the least amount of disturbance. These trajectories, or "tracks," can be used to measure the momentum of the particles based on their curvature in the magnetic field and also to infer the position of the interaction vertices, from where multiple tracks originate. The successful design of a tracking system requires compromises between strict and competing constraints. Trackers should reach as close as possible to the beam line (within a few centimetres) to provide accurate vertexing, but they need to maintain sparse channel occupancy for unambiguous assignment of hits from nearby particles in busy environments. Together, these requirements impose a channel segmentation of the order of 100 μm. Trackers should also extend to large radii from the interaction point, with as many intermediate measurement layers as possible, to ensure accurate curvature measurement for very high momentum and straight tracks. The ideal detector technology that can meet practically all of these limitations, particularly those related to accuracy, timing, radiation stiffness, and mass, are silicon sensors. In a region with a radius of less than 10 cm, higher track density requires the use of pixel sensors to ensure an occupancy of less than 1%. At larger radii, the occupancy can be controlled using narrow sensors in only one dimension, the so-called ”strips”. A diagram of the entire tracking system is shown in Figure 2.5.

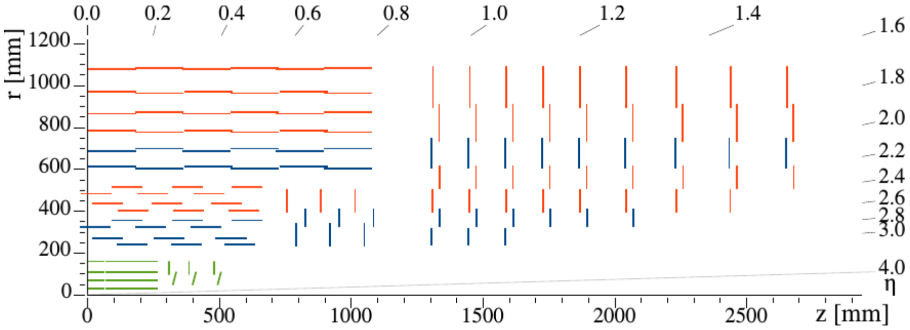

Figure 2.5: Sketch of one quarter of the Phase-1 CMS tracking system in r-z view. The pixel detector is shown in green, while single-sided and double-sided strip modules are shown as red and blue segments, respectively [58]

Pixel Detector

The pixel detector is the closest detector to the point of interaction and is responsible for providing accurate measurements of the impact parameters needed to achieve effective vertexing as well as providing seeds for track reconstruction. The original CMS pixel detector has been replaced with an upgraded pixel system (CMS Phase-1 pixel detector) in the extended year-end technical stop of the LHC in 2016/2017. The upgraded CMS pixel detector is designed to cope with the higher instantaneous luminosities that have been achieved by the LHC after the upgrades to the accelerator during the first long shut-down in 2013-2014. Compared to the original pixel detector, the upgraded detector has better tracking performance and lower mass with four concentric barrel layers (L1-L4) at radii of 29, 68, 109, and 160 mm, and three disks (D1-D3) on each side at distances of 291, 396, and 516 mm, to provide hit coverage up to an absolute value of pseudorapidity of 2.5. The pixel detector diagram can be seen in Figure 2.6.

Strip Tracker

On their way out of the tracker, particles pass through ten layers of silicon strip detectors, reaching out to a radius of 130 centimetres [60]. Since the track impact

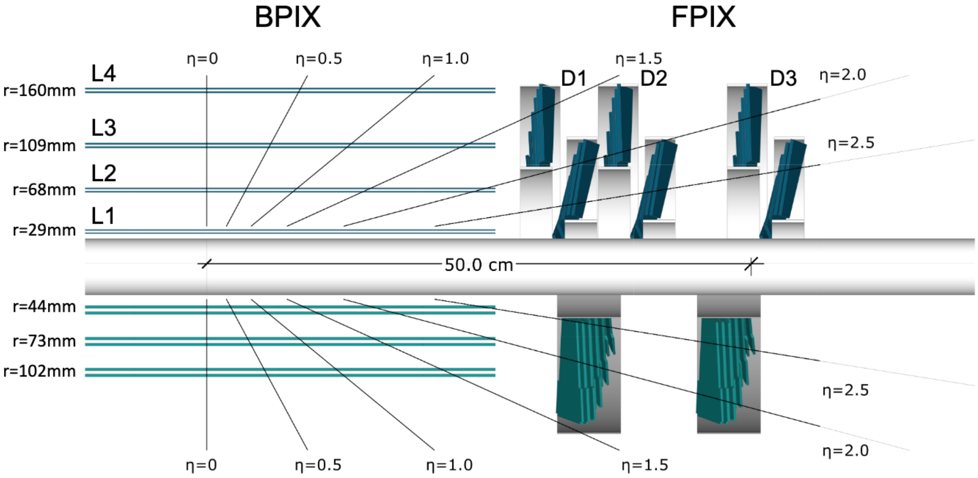

Figure 2.6: Layout of the CMS Phase-1 pixel detector in longitudinal view, where BPIX is the barrel pixel detector and FPIX is the forward disks [59].

parameters are already very precisely constrained by the pixel detector, the primary purpose of the strips is to carefully follow the track curvature in the magnetic field, with a longer arm and better sensitivity to small angular deviations from straight tracks. The strip detectors work in much the same way as pixels: as a charged particle crosses the material, it knocks electrons from atoms, and within the applied electric field, this movement gives a very small pulse of current lasting a few nanoseconds. This small amount of charge is then amplified, giving us "hits" when a particle passes, allowing us to reconstruct its path. The layout of the CMS silicon strip tracker is shown in Figure 2.7. The detector has 10 layers in the barrel region, with 4 layers in the Tracker Inner Barrel (TIB) and 6 layers in the Tracker Outer Barrel (TOB). The TIB is supplemented with 3 Tracker Inner Disks (TID) at each end. In the forward region, the detector consists of Tracker End-Caps (TEC) at each end, as shown in Figure 2.7. Each TID is composed of 3 rings, and each TEC is composed of up to 7 rings.

2.2.2 Calorimeter

The CMS calorimeter system is designed to measure the energy of hadronic jets and electromagnetic cascades produced by photons and electrons and to provide tight coverage to allow measurement of the missing transverse energy. There are two

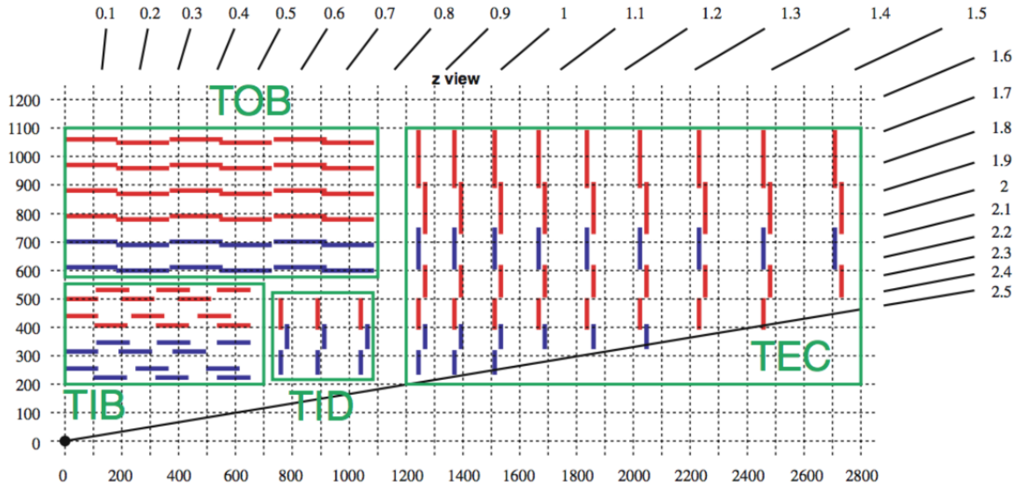

Figure 2.7: The layout of the CMS Silicon strip trackee [60].

kinds of "calorimeters" in CMS. The Electromagnetic Calorimeter (ECAL) is the inner layer of the two and measures the energy of electrons and photons by stopping them completely. Hadrons, which are composite particles made up of quarks and gluons, fly through the ECAL and are stopped by the outer layer called the Hadron Calorimeter (HCAL).

Electromagnetic Calorimeter ECAL

The electromagnetic calorimeter (ECAL) aims to measure electrons and photons emerging from the interaction point. At higher energies, electrons interact mainly with matter through bremsstrahlung radiation. High-energy photons, in turn, produce pairs of electrons and positrons, so photons or electrons can rapidly multiply in an electromagnetic shower or cascade containing thousands of electrons, positrons, and photons. Electromagnetic showers are easy to describe, with predictable size and particle composition, as well as minimal energy loss by invisible excitation. The ECAL is a scintillating crystal calorimeter, with lead tungstate ($PbWO_4$) selected as the crystalline material. Lead tungstate is a strong radiation scintillating material characterized by a small moliere radius (21.9 mm) and a short radiation length (8.9 mm), which allows for good shower containment in the limited space available for the ECAL. A longitudinal view of the ECAL quadrant is shown in Figure 2.8. The

ECAL consists of 61200 crystals in the barrel (EB), covering a pseudorapidity range of $|\eta| < 1.5$ and 14648 crystals at the endcaps (EE), which cover a pseudorapidity range of $1.5 < |\eta| < 3.0$.

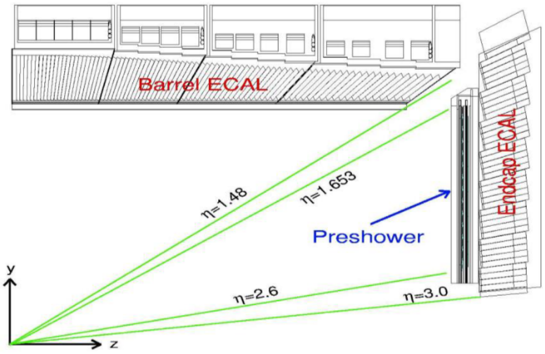

Figure 2.8: The ECAL geometry and preshower detector for a CMS detector quarter [61].

Hadron Calorimeter HCAL

The hadronic calorimeter (HCAL) [62] is outside of the ECAL but still mostly contained within the solenoid. HCAL identifies different particles, especially hadronic jets [63], but can also identify electrons, photons, and muons along with information from ECAL and muon systems. The HCAL is placed in a space bound on one side by the electromagnetic calorimeter (R = 1.77 m) and on the other side by the magnetic coil (R = 2.95 m). Due to the limited space, the CMS HCAL is compact in design and mainly made of materials with short interaction lengths. The HCAL is also supported by an external hadron calorimeter or tail catch to compensate for its smaller size and increase accuracy by capturing hadron shower tails. The HCAL is a compact, uncompensated, sampling calorimeter [64], consisting of layers of brass absorbers and plastic scintillators, that destructively measures the energy of hadron jets. The forward hadron calorimeter is placed 11.2 meters from the interaction point to expand the pseudorapidity coverage ($3.0 < |\eta| < 5.0$). The HF subdetector is a Cerenkov light detector consisting of quartz fibers embedded within a steel absorber 165 cm long.

Figure 2.9 shows the longitudinal view of a CMS HCAL. The HCAL detector is organized into four main sub-sections. These are the barrel (HB), endcap (HE),

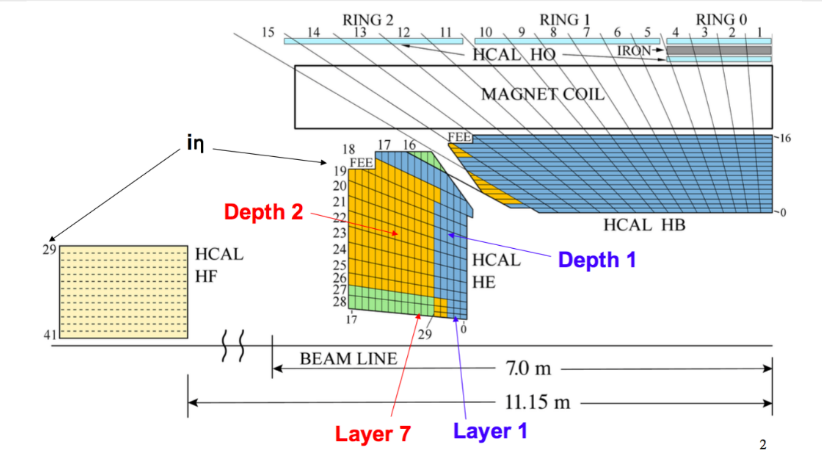

Figure 2.9: CMS Hadron Calorimeter layout (longitudinal view) [65].

forward calorimeter (HF) and external calorimeter (HO). The HB covers the pseudorapidity range up to 1.4, HE covers the range 1.4 to 3.0, and HF covers the range from 3 to 5.

2.2.3 Superconducting Magnet

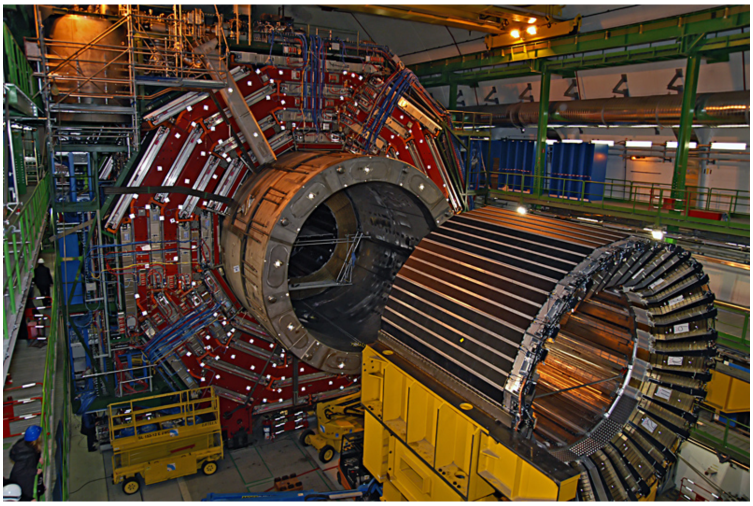

Figure 2.10: The central part of a CMS is held by a magnet in the large experimental cave [66].

The CMS superconducting magnet is a hollow cylinder (13 meters long and 6 meters in diameter, as shown in Figure 2.10). An electrical current of 19 kA flows through the niobium and titanium fibers that form the solenoid, providing a maximum magnetic field of 3.8 Tesla and storing a maximum energy of 2.6 GJ. The superconducting conditions are maintained by a liquid helium cooling system, which keeps the temperature of the solenoid at 4.5 K to avoid stray fields. The magnetic field lines are closed by the return yoke, consisting of 10 kilotons of magnetized iron blocks, which is located outside part of CMS and alternates with muon chambers. The homogeneous magnetic field inside the detector bends the tracks of the charged particles, allowing the measurement of their momenta. The momentum analysis of the charged particles is performed by measuring the paths of the particles within the solenoid. Expressing r in metres, B in T, and the transverse momentum in GeV is given by: $\mathrm{p}\ [\mathrm{GeV}] = 0.3 \times \mathrm{B}\ [\mathrm{T}] \times \mathrm{r}\ [\mathrm{m}]$. Where p is the momentum of the particles, B is the range of magnetic field strength, and r is the radial coordinates of the trajectory. Therefore, a strong field and a large radius are an efficient approach to reaching optimal momentum resolution. CMS made the choice of a high field within a compact space.

2.2.4 Muon System

The muon system occupies the outermost regions of CMS. Muons are a very powerful handle in the LHC that is distinctive and easily measured, and is often a signature of an interesting process worth recording. Thanks to their large mass, which is 200 times that of an electron, high-energy muons are less sensitive to deflection by atomic electrons in the material they cross and have small radiation losses and no hadronic interaction. As a result, they can travel farther through the material (about 1 meter of rock per GeV!) and easily penetrate the CMS calorimeters and the solenoid. Dedicated detectors outside the solenoid can easily recognize muons and carefully measure their tracks, which are still relatively faithful representations of their initial momenta.

Muons hold significant branching ratios for the final states of nearly all of the interesting Standard Model particles that can be observed in the LHC: Higgs, W, Z bosons, top quarks, and B-flavor hadrons, as well as many extensions of the Standard Model, such as the higher mass gauge bosons (Z') or heavy Neutral Lepton (HLN) (subject of this thesis). For decades, muons have been a fundamental tool in the discovery of every new massive elementary particle. For example, the production of $\mathrm{H} \rightarrow \mathrm{ZZ} \rightarrow 4\mu$ was considered the golden channel for detection of Higgs, with low background and excellent mass resolution provided by muons.

There are three muon systems in the determination CMS: drift tubes (DTs), which occupy the barrel; cathode strip chambers (CSCs), covering the endcap region; and resistance plate chambers (RPCs), which give redundancy in both the barrel and end cap regions.

Resistive plate chamber (RPC)

Resistance plate chambers are parallel plate gas detectors with a positively-charged anode and a negatively-charged cathode, both made of a very high resistivity plastic material and separated by a gas volume. Figure 2.11 depicts a single RPC. When a muon passes through the chamber, electrons are knocked out of gas atoms. These electrons in turn hit other atoms, causing an avalanche of electrons. The electrodes are transparent to the signal (the electrons), which is instead picked up by external metallic strips after a small but precise time delay. The pattern of hit strips gives a quick measure of the muon momentum, which is then used by the trigger (see chapter 3) to immediately decide whether the data is worth keeping. RPCs combine good spatial resolution with a time resolution of just one nanosecond (one billionth of a second). The RPCs are used in both the barrel and end-cap regions.

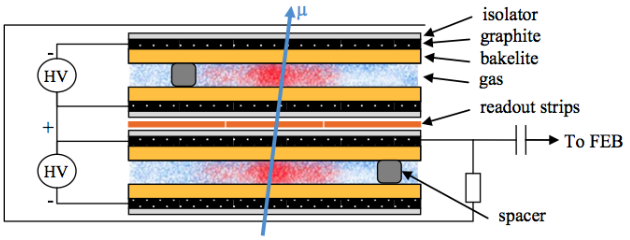

Figure 2.11: A slice of one of the CMS muon resistive plate chambers [67].

Drift tubes (DT)

The choice of the drift tube detector in the barrel is motivated by the relatively low particle rates and magnetic field strength in this region. When a muon or any charged particle passes through the volume, it knocks electrons off the atoms of the gas. These follow a cloud of electrons that are drifting towards the positively-charged wire. The drift time is measured and converted to distance using the knowledge of the drift velocity. A single drift cell, as shown in Figure 2.12, has a cross section of $42 \times$ x 13 mm^2 and a wire length of 2 to 3 m. It is filled with a mixture of 85/15% Argon and $_2$, giving a maximum drift time of 350 ns.

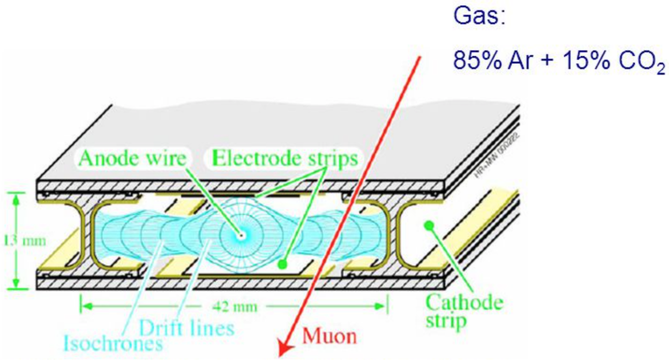

Figure 2.12: Drift tube layout [56].

Cathode strip chambers (CSC)

To deal with significantly higher endcap occupancy, it is essential to use ionization chambers with a finer wire pitch (and thus faster signals) and the ability to measure the coordinates of each avalanche. Cathode strip chambers achieve this by using anode wires with a 3.2 mm pitch of measurement, wrapped around cathode strips that measure ϕ. The strips and wires were arranged according to the wedge geometry shown in Figure 2.13. Ionization signals from muons form avalanches near the anode wires just as they do in drift tubes, but in addition to this, the avalanche forms an image charge on the cathode strips, and interpolation between analog signals gives a precise measurement of coordinates ϕ. Each CSC chamber contains 7 layers of cathode strip panels, with wires wrapped around alternating layers, for a total of 6 wire layers. The resolution combining all the layers in each chamber is approximately 70–150 μm toward the ϕ direction, and the signals are resolved in 25 ns with an ultimate time resolution of 4 ns (for a drift velocity of 60 μm ns^{-1}, this indicates a z resolution of a couple hundred μm).

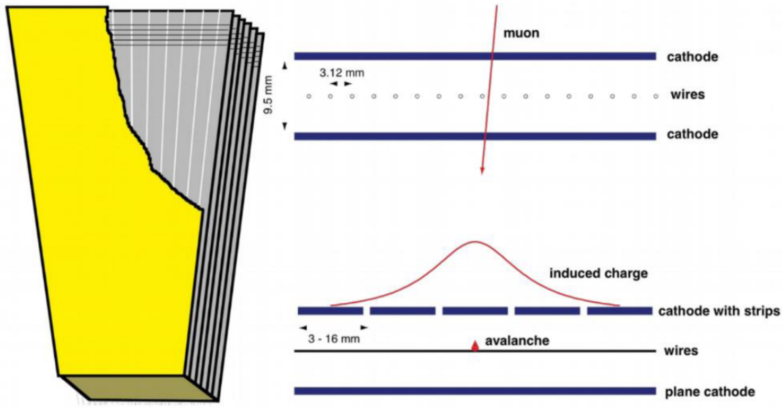

Figure 2.13: CSC with 6 layers, with radial cathode strips and transverse anode wires (left) and a gas-gap schematic view showing the charge induced by the traversing muon [68].

2.2.5 Overview of CMS during LHC Run 2

The Compact Muon Solenoid (CMS) detector is one of the two multipurpose experiments at the Large Hadron Collider (LHC). CMS has successfully collected data during run1 (2010–2013) and achieved important physics results, like the discovery of the Higgs boson announced in 2012.

The LHC run2 started in 2016 and finished in November 2018, for a total delivered luminosity (number of collisions per unit area over a period of time) of $\sim$137 fb^{-1}, during which the CMS detector ran in general stably and with very high efficiency and negligible dead time, also at the highest luminosities. Several upgrades and changes were made in 2017-2018. For example, in 2017, a new pixel detector was installed, and the readout of the Hadron Forward (HF) calorimeter and of a 20° sector of HCAL were upgraded. The upgrades already showed the detector performance benefits, and CMS worked well with very good recording efficiency and a high and stable fraction of active channels, and is ready to unravel further open questions, such as the ones not yet explained by the Standard Model.

Chapter 3

Trigger and Data Acquisition

In this chapter, we will discuss the CMS trigger system in detail, with special attention to HLT (High Level Trigger), since I have participated in the CMS data taking process in 2018 by doing many shifts as an HLT DOC (Expert Detector On Call). I even broke the record for the number of shifts performed in one year by one person, and as a result, was awarded the 2018 CMS Achievement Award through the HLT group.

The trigger system in a High Energy Physics (HEP) experiment determines when the signals are read from the detector and written for storage for later analysis. The first trigger ever, for example, activated a cloud chamber when a passing high-energy particle caused synchronized signals in Geiger counters surrounding the chamber [69]. The triggers in LHC experiments perform the same process; they determine when something interesting is occurring and trigger the read-out of the detector for later analysis. The CMS systems can perform a considerably more complex analysis to make a decision, but the principle is the same. At the center of mass energy of 13 TeV (during the second run), the total pp cross-section is about 72–78 mb [70], which is a much larger production cross-section than the one for the more interesting processes in the LHC, such as the ee cross-section ($\sim$40 nb [71]). This high pp cross-section leads to an average of 25 interactions within the CMS detector for each bunch crossing. Given the typical event size of about 1MB, recording each bunch crossing at 25 ns intervals could produce 40 terabytes of data per second [70]. The job of the CMS experiment operating systems is to keep this data acquisition rate within the maximum range of 1000 events per second. The CMS trigger design layout is illustrated in Figure 3.1, which is implemented as a two-tier system, with the first level (Level 1) based on dedicated hardware triggers and the second level software-based triggers (HLT) running on a large farm of computers [70].

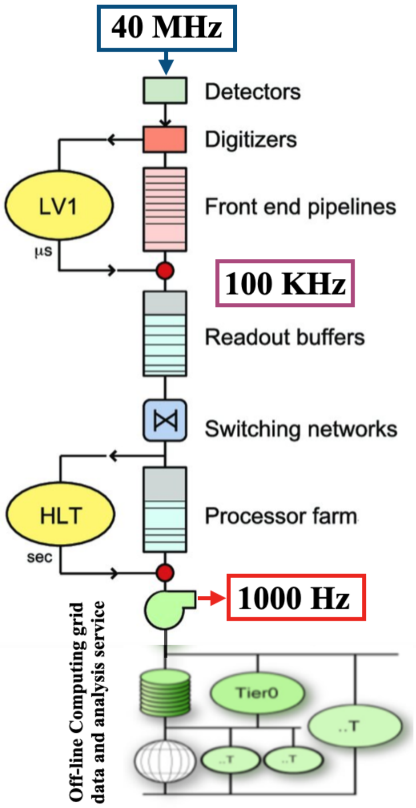

Figure 3.1: Data flow architecture of the CMS trigger and data [72].

3.1 Level-1 Trigger

The L1 Trigger [73] is a hardware-implemented fixed-latency trigger with a design output rate of 100 kHz and a response time of about 3.8 μs. L1 trigger hardware consists mainly of field programmable gate array processor technology with application-specific integrated circuits and programmable memory look-up search tables used in a special case where speed and radiation resistance are of great importance. The L1 trigger system relies on the coarse information provided by the calorimeters and the muon system to identify or reject objects. A schematic representation is shown in Figure 3.2.

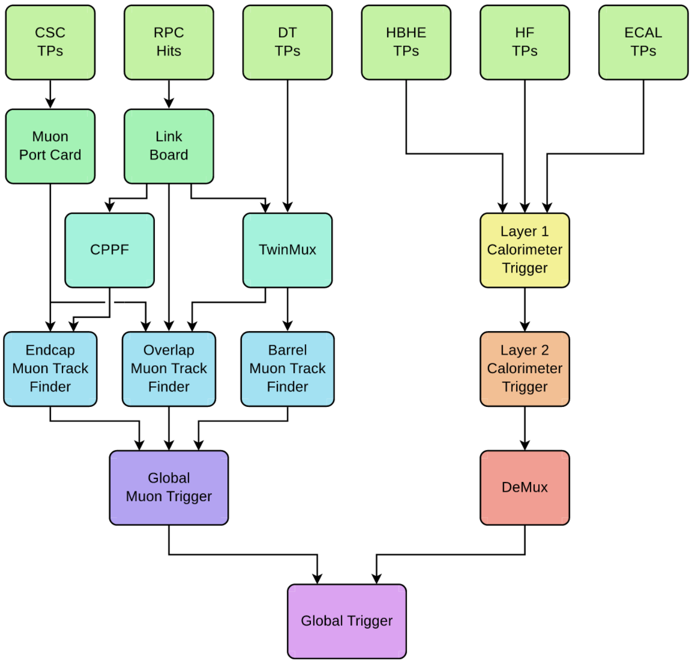

Figure 3.2: CMS Level-1 trigger block diagram: Calorimeter and muon detectors [73].

The muon trigger is divided into three subsystems, each of which processes muon hits within a defined η range. The barrel muon track finder (BMTF) looks for tracks in the detector's $|\eta| < 0.8$ region, where muons only hit the barrel's DTs and RPCs. The overlap muon track finder (OMTF) processes data in the $0.8 < |\eta| < 1.25$ region, which corresponds to the muon detector overlap between the barrel and endcap. The endcap muon track finder (EMTF) reconstructs muon tracks in the $|\eta| > 1.25$ range, which corresponds to the region where the endcap muon detectors (RPCs and CSCs) are located. The muon candidates are then sent to the Global Muon Trigger (GMT), which ranks them according to p_T and quality and removes duplicates.

The calorimeter information is read in units known as "trigger towers" (TT), the transverse energy measured in the calorimeters is transferred to the L1 Calorimeter Trigger in the form of "trigger primitives". The data is transmitted via the Time Multiplexed Trigger (TMT) architecture, which allows the whole calorimeter data to be processed at once by a single trigger processor. The trigger primitives are then combined to reconstruct calorimeter trigger objects such as electrons, photons, hadronic tau leptons, jets, and energy sums.

Finally, the Global Trigger (GT) decides whether to keep or reject the event depending on the information collected by the L1 Calorimeter Trigger and the L1 Muon Trigger. L1 selection algorithms are commonly referred to as ”seeds”.

3.2 High Level Trigger HLT

The HLT is responsible for the final trigger decision before storing the event to disk. During the first and second runs, the HLT is a farm of CPUs located on the surface directly above the CMS detector, consisting of about 1000 compute nodes. The software operating on nodes implements several ”trigger paths”, which require reconstructions of sub-detector signals in particle hypotheses and kinetic parameters on particles that determine whether the path succeeds or fails. The software running at the HLT farm is a modified version of the CMS software, CMSSW [74], optimized for low latency to create a trigger decision.

3.2.1 HLT Menu

The HLT menu in CMS is a set of modules written in C++, shown graphically in Figure 3.3. The menu is divided into paths (more than 400 different HLT paths have been prepared for the data taking at Run2). Each path is a sequence of reconstruction and filtering modules and reproduces the offline selection for a given physics object (photons, electrons, muons, jets, missing momenta, b-tagged jets, etc.). The modules within a path, either object producers or filters, as shown in Figure 3.4, are arranged in blocks of increasing complexity, so that the faster algorithms run first and their products are filtered. If a filter fails, the rest of the path is skipped.

In order to explain in some details the functioning of a HLT trigger path [76], we consider as an example a hypothetical trigger that requires MET (Missing Transverse Energy) $>$ 120 GeV plus one b-tagged jet (jets originating from bottom quarks). A typical sequence of selections used in a HLT path with b tagging uses the following

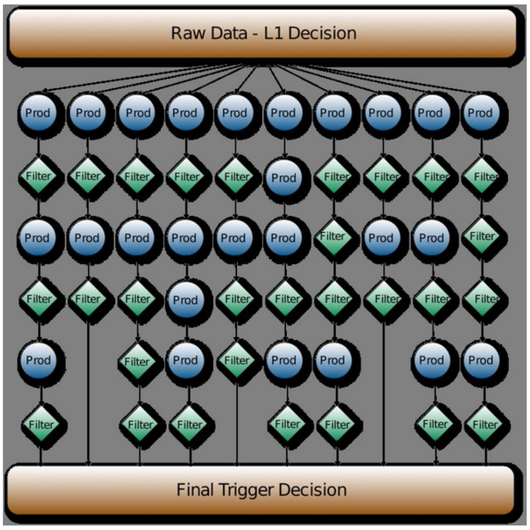

Figure 3.3: Schematic representation of HLT menu in CMS and of the HLT paths. The final trigger decision is the logical OR of the single path decisions. [75].

information: L1 seed (L1T precondition), calorimetric objects (objects reconstructed in a calorimeter sub-detector), b tagging with regional tracking (tracks reconstructed around physical objects), and PF (Particle Flow) objects.

- **L1 seed** [Input rate ∼100 kHz; Time < 1 ms]. Each HLT path runs over every event accepted by the L1 trigger (∼100 kHz). The first cut of a HLT path is the selection of a specific L1 trigger seed, i.e., a specific trigger in the L1 menu or a logical combination of them. In the example, the L1 seed used is MET > 70 GeV. The cut on the L1 seed reduces the rate by a factor ∼10.

- **L2 Calorimetric selection** [Input rate ∼10 kHz; Time ∼50 ms]. Since the reconstruction of the calorimetric objects (e.g., calorimetric MET) is very fast, it usually takes place right after the L1 seed selection. The resolution of these objects is worse compared to the PF objects, but they can be reconstructed in only ∼50 ms, 20 times faster than the corresponding PF objects. In the example, the L2 cuts used are: calorimetric MET > 70 GeV and two calorimetric jets with $p_T > 30$ GeV and $|\eta| < 2.6$. Usually, the L2 cuts reduce the rate by a factor of 5 to 10.

- **L3 Regional tracking** [Input rate ∼2 kHz; Time ∼100 ms]. As tracking is a slow process, the tracker information is not used in the L1 and L2 stages. Still, tracks are essential for many tasks, such as distinguishing between photons and electrons, identifying b and τjets (jets originate from tau decay), evaluating the track-based lepton isolation, and measuring precisely the lepton momentum. To take advantage of the tracking information at HLT, two strategies are used: run tracking over a small fraction of events and only in the regions of interest (cones of size $\Delta R = 0.4$ around the calorimetric objects). In the example, regional tracking is used to perform b tagging and it is used to reduce the rate down to ∼500 Hz.

- **PF sequence** [Input rate ∼500 Hz; Time ∼1000 ms]. The Particle Flow (PF) sequence is the most accurate and slowest reconstruction sequence available at HLT. Usually, the tightest cuts at HLT are applied to PF objects. The PF sequence used at HLT is similar to the offline version but uses a simplified version of tracking. The HLT PF tracking reconstructs only tracks close to the leading primary vertices and with $p_T >$ of 500 MeV. Then, tracks are linked to objects reconstructed with the calorimeters and the muon chambers. The PF sequence reconstructs all high-level objects: jets, MET, electrons, photons, muons, τ leptons, etc. In some HLT paths, the PF tracks are also used to perform b-tagging on PF jets. In the example, the PF objects are used for the final cut MET $>$ 120 GeV, reducing the rate to ∼10 Hz.

The example above shows how HLT can reduce the rate from 100 kHz to 10 Hz using a specific path targeting a specific physics channel, and we can generalize the same concept to all physics channels.

Subsequently, the output events are grouped into a set of streams, with special sets of data files produced for each stream. The grouping of events is done based on their offline usage. For example, the primary stream is "Stream A," or the "physics" stream Figure 3.5, which consists of events that meet the needs of most offline physics analysis. Other streams serve special purposes, such as monitoring the performance of the HLT algorithms.

HLT menus are validated in an on-line environment using the HLT on-line ("HiLTOn") test stand [78]. In order to be as close as possible to the on-line environment, the HiLTOn is operated using the same run control interface as the CMS DAQ (Data Acquisition System). The HLT validation is designed to maximize the performance and stability of HLT algorithms. Since every event that meets L1 trigger requirements is examined by the HLT, and various HLT decisions are based on analysis-quality physics objects reconstructed using information from all CMS sub-detectors, the reliability of the HLT is essential to the success of the experiment.

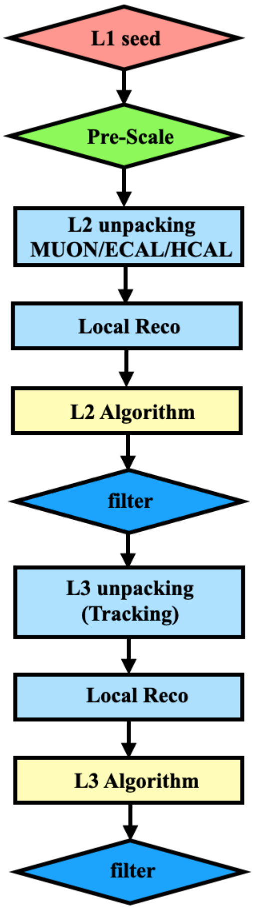

Figure 3.4: Schematic representation of the standard HLT sequence which define input and output of the HLT path.

3.2.2 HLT Menu Development

The flexibility of the trigger system allows for effective modifications to achieve optimum performance, proportional to actual operating conditions while data is being taken. The robustness of the algorithms defining the trigger primitives also ensures that the system will not be overly sensitive to small changes with respect to expected conditions. In preparation for data taking, the HLT menus were developed using fully simulated and reconstructed Monte Carlo events for well-known standard model processes, dominated by QCD events at low transverse momentum, also known as minimum bias events.

The goal is to achieve a reduction factor of ~ 1000 on the HLT input rate while maintaining the highest possible efficiency for the events of interest, with an average

Figure 3.5: Stream A which responsible for the physics of primary data set [77].

processing time per event for a single HLT instance not exceeding 50 ms [79]. To meet these requirements, the menus are organized as a set of playback paths, each dedicated to identifying events with a specific topology and mobility. The CPU time required to implement HLT algorithms in a filter farm is reduced by rejecting events as quickly as possible, using a limited amount of detector information. Filter modules are added between the reconstruction sequences in each path, such that if the requirements do not match, the rest of the path will not be executed.

In particular, each HLT path begins with a specific L1T precondition (i.e., a logical combination of a set of L1 bits). Moreover, the parts of the detector indicated by the L1T candidates (the candidate physical elements on which the L1T decision was based) are usually considered for further validation of the trigger object being examined. The physical parameters (transverse momentum, pseudorapidity, and azimutal angle) of the L1T candidates can also be used as a starting point (”seed”) for the HLT reconstruction process. Obviously, choosing to consider only a portion of the detector information to reconstruct the event is not mandatory but is driven by the need to save processing time. In any case, the entire detector data is at our disposal in any case to be used by HLT algorithms if required. The repetition of the same operations is reduced. The framework ensures that identical instances of the same reconstruction are executed on multiple paths only once. After each possible reconstruction step, a set of selection criteria applied to the reconstructed objects rejects a large portion of the events, thus reducing CPU usage in the next step.

3.2.3 Object Reconstruction at HLT

As we explained in the previous section, the HLT menu contains several paths, each corresponding to a custom trigger (such as a single-electron or a 3-jet-with-MET). The path consists of several steps (software modules), each module performing a well-defined task such as unpacking (from raw to Digi), reconstructing physics objects such as electrons, muons, jets, and MET, and implementing intermediate decisions that lead to more accurate reconstructions in subsequent modules, or calculating the final decision of the trigger path. The CMSSW framework ensures that if the decision of the intermediate filter on the trigger path is negative, the rest of the path will not be executed and the specified trigger will be considered to have rejected the event. To save the CPU time, each reconstruction step is followed by a filter, which prevents time-consuming reconstruction code from being run if it is already clear that it will not be needed. Each HLT trigger path must be seeded by one or more L1 trigger bit seeds. The first filter module in each HLT path searches for an appropriate L1 seed to use as a starting point for that specific HLT trigger.

Track Reconstruction

Tracking is very crucial for reconstruction at the HLT level. Powerful and effective tracking can assist in particle reconstruction and can enhance their resolution in various ways. For example, it reduces the trigger rate of muons by greatly improving the momentum resolution. The cluster energy in electromagnetic calorimeters can be identified as electrons or photons depending on the presence of the track. The background rejection rate of lepton triggers can be increased by requiring the isolation of leptons. It is also possible to trigger the jets produced by b quarks by calculating the number of trajectories in a jet with a transverse impact parameter inconsistent with tracks arising from the beamline. It is possible to trigger hadronic τ decay by finding a narrow, isolated jet using tracks along with calorimeter information.

Muon Identification and Reconstruction

The high-level muon triggers in a CMS collect information from tracker and muon sub-detectors to identify muon candidates and measure their transverse momenta p_T. The algorithm consists of two main steps: Level 2 (L2), which uses information from the muon system only, and Level 3 (L3), which combines measurements from both the tracking system and muon sub-detectors as shown in Figure 3.4. In L2, the track reconstruction in muon spectrometry begins from an initial state, called a seed, constructed from the RPC, DT and CSC segment patterns. The L3 muon trigger algorithm consists of three main steps: seeding candidate muon tracks starting from the L2 information; track reconstruction in the tracker; and combined fit in the tracker and muon systems. In Figure 3.6, the efficiency turn-on curve for an isolated trigger path requiring a single muon with a p_T threshold of 24 GeV is shown. The isolation of L3 muons is evaluated by combining information from the silicon tracker, electromagnetic ECAL, and hadronic calorimeters (HCAL). The tracks in the silicon tracker are reconstructed into a geometric cone of size $\Delta R = \sqrt{\Delta\eta^2 + \Delta\phi^2} = 0.3$ around the L3 muon. In the same cone, the deposits of ECAL and HCAL are reconstructed. To minimize the dependence of the isolation variable on the pileup of pp collisions, the calorimeter deposits are corrected for the average energy density of the event.

Particle Flow Jets

In the HLT, jets are reconstructed using the clustering algorithm anti-K_T with a cone size of R = 0.5 [81]. The inputs to the jet algorithm can be calorimeter towers (called CaloJet) or reconstructed particle flow objects (called PFJet). The particle flow technique allows information from all detectors to be used and combined together to reconstruct objects [81]. Most jet trigger paths use a PFJet. Due to the large CPU consumption of the HLT particle flow algorithm, PFJet trigger paths will have CaloJet based on pre-selection before the reconstructing of particle flow objects, and PFJets will be formed. Matching between CaloJet and PFJet is also required in individual PFJet paths. In Figure 3.7, the efficiency turn-on curve is shown for three different trigger paths requiring PFJets with different p_T thresholds.

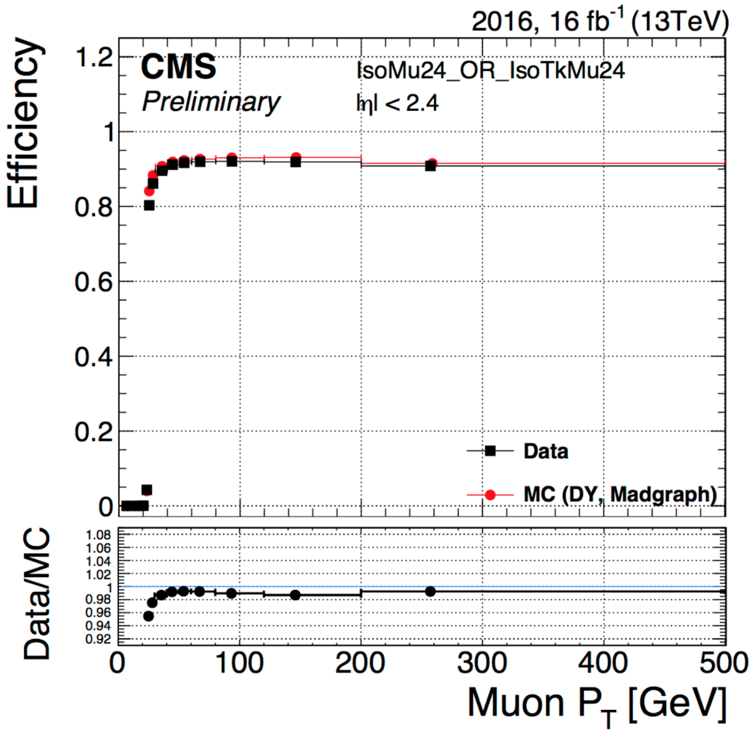

Figure 3.6: efficiency as a function of p_T with respect to the offline reconstructed muon passing identification and isolation requirements [80].

Photon and Electron at HLT

In HLT, electron and photon selection continues, requiring a super cluster with an E_T above a certain threshold matching the L1 electromagnetic candidate. HLT runs the standard ECAL super-clustering algorithm with nearly identical settings as for offline reconstructions. The global selection of electrons and photons goes through three steps. The first step uses only the calorimeter information. The second step requires hits in pixel detectors, consistent with the electron candidate. The success of the ECAL super-cluster matching to hits in the pixel detector causes the candidate to be distinguished as an electron, otherwise the candidate is marked as a photon. In the final step, the electron selection uses full track reconstruction, seeded by the hits in pixels obtained through the matched step. Alternatively, the selection of photons can be done by cutting on the isolation, rejecting π^0 based on the lateral shape of the shower and the reconstruction of converted photons. In Figure 3.8, the efficiency turn-on curve is shown for electrons as a function of the reconstructed electron transverse momentum.

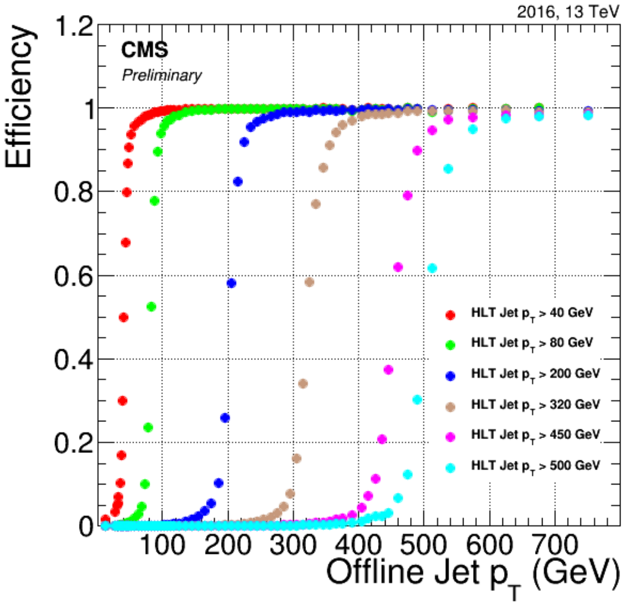

Figure 3.7: The efficiency to reconstruct and identify the (AK4) jet at the High Level Trigger (HLT) [80].

3.3 CMS Trigger Performance at Run2

The performance of the CMS trigger system has been evaluated in two stages [77]. First, using tag-and-probe techniques, the performance of the L1 and HLT systems was evaluated for individual trigger objects such as electrons, muons, photons, or jets. This is a generic tool developed to measure any defined object's efficiency by exploiting di-object resonances like Z or J/Psi [82]. Most of the measurements considered come from the 2016 CMS data set, where data has been collected at $\sqrt{s}$ = 13 TeV. Performance has been evaluated in terms of efficiency with respect to offline quantities to find the appropriate trigger rate. Both the L1 and HLT performances have been studied, showing the high selection efficiency of the CMS trigger system. Second, the performance of the trigger system has been demonstrated by considering key examples across different physics analyses. In CMS, the HLT decisions are often derived from complex correlated combinations of single objects such as electrons, muons, or τ leptons. The trigger system's wide range of capabilities has been shown through examples in Higgs boson, top quark, and B physics, as well as in searches for new physics (e.g., Heavy Neutral Lepton HNL). The trigger system has played an important role in the successful collection of the data for physics

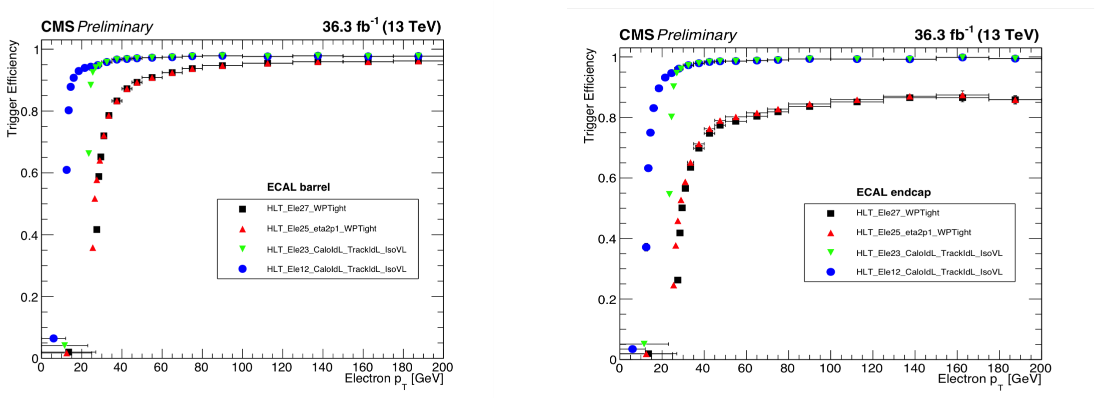

Figure 3.8: The electron efficiency as a function of reconstructed electron transverse momentum (p_T) , in the left) barrel and on the right) endcap parts of the detector [80].

analyses in Run 2 of the CMS experiment at the LHC. Efficiencies were measured in data and compared to simulation, and were shown to be high and well-understood. Many physics signals were collected with high efficiency and flexibility under rapidly changing conditions, enabling a diverse and rich physics program, which has led to hundreds of publications based on the Run 2 data samples.

Chapter 4

Physics Object, Data and Monte Carlo Simulation

After the collision of the proton bunches inside the detector, the collision debris in the form of charged particle tracks in the tracker, energy clusters in the calorimeters, and hits in the muon system is first reconstructed (based on trigger decision). These in turn are given as input to advanced algorithms to reconstruct higher level physics objects such as electrons, muons, jets, tau, and missing energy. This chapter describes the definition of the selection criteria of physics objects used in this analysis, after presenting a list of background Monte-Carlo samples used together with datasets and triggers. The second part of the chapter is dedicated to studies on secondary vertex reconstruction, in particular, the tuning of the Inclusive Vertex Finder (IVF) algorithm, which uses a variant of the CMS standard b-quark tagging. Finally, we introduce a custom deep neural network architecture for secondary vertex tagging.

4.1 Data and Monte Carlo simulation

The results presented in this thesis are based on the pp collision dataset recorded at a centre of mass energy of 13 TeV by the CMS detector in 2016, 2017 and 2018, corresponding to an integrated luminosity of 35.9 fb^{-1}, 41.5 fb^{-1}, and 59.7 fb^{-1}, respectively. Two datasets are used, depending on the flavour of the prompt lepton produced in association with the HNL:

- SingleMuon.
- SingleElectron (called EGamma in 2018).

Apart from the differences in proton–proton collisions provided by the LHC over the years (e.g., luminosity, number of interactions per bunch crossing, etc.), the CMS detector has undergone various upgrades and improvements during the Run 2 time period. To name a few that have an impact on this work, during the upgrade period between 2016 and 2017, a new pixel detector was installed [83] (see Section 2.2.1), the readout of the Hadron Forward Calorimeter and a 20° sector of HCAL were upgraded [84], and five chambers of new GEM detectors were installed in the Muon System's negative endcap [85]. In 2018, the pixel detector's DC–DC converters were replaced [83], the silicon strip tracker began operating at a lower temperature [60], a new mechanism for automatically recovering errors caused by particle interactions was installed in the ECAL DAQ [86], silicon photo multipliers were installed in the HCAL endcaps [84], and DTs were enhanced with micro trigger control and acquisition ROS [87]. All of the modifications to collisions and the detector have resulted in changes in the data. As a result, in this analysis, all of the results are split by the year of taking data.

The Monte Carlo (MC) simulations are used in this search to model both the known SM background processes based on the SM theory and the signal samples based on the νMSM. The MC events are the simulation of collisions produced in the LHC, including the detector response modeled here using the CMS detector simulation based on GEANT4 [88]. Simulated SM data sets include: V+jets, where V refers to W or Z bosons, tt+jets, single-top quark samples, diboson and triboson samples (WZ, WZZ, etc.). Three MC generators were used in the analysis: PYTHIA8.205 [89], POWHEG v2.0 [90] , and MADGRAPH5 aMC@NLO v2.4.2 [91]. For the purpose of hadronization and parton showering (which simulate the final states of the collisions), these samples use PYTHIA8.205. The 2016 (2017 and 2018) simulated dataset uses CUETP8M1 [92] (CP5[93]) PYTHIA8.205 underlying event parameters. The parton distribution function (PDF) [94] used in the 2016 (2017 and 2018) simulated data samples is NNPDF3.0 (N)LO [95] (NNPDF3.1NNLO [96]).

All background samples used are reported in Tables 4.1, 4.2, and 4.3 are generated to meet the data conditions. This includes information about the multiple pp interactions (pileup) conditions and the triggers used for the data.

Table 4.1: Simulated background samples with 2016 data-taking conditions and their effective cross sections.

Sample	No. events	Cross-sec. [pb]
TT_TuneCUETP8M2T4_13TeV-powheg-pythia8	76874504	831.76
DYJetsToLL_M-50_TuneCUETP8M1_13TeV-amcatnloFXFX-pythia8	120777245	6225.42
DYJetsToLL_M-10to50_TuneCUETP8M1_13TeV-amcatnloFXFX-pythia8	40364234	18610
WJetsToLNu_TuneCUETP8M1_13TeV-amcatnloFXFX-pythia8	237263153	61526.7
ST_s-channel_4f_leptonDecays_13TeV-amcatnlo-pythia8_TuneCUETP8M1	1000000	3.68064
ST_tW_top_5f_inclusiveDecays_13TeV-powheg-pythia8_TuneCUETP8M1	6952830	35.85
ST_tW_antitop_5f_inclusiveDecays_13TeV-powheg-pythia8_TuneCUETP8M1	6933094	35.85
ST_t-channel_top_4f_inclusiveDecays_13TeV-powhegV2-madspin-pythia8_TuneCUETP8M1	67105876	80.95
ST_t-channel_antitop_4f_inclusiveDecays_13TeV-powhegV2-madspin-pythia8_TuneCUETP8M1	38811017	136.02
WGToLNuG_TuneCUETP8M1_13TeV-amcatnloFXFX-pythia8	12219986	489
WWTo2L2Nu_13TeV-powheg-CUETP8M1Down	1988000	12.178
WWToLNuQQ_13TeV-powheg	6655400	49.997
WZTo3LNu_TuneCUETP8M1_13TeV-powheg-pythia8	1993200	4.42965
WZTo1L3Nu_13TeV_amcatnloFXFX_madspin_pythia8	1703772	3.033
ZGTo2LG_TuneCUETP8M1_13TeV-amcatnloFXFX-pythia8	14372682	117.864
ZZTo4L_13TeV-amcatnloFXFX-pythia8	10711278	1.212
ZZTo2L2Nu_13TeV_powheg_pythia8	8931750	0.564
ZZTo2L2Q_13TeV_amcatnloFXFX_madspin_pythia8	15462693	3.22
GluGluHToZZTo4L_M125_13TeV_powheg2_JHUgenV6_pythia8	999800	0.001034
TTGJets_TuneCUETP8M1_13TeV-amcatnloFXFX-madspin-pythia8	9877942	3.697
TTWJetsToLNu_TuneCUETP8M1_13TeV-amcatnloFXFX-madspin-pythia8	3120397	0.2043
TTZToLLNuNu_M-10_TuneCUETP8M1_13TeV-amcatnlo-pythia8	5934228	0.2529
VHToNonbb_M125_13TeV_amcatnloFXFX_madspin_pythia8	1007898	0.9520
WpWpJJ_QCD_TuneCUETP8M1_13TeV-madgraph-pythia8	146436	0.02696
WWW_4F_TuneCUETP8M1_13TeV-amcatnlo-pythia8	240000	0.2086
WWZ_TuneCUETP8M1_13TeV-amcatnlo-pythia8	250000	0.1651
WZZ_TuneCUETP8M1_13TeV-amcatnlo-pythia8	246800	0.05565
ZZZ_TuneCUETP8M1_13TeV-amcatnlo-pythia8	249237	0.01398

Table 4.2: Simulated background samples with 2017 data-taking conditions and their effective cross sections.

Sample	No. events	Cross-sec. [pb]
DYJetsToLL_M-50_TuneCP5_13TeV-madgraphMLM-pythia8	97620827	5340
DYJetsToLL_M-10to50_TuneCP5_13TeV-madgraphMLM-pythia8	39489640	15810
TTJets_DiLept_TuneCP5_13TeV-madgraphMLM-pythia8	27467268	54
TTJets_SingleLeptFromT_TuneCP5_13TeV-madgraphMLM-pythia8	61553087	109
TTJets_SingleLeptFromTbar_TuneCP5_13TeV-madgraphMLM-pythia8	55885392	109
WJetsToLNu_TuneCP5_13TeV-madgraphMLM-pythia8	77631106	52940.0
ST_s-channel_4f_leptonDecays_TuneCP5_13TeV-amcatnlo-pythia8	6167441	3.74
ST_t-channel_top_4f_InclusiveDecays_TuneCP5_PSweights_13TeV-powheg-pythia8	103813600	67.91
ST_t-channel_antitop_4f_InclusiveDecays_TuneCP5_PSweights_13TeV-powheg-pythia8	63488400	113.3
ST_tW_top_5f_inclusiveDecays_TuneCP5_13TeV-powheg-pythia8	7734344	34.97
ST_tW_antitop_5f_inclusiveDecays_TuneCP5_13TeV-powheg-pythia8	6509512	34.97
WWToLNuQQ_NNPDF31_TuneCP5_13TeV-powheg-pythia8	16354527	45.99
WWTo2L2Nu_NNPDF31_TuneCP5_PSweights_13TeV-powheg-pythia8	1992526	11.08
WZTo1L1Nu2Q_13TeV_amcatnloFXFX_madspin_pythia8	11347099	11.66
WZTo2L2Q_13TeV_amcatnloFXFX_madspin_pythia8	536667	6.331
WZTo1L3Nu_13TeV_amcatnloFXFX_madspin_pythia8_v2	2717911	3.342
WZTo3LNu_TuneCP5_13TeV-amcatnloFXFX-pythia8	6820606	5.052
ZZTo2L2Q_13TeV_amcatnloFXFX_madspin_pythia8	10695125	3.688
ZZTo2L2Nu_13TeV_powheg_pythia8	8733658	0.564
ZZTo4L_13TeV_powheg_pythia8	15261030	1.256
WGToLNuG_TuneCP5_13TeV-madgraphMLM-pythia8	19282022	462.8
ZGTo2MuG_MMuMu-2To15_TuneCP5_13TeV-madgraph-pythia8	5934228	54.18

Table 4.3: Simulated background samples with 2018 data-taking conditions and their effective cross sections.

Sample	No. events	Cross-sec. [pb]
DYJetsToLL_M-50_TuneCP5_13TeV-madgraphMLM-pythia8	99146219	6225.42
DYJetsToLL_M-10to50_TuneCP5_13TeV-madgraphMLM-pythia8	86369014	18610
TTJets_DiLept_TuneCP5_13TeV-madgraphMLM-pythia8	28615541	54
TTJets_SingleLeptFromT_TuneCP5_13TeV-madgraphMLM-pythia8	57259880	109
TTJets_SingleLeptFromTbar_TuneCP5_13TeV-madgraphMLM-pythia8	57999878	109
WJetsToLNu_TuneCP5_13TeV-madgraphMLM-pythia8	70398276	52940.0
ST_s-channel_4f_leptonDecays_TuneCP5_13TeV-amcatnlo-pythia8	19892000	3.740
ST_t-channel_top_4f_InclusiveDecays_TuneCP5_PSweights_13TeV-powheg-pythia8	129031100	115.3
ST_t-channel_antitop_4f_InclusiveDecays_TuneCP5_PSweights_13TeV-powheg-pythia8	79090800	69.09
ST_tW_top_5f_inclusiveDecays_TuneCP5_13TeV-powheg-pythia8	9598000	34.97
ST_tW_antitop_5f_inclusiveDecays_TuneCP5_13TeV-powheg-pythia8	6709000	34.91
WWToLNuQQ_NNPDF31_TuneCP5_13TeV-powheg-pythia8	19066700	45.99
WWTo2L2Nu_NNPDF31_TuneCP5_13TeV-powheg-pythia8	7758900	11.08
WZTo1L1Nu2Q_13TeV_amcatnloFXFX_madspin_pythia8	18664164	11.66
WZTo2L2Q_13TeV_amcatnloFXFX_madspin_pythia8	536667	6.331
WZTo1L3Nu_13TeV_amcatnloFXFX_madspin_pythia8	1690064	3.054
WZTo3LNu_TuneCP5_13TeV-amcatnloFXFX-pythia8	10749269	5.052
ZZTo2L2Q_13TeV_amcatnloFXFX_madspin_pythia8	25040328	3.688
ZZTo2L2Nu_TuneCP5_13TeV_powheg_pythia8	20469000	0.564
ZZTo4L_TuneCP5_13TeV_powheg_pythia8	15261030	1.256
WGToLNuG_TuneCP5_13TeV-madgraphMLM-pythia8	6108186	467.8
ZGToLLG_01J_5f_TuneCP5_13TeV-amcatnloFXFX-pythia8	5934228	55.41

4.2 Trigger Strategy

At a crossing frequency of 25 ns, the average crossing rate of the two proton beams in the LHC is more than 40 MHz, meaning millions of proton-proton collisions per second. This massive amount of data far exceeds the input rate of the online computer farm. In order to select the most interesting events produced in each collision, a highly dedicated trigger system (explained in the section 3.2) was included in the design of CMS. Events of interest to this analysis are determined using triggers that require a well-defined and isolated lepton (e.g., electron or muon). As we discussed earlier, we have two leptons, where a prompt lepton comes from a W boson at the interaction vertex and a second lepton comes from the HNL at the secondary vertex. In order to obtain the maximum signal efficiency and lowest systematics, it is better to trigger the events based on the prompt lepton using a single lepton trigger rather than the displaced one. The specific trigger path used for the muon channel is `HLT_IsoMu24`. As the path name implies, it selects events containing at least one muon isolated with transverse momentum p_T above 24 GeV. It is the inclusive single muon path with the lowest p_T threshold that was unprescaled, which means that all events passing this trigger were stored. The single electron trigger used for the electron channel is `HLT_Ele27_WPTight_Gsf`, where events containing at least one isolated electron are identified with p_T, larger than 30 (34) GeV are selected as in the muon channel. This electron trigger is the lowest p_T threshold that is not pre-scaled as well. The list of triggers and datasets used is summarized in Table 4.4.

Table 4.4: Summary of the trigger used in the analysis.

Dataset	Trigger		
	2016	2017	2018
SingleMuon	HLT_ISO(TK)Mu_24	HLT_ISOMu_24(27)	HLT_ISOMu_24
SingleElectron	HLT_Ele27_WPTight_Gsf	HLT_Ele32_WPTight_Gsf(_L1DoubleEG)	
EGamma			HLT_Ele32_WPTight_Gsf

4.3 Physics Objects

4.3.1 Primary vertex

In order to collect a good collision event, it is important to reconstruct the primary vertex. The primary vertex is the proton-proton interaction point. It is reconstructed from tracks with low impact parameters with respect to the nominal interaction region, which is the center of the detector and the z axis along the beam direction. In cases of multiple interactions in the same bunch crossing (pile-up events), the primary interaction vertex is chosen to be the one with the largest sum of the square transverse momentum $S_T = \sum p_{Ti}^2$, where the sum runs over all tracks associated with the vertex. Events in data and simulations should contain at least one good primary vertex (PV) to ensure that they are good collision events. The primary vertex must have more than 4 degrees of freedom, which is defined as follows:

$$n_{dof} = -3 + 2 \sum_{i=1}^{\#tracks} w_i$$

where w_i is the weight of the i track (the probability that track i belongs to a vertex). The z-position of the vertex should be within 24 cm of the center of the nominal detector, and the transverse position should be within 2 cm of the beam spot. The primary vertex of the associated tracks that meet the above requirements is the vertex with the largest square sum-p_T. The number of reconstructed vertices in the Monte Carlo samples does not model well what we see in the data. To correct for this, we re-weight the Monte-Carlo samples, including the signal, to match the data. This correction is based on a minimum bias cross section of 69.2 mb, which is almost the total proton-proton cross section.

4.3.2 Particle Flow

The particle flow (PF) event reconstruction algorithm aims to identify and reconstruct every particle produced by the proton-proton collision by combining information from all sub-detectors. The resulting particle flow event reconstruction leads to an improved performance for jet and MET reconstructions, and for the identification of electrons, muons, and taus. The CMS detector is well suited for this technique. In fact, the presence of a large internal silicon tracker immersed in an intense solenoidal magnetic field allows the charged particles to be reconstructed with high efficiency and a small fake rate, providing a high resolution measurement of the particle p_T down to about 150 MeV, for $|\eta| < 2.5$. The good performance of the tracking system plays a key role in the PF technique and is achieved by means of an iterative tracking strategy [97], based on the Kalman Filter algorithm [98]. The high granularity of ECAL is an additional key element for the high quality of PF results, allowing photons and electrons to be reconstructed with high energy resolution in a dense particle environment. The high detection efficiency of the calorimeters is based on a specific calorimeter clustering algorithm, which is performed separately for each subdetector. The algorithm is based on three steps: In the first step, "cluster seeds" are identified as local calorimeter cells with an energy deposit above a given threshold. Then "topological clusters" are grown from the seeds by collecting cells with at least one side in common with a cell already in the cluster and with an energy above a given threshold. A topological cluster usually gives rise to as many "particle flow clusters" as its seeds. Thus, the energy of each cell is shared between the particle flow clusters according to the cell-cluster distance. These elements are then connected to each other using a linking algorithm that determines which elements are topologically compatible.

4.3.3 Track Reconstruction

The charged particles follow a helical path parallel to the magnetic field inside the CMS detector. These particles leave energy deposits (hits) along their trajectories in the inner tracking system (see Figure 4.1). The path of the reconstructed charged particle is usually indicated by track hits. The charged particle tracks are of great importance in reconstructing collision events, contributing to the reconstructions of the electron, muons, tau, and hadron candidates, as well as determining the primary interaction and displaced vertices. The path of the reconstructed charged particle is on the basis of hits track reconstruction [97]. This is based on the collection of hits from the pixel and strip trackers and is performed by the Combinatorial Tracker Finder (CTF) algorithm, which is an adaptation of the combinatorial Kalman filter [99], which in turn is an extension of the Kalman filter (An algorithm for fitting tracks to estimate the trajectory of a dynamical system's state vector from a set of measurements taken at different times [98]). To allow pattern recognition and track fitting to occur in the same framework. The set of reconstructed tracks is produced by multiple paths (iterations) of the CTF track reconstruction sequence, in a process called iterative tracking. Initially, tracks are seeded and reconstructed with very tight criteria, leading to a moderate tracking efficiency but a negligibly small fake rate. The next steps proceed by removing hits unambiguously assigned to the tracks found in the previous iteration and by progressively loosening track seeding criteria. An iteration typically consists of four steps. In the first step, a seed defines the initial estimate of the trajectory parameters and their uncertainties, and provides initial track candidates made up of typically 2-3 hits. In the second step, track finding based on Kalman filter, extrapolates the seed trajectories along the expected flight path of a charged particle, searching for additional hits that can be assigned to the track candidate. In the third step, track candidates are fitted with a Kalman filter and a smoother to provide the best possible estimate of the parameters of each trajectory. Finally, track selection sets quality flags and discards tracks that fail certain specified criteria. The often used perigee (the point in the orbit of an object) parametrization has been chosen to describe a charged particle

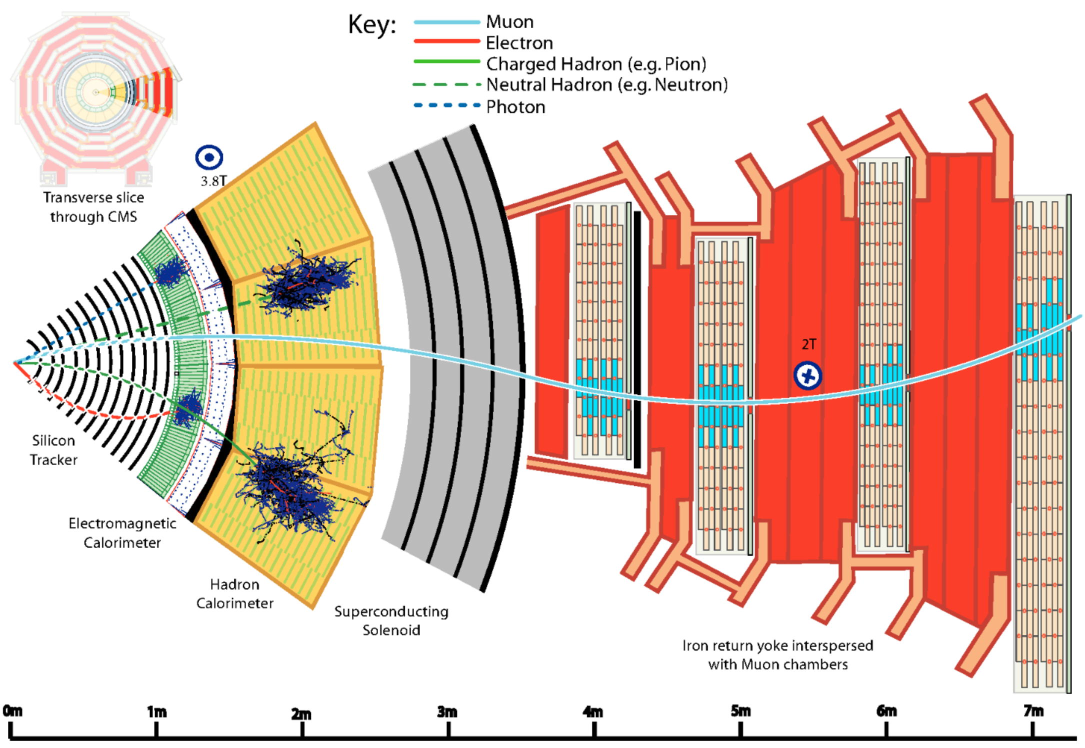

Figure 4.1: A sketch of the specific particle interactions in the transverse slice of CMS detector, from the beam interaction region to the muon detector. The muon and charged points are positively charged , and the electron is negatively charged [100].

track in a magnetic field. This parametrization is defined with respect to a reference point and defines the track at its point of closest approach (in the transverse plane) to the reference point (see Figure 4.2). The five parameters are:

- ρ: signed transverse curvature.
- z: longitudinal distance of the point of closest approach.
- ε: signed transverse distance of the point of closest approach. By convention, the sign is positive if the reference point is at the left of the point of closest approach.
- ϕ: azimuthal angle of the momentum vector at the point of closest approach.
- θ: polar angle of the momentum vector.

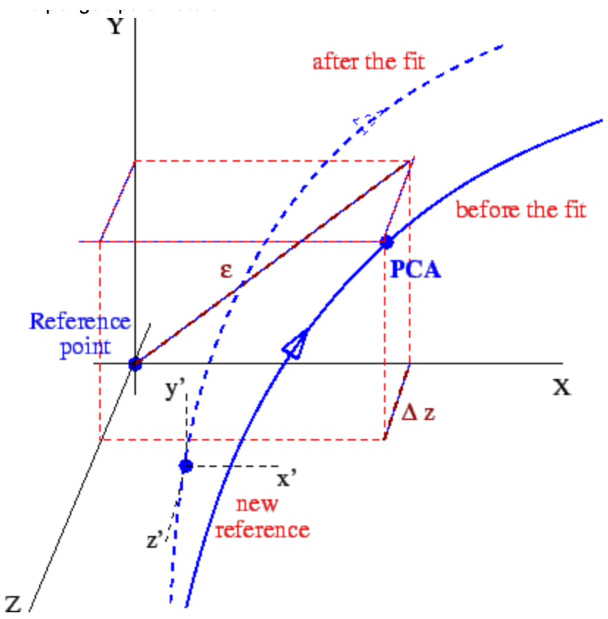

Figure 4.2: A sketch of track parameters [101].

Another important ingredient that can elaborate on the origin of the tracks is the impact parameter IP of the tracks. The impact parameter is defined as the transverse distance from the track's closest approach to the primary vertex (see Figure 4.3). The smaller the IP, the more likely the track is from the primary vertex, and the larger the IP, the more likely the track is from a vertex other than the primary vertex. Since the HNL is assumed to come from a long-lived scenario in this analysis, the decays of HNL would originate from a secondary vertex relative to the primary vertex, resulting in the tracks of decays being displaced. To select those tracks for seeding vertex algorithms, as we'll see in section 4.4, we apply a cut to the IP to be greater than a certain number so that the track is most likely generated from a secondary vertex with respect to the primary vertex.

4.3.4 Muons

Muons are characterized by signals in the tracking system and in the muon chambers. There are two different reconstruction algorithms, depending on which information is used as a seed [102]. If the reconstruction starts from the muon system, then the muon will be called the global muon. In this case, a track in the muon system is extrapolated from a seed in the RPC, CSC, or DT chambers, and then matched

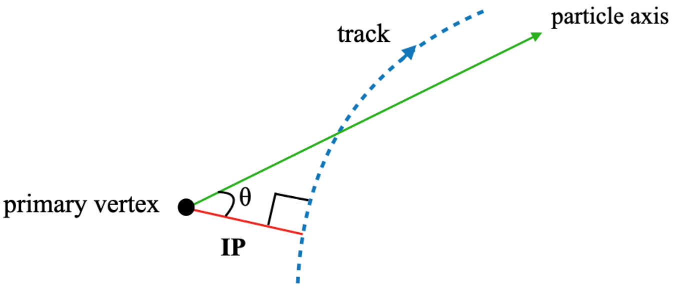

Figure 4.3: Visualization of the Impact Parameter (IP, red line) of a track.

with a reconstructed track in the inner tracking system. The tracker muon is reconstructed when an inner track is matched with some hits in the muon chambers. To be tagged as a good muon, both global and tracker identifications are often required. Muons that are only reconstructed in muon chambers are called standalone muons. This is, for example, the case of muons from cosmic rays.

Prompt muons

To obtain a more efficient prompt muon (originating at the primary vertex) reconstruction, combinations of different algorithms are used. Physics analyses can set the desired balance between reconstruction efficiency and purity by applying a selection based on various muon identification variables. In this thesis, the tight muon selection [103] is used to find prompt muons that come from a W decay at the primary vertex (see Table 4.5). Tight Muon selection: the candidate muon is reconstructed as a global muon by using the global muon reconstruction approach with a global muon track fit χ^2/ndof less than 10. In addition, its corresponding tracker track must be matched to muon segments in at least two muon stations. That means the muon is also reconstructed as a tracker muon by using the tracker muon reconstruction approach. The stations use five inner-tracker hits and have a transverse impact parameter of $d_{xy} < 2$ mm and a longitudinal distance of $d_z < 5$ mm with respect to the primary vertex to suppress the QCD background. In order to subtract the pileup contribution for muons, a "Delta Beta" $\Delta\beta$ correction is applied, where $\Delta\beta$ is defined as the scalar sum of the p_T of tracks or E_T of energy deposits in the calorimeters in a cone along the muon direction with a cone radius of 0.3 in η and ϕ. As a result of all the mentioned selections, good reconstruction efficiency is obtained, as shown in Figure 4.4. The prompt muon reconstruction efficiency is defined as the ratio of the number of events that have the mentioned tight muon ID after being matched with the generator by $\Delta R = \sqrt{(\Delta\eta)^2 + (\Delta\phi)^2} < 0.1$ to the number of events that contain all the tight ID muons.

Displaced muons

The standard CMS medium muon ID [103] is optimized for prompt muons and for muons from heavy flavor decay. After a few changes have been applied to allow the displacement, we could use it to define the displaced muon (a muon originated from the secondary vertex). The first modification made to the medium ID is to remove the requirement that more than 80 % of muon track hits must be in the inner tracker layers. We are looking for a displaced muon, so it is expected to have more muon track hits outside the inner tracker layers. The second change made is to remove the requirement for the goodness of fit per degree of freedom. As this muon does not come from the primary vertex, the goodness of fit will not be as high as for prompt muon. The rest of the ID requirements that were used have no effect on the displacement feature and are listed in Table 4.5. Finally, a cut has been applied to the transverse impact parameter $d_{xy} > 0.2$ mm, to confirm the displacement of the muon. As a result of using the medium ID with the modifications, a good reconstruction efficiency of displaced muons has been obtained (as shown in Figure 4.4).

Selection		Prompt muon	Displaced muon
$\|\eta\|$		> 2.4	>2.4
p_T		$>$ 25-28 GeV	$>$ 5 GeV
$\|d_{xy}\|$		$<$ 0.005 cm	$>$ 0.02 cm
$\|d_z\|$		$<$ 0.1 cm	—
RelIso04		< 0.1	—
Loose ID		True	True
Fraction of valid tracker hits		< 0.8	—
Global muon	Global muon fit	True	True
	Particle flow	True	—
	No. of valid muon hits	> 0	—
	No. of matched stations	> 1	—
	No. of valid pixel hits	> 0	—
	No. tracker layers with measurement	> 5	—
	Global track χ^2/dof	< 10	—
	Track–muon matching χ^2/dof	—	< 12
	”Kink finder” estimator	—	< 20
	Segment-compatibility estimator	—	> 0.303
Tracker muon	Segment-compatibility estimator	—	> 0.451

Table 4.5: Requirements of muon selections for both prompt and displaced muon.

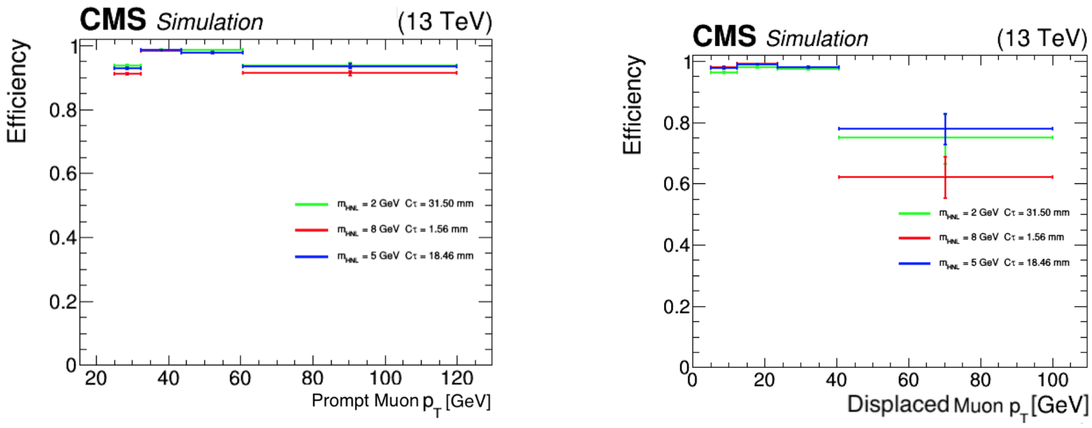

Figure 4.4: Muon reconstruction efficiencies in HNL decay process as a function of muon p_T , as left) the prompt muon, right) the displaced muon.

4.3.5 Electrons

Electrons are charged particles that interact mainly electromagnetically with matter. Their signature in CMS is then characterized by some hits in the tracker and by the production of an electromagnetic shower in the ECAL (made by photons from bremsstrahlung and electron-positron pairs). Since the ECAL has high granularity, an electromagnetic shower consists of many cells. Neighbour cells contain energy deposits that form a cluster, while groups of clusters are arranged into super clusters (SC). The reconstruction of an electron consists of matching a SC with a track obtained by fitting different hits into the tracker. Of all the reconstruction algorithms developed by the CMS collaboration [104], the Gaussian Sum Filter (GSF) [105] has been used. GSF is an algorithm for electron track reconstruction used to model the bremsstrahlung energy loss distribution by a Gaussian mixture (function comprised of several Gaussians) rather than a single Gaussian. Electrons reconstructed in this way are called GSF-electrons. The charge of an electron can be measured in different ways. It can be inferred from the curvature of the associated track (GSF-track charge) or by studying the energy distributions in the shower (SC charge). A redundant approach is used: an electron charge is considered well measured if both methods are in agreement. Many other variables are considered for electron identification in order to avoid, for example, the occurrence of an electron from a photon conversion, non-prompt electrons (not originated in the primary interaction) or jets misidentified as electrons.

Prompt Electrons

Prompt electrons (originated from the primary vertex) are required to be tight electrons [106] (see Table 4.6). Additional requirements on electron tracks are used to reject products of photon conversions. Electron isolation criteria exploit the full particle flow based event reconstruction by using particles within a cone around the electron direction with a radius of 0.3. The isolation requirement is $I < 0.1$. Electrons must have $p_T > 30$ (34) GeV for 2016 (2017/2018) and be reconstructed within the pseudorapidity range $|\eta| < 1.44$ and $1.57 < |\eta| < 2.5$, which excludes the barrel-endcap transition region. Additionally, two cuts were applied to the transverse and longitudinal impact parameters, $d_{xy} < 0.02$ cm and $d_z < 0.04$ cm, to pick up only

Selection	prompt electron	displaced electron
P_T >	30-34 GeV	5 GeV
$\|\eta\|$ <	2.5	2.5
$\sigma_{i\eta i\eta}$ <	(0.00998 , 0.0292)	(0.011 , 0.0314)
H/E <	(0.0414 , 0.0641)	(0.298 , 0.101)
$\Delta\eta_{in}$ <	(0.00308 , 0.00605)	(0.00477 , 0.00868)
$\Delta\phi_{in}$ <	(0.0816 , 0.0394)	(0.222 , 0.213)
$\frac{1}{E} - \frac{1}{\rho}$ <	(0.0129 , 0.0129)	(0.241 , 0.14)
missing inner hits <=	1	--
pass conversion veto	yes	yes
d_{xy}	< 0.02 cm	> 0.02 cm
d_z	< 0.04 cm	--
I_{rel}	< 0.1	--

Table 4.6: Requirements of electron selections for both prompt and displaced electrons in barrel cuts ($|\eta$ super cluster$| \leq 1.479$) and endcap cuts $|\eta$ super cluster$| > 1.479$).

electrons at the primary vertex. Finally, the good efficiency curve of the prompt electron ID was obtained and is plotted in Figure 4.5).

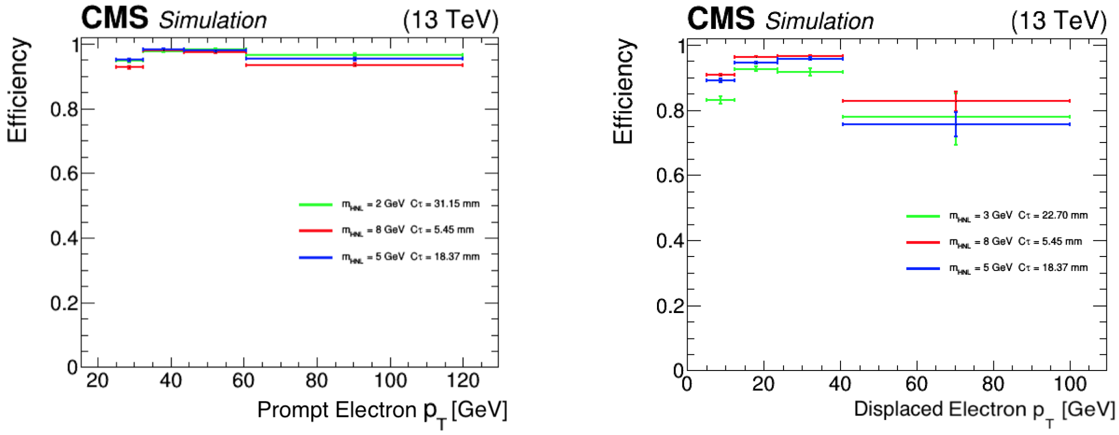

Figure 4.5: Reconstruction electrons identification efficiencies in HNL decay process as a function of electron p_T , as left) the prompt electron, right) the displaced electron.

Displaced Electrons

Displaced electron candidates are defined using the standard CMS loose electron ID [106] (see Table 4.6), and similar to displaced muons, we had to make a change in the ID requirements to allow the displacement of the electron. Therefore, the requirement for the maximum number of missing inner hits has been removed, as this electron should be displaced so it can have very few hits in the inner tracker. The displaced electrons must have a p_T greater than 5 GeV, which is currently the lowest p_T we can have for the electrons. Additionally, a cut was applied to the transverse impact parameters d_{xy} > 0.02 cm to confirm the displacement of the electron. As a result of these selections, a good reconstruction efficiency of the displaced electron is obtained, as shown in Figure 4.5.

4.3.6 Jet reconstruction

Events that contain one prompt and one displaced lepton arising from a secondary vertex are selected. To further reduce the amount of expected background, events must also have at least one jet close to a displaced lepton with ΔR < 0.7 and p_T > 20 GeV. Jets are reconstructed using the Anti-k$_T$ jet algorithm with a cone radius of R = 0.4. To reject jets that are mismeasured or that are likely to originate from an anomalous energy deposit, the jets are required to pass the tight working point selections [107], which includes the following requirements:

- The neutral energy fractions of the jet energy must be less than 90%.
- The neutral hadronic energy fraction of the jet energy must be less than 90 %.
- The charged electromagnetic EM energy fractionsof of the jet energy must be less than 99%.
- There is at least one charged hadron in the jet and the charged hadronic fraction must be greater than zero.

Charged hadrons not originating from the primary vertex are included in jet reconstruction as we search for a displaced jet. The jets are corrected using the official CMS analysis recipe. First, the average amount of energy per unit area is used to subtract the contributions from neutral particles from the jet energy using the "L1FastJet" correction. The jets are then corrected to account for the non-uniform response of the detector, so-called (L2, L3 corrections). Further residual jet energy corrections are applied to jets in the data to match their response with the simulation (L2L3Residual). The jets in the simulation are smeared to better match the data. This is done using (Jet Energy Resolution) JER scaled factors. The jet calibration is repeated for each data collection year in order to take into account the different conditions. As a result of these selections and identifications, a high reconstruction efficiency of the so-called lepton-Jet (due to the jet's being very close to the second lepton) is achieved, as shown in Figure 4.6.

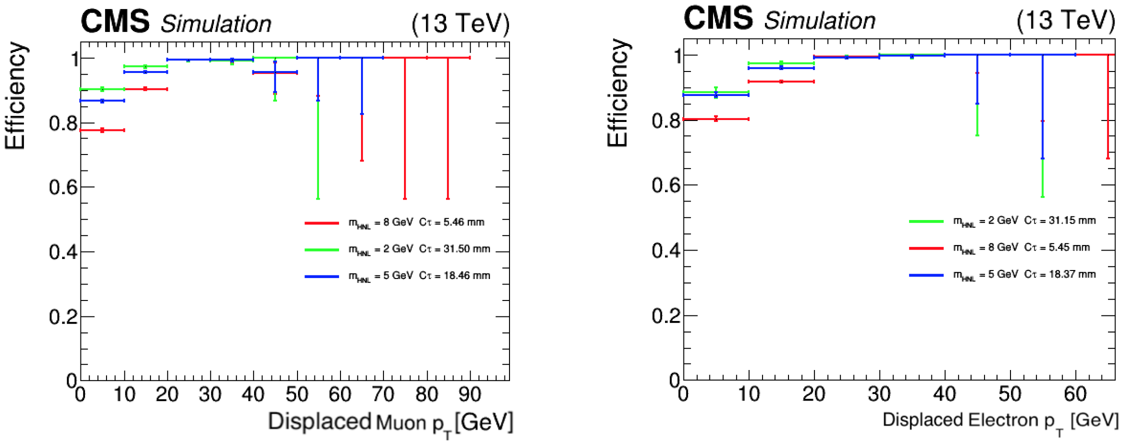

Figure 4.6: Reconstruction Jet identification efficiencies in HNL decay process as a function of second lepton p_T , as left) the muon, right) the electron.

4.4 Secondary Vertex

As seen in figure 4.7 , the target signal we search for in this analysis has two leptons and two quarks (from the hadronic W off-shell decay) in the final state, where we assume an on-shell W that decays into a charged lepton (electron or muon) plus HNL. This decay is prompt and the lepton will emerge from the interaction vertex. The HNL instead lives for a short time, traversing the detector, and then decays to another lepton (electron or muon) plus an off-shell W boson. The off-shell W boson is assumed to decay hadronically into two jets. So we will have a secondary vertex coming from the HNL decaying system. A method for reconstructing the displaced vertex has been constructed based on the tuning of the Inclusive Vertex Finder (IVF) algorithm, which uses a variant of the CMS standard b-quark tagging [108]. The b tagging algorithm identifies the b quark by reconstructing a jet that emerges from the secondary vertex.

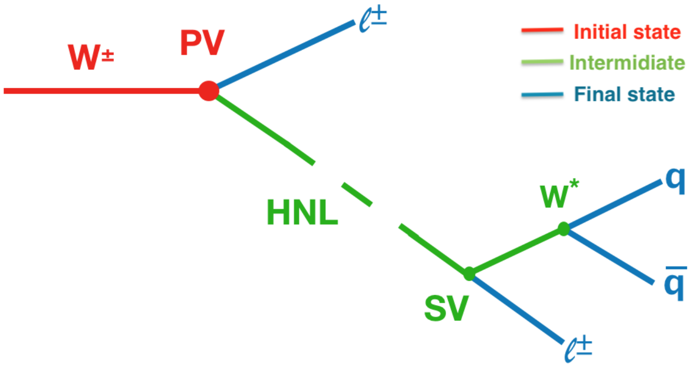

Figure 4.7: Heavy Neutral Lepton (HNL) decay process diagram

4.4.1 Secondary Vertex Reconstruction

In order to find and reconstruct secondary vertices, it is important to reconstruct the primary vertex first (see section 4.3.1). The approach for finding primary vertices does not apply directly to the secondary vertex. Neither the track selection criteria nor the seed finding scheme can be employed. However, the vertex fitting process is based on the same hypothesis. A global vertex finding algorithm finds the seeds to reconstruct secondary vertices coming from displaced decays of long-lived particles. For this purpose, inclusive secondary vertex finding (IVF), completely independent of jet reconstruction, is applied. This technique reconstructs secondary vertices by clustering tracks around a so-called seeding track characterized by high three-dimensional impact parameter significance $S_d = d/\sigma(d)$ where d and $\sigma(d)$ are the impact parameter and its uncertainty at the primary vertex (PV), respectively. The tracks are clustered to a seed track based on their compatibility given their: separation distance in three dimensions, separation distance significance (distance normalized to its uncertainty), and angular separation. The clustered tracks are then fitted to a common vertex with an outlier-resistant fitter [109]. The vertices sharing more than 70% of the tracks that are compatible within the uncertainties are merged. As a final step, all tracks are assigned to either the primary or secondary vertices on the basis of the significance of the track to vertex distance.

4.4.2 Secondary Vertex Definitions

The flight direction of a secondary vertex (SV) is defined as the three-dimensional vector from the primary vertex (PV) position to the SV position, see Figure 4.8. The flight distance d_{3D} is computed as the distance between PV and SV, and the 2D flight distance d_{2D} is the projection on the xy plane. In 3D, the flight distance significance is $S_{3D} = d_{3D}/\sigma(d_{3D})$ and in 2D, it is $S_{2D} = d_{2D}/\sigma(d_{2D})$. The errors $\sigma(d_{3D})$ and $\sigma(d_{2D})$ are calculated using the covariance matrix of the secondary vertex. The four-momentum of the vertex is calculated as the sum of the four-momenta of all tracks i, with a weight w_i>0.5 for the vertex (the vertex momentum is shown in Figure 4.8). The weight w_i can be interpreted as the probability that track i belongs to a vertex. To obtain the track energy, the pion mass hypothesis is used for the tracks. The vertex mass is then calculated as $m_{sv} = \sqrt{E_{sv}^2 - P_{sv}^2}$ (see Figure 4.9) to be fitted for constructing the signal regions, as we will see in Chapter 7. The angle between the vertex momentum and the flight direction is θ_v and ΔR_V is ΔR between those two directions. The quality of the vertex quality is estimated by the total χ^2 of the fit or χ^2 divided by the degrees of freedom (ndof). For unconstrained vertex fits, the number of degrees of freedom is defined as $ndof = 2\sum_i w_i - 3$ where the sum runs over all the tracks used for the vertex fit.

4.4.3 Inclusive Vertex Finder (IVF) tuning

Starting with the LHC run2 data, CMS adopted as a default the IVF algorithm to reconstruct secondary vertices. The standard IVF algorithm takes into account all reconstructed tracks in the event that satisfy the $p_T > 0.8$ GeV and the longitudinal impact parameter IP < 0.3 cm (impact parameter measured in the z-direction, see section 4.3.3) requirements and is optimized to reconstruct secondary vertices originating from the decay of B-hadrons within a b-quark jet that have an average displacement from the primary vertex of a few millimeters (for more details see [108]). A customized version of the IVF algorithm, but with looser cuts allowing

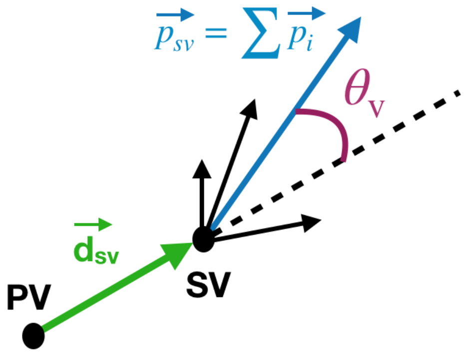

Figure 4.8: Definition of the vertex flight direction $\vec{d}_{sv}$ (direction from the PV to the SV position), the vertex momentum $\vec{p}_{sv}$ (sum of the track momenta). The angle between the flight direction and the momentum is $\theta_{\rm v}$.

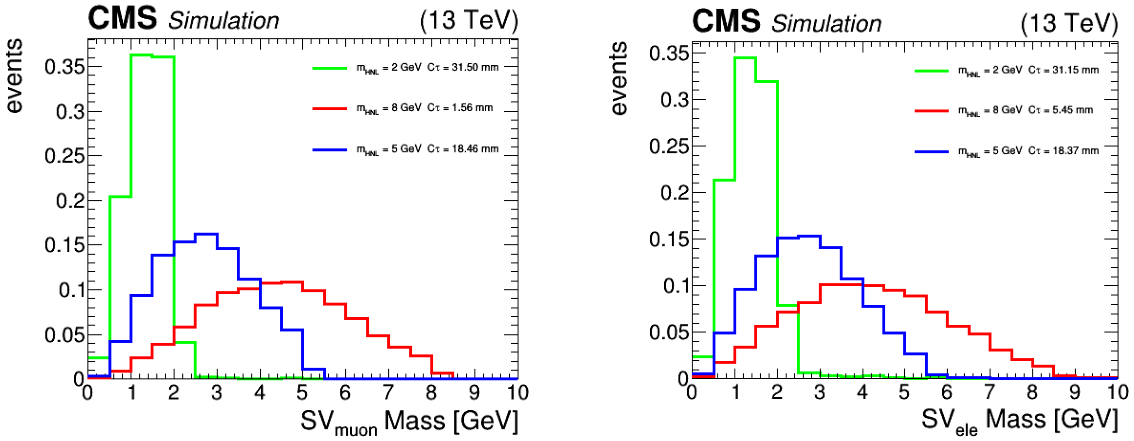

Figure 4.9: The mass distribution of reconstructed secondary vertex for both $\mu\mu$ channel on the left and ee channel on the right.

reconstruction of farther displaced vertices such as those coming from the decay of an HNL candidate, is used in this analysis. The following changes have been made to adapt the IVF to this specific physics case: The minimum number of hits in the tracker is reduced from 8 to 6, removing the requirement on the number of hits in the silicon pixel tracker; the maximum longitudinal IP of each track is allowed to be as large as 20 cm; and the maximum distance and ΔR between each track and the SV are relaxed to 0.1 cm and 1.0, respectively. In order to cope with the high number of tracks and reconstructed secondary vertices, only a secondary vertex where one of the tracks matches the selected displaced lepton is considered. Therefore, if the electron is the displaced lepton, the secondary vertex is labelled SV_{ele}, and if it is the muon, then it is labelled SV_{muon}.. Before relying on the IVF algorithm for secondary vertex reconstruction, it is important to evaluate its efficiency after running it with the modifications mentioned above. The efficiency here is defined as the ratio of the number of secondary vertices reconstructed by IVF and matched with the generator level vertex to the number of produced generator level vertices. The generator level denotes the level before applying detector simulation to the signal, so in other words, the signal is ideal. Figure 4.10 shows the efficiency as a function of the flight distance L_{xyz}, which allows us to determine how well the IVF can reconstruct the secondary vertex and how close the reconstructed vertex is to the generator level vertex. By plotting the flight distance L_{xy} distribution (the distance between PV and SV in two dimensions) of selected vertices (Figure 4.11 left plot) and comparing it to the generator level distribution (Figure 4.11 right plot), we can determine how far HNL can be displaced and still be reconstructed. The charge multiplicity of HNL decays at the generator level is shown in Figure Figure 4.12 (right plot), where the even number of charged particles is due to charge conservation, as the HNL has zero charge. The secondary vertex track multiplicity is shown in Figure 4.12 (left plot), and it is clear that it does not have the same distribution as the multiplicity at the generator level. This is due to the fact that not all charged decays are reconstructed, but the IVF may still reconstruct the vertices using the few tracks available. All the mentioned comparisons allowed us to prove that IVF is the best algorithm for secondary head reconstruction.

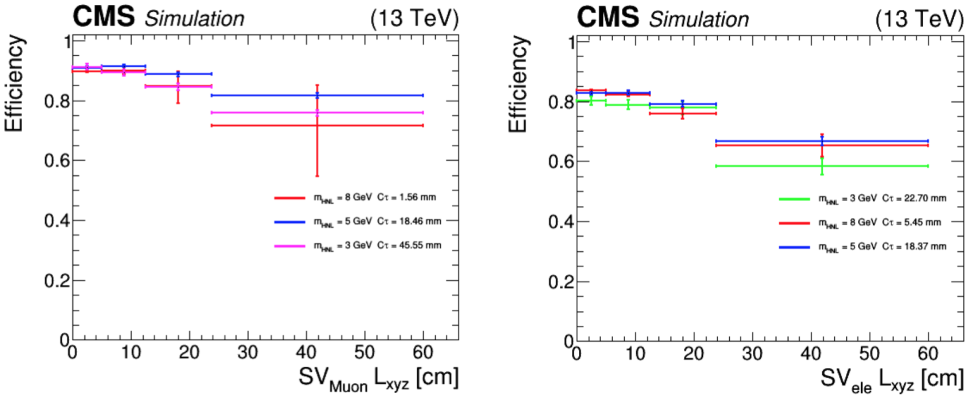

Figure 4.10: Secondary vertex reconstruction efficiency in HNL decay process as a function of flight distance L_{xyz} as muon within SV tracks (upper left) and electron with SV track (upper right).

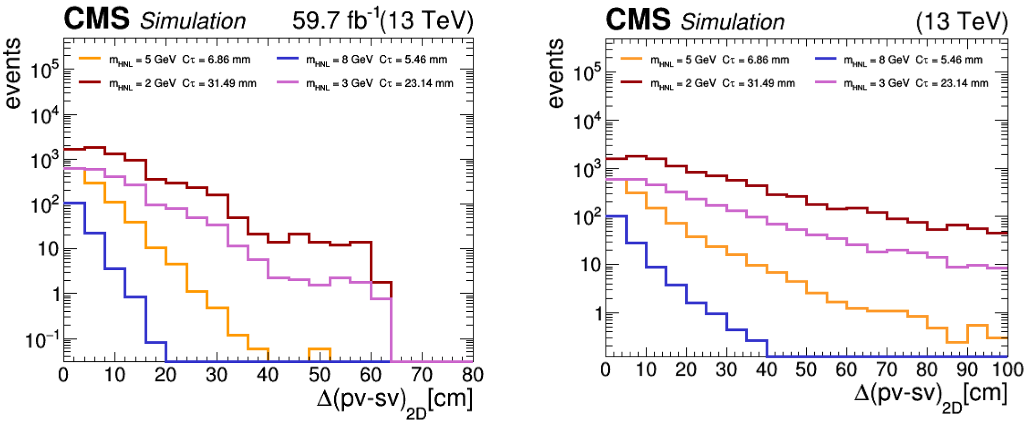

Figure 4.11: The flight distance L_{xy} distribution (the distance between PV and SV in two dimensions) for a reconstructed secondary vertex (left) and at generator level (right).

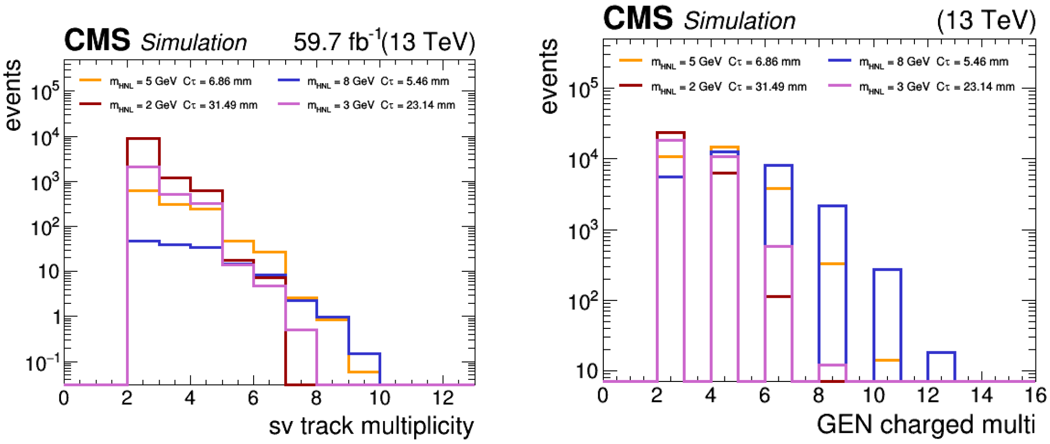

Figure 4.12: The track multiplicity of reconstructed secondary vertex (left), and charge multiplicity HNL decays at generator level.

4.4.4 Secondary Vertex CNN Tagger

The identification of secondary vertex from HNL can be improved by using the advances in the field of deep machine learning. The Secondary Vertex CNN (SVCNN) tagger was developed using a deep neural network with hidden layers, nodes per layer, and simultaneous training in vertex categories (SV_{ele} , SV_{muon}). The tracks of the IVF secondary vertex are used in the training of SVCNN. Convolutional neural networks (CNNs) have been widely applied in the computer imaging community to solve complex problems in image recognition and analysis. We describe an application of the CNN technology to the problem of identifying the secondary vertex in HNL decay. The multi-layer perceptron (MLP) is a machine learning algorithm in wide use in HEP [110]. The structure of a MLP consists of an input layer, one or more hidden layers, and an output layer. All layers in traditional MLPs are fully connected, meaning that the output of each node is the weighted sum of the outputs of all nodes in the previous layer. A convolutional neural network is a type of MLP algorithm that analyzes an input image, assigns weights and biases to various aspects/objects in the image, and can differentiate one from another using those weights and biases. Digital images are binary representations of visual data. It consists of rows and columns of pixels arranged in a grid-like format, each with a pixel value to describe how bright and what color it should be. In the moment of seeing an image, the human brain processes a large amount of information. Each neuron functions within its own receptive field, and it is connected to other neurons so that they cover the entire visual field. As each neuron responds to stimuli only in its receptive field in the biological vision system, so too does each neuron in a CNN process data only in its receptive field. In this approach, the layers are arranged so that simpler patterns (lines, curves, etc.) can be detected first and more complex patterns (faces, objects, etc.) further along. From the above, the secondary vertex image is used as the input layer to our neural network. As such, the secondary vertex reconstruction algorithm uses as input the collection of reconstructed tracks in the event. So each vertex consists of a set of tracks, and we used their features to feed the CNN model to tag our HNL secondary vertex from standard model background processes. The main features used are:

- Tracks charge;

- Tracks p, p_T, η, ϕ;
- Transverse impact parameter, d_{xy} and its significance;
- Three dimensional impact parameter, d_{xyz}.

For each track belonging to the secondary vertex, the eight features mentioned above are extracted. A shared dense neural network of 3 layers and ELU activation is used to project each track into a 32-dimensional embedding space. The Exponential Linear Unit (ELU) is a function that is added to an artificial neural network in order to help the network learn complex patterns in the data. In a sense, it decides whether a neuron should be activated or not. This means that it will decide whether the neuron's input to the network is important or not in the process of prediction using simpler mathematical operations. The whole architecture is trained end-to-end for 25 epochs with binary classification and the ADAMAX optimizer [111]. The number of epochs is a hyper-parameter that defines the number of times that the learning algorithm will work through the entire training dataset.

Plots of model loss and classification accuracy as a function of the epoch are shown in Figures 4.13, 4.14 and 4.15 for the 2016, 2017 and 2018 datasets, respectively. A loss model implies how poorly or well a model behaves after each iteration of optimization. A classification accuracy is used to measure the algorithm's performance in an interpretable way. Two labels can be seen in the plots. Validation is referred to as "val," and training is referred to as "train". Training means that the same data is used both for training and testing, while validation means that the trained model identifies independent data that was not used in training. Train/Val is a method to measure the accuracy of the model. It is called Train/Val because we split the data set into two sets: a training set and a validating set, with 80% for training and 20% for validating. We train the model using the training set, and then we validate the model using the validating set.

Figure 4.16 shows the distribution of discrimination values of the CNN tagger for secondary vertices selected SV_{muon} on the left side and SV_{ele} on the right side. Good secondary vertex tagging is achieved to separate the signal from the background. However, this is not the end of the story of signal background discrimination because the SVCNN tagger output is used as an input in a further multi-variate discriminator, described in the next chapter.

To summarize this chapter, we discussed an overview of the reconstruction of physics objects produced in pp collisions in CMS. We have paid special attention to those objects that play a crucial role in the analysis pursued in this thesis (muon (prompt or displaced), electron (prompt or displaced), jet, and secondary vertex). The particular choices used in the analysis in terms of reconstruction and identification parameters were also listed and justified. As we will see in the next chapter, we will combine all of the objects to define the analysis strategy.

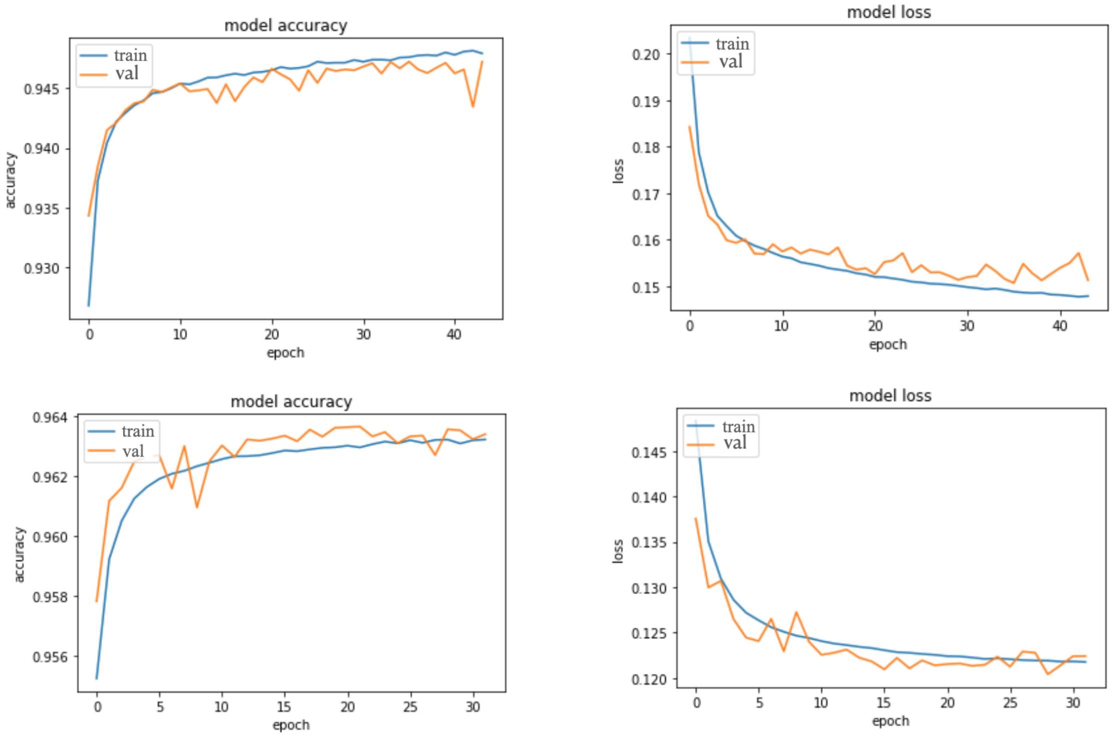

Figure 4.13: CNN classification accuracy (left) and model loss (right) as a function of the training epoch, for SV_{muon} (top) and SV_{ele} (bottom) for 2016.

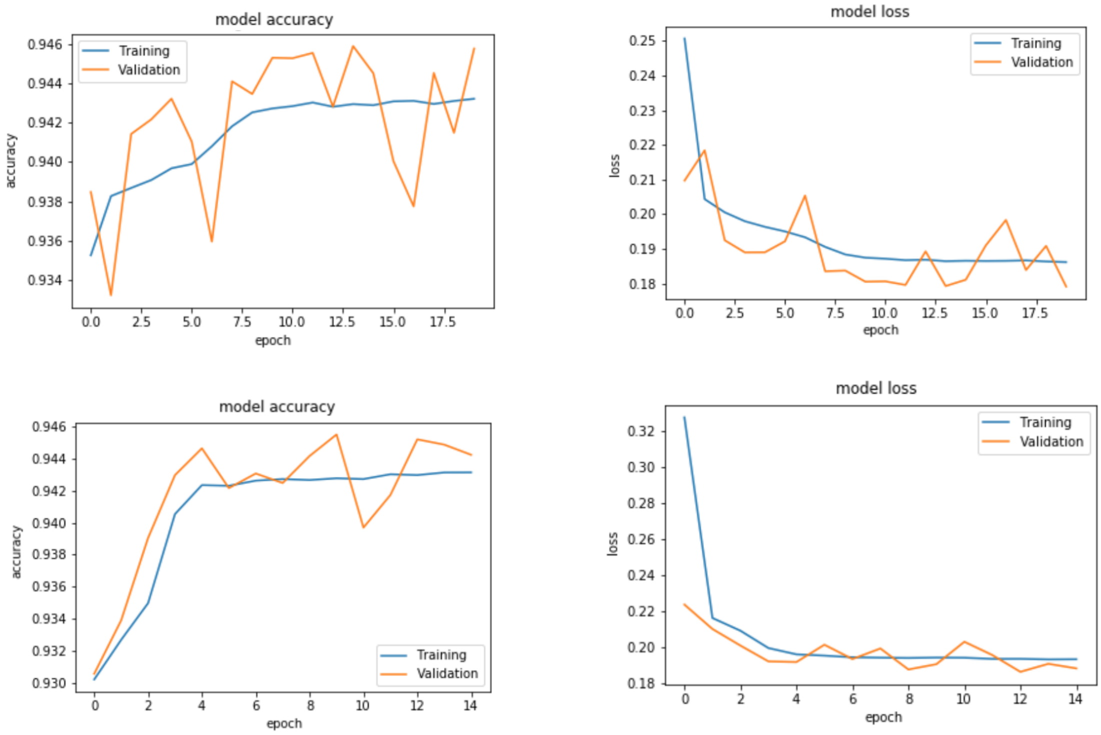

Figure 4.14: CNN classification accuracy (left) and model loss (right) as a function of the training epoch, for SV_{muon} (top) and SV_{ele} (bottom) for 2017.

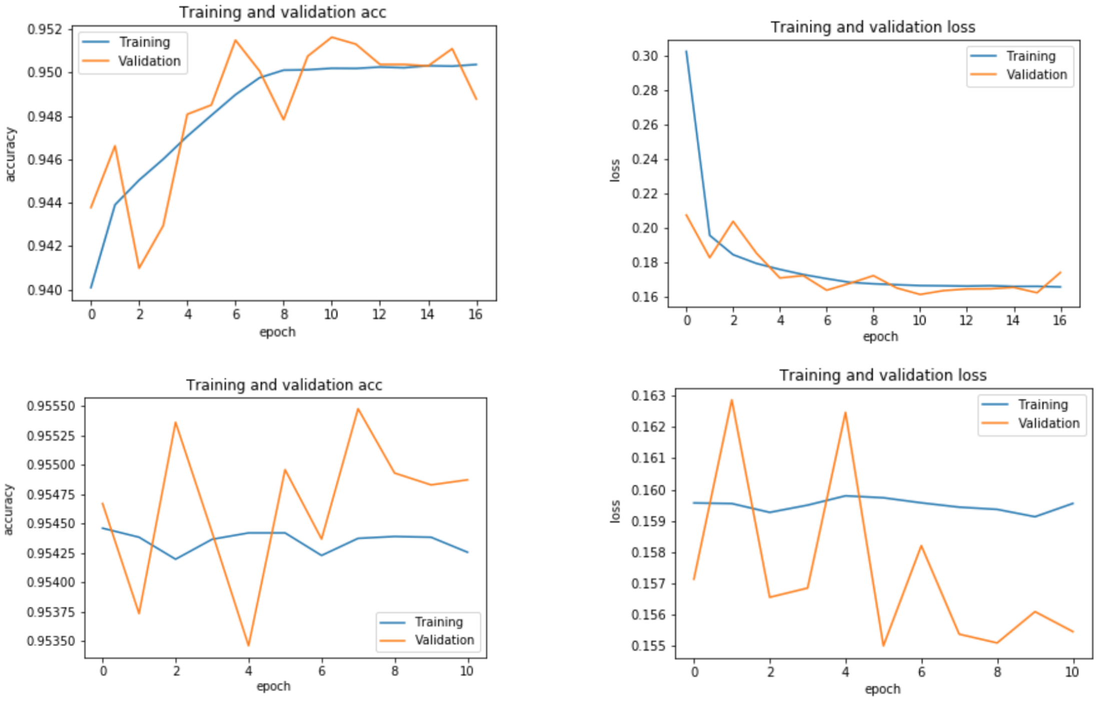

Figure 4.15: CNN classification accuracy (left) and model loss (right) as a function of the training epoch, for SV_{muon} (top) and SV_{ele} (bottom) for 2018.

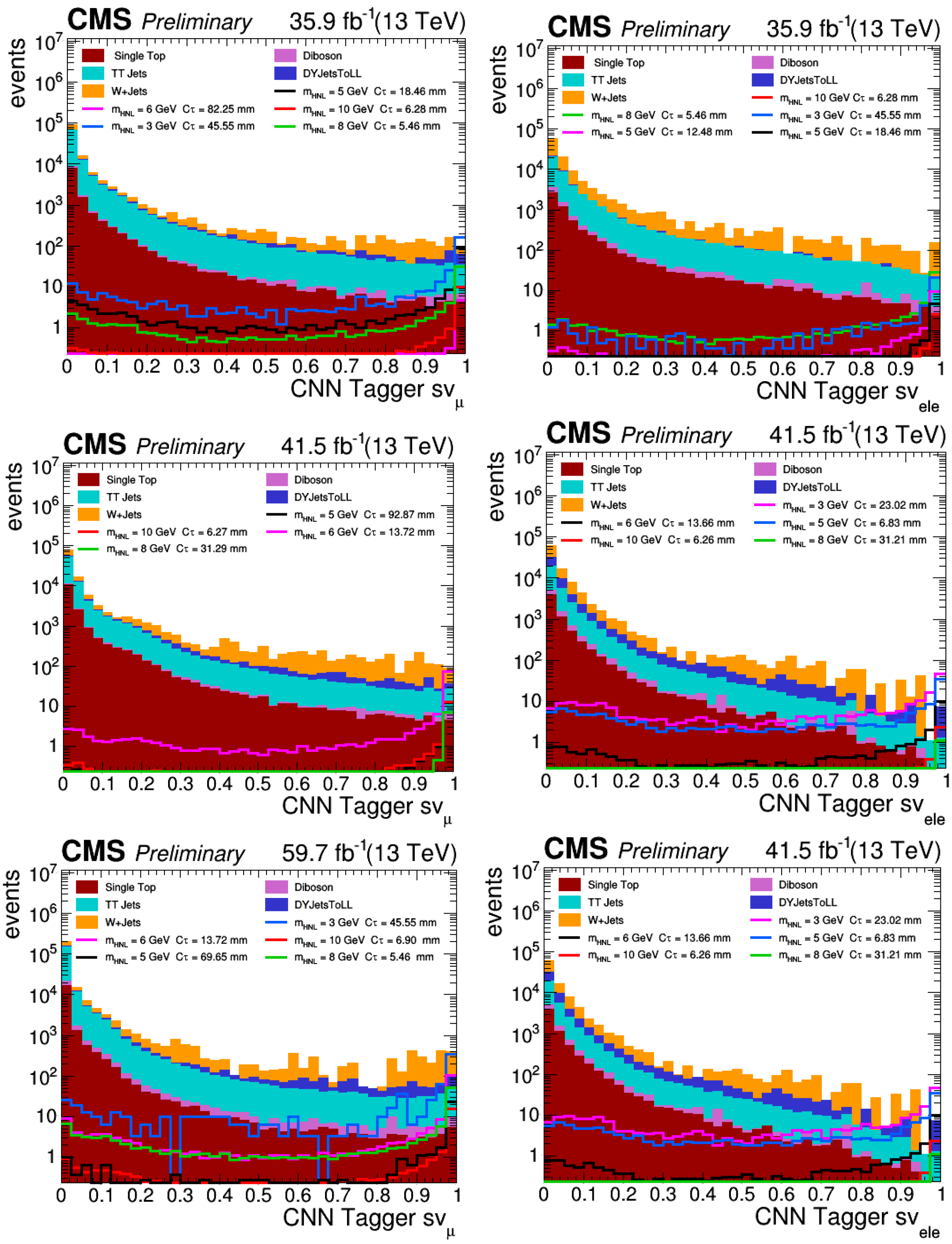

Figure 4.16: The distribution of discrimination value of CNN tagger for secondary vertex selected SV_{muon} on left side and SV_{ele} on right side. The total number of entries in the simulation is normalized to the collected data in 2016(top), 2017(middle) and 2018(bottom) respectively.

Chapter 5

Event Selection and Background Estimation

As introduced in chapter 1, the signature searched for in this analysis consists of a prompt lepton and a secondary vertex, formed by a lepton and at least one charged track coming from a charged hadron. The secondary vertex displacement can vary from a few millimetres to tens of centimetres depending on the mass and the coupling of the HNL candidate. However, only HNL candidates decaying within the tracker volume are considered and reconstructed. In chapter 4, we showed that the event selection starts with the identification of a prompt and a displaced lepton (hereafter referred to as l_1 and l_2, respectively), either muons or electrons as explained. A modified lepton identification as compared to the standard CMS ID is applied to displaced electrons and muons. For each of the selected events, a modified version of the Inclusive Vertex Finding (IVF) is run to identify and reconstruct a secondary vertex compliant with the signature of an HNL candidate. For a further improvement in secondary vertex identification, we used a CNN model to tag our vertex from the standard model background. Details on the modified IVF are given in section 4.4. Following the leptons identification and the secondary vertex reconstruction, a cut-based pre-selections are applied. The only purpose of these selections is to remove phase-space regions where only background events are present. A summary of the pre-selection cuts is presented along with the analysis strategy in the next sections. After this step, events surviving the pre-selection are fed into the multivariate selection (BDT) described later. The second part of this chapter is dedicated to the estimation of the background resulting from various standard model processes.

5.1 Analysis Strategy and Event Selection

This section will describe the analysis strategy used in this thesis, where we will briefly review all the steps we have taken to perform this analysis. Figure 5.1 shows the main stages of the analysis, starting with selecting the data and generating the signal (see Figure 5.2), as well as the background Monte-Carlo. All of the selected datasets should pass through a highly dedicated trigger system in order to select the most interesting events based on our signal characterization. As discussed in section 4.2, this analysis is based on triggers that require at least one well-defined and isolated lepton (electron or muon). Following that, we looked for a good object ID (tight, medium, loose, etc.) that resulted in a high reconstruction efficiency for the physics object we expected to be in our analysis (e.g., muons, electrons, and jets).

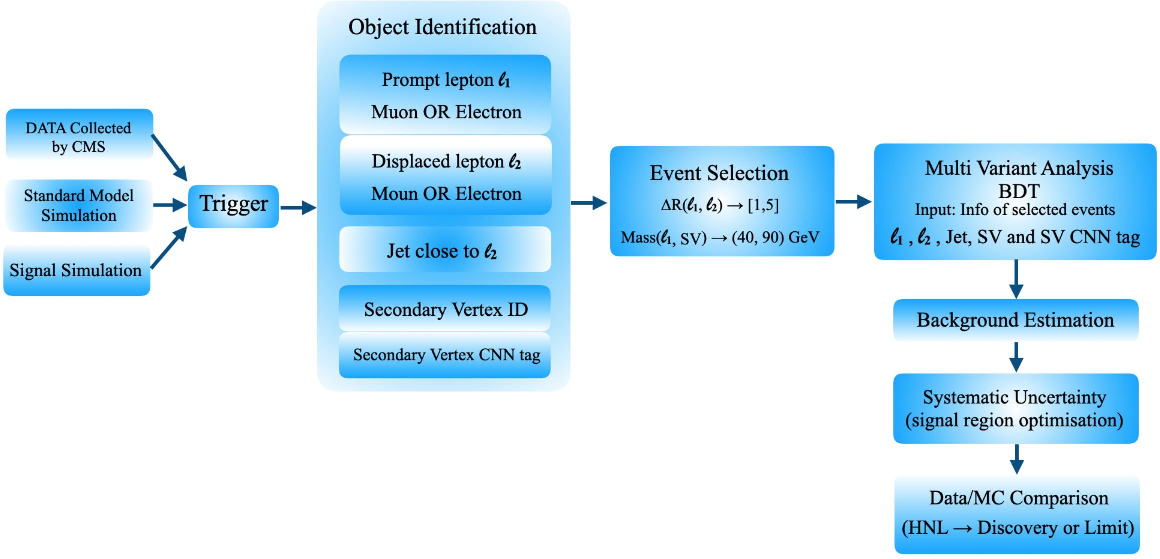

Figure 5.1: Analysis strategy diagram.

In the next step, we select our events using a combination of those physics objects

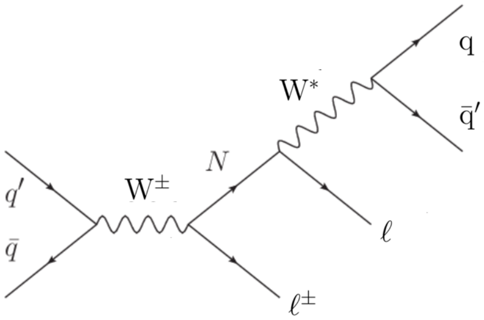

Figure 5.2: Feynman diagram of N production in a semi leptonic W decay, leading to a final state with one charged lepton and jets.

described in chapter 4 where each event is required to have at least two leptons in the final state, with any of the following flavors and charge composition:

- $\mu^{\pm}\mu^{\mp}$ or $\mu^{\pm}\mu^{\pm}$
- $e^{\pm}e^{\mp}$ or $e^{\pm}e^{\pm}$
- $\mu^{\pm}e^{\mp}$ or $\mu^{\pm}e^{\pm}$
- $e^{\pm}\mu^{\mp}$ or $e^{\pm}\mu^{\pm}$

These two leptons will be referred to as l_1 and l_2, respectively. The leading lepton l_1 is a prompt lepton (originating from PV) with the highest p_T, and the sub-leading lepton l_2 is a displaced lepton (originating from SV) with p_T less than l_1 p_T. As the list above indicates, we will consider 8 channels based on the flavors of l_1 and l_2 as well as the charge of l_1 with respect to the l_2 charge. As an example, the $\mu\mu$ channel denotes that both flavors of l_1 and l_2 are muons and can be divided into OS and SS. In the OS channel ($\mu^{\pm}\mu^{\mp}$), l_1 carries an opposite charge w.r.t l_2 and vice versa in the SS channel $\mu^{\pm}\mu^{\pm}$, where l_1 carries the same charge as l_2. A similar approach is applied to the rest of the channels (whether they are ee, eμ, or μe). A jet reconstructed using the Anti-k$_T$ jet algorithm with a cone radius of R = 0.4 and p_T > 20 GeV is required to be present in the event. This jet should be close to l_2 within a cone radius of ΔR less than 0.7. The final piece of the event definition is requiring a secondary vertex, reconstructed using the IVF algorithm described in section 4.4. This secondary vertex was tagged from the standard model background processes using a special Convolution Neural Network CNN model (see section 4.4.4). As a result, the event structure should include the following (l_1, l_2, Jet, and SV).

The next step is to add a few pre-selection cuts to reduce the background as much as possible while keeping a high efficiency for signal events. Table 5.1 shows the list of pre-selection requirements, which were chosen based on the characteristics of the HNL decay process. Since the signal process contains a W decay, the invariant mass of the prompt lepton l_1 plus the secondary vertex should match the mass of the W boson (m$_W$ =80.379 ± 0.012 GeV). To account for uncertainties in the W mass, a mass region of 40 GeV < Mass(l_1, SV) < 90 GeV is chosen around the W peak. Figures 5.3 and 5.4 show the comparison of signal and background processes as a function of mass(l_1, SV) for the main channels $\mu\mu$, ee, eμ , and μe in each year (2016, 2017 and 2018). As shown, the signal mass(l_1, SV) window is between 40 GeV and 90 GeV, in contrast to the background, which is spread out over a wider range. For the ΔR cut, we found that in the HNL models, the two leptons (l_1 and l_2) in each event are expected to have a unique signature of back-to-back tracks in the azimuthal (ϕ) plane. Figures 5.5 and 5.6 show the comparison of signal and background processes as a function of ΔR for the main channels $\mu\mu$, ee, eμ , and μe in each year (2016, 2017, and 2018). When the ΔR is close to π ($\pi =\sim 3.14$), the geometry of two leptons appears to be back-to-back, and as we can see from the plots, the peak of signal is almost around π, so we chose the cut range [1,5] to preserve the high amount of signal while removing background as much as possible. After applying the pre-selection as shown in Figures (5.3 -5.6) , it is clear how difficult it is to find a new signal in such a large number of background events. As a result, the next step was to use multivariate analysis to distinguish the signal from the background, as we will discuss in section 5.2.

variable	cut window
$\Delta R(l_1, l_2)$	[1,5]
Mass(l_1, SV)	(40, 90) GeV

Table 5.1: Pre-selection cuts applied to the datasets. Same selection is chosen for all the datasets (2016, 2017 and 2018, muons and electrons).

Estimating event yields from different background processes, as well as the shape of these backgrounds as a function of various variables, is a central task for any analysis.

By a data-driven background estimate, we mean an estimate that is essentially based on observed real collision events (data), though these estimates frequently include some simulation-based information as well. Furthermore, in our signal, we found that our simulations are unable to provide a fully reliable background estimate, so a data-driven background estimate is required, as we will see in section 5.3.1. Last but not least, before comparing data and MC to see if we have a new discovery or not, we would need to estimate the systematic uncertainties that would affect our signal region, as we will see in the next chapter.

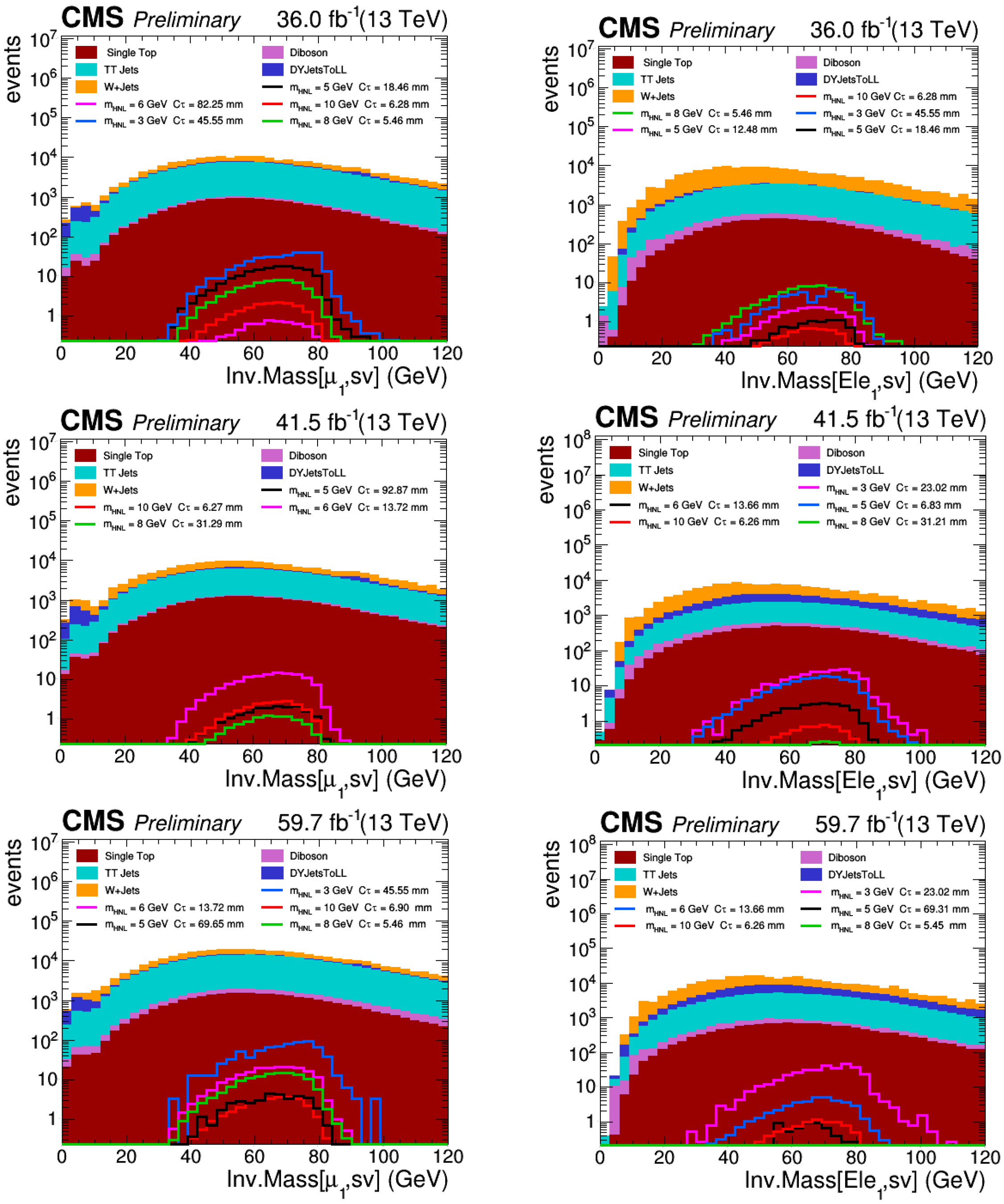

Figure 5.3: MC signal and background simulations distribution of the invariant mass of prompt lepton l_1 plus the secondary vertex [l_1,SV] for $\mu\mu$ channel (left) and ee channel (right) in years 2016 (top), 2017(middle) and 2018 (bottom)

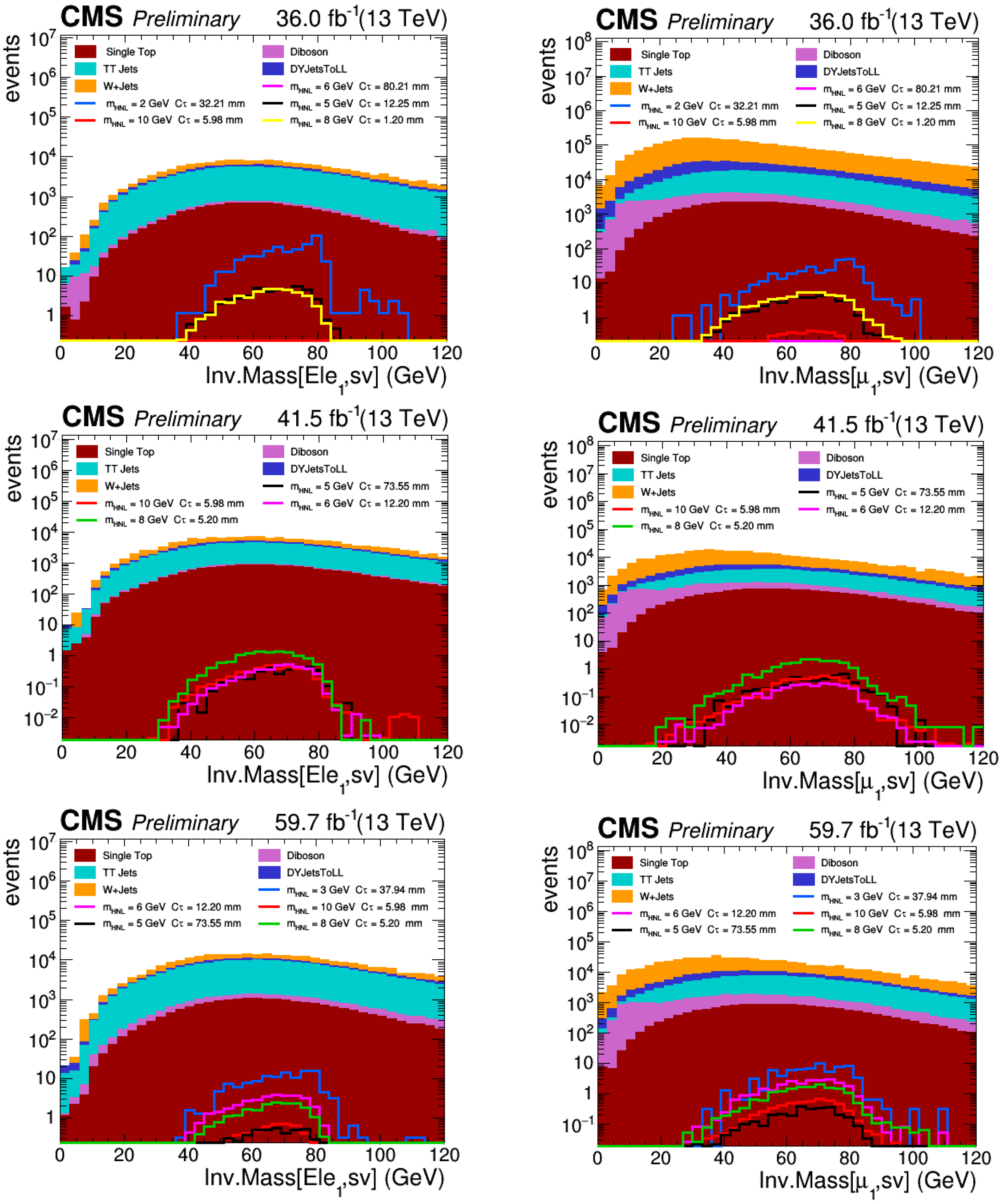

Figure 5.4: MC signal and background simulations distribution of the invariant mass of prompt lepton l_1 plus the secondary vertex $[l_1,\mathrm{SV}]$ for eμ channel (left) and μe channel (right) in years 2016 (top), 2017(middle) and 2018 (bottom).

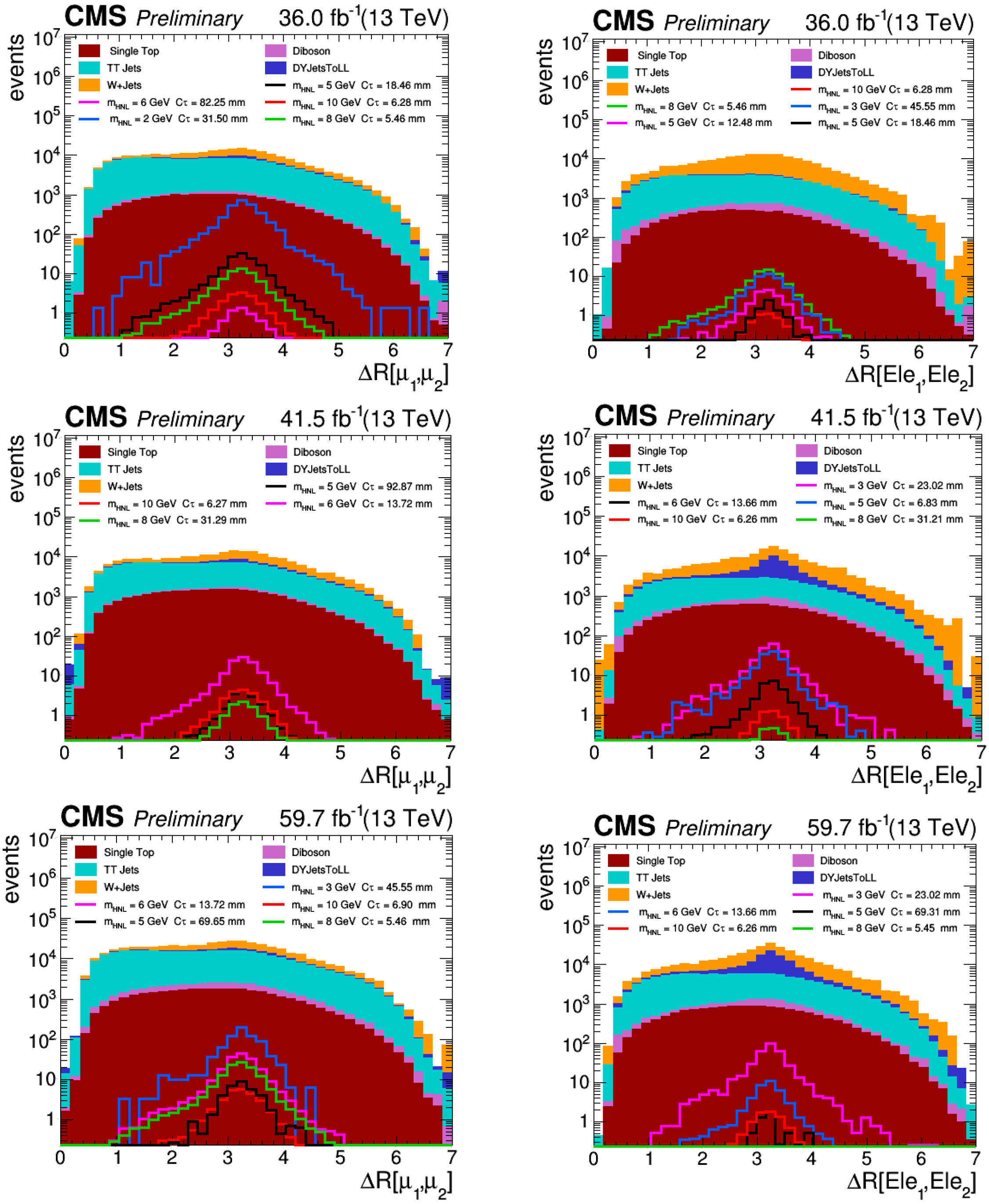

Figure 5.5: MC signal and background simulations distribution of Δ R between the prompt lepton l_1 and displaced lepton l_2 for $\mu\mu$ channel (left) and ee channel (right) in years 2016 (top), 2017(middle) and 2018 (bottom).

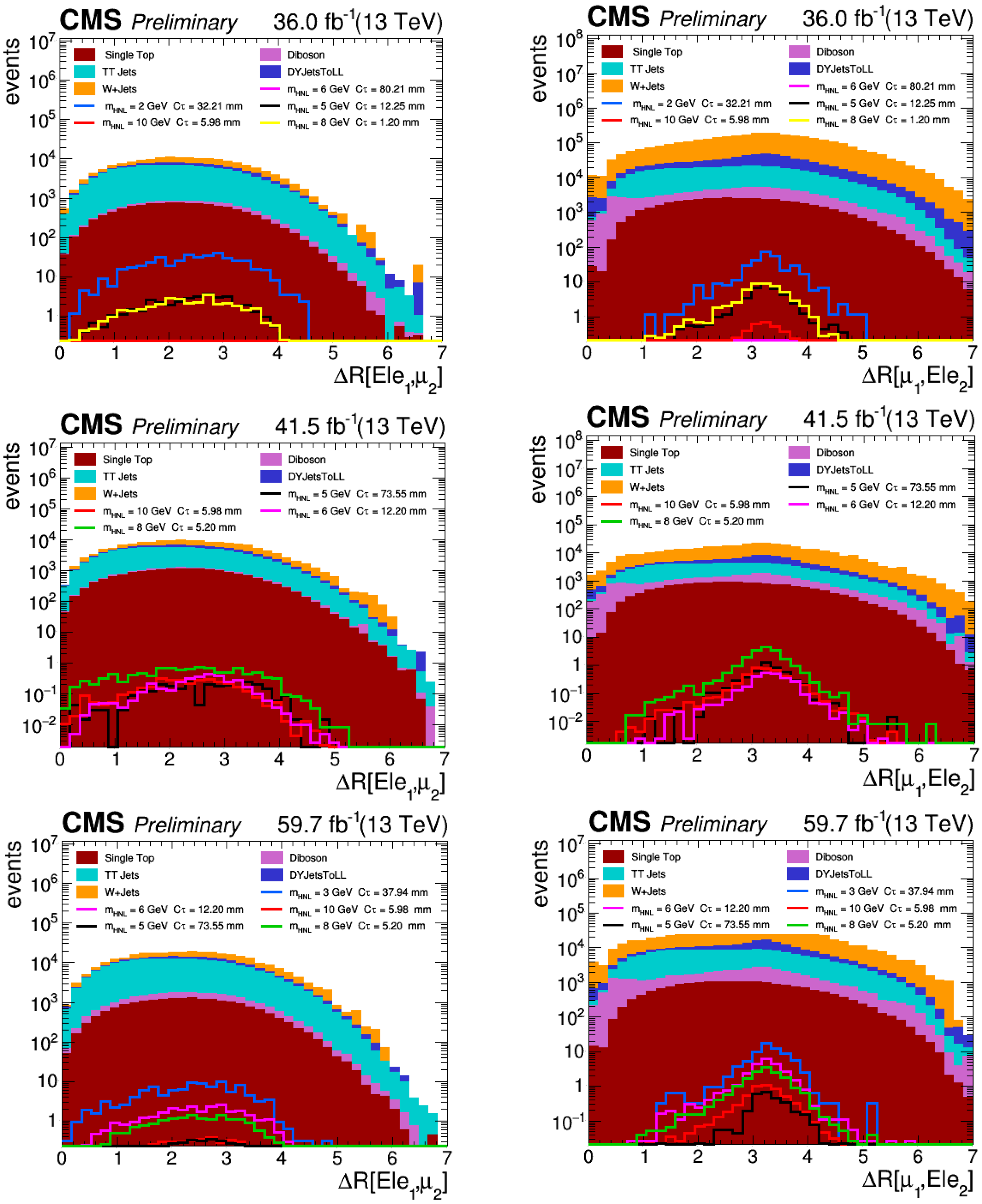

Figure 5.6: MC signal and background simulations distribution of Δ R between the prompt lepton l_1 and displaced lepton l_2 for eμ channel (left) and μe channel (right) in years 2016 (top), 2017(middle) and 2018 (bottom)

5.2 Multivariate Analysis in Particle Physics

Separating new physics signals from SM background processes is accomplished using algorithms that start with a sample of final objects and reject events that do not meet a set of pre-defined criteria. Discriminative algorithms may be further subdivided into cut-based and multivariate techniques. Cut-based techniques use a set of criteria motivated by physical considerations and cut values determined entirely by analyzing pure samples of signal and background objects, and optimising the different cut values by hand. Multivariate techniques use a large number of physically motivated variables to generate a discriminant, which is a single number that summarises the final discriminant performance of various cuts when applied to the input variables. It is generally prohibitive to analyze so many variables by hand, so signal and background samples are fed to a multidimensional space algorithm (dataset's dimensionality is defined as the number of input variables or features) seeking to simultaneously maximise the efficiency of selecting true events (signal) and rejecting fake events (background). The multivariate technique used in this analysis is the Boosted Decision Tree (BDT) [112].

5.2.1 The Boosted Decision Tree (BDT)

Machine learning (ML) is being more and more used in the field of data analysis. For example, it is used for particle identification and to search for rare signals while suppressing the background as much as possible in high energy physics (HEP). Among various ML methods, boosted decision tree (BDT) methods are often shown to be effective and robust [113]. All BDT methods use decision trees as weak learners and obtain strong classification power by combining many weak learners [114]. A weaker model of learnability, known as weak learnability, eliminates the necessity for the learner to reach arbitrarily high accuracy; instead, a weak learning algorithm must simply provide a hypothesis that performs slightly better than random guessing. The training process in any BDT algorithm is to minimize a loss function in a staged way. Boosting implies that each tree is dependent on previous trees. Whereas the algorithm learns by building each regression tree step by step, using a predefined loss function to assess and correct for errors in each step. As a result, boosting in the decision tree ensemble improves accuracy while posing a small risk of reducing coverage.

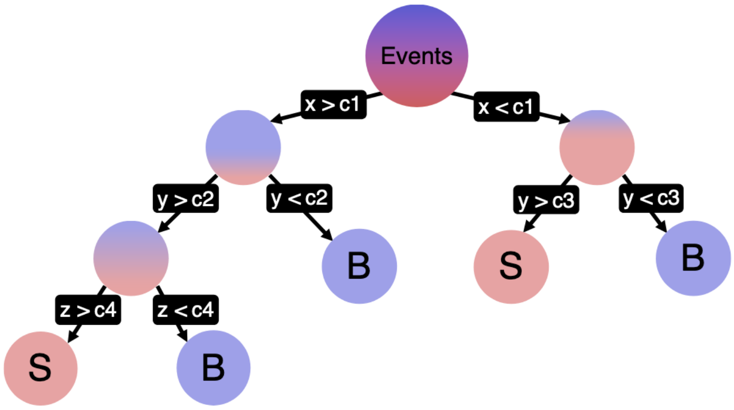

Figure 5.7: Schematic of a basic decision tree. An event passes through a series of nodes where a binary cut on a discriminating variable (x, y, z) is applied. The nodes at the very end of the tree are labelled as signal (S)or background (B) depending on the majority of events that end up in these nodes [115].

The algorithm is implemented in a software package called XGBoost [116], which offers fast training speed and good accuracy. In the common supervised learning scenario, the data set can be represented by a set containing n paired feature vectors and labels: $A = \{(x_i, y_i)\}(|A| = n)$. In the context of HNL classification, x_i is the vector of physics properties of the i-th event, while $y_i \in \{-20, 20\}$ indicates whether it is a signal event.

In general (Multi-Variate Analysis), MVA methods combine information from all observables x of an event into one or more output variables y , and this variable can then be used to decide if the event is selected as a signal or rejected as background, as indicated in figure 5.8.

Input Datasets

For a typical classification problem in HEP, we have two categories: signal and background, and we assign different values to them, which is called the truth value Y. It is 1 for signal events and 0 for background events by convention. For training purposes, two types of trees are involved: the signal tree and the background tree. The signal tree consists of all the features describing the signal events. The background

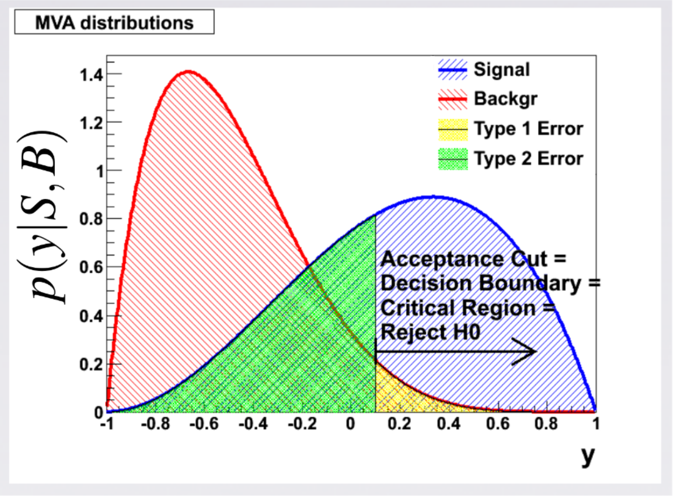

Figure 5.8: Shows a BDT plot for classifier output distributions for signal and background events [117]

.

tree consists of exactly the same features that passed through the same pre-selection cuts as the signal. For our study, the signal candidates have been produced with dedicated Monte Carlo generators for different decay lengths and HNL mass assumptions, in the range of [1-20] GeV of mass and for decay lengths of [1-200] mm. For the background we take, candidates are Standard Model MC samples (Wjets, Drell Yan, TTbar, DiBoson, Single Top, TriBosons). Events passing all the pre-selections and vertex matching in the case of a signal are used for training. Several variables are selected as inputs in the BDT training, for example, the four-momenta of the final particles or various mass variables, etc.

Input Variables

A list of input variables was constructed, containing a few dozen variables that have the potential to discriminate between HNL signal and SM background events. The variables were chosen so that the BDT output response should be independent of all prompt lepton features for background estimation purposes (see section 5.3.1). Therefore, the kinematics properties used mainly are related to the three physics objects (displaced lepton l_2, secondary vertex SV, and jet close to displaced lepton). The BDT model will depend on the displaced lepton flavour, so two BDT models have been created. The first model includes information about displaced muons and will be used for HNL channels where the displaced lepton flavor is muon($\mu\mu$ and eμ). The second model will be used for HNL channels containing a displaced electron (ee and μe). In order to narrow the list of potential BDT variables, an elimination procedure is applied, as illustrated in Figure 5.9. Starting from the large list of variables, the BDT is trained and the variable ranking is examined (the top left plot of Figure 5.9). The lowest-ranked variable is removed from the list, and the BDT is trained again. This process is repeated until we reach a list of about 40 variables. At this point, we began investigating some of the other figures of merit for the variable performance, such as their correlation with other variables (see Figure 5.9, top right plot). If two variables have a correlation of 40%or above, both of the variables are taken out of the training one by one to check which of the two achieves a better overall performance in the BDT (the bottom plot of Figure 5.9). The one performing less well is then discarded. With this elimination method, we reach a list of ∼25 variables performing well inside the BDT and can be found in appendix A. The major sensitivity of the input variables comes from the secondary vertex CNN tagging described in section 4.4.4. The displacement distance between the primary and secondary vertex in two and three dimensions (L_{xy}, L_{xyz}) and their significances (L_{xySig}, L_{xyzSig}) are found to strongly distinguish the signal from the background. Figures 5.10 and 5.11 show a comparison of data and Monte-Carlo background for various input variables used in BDT training for $\mu\mu$ and ee channels in 2016. A good match between the data and MC can be seen, providing more confidence in background Monte-Carlo for use in BDT training where it can represent real data.

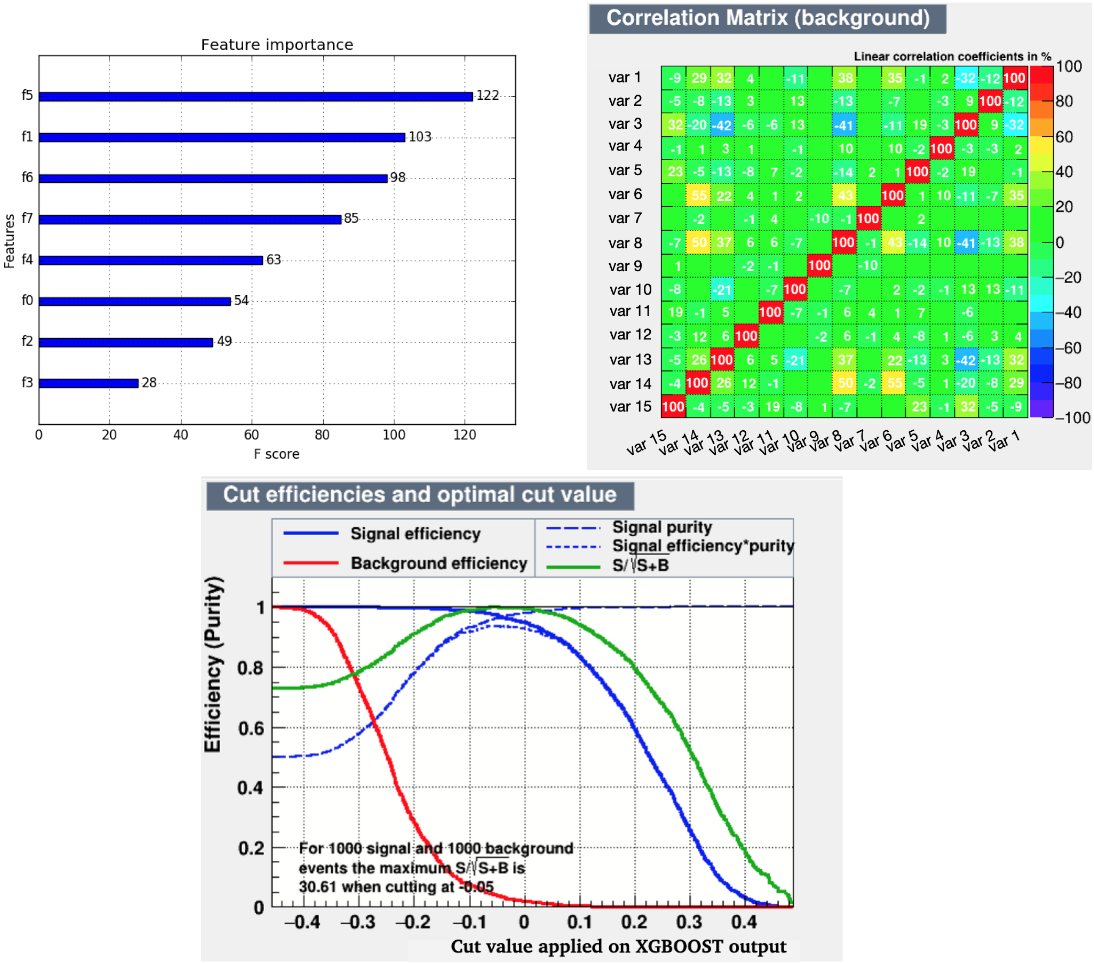

Correlation Matrix (background)

Linear correlation coefficients in %

	var 15	var 14	var 13	var 12	var 11	var 10	var 9	var 8	var 7	var 6	var 5	var 4	var 3	var 2	var 1
var 1	-9	29	32	4		-11		38		35	-1	2	-32	-12	100
var 2	-5	-8	-13	3		13		-13		-7		-3	9	100	-12
var 3	32	-20	-42	-6	-6	13		-41		-11	19	-3	100	9	-32
var 4	-1	1	3	1		-1		10		10	-2	100	-3	-3	2
var 5	23	-5	-13	-8	7	-2		-14	2	1	100	-2	19		-1
var 6		55	22	4	1	2		43		100	1	10	-11	-7	35
var 7		-2		-1	4		-10	-1	100		2				
var 8	-7	50	37	6	6	-7		100	-1	43	-14	10	-41	-13	38
var 9	1			-2	-1		100		-10						
var 10	-8		-21		-7	100		-7		2	-2	-1	13	13	-11
var 11	19	-1	5		100	-7	-1	6	4	1	7		-6		
var 12	-3	12	6	100			-2	6	-1	4	-8	1	-6	3	4
var 13	-5	26	100	6	5	-21		37		22	-13	3	-42	-13	32
var 14	-4	100	26	12	-1			50	-2	55	-5	1	-20	-8	29
var 15	100	-4	-5	-3	19	-8	1	-7			23	-1	32	-5	-9

Figure 5.9: XGBoost feature importance bar chart illustration on the top left, linear correlation between the variables for the signal sample on the top right and the BDT performance study by checking the signal and background efficiencies after applying a cut to the BDT output response.

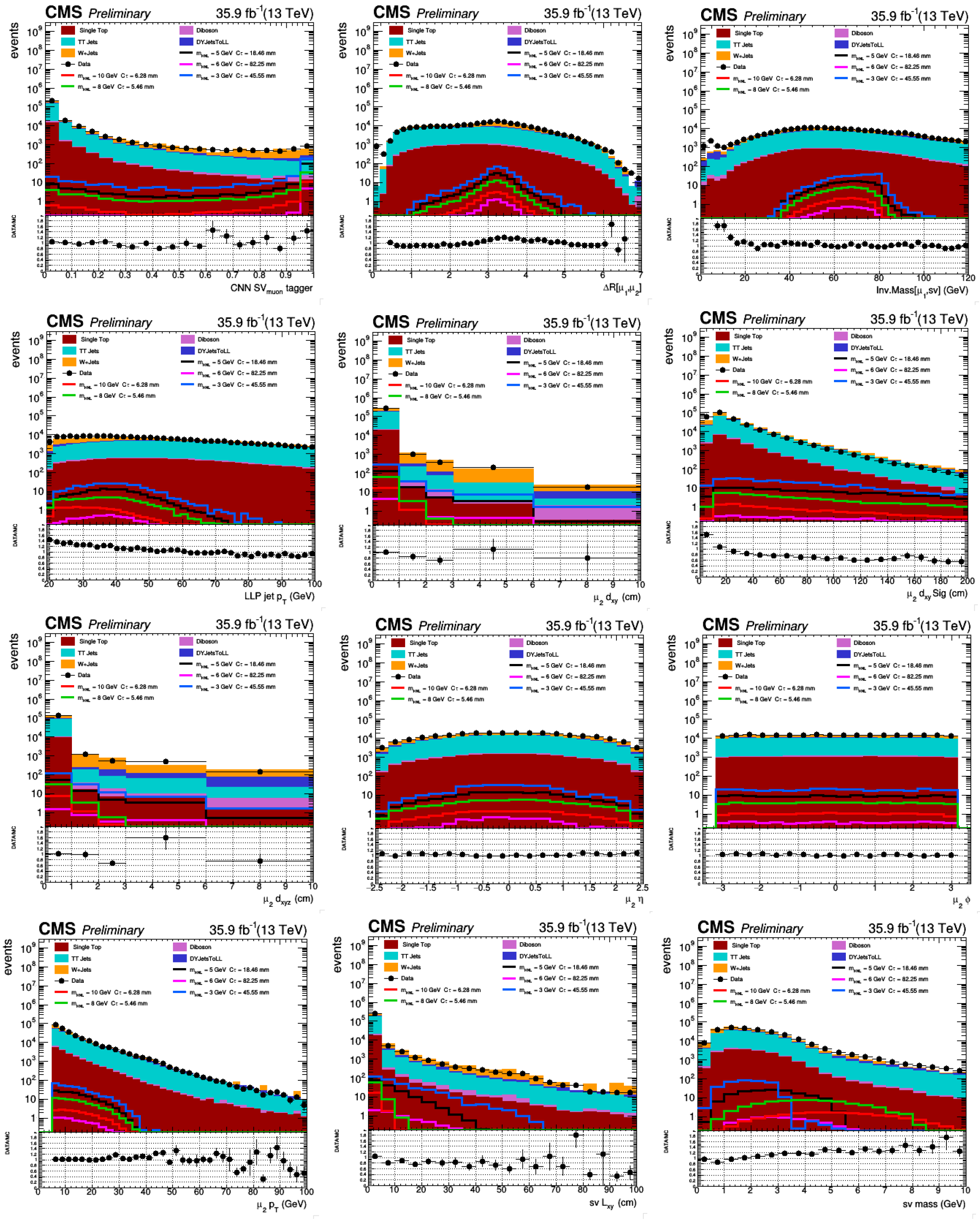

Figure 5.10: Distributions of some input variables for the BDT in $\mu\mu$ channel events.

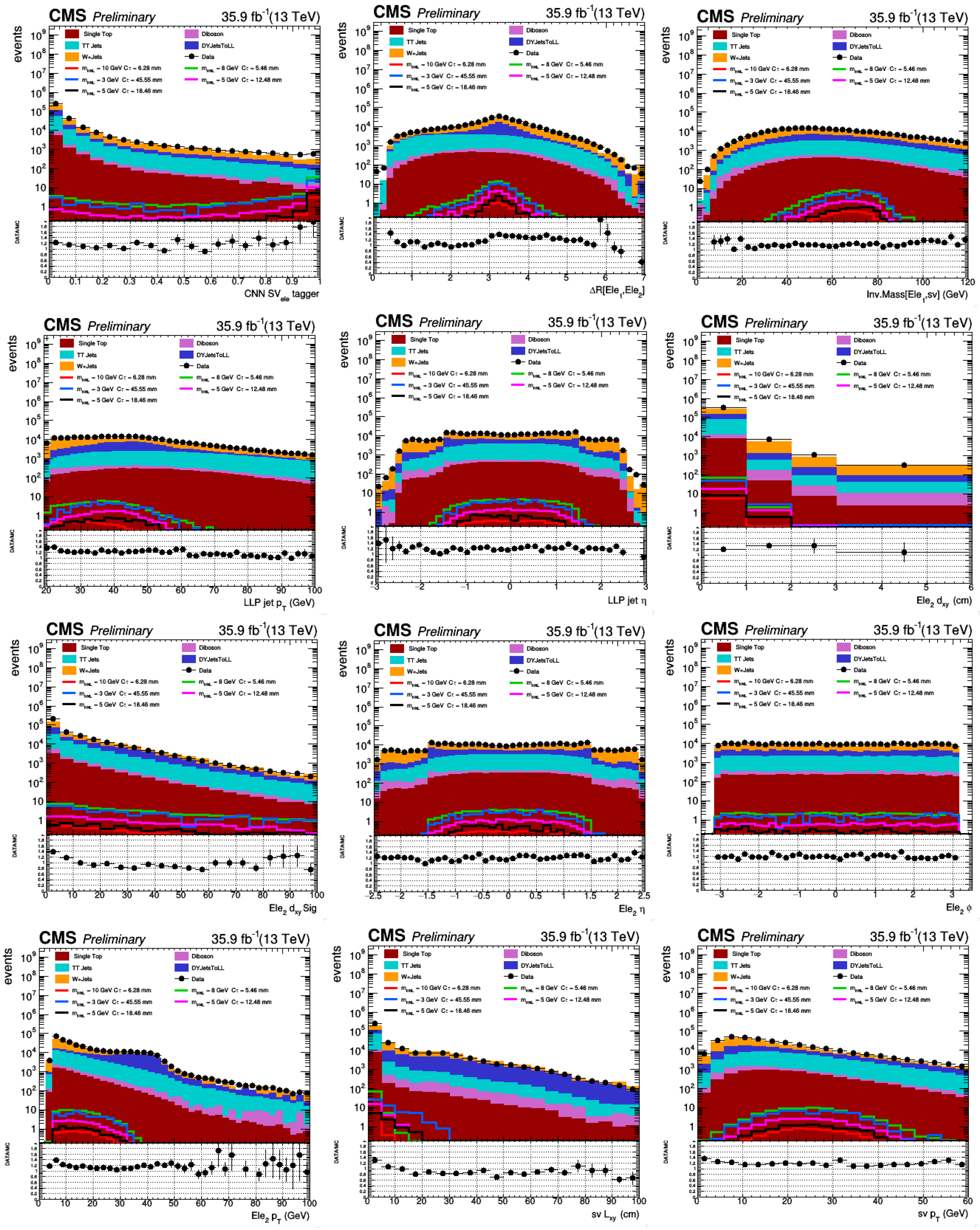

Figure 5.11: Distributions of some input variables for the BDT in ee channel events.

BDT Hyper-Parameters

In machine learning, a hyper-parameter is a parameter whose value is used to control the learning process. In the first optimization step, different hyperparameters for the BDTs are optimized. The boosting algorithm, the number of trees in the boost, the maximum depth of the tree, the minimum number of events in the final nodes, and the learning rate are varied in a grid scan. As a result, the best model was discovered by employing the XGBoost [116] boosting algorithm, with a learning rate of 0.01, 2000 estimators (trees number), and a maximum depth of 9. To asses the performance of the model, the "k-folding" technique is applied (see next section).

Over-Fitting

If the classifier is observed to perform well only on the training set and has low accuracy in classifying events in the testing set, it is said to suffer from the problem of over-fitting. This phenomenon can happen if we have used too many variables or if the size of the training dataset used is not large enough. To avoid over-fitting problems and increase the dimension of the training sample, the following strategy is adopted, also known as the "k-folding" technique. Both signal and background samples are split into n parts for each of the two categories, signal and background. The training samples are made up of (n-1) sub-samples. To apply the BDT classifier to each of the n sub-samples, a cyclical permutation is performed. The BDT output response should be matched between training and testing so that we can declare we are safe from over-fitting problems (see Figure 5.12).

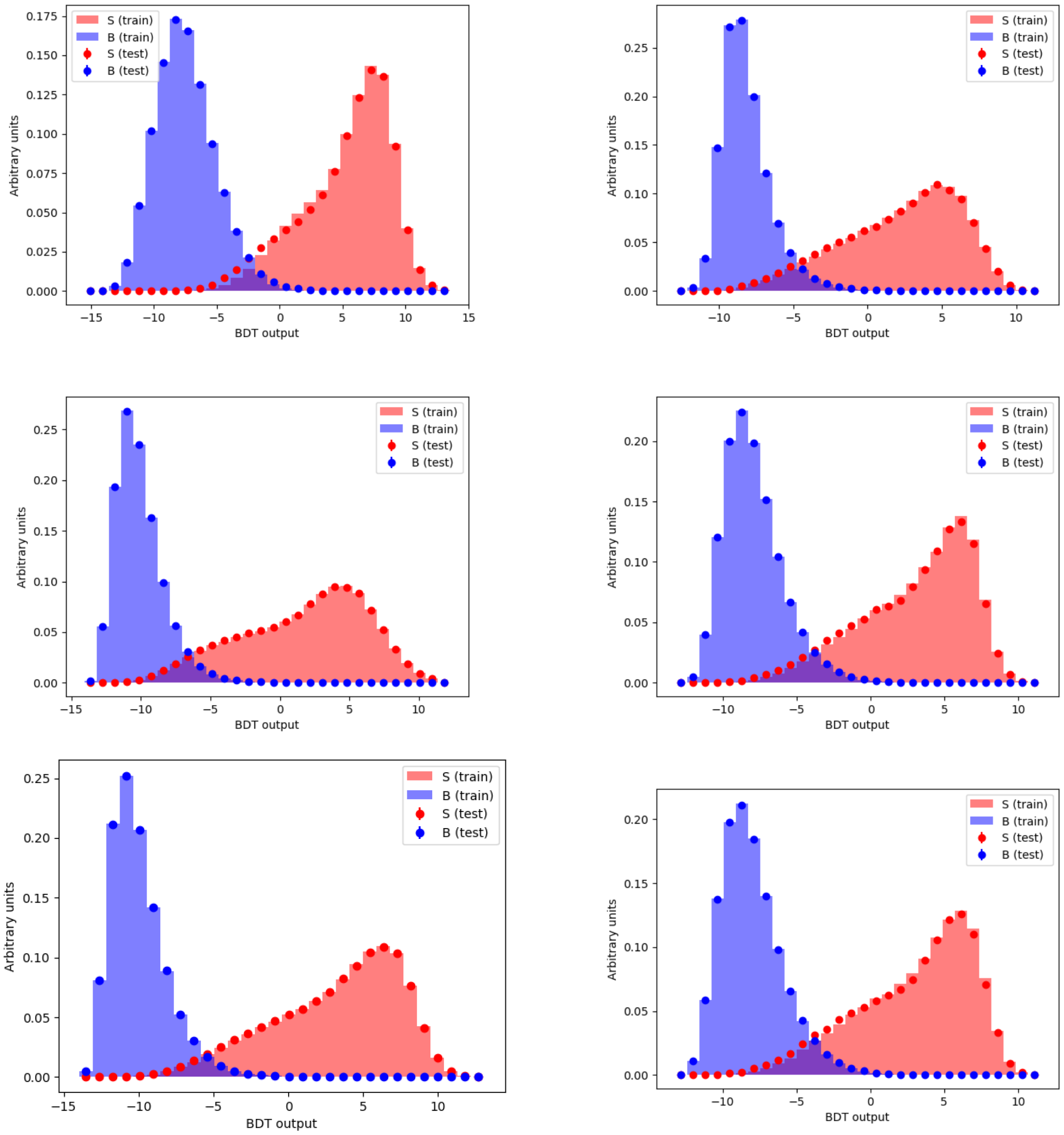

Figure 5.12: Over-fitting checks plots produced by comparing training and testing as a function of BDT output response for $\mu\mu$ (left) and ee (right) channels in 2016, 2017, and 2018.

BDT Response

The performance of a BDT can be quantified by its area under the ROC Curve (AUC). The Receiver Operating Characteristics (ROC) curve plot is the signal efficiency as a function of the background rejection. The area under this curve tells us how well our multivariate analysis is capable of distinguishing signal from background events, with a larger area indicating better performance. Figure 5.13 shows the area under the curve ($\sim$99%) of the ROC curve study for $\mu\mu$ and ee channels in 2016, 2017, and 2018. Figures 5.14 and 5.15 show the distributions of the BDT discriminants for signal and background models in the two categories of lepton flavours. Both BDTs provide a powerful separation between signal and background processes. As we can clearly see, this is the main advantage of ML, as it allows us to define only one variable to use for obtaining our signal region (a region where we can see the signal in a highly sensitive way among the background) rather than cutting on several variables (sometimes more than 20 variables). This variable, or so-called ML response, comes from learning the ML model about the features of our signal after comparing it to the expected background by training the BDTs on both signal and background. The BDT models obtained from this training step are then directly applied to real data as well as all Monte-Carlo samples (signal and background) to start the process of looking for our mystery particle in the signal region. But first we need to study and estimate the expected SM background in the signal region (see next section).

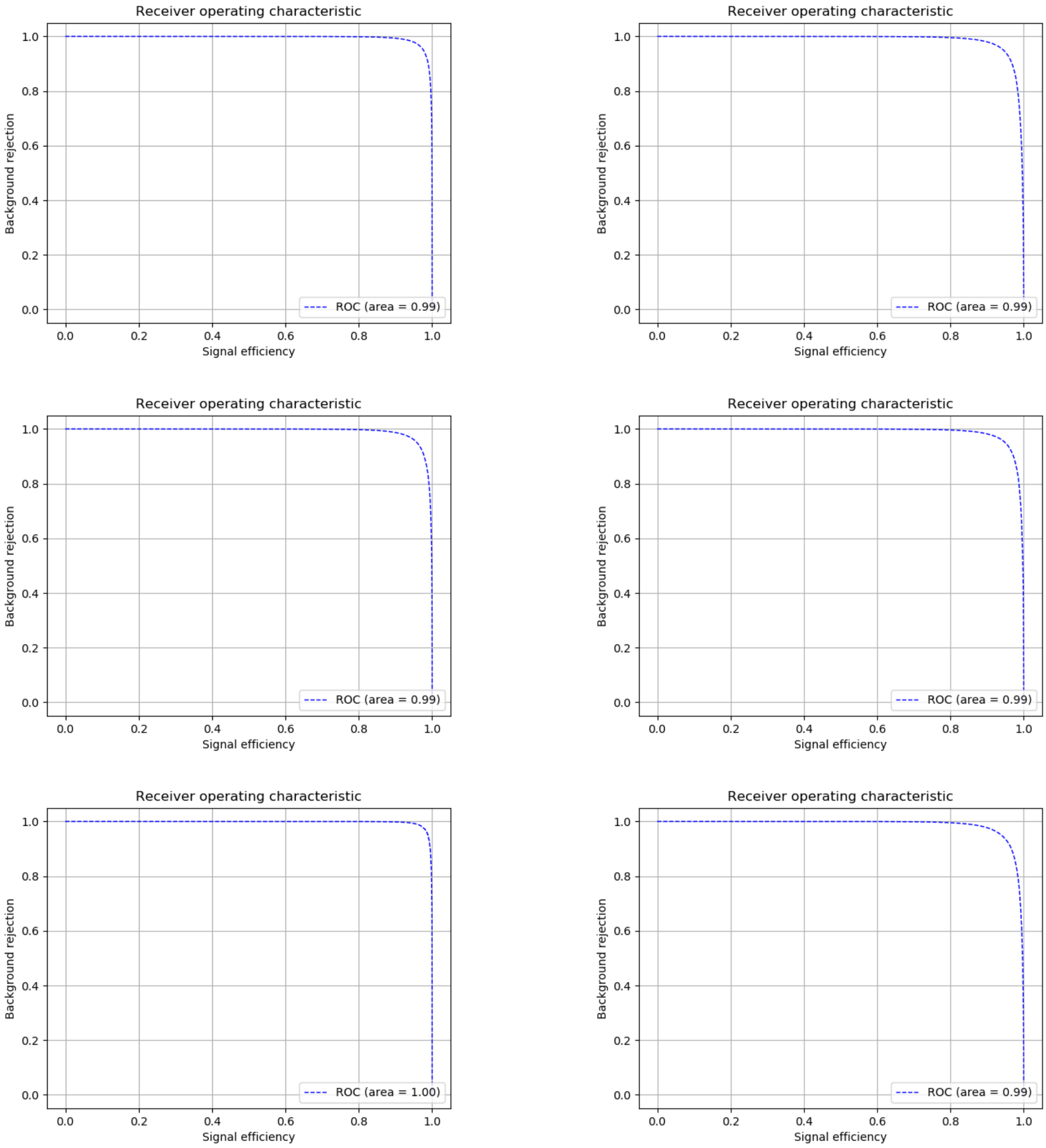

Figure 5.13: ROC curves obtained from the training of the BDT for $\mu\mu$ (left) and ee (right) in years 2016 (top), 2017(middle) and 2018(bottom).

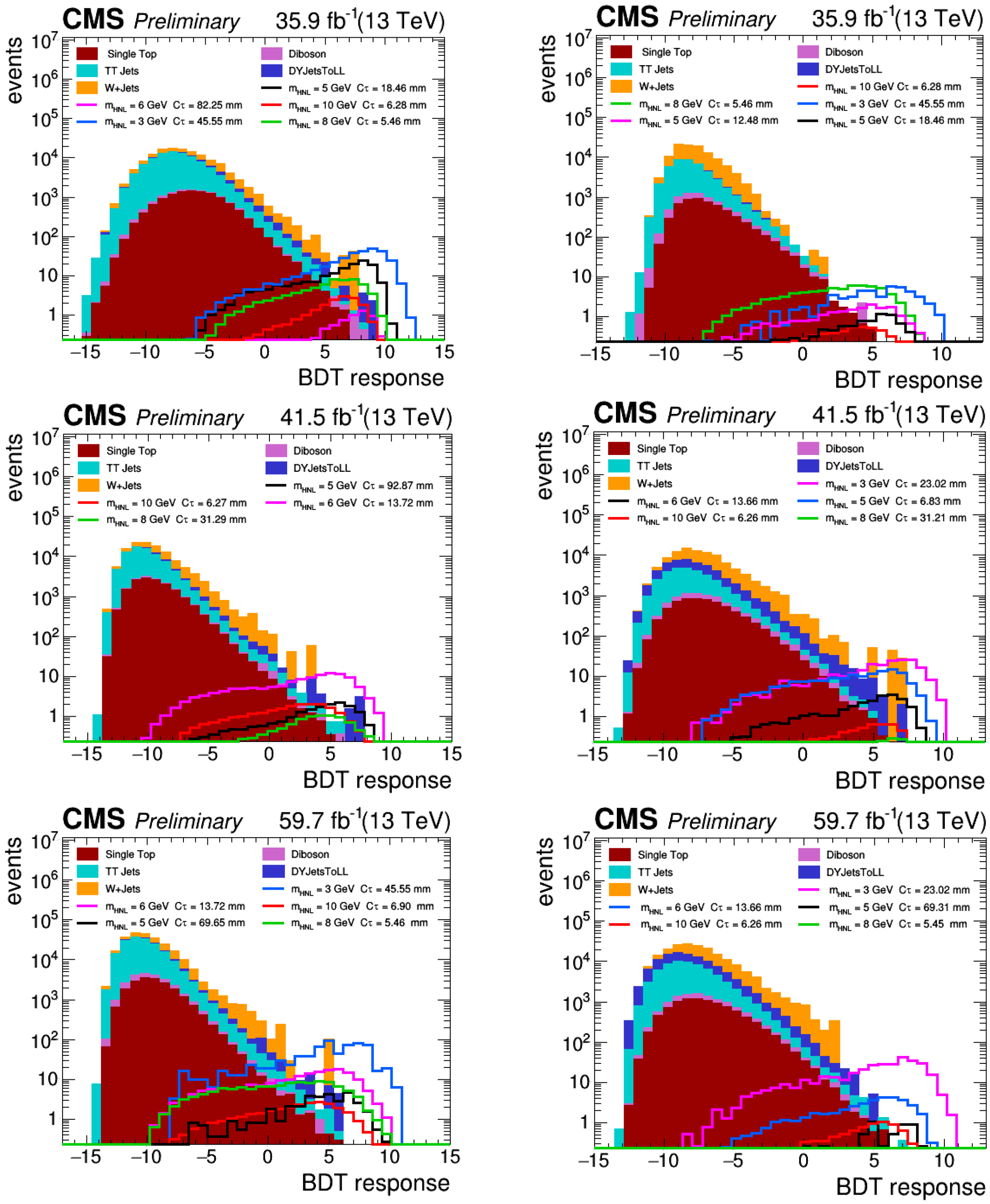

Figure 5.14: Response plots obtained from the training of the BDT for $\mu\mu$ (left) and ee (right) in years 2016 (top), 2017(middle) and 2018(bottom).

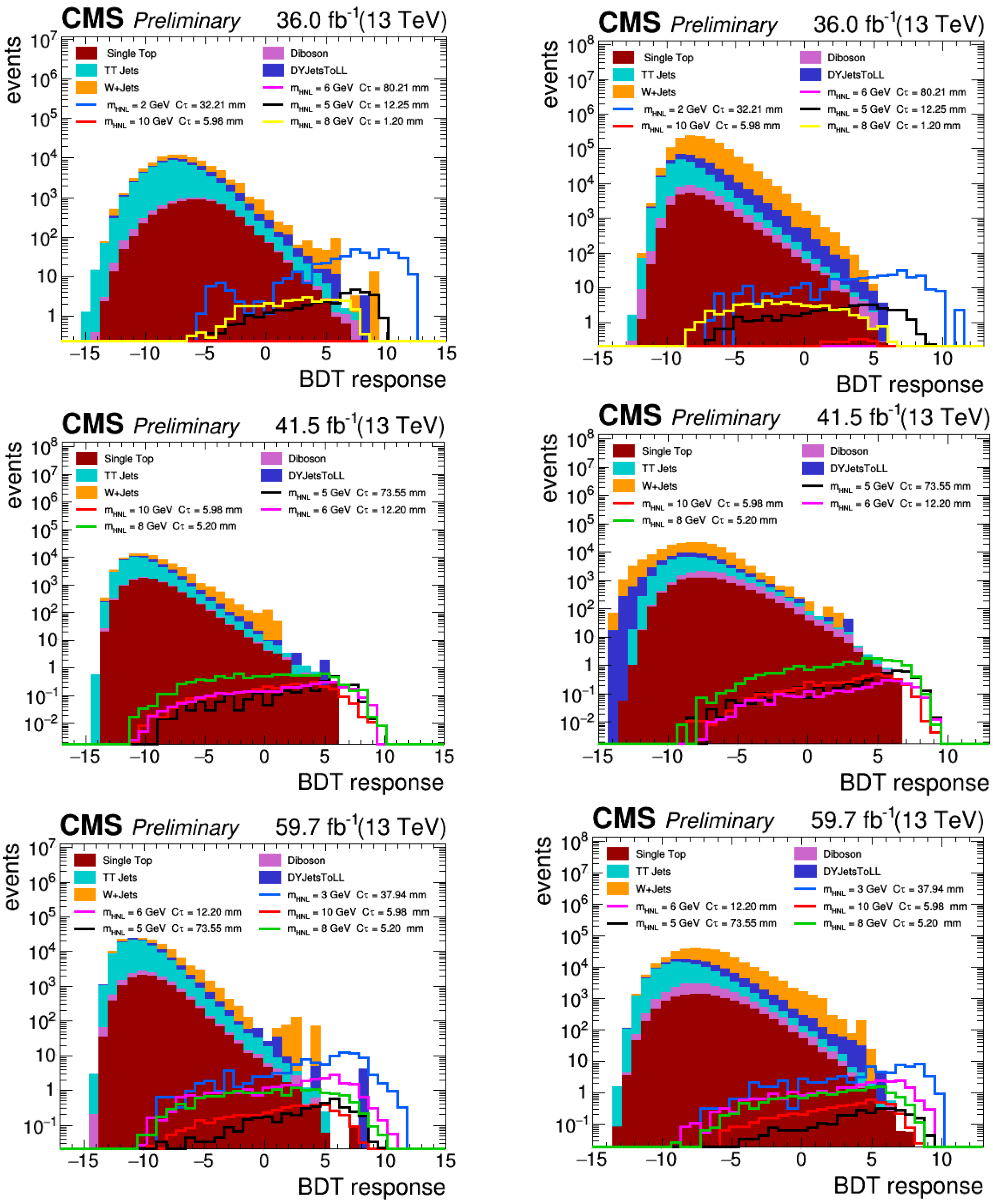

Figure 5.15: Response plots obtained from the training of the BDT for eμ (left) and μe (right) in years 2016 (top), 2017(middle) and 2018(bottom).

5.3 Background Estimation

The discovery of a new physics signal is based on the count of events exceeding the Standard Model background in the signal region after applying a properly defined analysis cut. Keeping the background under control is then the fundamental task of the whole analysis, and this could be done in several ways. The first, and more immediate, could be a quantitative use of Monte Carlo backgrounds, that is, a search for an excess with respect to what is predicted by simulations. This method has severe limitations, one of which is that the simulations are unable to predict the non-prompt lepton properly (from the generation of the hard scattering to the simulations of the detectors). So it was important to first study the simulation events that we have in the signal region to get an appropriate picture of the expected background. Within the framework of this search, leptons that directly come from W or Z boson decays are considered prompt leptons, whereas those originating from semi-leptonic heavy quark decays within jets or from other misidentified detector signatures are labelled as misidentified (fake or non-prompt) leptons. Additionally, a smaller fraction of non-prompt leptons is due to internal or external asymmetric conversions of photons, and such leptons are labelled as "conversion leptons."

5.3.1 Background Study

We have studied the expected background composition from simulation in the signal region and checked for each reconstructed lepton what "true" particle it corresponds to, i.e., if the lepton is prompt or fake. This information can be easily obtained from Monte Carlo "Truth" information.

We concluded from this study (Figure 5.16) that the first lepton would be a "prompt" and the second lepton would be a "fake" in most cases. Given that the second lepton is frequently "fake", simulations are unable to provide a reliable background estimate, and hence it was necessary to develop methods more directly linked to real data and less to the predictions of Monte Carlo simulations. These methods are called "data-driven methods," where the control of the residual background is based on the data. Many data-driven techniques have been developed by the CMS collaboration. The method developed in this thesis belongs to the class

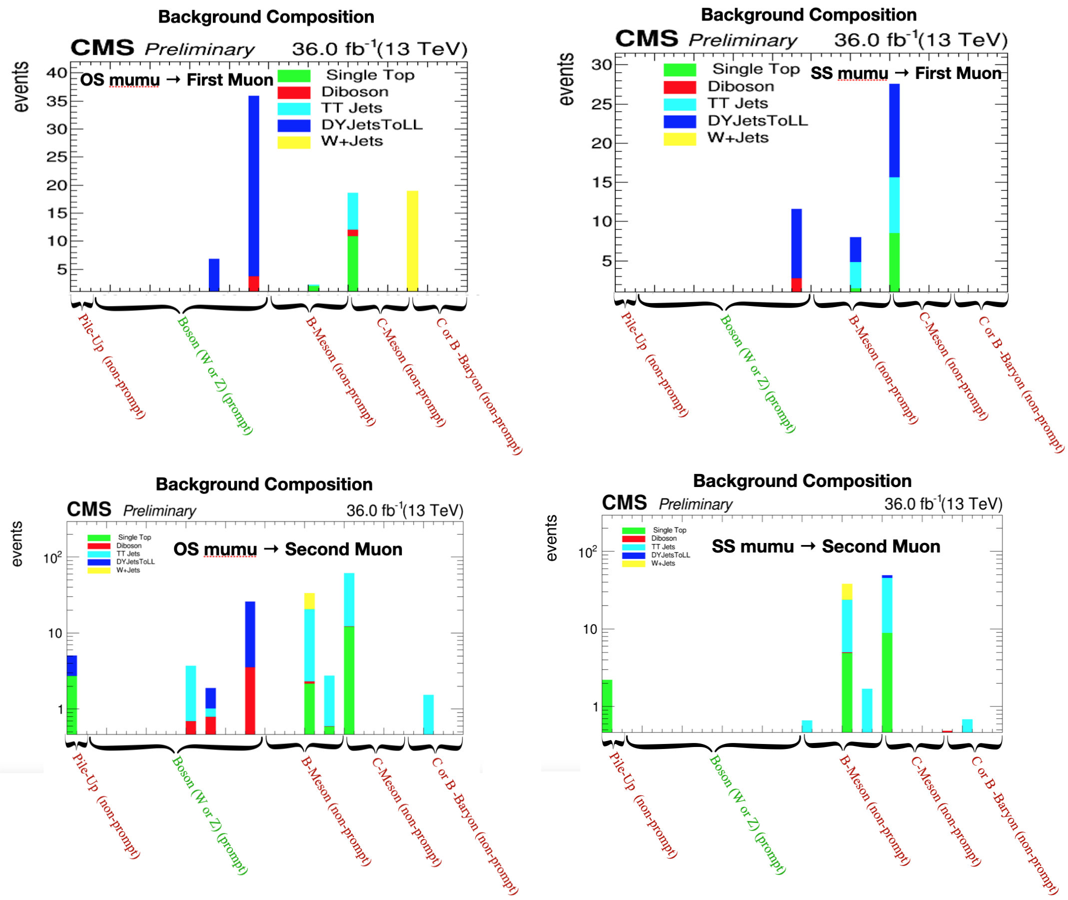

Figure 5.16: Background composition study for $\mu\mu$ channel; First muon (top) and second muon (bottom) classified to opposite sign muons (OS) (left) and same sign muons (SS) (right) .

of the fake-rate estimate. Low statistics and numerous fake-rate dependencies pose a serious challenge to the conventional tight-to-loose method (see next section). In order to deal with these short-comings, a new background estimation was developed by reformulating the fake-rate measurement as a classification problem for a deep neural network (DNN).

5.3.2 Date Driven Background Prediction

The basic idea of the fake rate method (tight-to-loose ratio) is to estimate backgrounds that have one or more leptons that do not originate from a W or Z. The probability of a loosely defined lepton passing the full set of selection criteria is measured in data, called the measurement region. Once measured, this probability is applied to a sample of events which pass the full kinematic selections of our signal regions but where at least one of the leptons fails the standard lepton selection while passing the loose requirement. Hence, we can predict the number of events from fake leptons entering each signal region. The loose-tight selection in this analysis can be determined by choosing two different cuts of the BDT response. So the contribution from non-prompt leptons is obtained by weighting events that pass the loose cut of BDT response but fail the tight requirements. Fake rates are measured for electrons and muons independently. To keep the measurement region and the application region as similar as possible, only the cut on the mass (l_1, SV) is inverted. This leads to three regions:

1. region 1 - measurement region: Mass$[l_1, SV] < 40$ GeV.
2. region 2 - application region: 40 <Mass$[l_1, SV] < 90$ GeV.
3. region 3 - measurement region Mass$[l_1, SV] > 90$ GeV.

Within each of those regions, two sub-regions are defined according to the score of the BDT output response. The first region is obtained by applying a "tight" cut on BDT response > 2, while the second is derived by applying a "loose" cut on BDT response (-4 $<$ BDT output $<$ 2). The tight selection of the application region corresponds to the signal region, and Table 5.2 contains a summary of all the regions we have.

In order to estimate the fake rate using a DNN model, this can be expressed as a classification problem between events that pass the loose selection but fail the tight requirements and events that pass the tight selection. The formulation of the problem as a classification problem is a practical way to leverage the universal approx theorem [118]. By training a neural network using those events as binary classification, the NN will learn the differences between the two samples. The DNN output score of events with loose criteria can be interpreted as the probability of such events belonging to tight selections. As a result, the NN can be directly interpreted as fake-rate probabilities and replace the tight-to-loose ratio weights. Following that, we trained regions (A and B) against regions (B and C). Hence, the output will be used to re-weight the control region (defined in Table Table 5.2) to predict

	Tight BDT cut (BDT output $>$ 2)	Loose BDT cut (-4 $<$ BDT output $<$ 2)
Mass[l_1,SV] $<$ 40 GeV (Measurement Region)	region A	region C
40 GeV $<$ Mass[l_1,SV] $<$ 90 GeV (Application Region)	signal region	control region
Mass[l_1,SV] $>$ 90 GeV (Measurement Region)	region B	region D

Table 5.2: Summary of measurement and application regions used in DNN model.

the background in the signal region (Figure 5.17). The input variable used in the training of the DNN are:

- p_T, η, l_{xy}, number of tracks and mass of secondary vertex.
- p_T and η of the displaced lepton.
- Secondary vertex CNN tagger.

The DNN model used consists of:

- An input layer with 16 nodes.
- Three hidden layers with 4096, 128 and 16 nodes, respectively, where each of them consists of a *dense layer*, a *dropout unit*, a *batch normalization layer* and an *activation unit* [119].
- An output layer with one node, activated by a sigmoid function.

The training model uses the Adam optimization [119]. The optimisation algorithm is a method that is iteratively run by comparing different solutions until an optimum or satisfying answer is identified. Adam is an adaptive learning rate optimisation technique, particularly for deep neural network training. It employs a mix of two gradient descent methods. Momentum: This approach is used to improve the gradient descent process by taking the ”exponentially weighted average” of the gradients into account. Using averages causes the algorithm to converge to the minima more

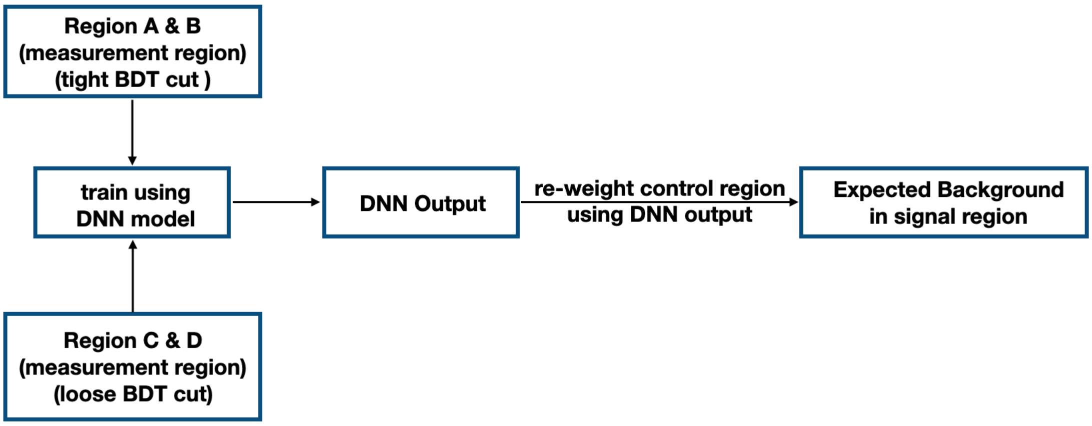

Figure 5.17: Diagram shows fake rate estimates using DNN model, re-weighting the control region to predict the background in the signal region.

quickly. RMSprop, or root mean square prop, is an adaptive learning technique that attempts to enhance the adaptive gradient algorithm (Adagrad). It uses the ”exponential moving average” rather than the cumulative sum of squared gradients like AdaGrad does. Finally, the output will be between 0 and 1, which is interpreted as the probability that a background event passes the tight selection.

The number of fake events in each bin, N^i_{fake} satisfies the following equation:

$$N^i_{fake} = \sum_{i\epsilon loose} f(p^i_T, \eta^i, m^i_{sv}, ...) = \sum_{i\epsilon(loose-tight)} \frac{f(p^i_T, \eta^i, m^i_{sv}, ...)}{1 - f(p^i_T, \eta^i, m^i_{sv}, ...)} \tag{5.1}$$

The distributions of the estimated background events, in the signal region, as a function of the secondary vertex mass, for the muon and the electron channels, are shown in Figures 5.18 and 5.19.

5.3.3 MC Closure Test

To validate the background estimation, we repeat the method using only the simulations. The $t\bar{t}$ Monte-Carlo simulation sample is used to perform the closure test. Using the Mass [l_1,SV] cut to define measurement and application regions as it is detailed in section 5.3.2.

The results of the MC closure tests for the $t\bar{t}$ sample are shown in Figures 5.20 - 5.31, comparing the measured and predicted lepton events. The distribution of events as a function of secondary vertex mass and displacement in the measurement and application regions is presented. The plots show that the observed and predicted yields in the $t\bar{t}$ simulation agree within the statistical band, thus showing the closure.

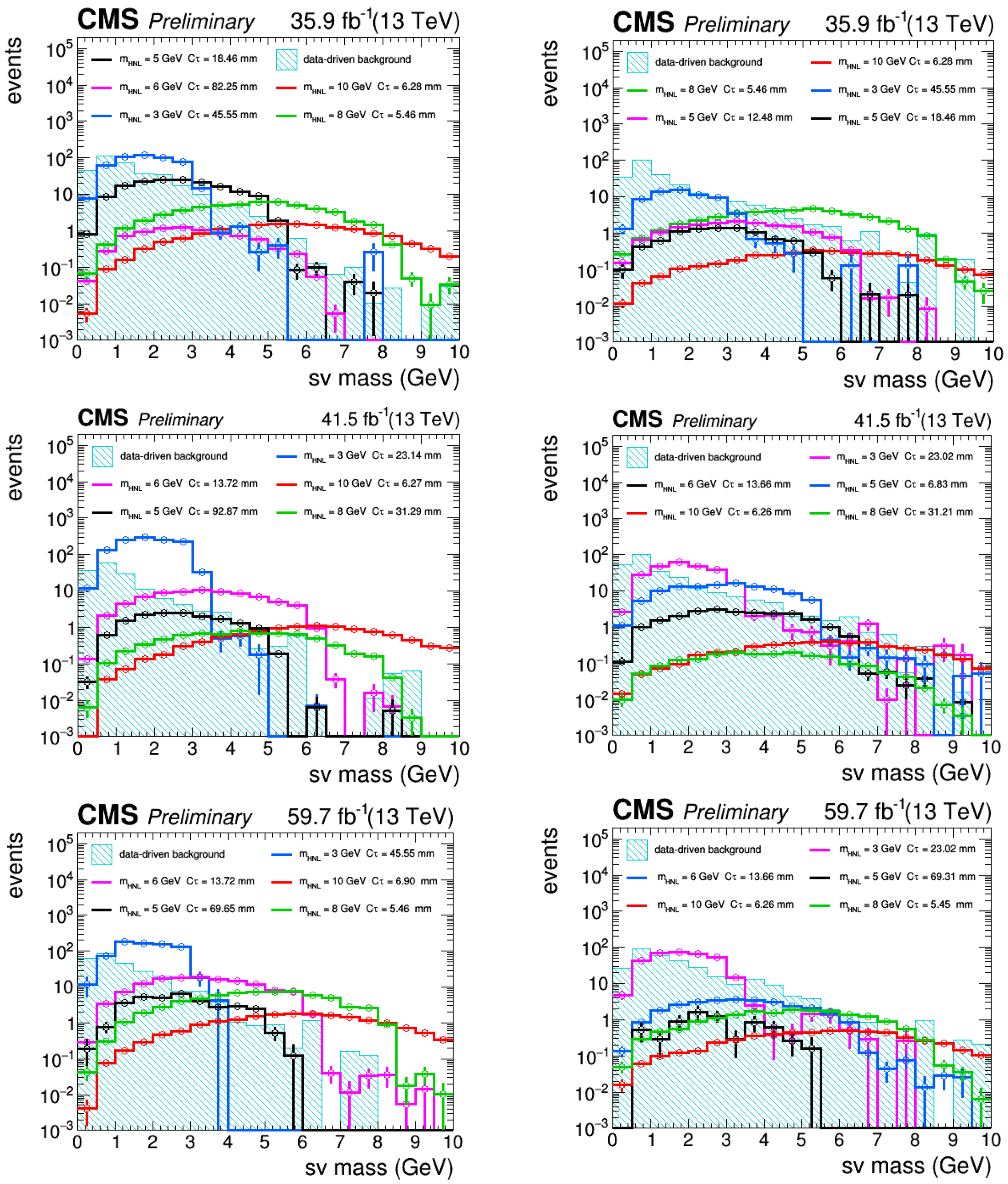

Figure 5.18: Distribution of estimated background events in the signal region as a function of the secondary vertex mass, for $\mu\mu$ (left) and ee (right) in 2016 (top), 2017 (medium) and 2018 (bottom).

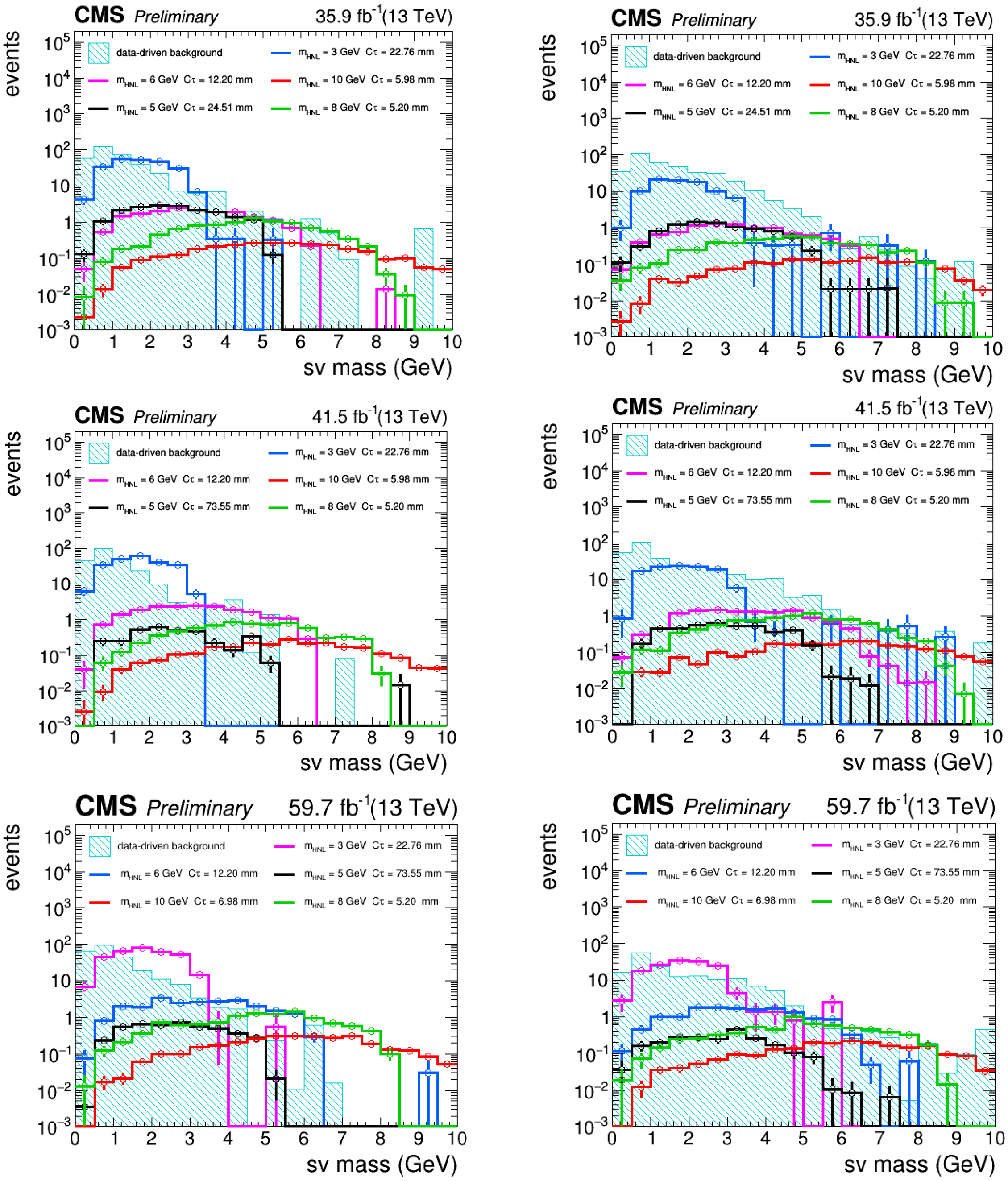

Figure 5.19: Distribution of estimated background events in the signal region as a function of the secondary vertex mass, for eμ (left) and μe (right) in 2016 (top), 2017 (medium) and 2018 (bottom).

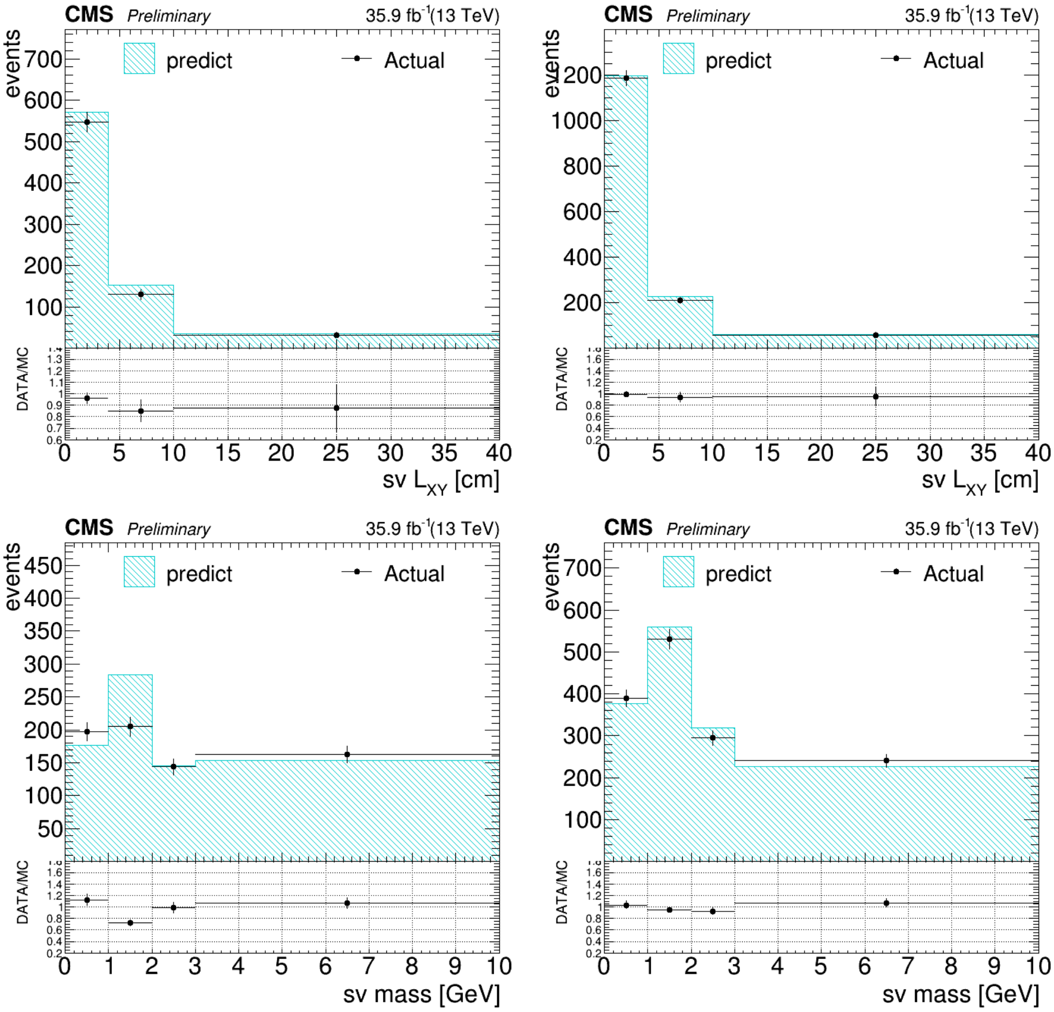

Figure 5.20: Distribution of observed and predicted yields in $t\bar{t}$ simulation for measurement(left) and application(right) regions as a function of the secondary vertex displacement (top) and mass (bottom), for $\mu\mu$ channel in 2016.

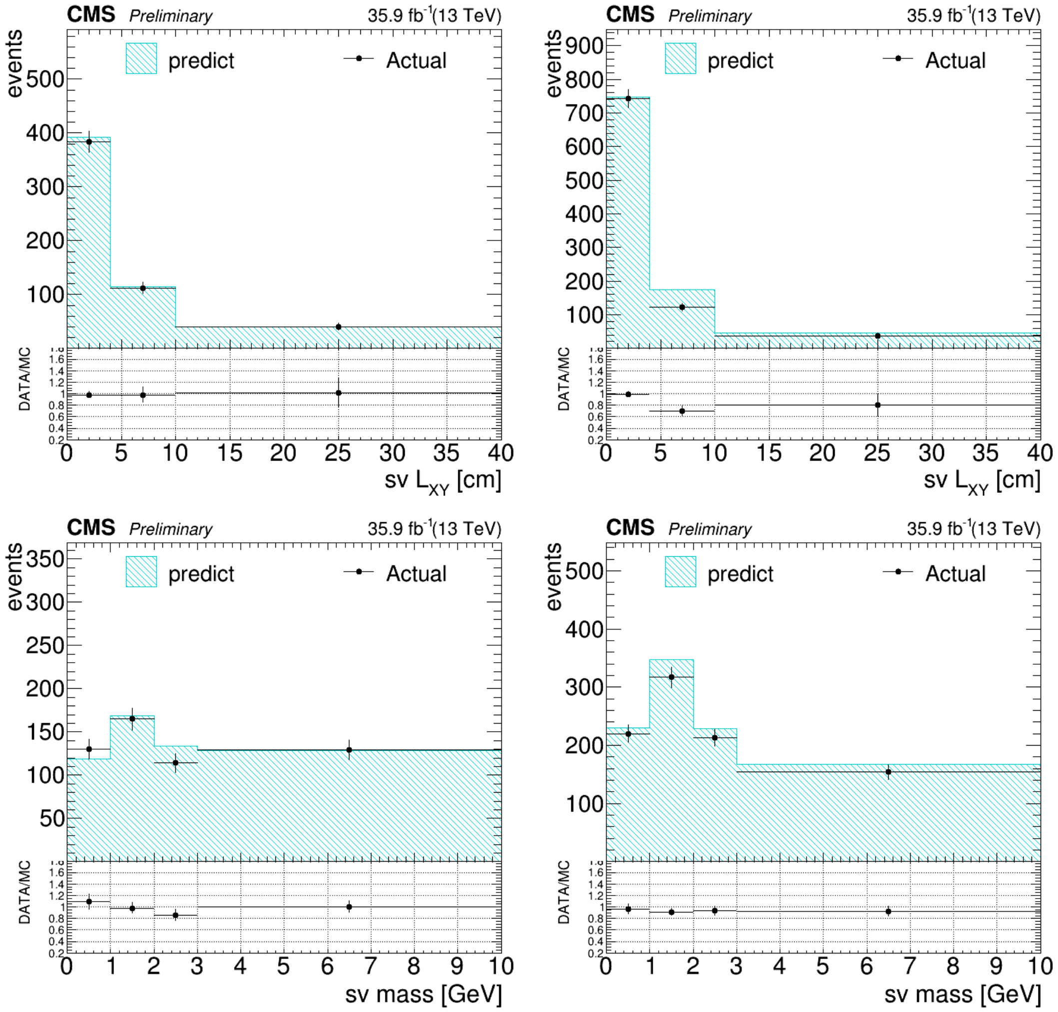

Figure 5.21: Distribution of observed and predicted yields in $t\bar{t}$ simulation for measurement(left) and application(right) regions as a function of the secondary vertex displacement (top) and mass (bottom), for $e\mu$ channel in 2016.

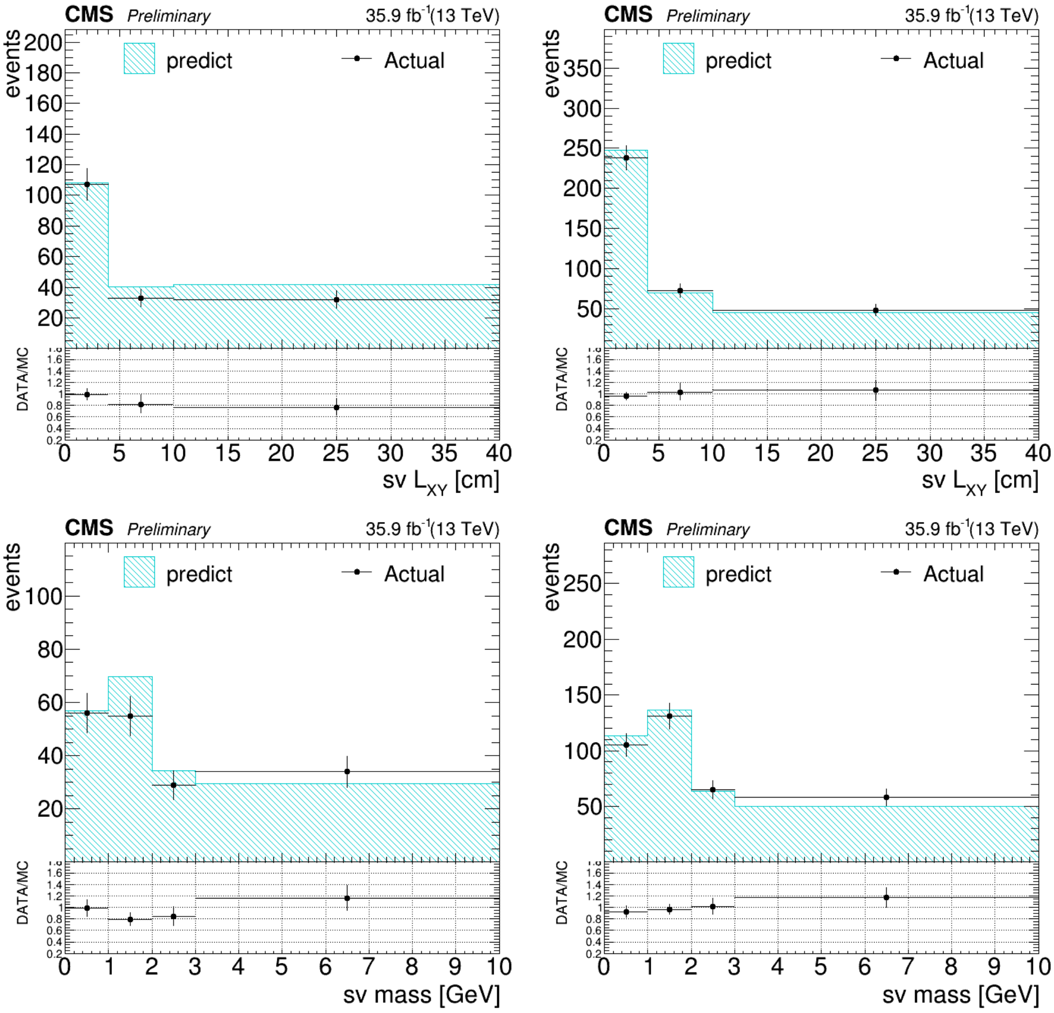

Figure 5.22: Distribution of observed and predicted yields in $t\bar{t}$ simulation for measurement(left) and application(right) regions as a function of the secondary vertex displacement (top) and mass (bottom), for μe channel in 2016.

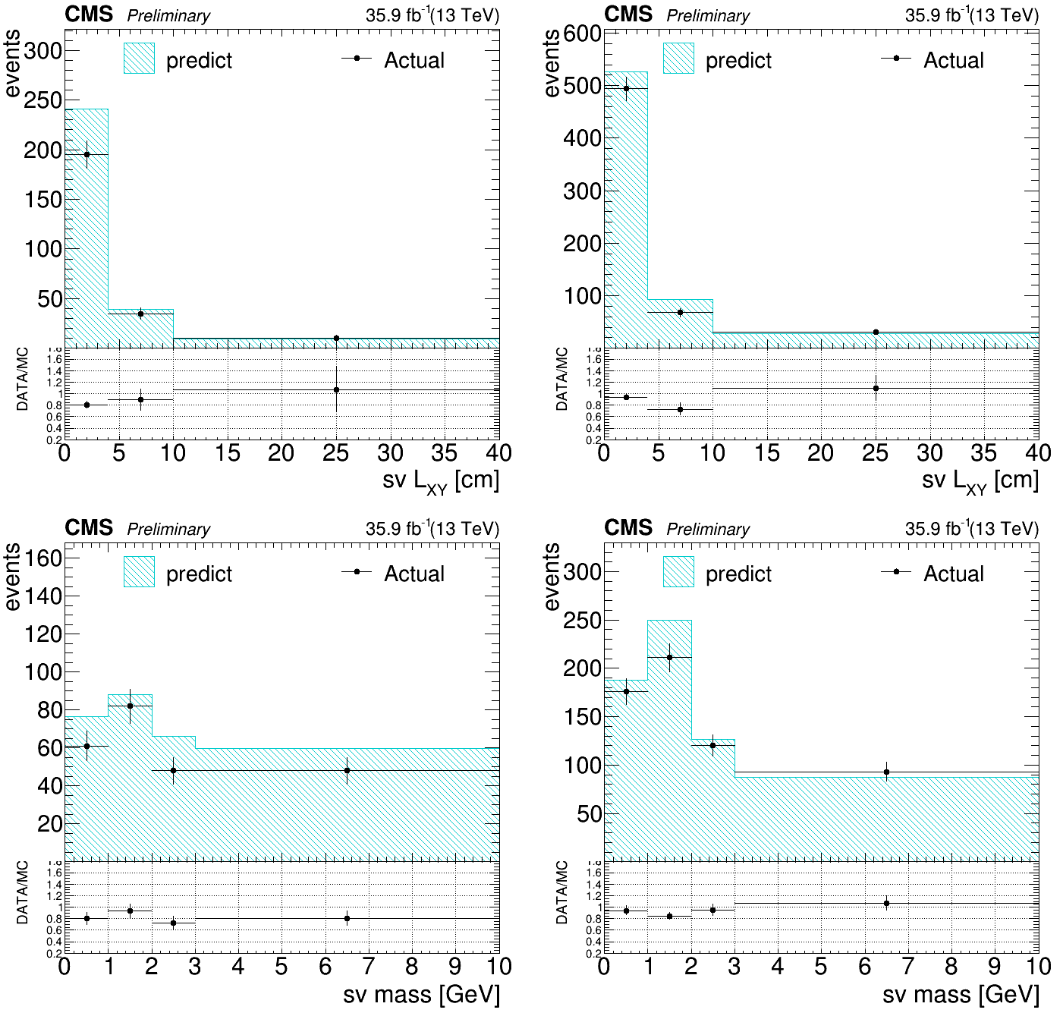

Figure 5.23: Distribution of observed and predicted yields in $t\bar{t}$ simulation for measurement(left) and application(right) regions as a function of the secondary vertex displacement (top) and mass (bottom), for ee channel in 2016.

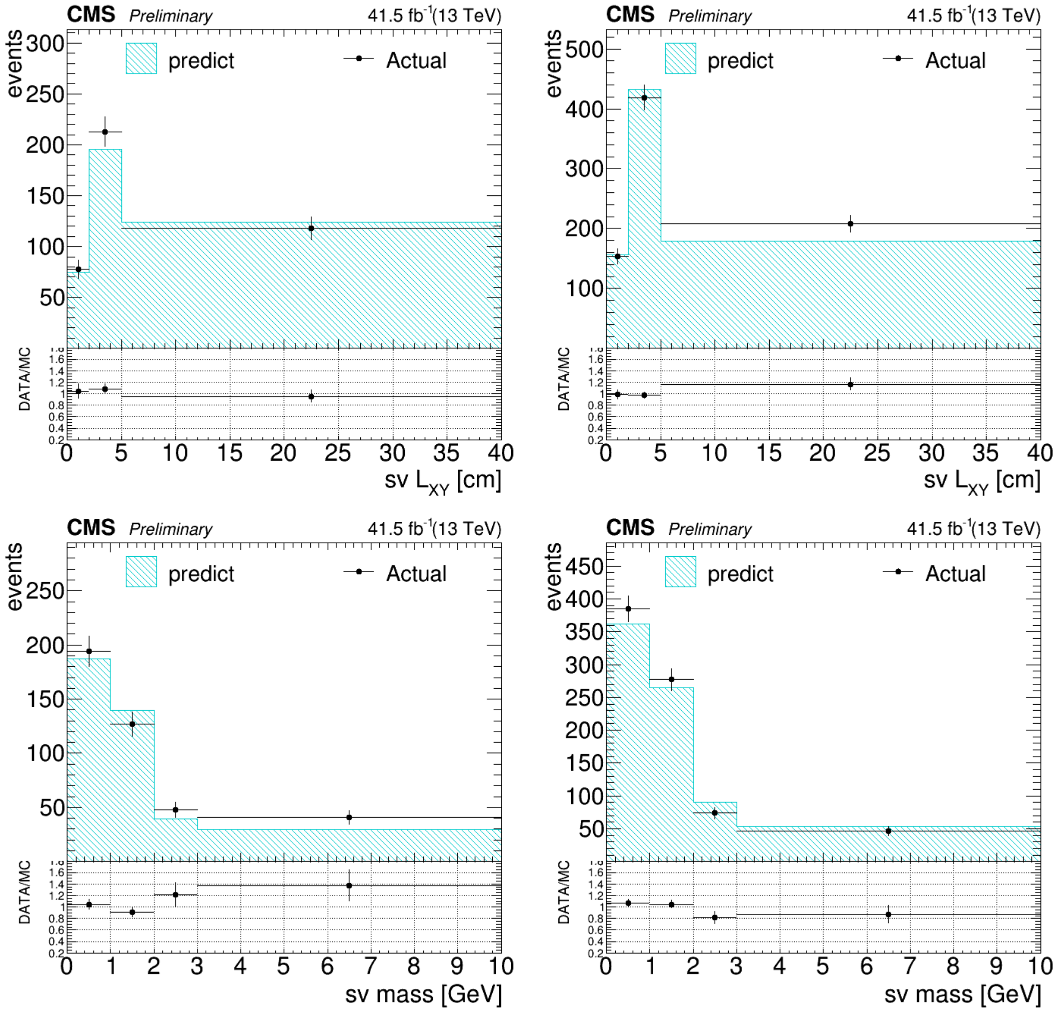

Figure 5.24: Distribution of observed and predicted yields in $t\bar{t}$ simulation for measurement(left) and application(right) regions as a function of the secondary vertex displacement (top) and mass (bottom), for $\mu\mu$ channel in 2017.

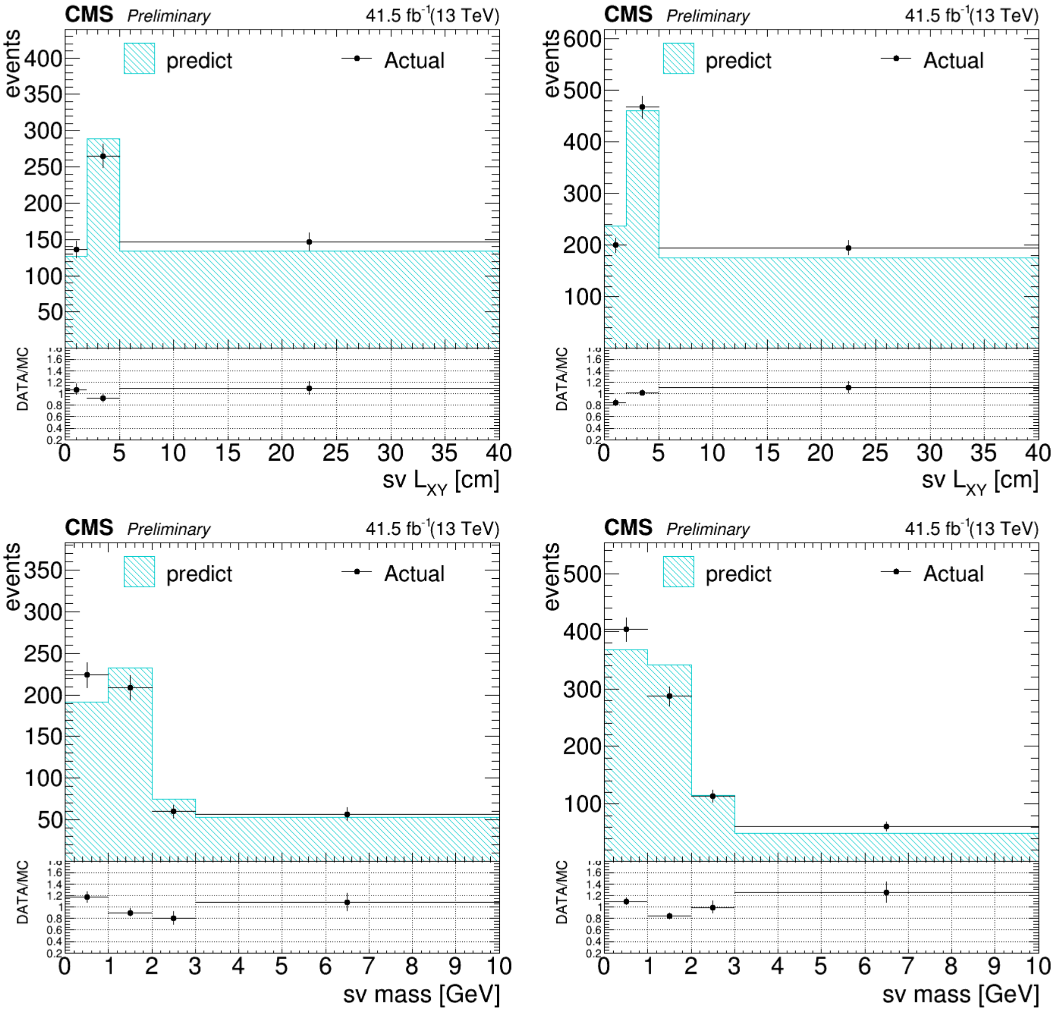

Figure 5.25: Distribution of observed and predicted yields in $t\bar{t}$ simulation for measurement(left) and application(right) regions as a function of the secondary vertex displacement (top) and mass (bottom), for $e\mu$ channel in 2017.

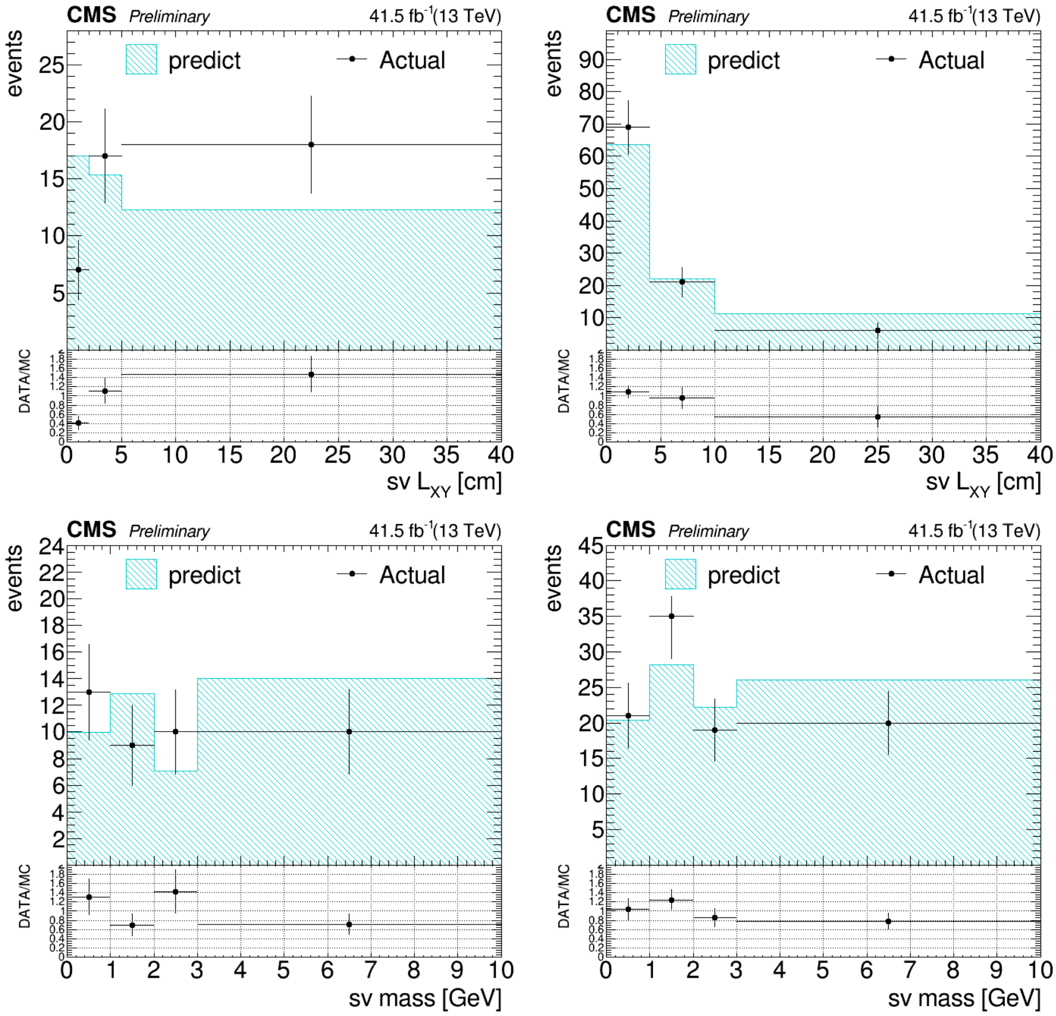

Figure 5.26: Distribution of observed and predicted yields in $t\bar{t}$ simulation for measurement(left) and application(right) regions as a function of the secondary vertex displacement (top) and mass (bottom), for μe channel in 2017.

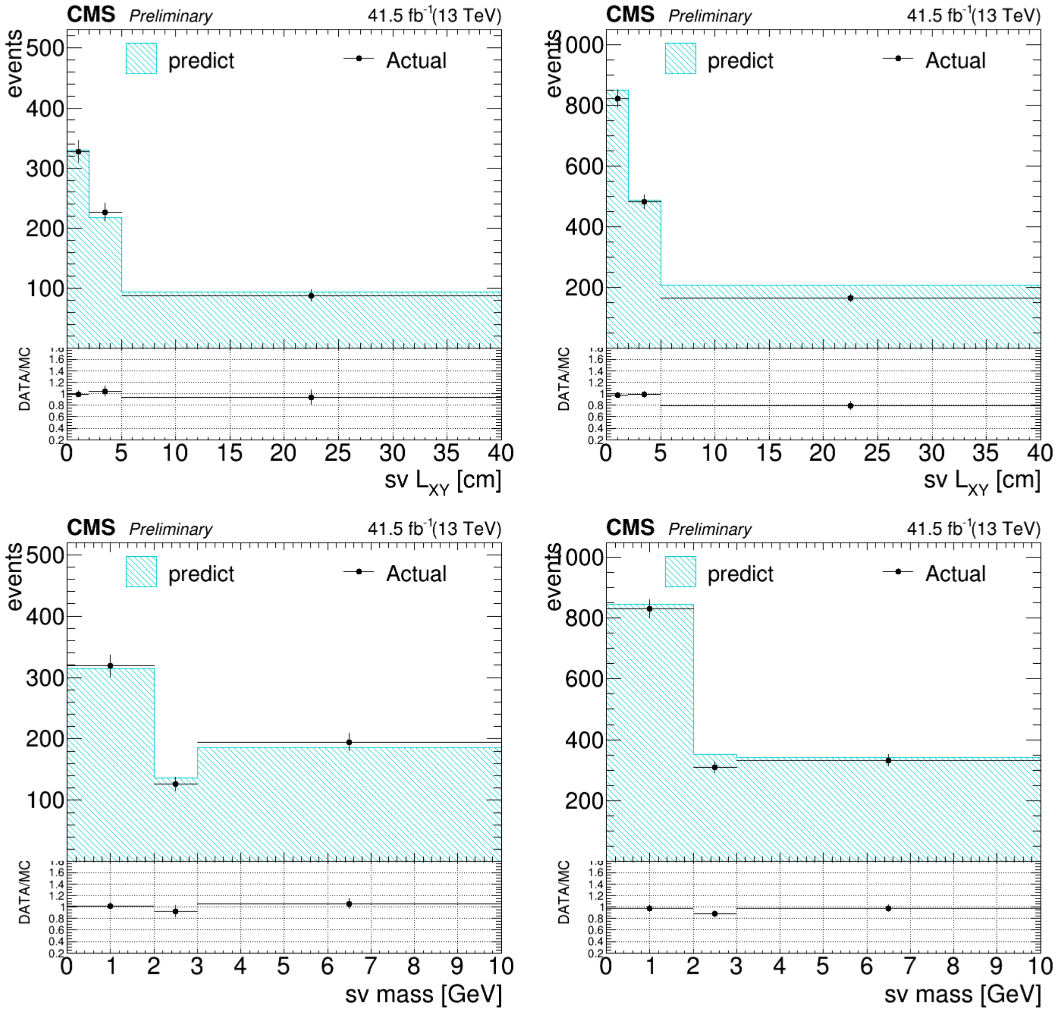

Figure 5.27: Distribution of observed and predicted yields in $t\bar{t}$ simulation for measurement(left) and application(right) regions as a function of the secondary vertex displacement (top) and mass (bottom), for ee channel in 2017.

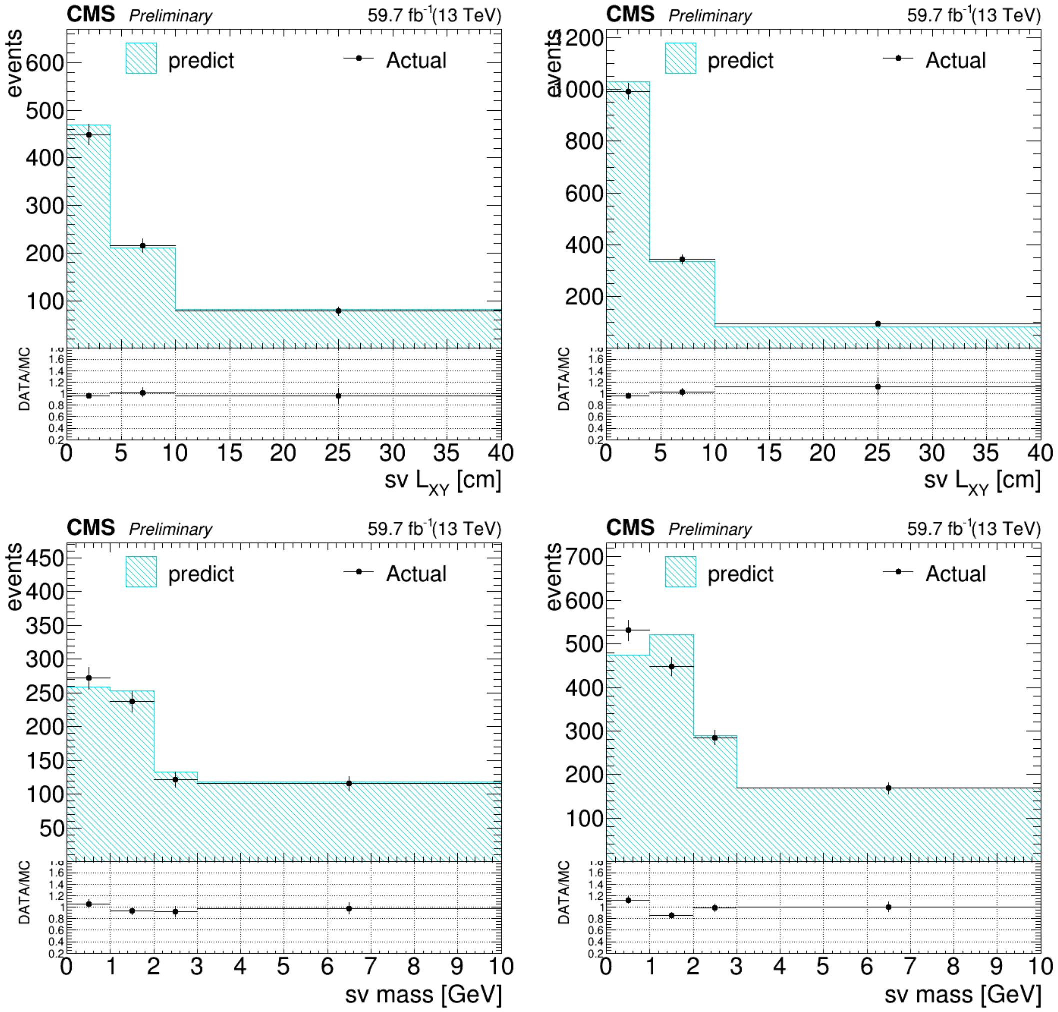

Figure 5.28: Distribution of observed and predicted yields in $t\bar{t}$ simulation for measurement(left) and application(right) regions as a function of the secondary vertex displacement (top) and mass (bottom), for $\mu\mu$ channel in 2018.

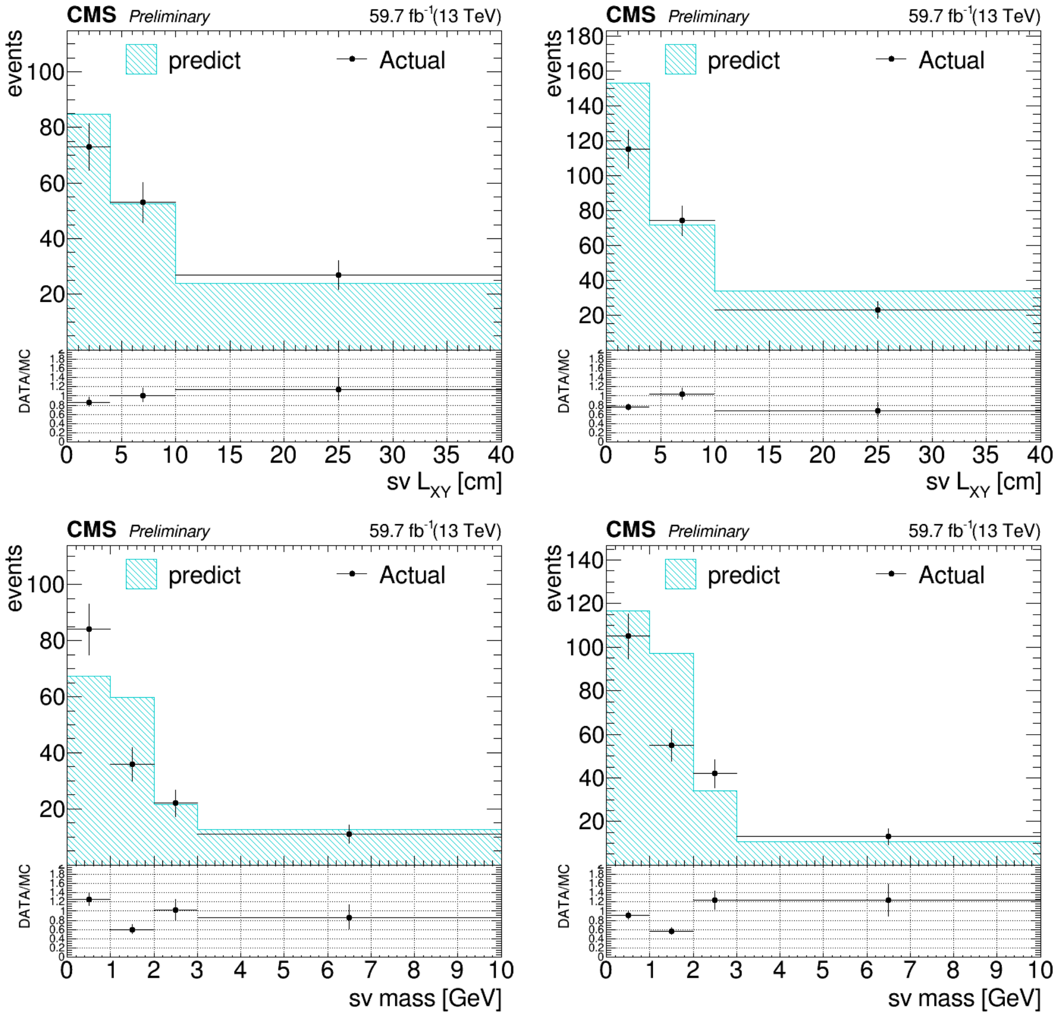

Figure 5.29: Distribution of observed and predicted yields in $t\bar{t}$ simulation for measurement(left) and application(right) regions as a function of the secondary vertex displacement (top) and mass (bottom), for eμ channel in 2018.

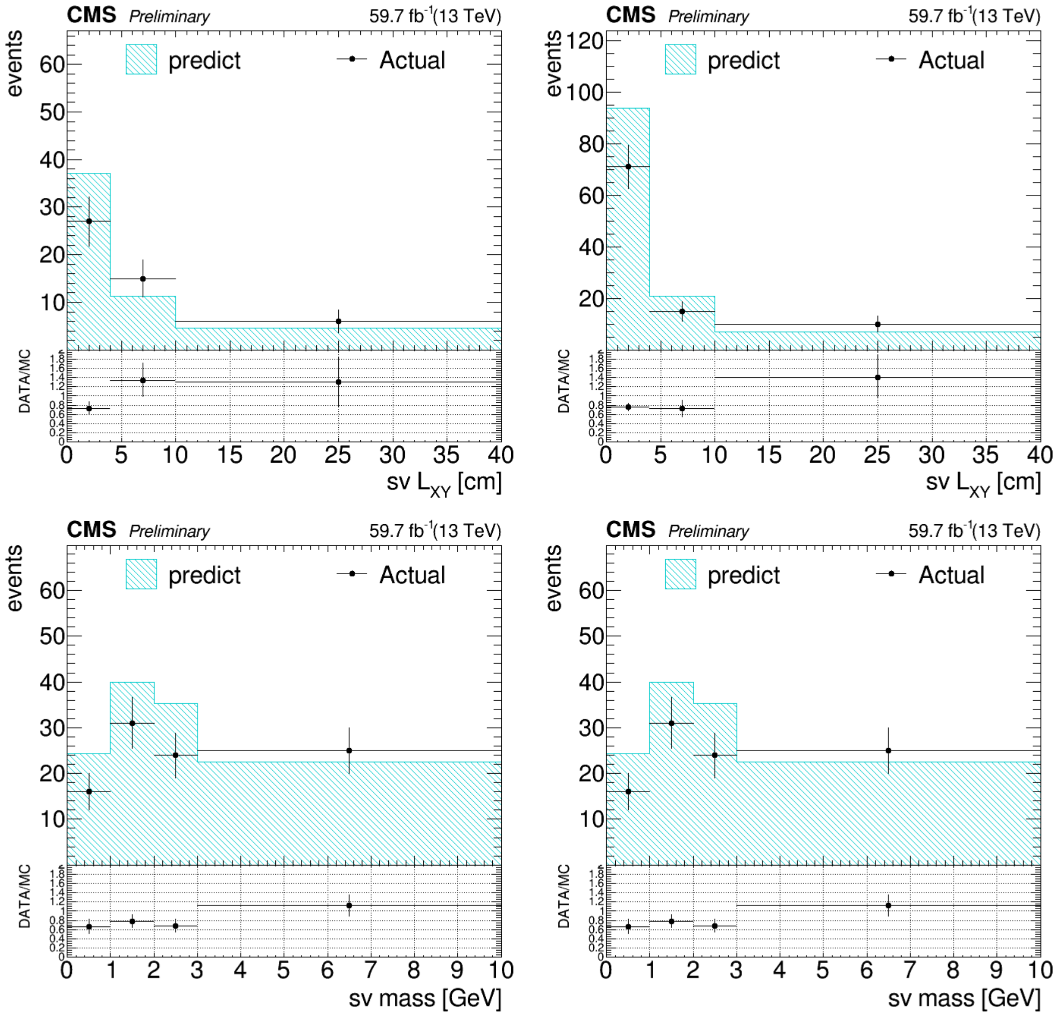

Figure 5.30: Distribution of observed and predicted yields in $t\bar{t}$ simulation for measurement(left) and application(right) regions as a function of the secondary vertex displacement (top) and mass (bottom), for μe channel in 2018.

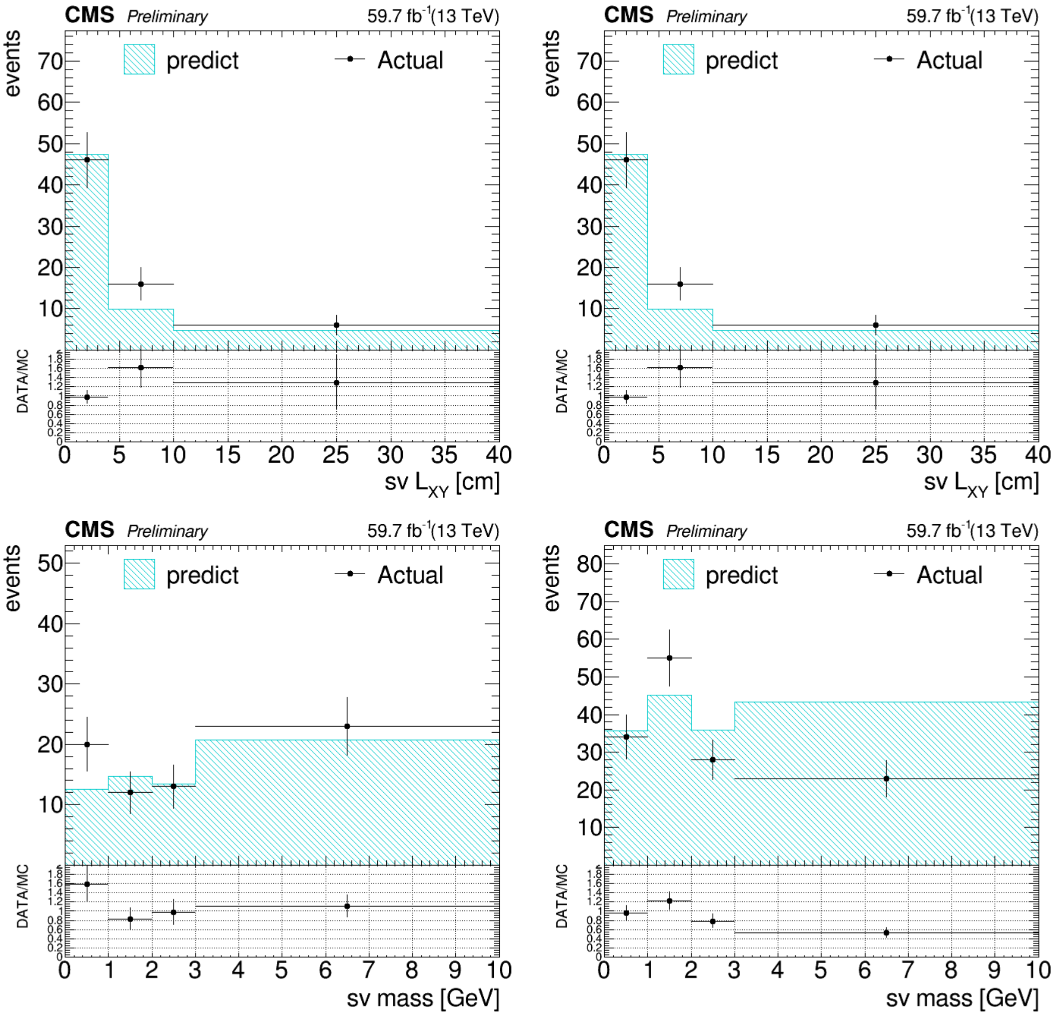

Figure 5.31: Distribution of observed and predicted yields in $t\bar{t}$ simulation for measurement(left) and application(right) regions as a function of the secondary vertex displacement (top) and mass (bottom), for ee channel in 2018 .

Chapter 6

Systematic Uncertainties

In this chapter, we discussed the several sources of systematic uncertainties that affect both the normalization of the components relevant for the analysis and the shapes of the invariant mass distribution of the reconstructed secondary vertex. The systematic uncertainties are assessed using either the simulated signal samples or the data-driven method for estimating the expected background. The next sections give details on individual contributions to the total systematic uncertainty of the analysis.

6.1 Integrated luminosity

The uncertainty in the integrated luminosity is shown in Table 6.1 for full run2 pp collisions at 13 TeV. The correlation scheme applied follows the recommendation provided by LUMI POG [120].

6.2 Pileup Uncertainties

The effect of the pileup uncertainty on the simulated samples is evaluated by reweighting the Monte Carlo datasets by the data pileup distribution [121]. The minimum bias cross section of 69 mb has an uncertainty of 5%. This uncertainty is used to shift the pileup contributions up and down. This leads to a change in

Year	Delivered Luminosity (1/fb)	Uncertainty (%)
2016	35.92	2.5
2017	41.53	2.3
2018	59.74	2.5
total	137.19	1.8

Table 6.1: The approved luminosity and uncertainty for run2 pp runs at 13 TeV during stable beam.

2016	
Data	`/SingleMuon/Run2016B-C-D-E-F-G-H-17Jul2018-v1/MINIAOD`
MC	`/DYJetsToLL_M-50_TuneCUETP8M1_13TeV-madgraphMLM-pythia8`
2017	
Data	`/SingleMuon/Run2017B-C-D-E-F-31Mar2018-v1/MINIAOD`
MC	`/DYJetsToLL_M-50_TuneCP5_13TeV-madgraphMLM-pythia8`
2018	
Data	`/SingleMuon/Run2018A-B-C-D-17Sep2018-v2/MINIAOD`
MC	`/DYJetsToLL_M-50_TuneCP5_13TeV-madgraphMLM-pythia8`
MC campaigns	
2016	`/RunIISummer16MiniAODv3-PUMoriond17_94X_mcRun2_asymptotic_v3_ext1-v2/MINIAODSIM`
2017	`/RunIIFall17MiniAODv2-PU2017RECOSIMstep_12Apr2018_94X_mc2017_realistic_v14-v1/MINIAODSIM`
2018	`/RunIIAutumn18MiniAOD-102X_upgrade2018_realistic_v15-v1/MINIAODSIM`

Table 6.2: Data and MC samples used to compute the SF on the prompt and displaced ID for muons.

the distribution of the invariant mass of the secondary vertex. This systematic uncertainty is only applied to signal samples.

6.3 Lepton ID's and Trigger Selection

Muon and electron efficiencies and scale factors (SF = Data/MC) are measured with the tag and probe (T&P) method [82] performed on $Z \to \mu\mu$ events. The MC and data samples used for the different years are listed in Table 6.2. Tag selection criteria and p_T and η, used for parameterazing efficiencies and SF, have been taken following the Muon POG recommendation [103]. The studied IDs for muons are defined in Table 6.3. The data and MC efficiency for the prompt and the displaced IDs are shown in Figures 6.1 and 6.2. The SF for the prompt and the displaced ID are shown in Figures 6.3 and 6.4.

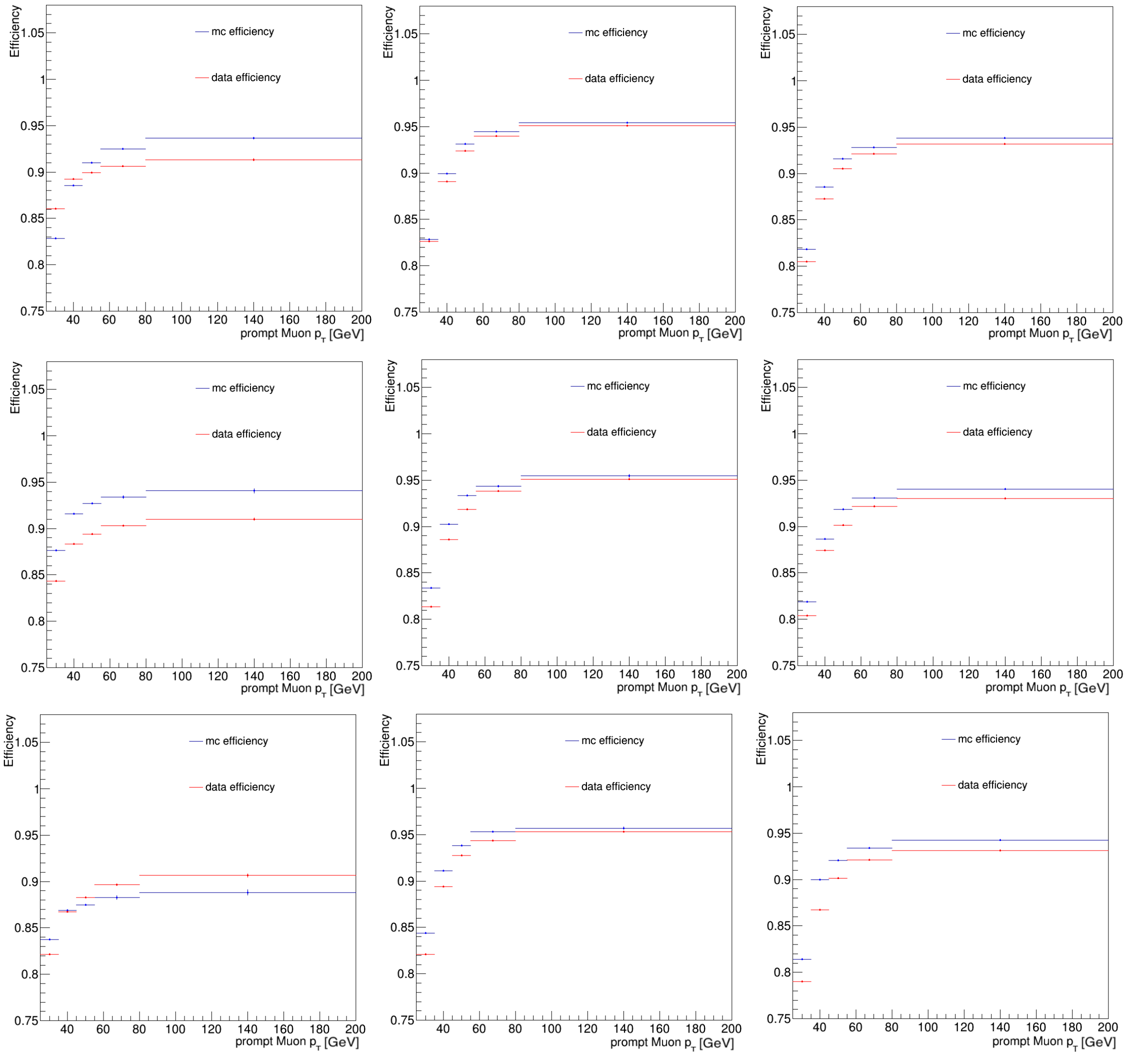

Figure 6.1: Data and MC efficiency of the muons prompt ID for the three different years (top 2016, center 2017 and bottom 2018) for three different η regions: $|\eta| < 2.4$ left, $1.6 < |\eta| < 2.4$ center and $|\eta| < 0.9$ right.

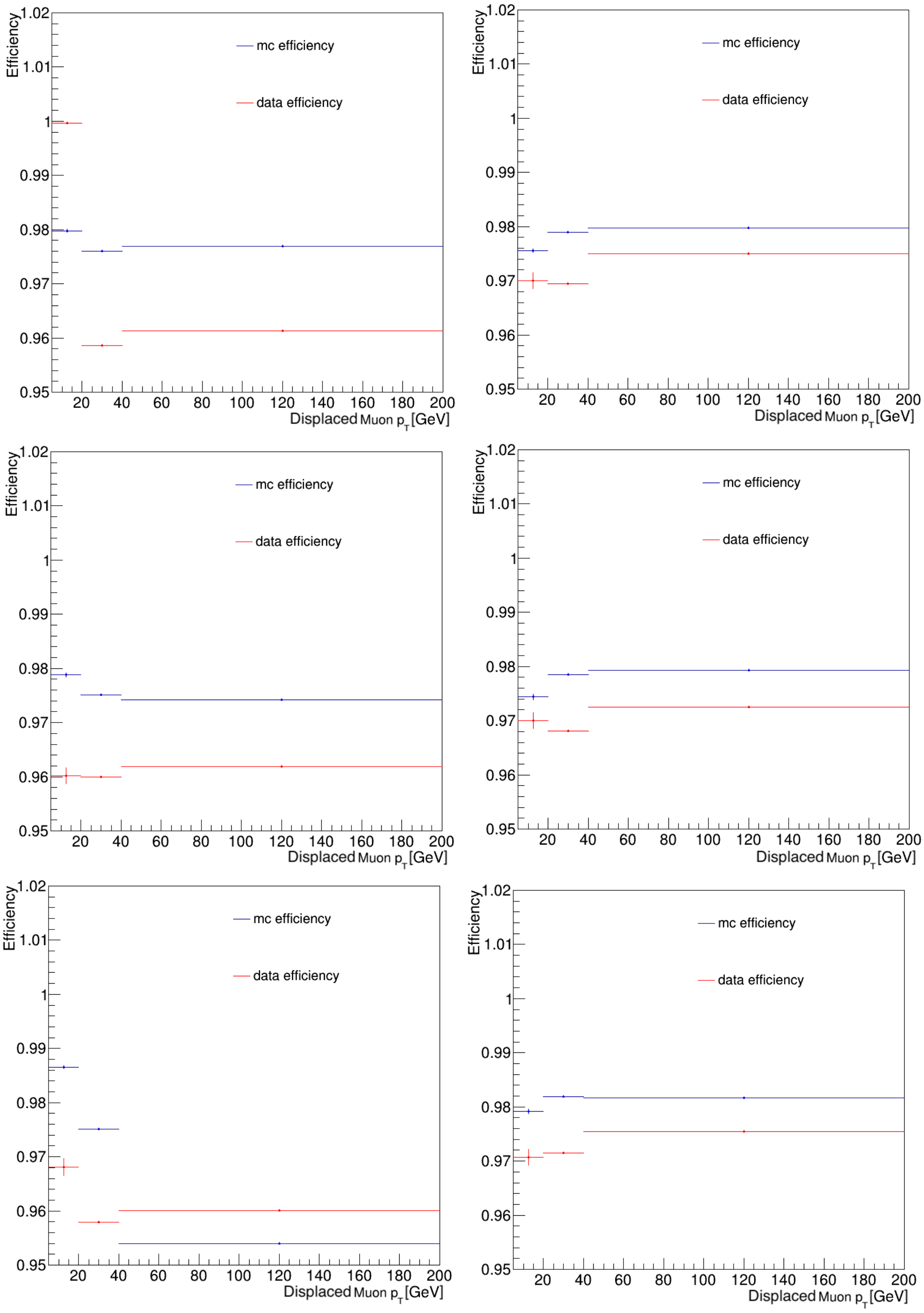

Figure 6.2: Data and MC efficiency of the muons displaced ID for the three different years (top 2016, center 2017 and bottom 2018) for two different η regions: $0.9 < |\eta| < 2.4$ left and $|\eta| < 0.9$ right.

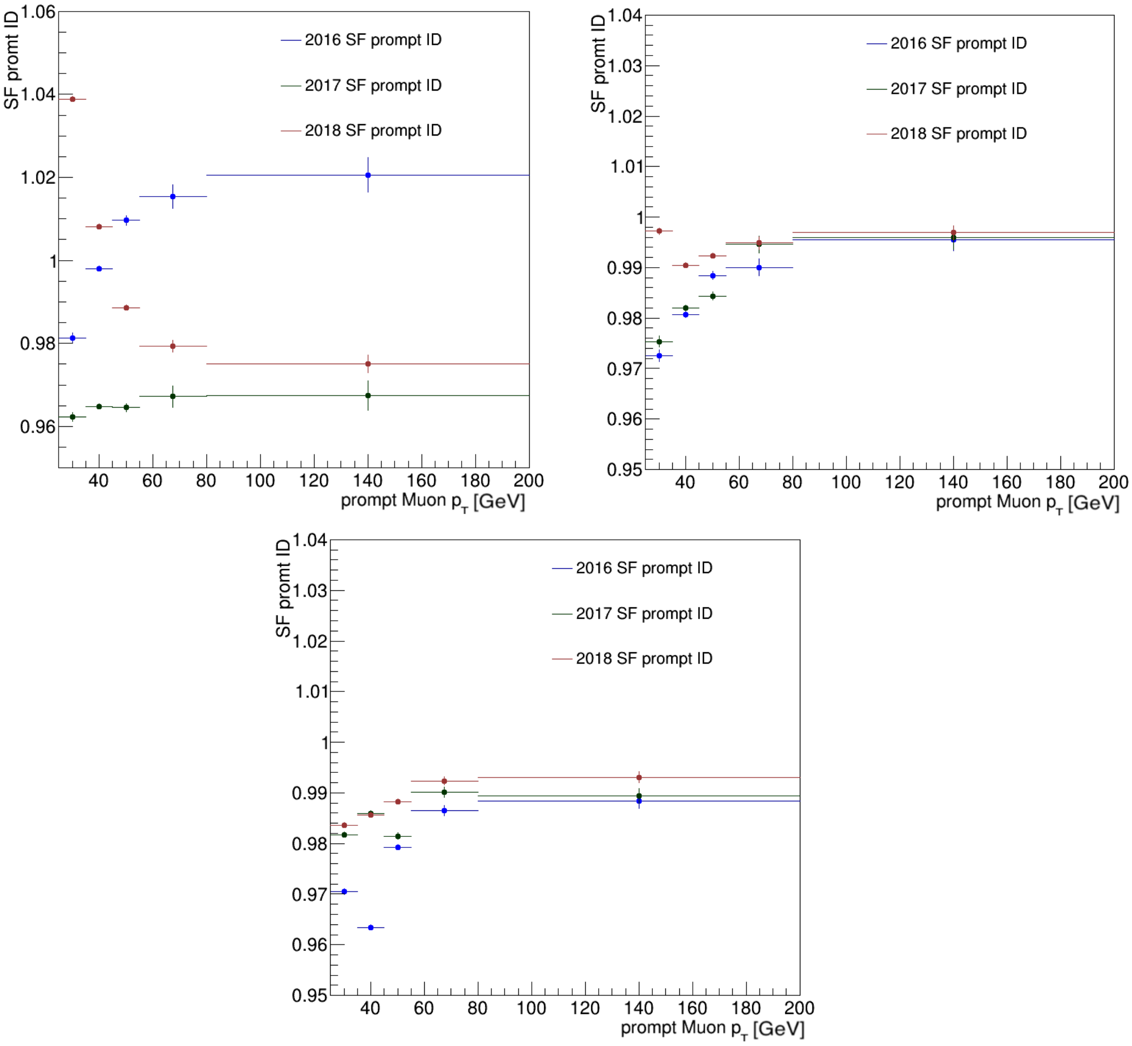

Figure 6.3: SF of the muons prompt ID for the three different years, calculated in three different η regions: $|\eta| < 2.4$ left, $1.6 < |\eta| < 2.4$ right and $|\eta| < 0.9$ bottom.

Prompt ID	Displaced ID
Tight ID from Muon POG	Tuned Medium ID
$p_T > 25$ GeV	$p_T > 5$ GeV
$\|\eta\| < 2.4$	$\|\eta\| < 2.4$
$d_{xy} < 0.005$ cm	$d_{xy} > 0.02$ cm
$d_z < 0.1$ cm	
iso < 0.1	

Table 6.3: Requirements of muon selections for both prompt and displaced muon .

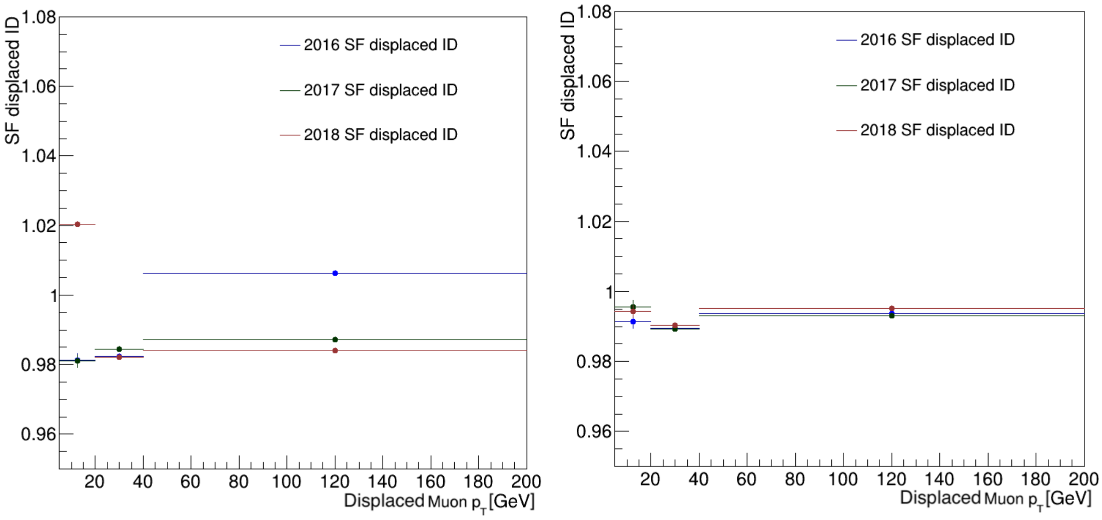

Figure 6.4: SF of the muons displaced ID for the three different years, calculated in two different η regions: $0.9 < |\eta| < 2.4$ left and $|\eta| < 0.9$ right.

The electron SF for the prompt ID is taken from the EGamma POG [106]; for the displaced ID, it is computed using the (T&P) method. The MC and data samples used for the different years are listed in Table 6.4. Tag selection criteria and p_T and η bin widths, used for parameterazing efficiencies and SF, have been adopted following the electron POG recommendation [106]. The data and MC efficiency for the electron displaced IDs are shown in Figure 6.5. The SF for the electrons' displacement ID is shown in Figure 6.6. For the electrons, the SF is close to 1, so corrections are neglected.

The systematics uncertainties on the leptons are computed using the T&P procedure but changing the fitting procedures (overall number of bins, bins range, function to simulate the signal and the background). The overall uncertainties are written in

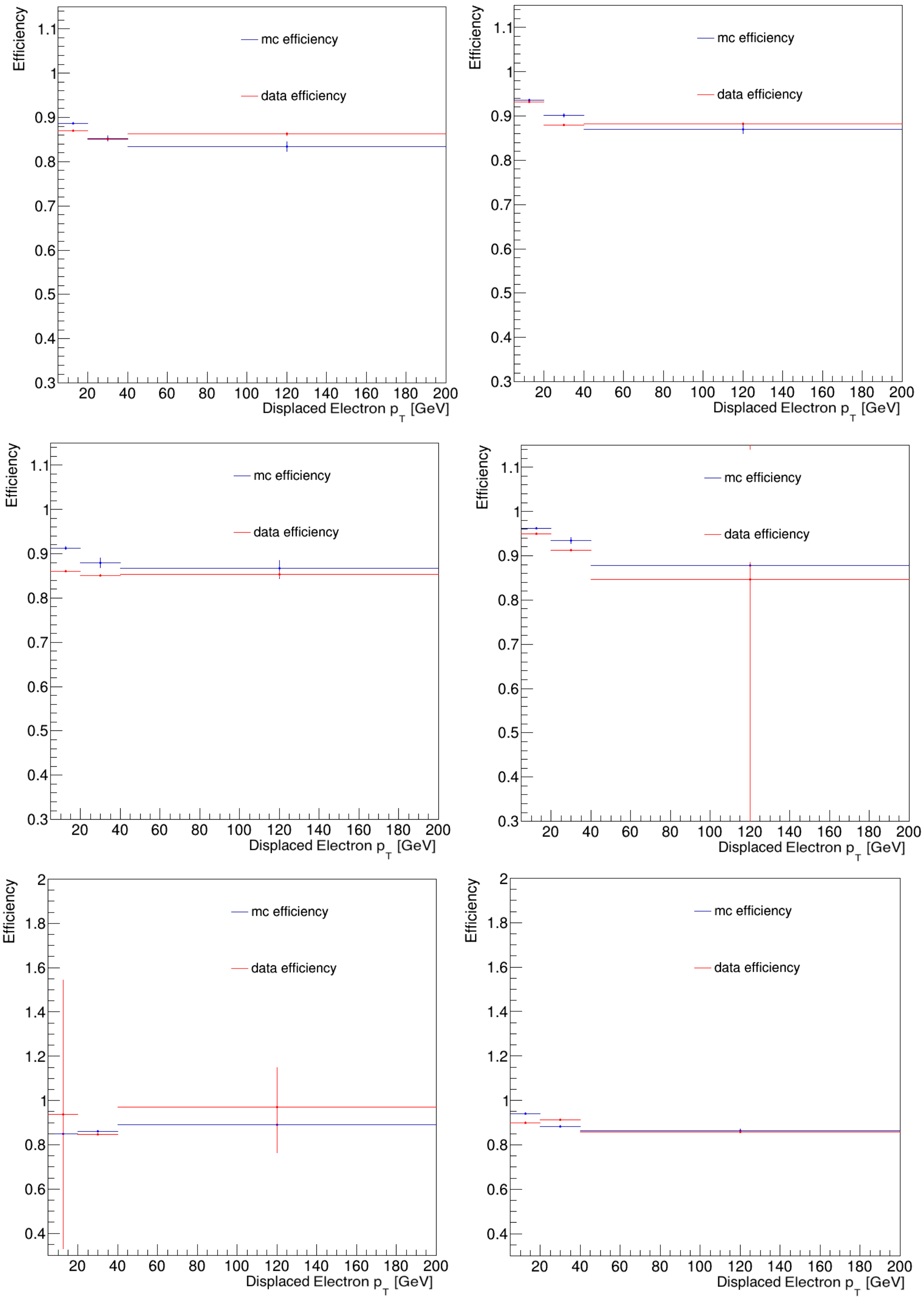

Figure 6.5: Data and MC efficiency of the electrons displaced ID for the three different years (top 2016, center 2017 and bottom 2018) for two different η regions: $0.9 < |\eta| < 2.4$ left and $|\eta| < 0.9$ right.

2016	
Data	`/SingleElectron/Run2016B-C-D-E-F-G-H-17Jul2018-v1/MINIAOD`
MC	`/DYJetsToLL_M-50_TuneCUETP8M1_13TeV-madgraphMLM-pythia8`
2017	
Data	`/SingleElectron/Run2017B-C-D-E-F-31Mar2018-v1/MINIAOD`
MC	`/DYJetsToLL_M-50_TuneCP5_13TeV-madgraphMLM-pythia8`
2018	
Data	`/EGamma/Run2018A-B-C-D-17Sep2018-v2/MINIAOD`
MC	`/DYJetsToLL_M-50_TuneCP5_13TeV-madgraphMLM-pythia8`
MC campaigns	
2016	`/RunIISummer16MiniAODv3-PUMoriond17_94X_mcRun2_asymptotic_v3_ext1-v2/MINIAODSIM`
2017	`/RunIIFall17MiniAODv2-PU2017RECOSIMstep_12Apr2018_94X_mc2017_realistic_v14-v1/MINIAODSIM`
2018	`/RunIIAutumn18MiniAOD-102X_upgrade2018_realistic_v15-v1/MINIAODSIM`

Table 6.4: Data and MC samples used to compute the SF on the prompt and displaced ID for electrons.

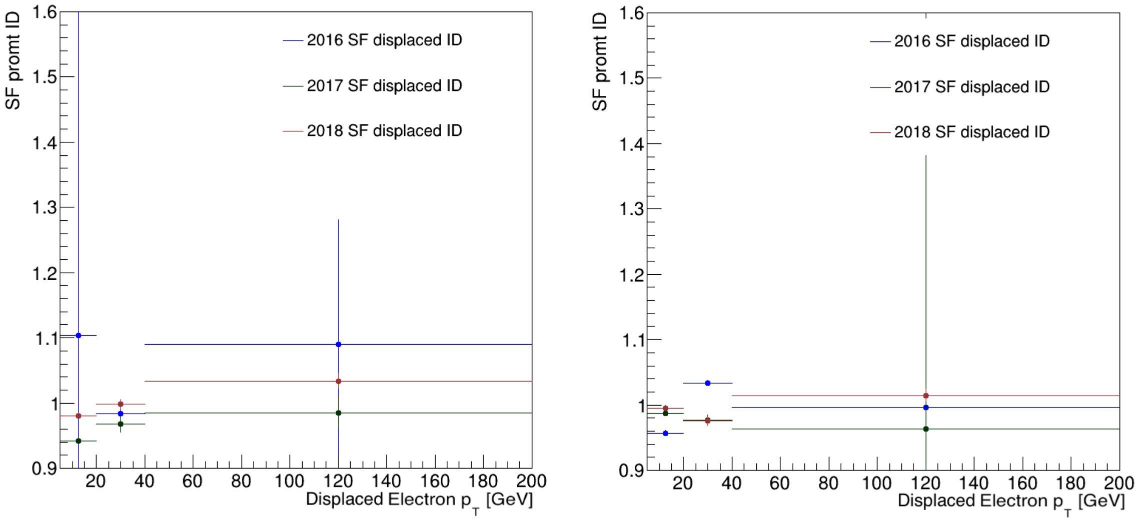

Figure 6.6: SF of the electrons displaced ID for the three different years, calculated in two different η regions: $0.9 < |\eta| < 2.4$ left and $|\eta| < 0.9$ right.

Year	Prompt ID Muons	Displaced ID Muons	Prompt ID Electrons	Displaced ID Electrons
2016	1%	1%	1%	2%
2017	1%	1%	1%	2%
2018	1%	1%	1%	2%

Table 6.5: Systematic uncertainties on the leptons IDs for the three different years.

Table 6.5.

6.4 Jet Energy Scale and Resolution

The effect of the jet energy scale uncertainty is evaluated on the simulated samples. This is done by increasing or decreasing the jet four-momentum by the uncertainty in the jet energy scale [122], which is about 5%. The p_T and η dependent corrections for jet energies and the uncertainties related to the pruning algorithm response applied to jets were included in the data and simulations. This results in a shape difference for the distribution of the secondary vertex invariant mass. The difference is found to be small, and this systematic uncertainty is applied to the signal samples.

The variation of the jet energy resolution is treated in a similar way to that of the jet energy scale. In order to have a resolution in the simulation similar to that in data, the momentum of the jets is smeared by $\pm 1\sigma$. These are the data/MC scale factors, which are shifted by $\pm\sigma$. Uncertainties from the jet energy resolution are assessed by varying the simulation-to-data scale factors within their uncertainties when correcting the resolution of the jets in simulation. A single source of uncertainty is considered, including both the statistical and systematic uncertainties of the measured resolution scale factors [123]. The effects of the jet energy resolution uncertainties are also applied to the signal samples, which results in a variation of the shape of the invariant mass distribution of the secondary vertex.

6.5 Uncertainty on signal MC cross section

The version of the heavy neutrino model used for the generation of Monte Carlo HNL events in this analysis [49, 124] did not allow for NLO QCD calculations. The simulation of HNL events was performed at LO, resulting in large theoretical uncertainties on the cross section (up to 15%) resulting from missing higher order QCD corrections and PDF uncertainties.

Instead of relying on these LO uncertainties, a general correction factor for the cross section from LO to NNLO was applied based on the SM production of W$\rightarrow l\bar{\nu}$. In HNL production, the only difference between this SM process and the HNL is the exchange of the SM neutrino by an HNL. The effect of the mass and coupling of the HNL can be factored in the calculation of the HNL cross section and is not affected by the PDF and scale variations. Because the dominant effect of these uncertainties appears during the production of the W boson, it can be studied in the SM process W $\rightarrow l\bar{\nu}$, for which recommended values for the cross section at NNLO exist along with the corresponding theory uncertainties. Our approach is to get an LO cross section for W $\rightarrow l\bar{\nu}$ calculated with MADGRAPH5 aMC@NLO v2.4.2 [91] using the same exact conditions as the HNL MC production. A correction factor from LO to NNLO can be derived based on this and can then be applied to HNL MC. The PDF and scale uncertainties at NNLO are applied as flat systematic uncertainties to cover the remaining uncertainty in the MC cross section.

It has been checked and verified that the generator conditions are similar between our MC production and the centrally produced W+jets samples, from which the recommended NNLO cross section was taken. The small differences that are present have no significant effect on the cross section calculation. Furthermore, because of lepton universality, we will be able to apply the scale factor and uncertainty to all HNL samples, regardless of which lepton flavour(s) they couple to.

The resulting LO cross section is 56500 pb for W $\rightarrow l\bar{\nu}$ (l = e , μ , τ). The recommended NNLO value is$61526.7^{+497.1}_{-264.6} \pm 2312.7$ pb, where the quoted uncertainties are scale and PDF uncertainties. Assuming uncorrelated uncertainties and taking the maximum of the two asymmetric errors, the combined uncertainty is 61526.7±2365.5 pb, an effect of 3.86%. This results in a scale factor of 1.089 ± 0.042.

6.6 Uncertainties on the Data-driven Background Estimations

In this section, the systematic uncertainties related to the non-prompt background and their effects on the fake rates are discussed. These systematic uncertainties are estimated in inclusive signal regions. The strategy adopted uses two measurement regions (control regions CR) and one application region (signal region SR). The three regions are defined.

- region 1 - measurement region (CR): Mass[l_1,SV] $<$ 40 GeV.
- region 2 - application region (include SR): 40$<$ Mass[l_1,SV] $<$90 GeV.
- region 3 - measurement region (CR): Mass[l_1,SV] $>$90 GeV.

	Tight BDT cut (BDT output $>$ 2)	Loose BDT cut (-4 $<$ BDT output $<$ 2)
Mass[l_1,SV] $<$ 40 GeV (Measurement Region)	region A	region C
40 GeV $<$ Mass[l_1,SV] $<$ 90 GeV (Application Region)	signal region	control region
Mass[l_1,SV] $>$ 90 GeV (Measurement Region)	region B	region D

Table 6.6: The list of the measurement and application regions used in the DNN model.

As described in section 5.3.1, we estimate the fake rate by training regions (A and B) against regions (C and D), and the output will be used to re-weight the control region to predict the background in the signal region (see Table 6.6). To estimate the systematic uncertainties introduced by this method, we train region A against C and B against D separately. The DNN output from both trainings will be used to re-weight the control region, and the output is supposed to be the background prediction in the signal region. The systematic uncertainty assigned to the DNN fake rate estimation is equal to the ratio between the two predictions that were derived from each measurement region separately. Systematics uncertainties are up to 10% to 50% for some very displaced bins (see Figure 6.7).

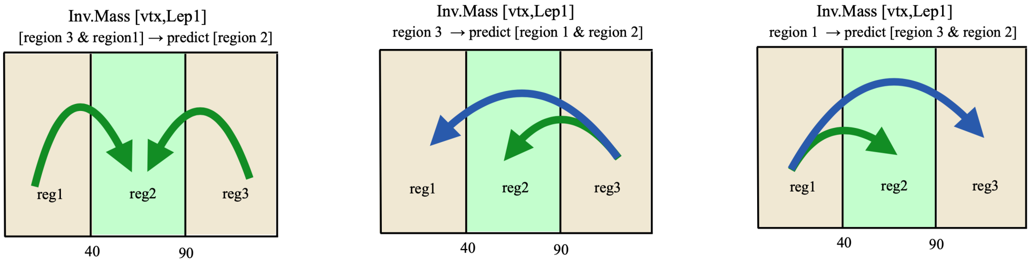

Figure 6.7: Sketch showing the application and measurement regions chosen to determine the fake rate, and what is used for the main measurements (left) and for cross checks and estimation of systematic uncertainties (center, right).

In order to validate this method, the predicted number of background events in region 3, obtained by training the DNN in region 1, together with the target distribution, is shown in Figure 6.8 as function of the secondary vertex mass. The results of the same exercise, inverting region 1 and region 3, is shown in Figures 6.9 - 6.11. The three different DNNs obtained, one trained in region 1, one in region 3, and one in (region 1 and region 3, are the used to predict the background in the SR.

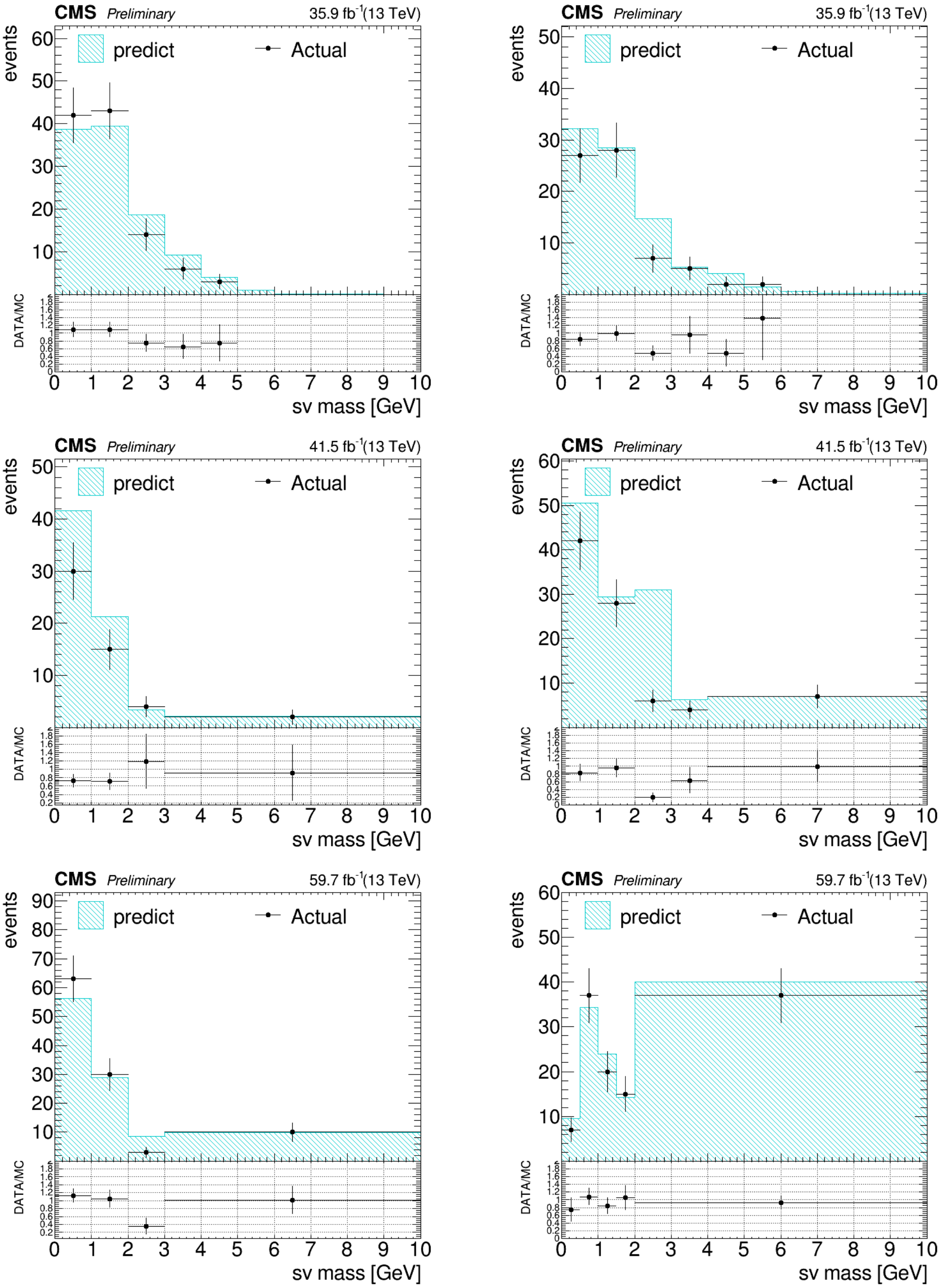

Figure 6.8: Distribution of estimated background events in region 3 as a function of the secondary vertex mass, compared to the real distribution, for $\mu\mu$ (left) and ee (right) in 2016 (top), 2017 (medium) and 2018 (bottom).

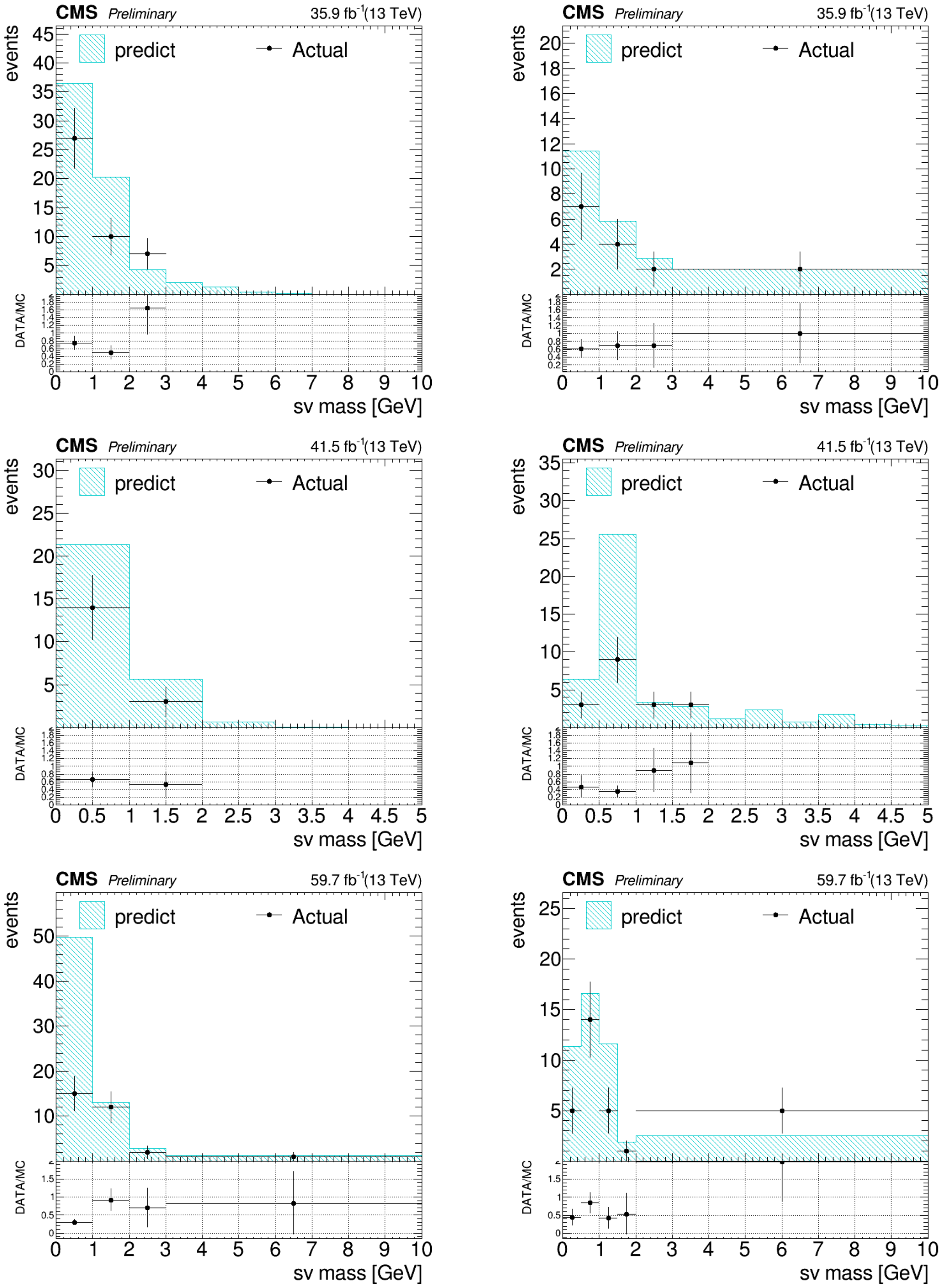

Figure 6.9: Distribution of estimated background events in region 1 as a function of the secondary vertex mass, compared to the real distribution, for $\mu\mu$ (left) and ee (right) in 2016 (top), 2017 (medium) and 2018 (bottom).

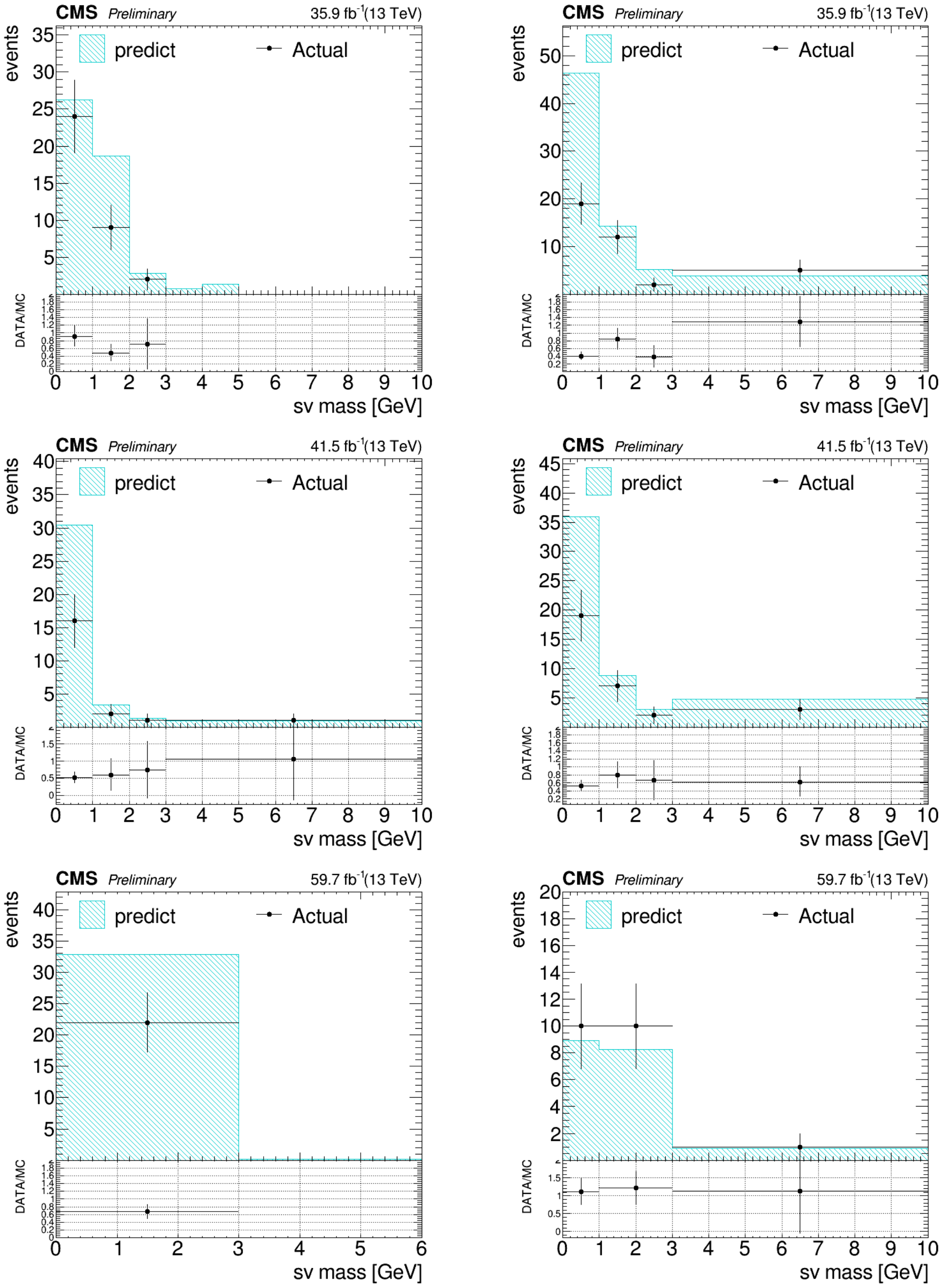

Figure 6.10: Distribution of estimated background events in region 1 as a function of the secondary vertex mass, compared to the real distribution, for eμ (left) and μe (right) in 2016 (top), 2017 (medium) and 2018 (bottom).

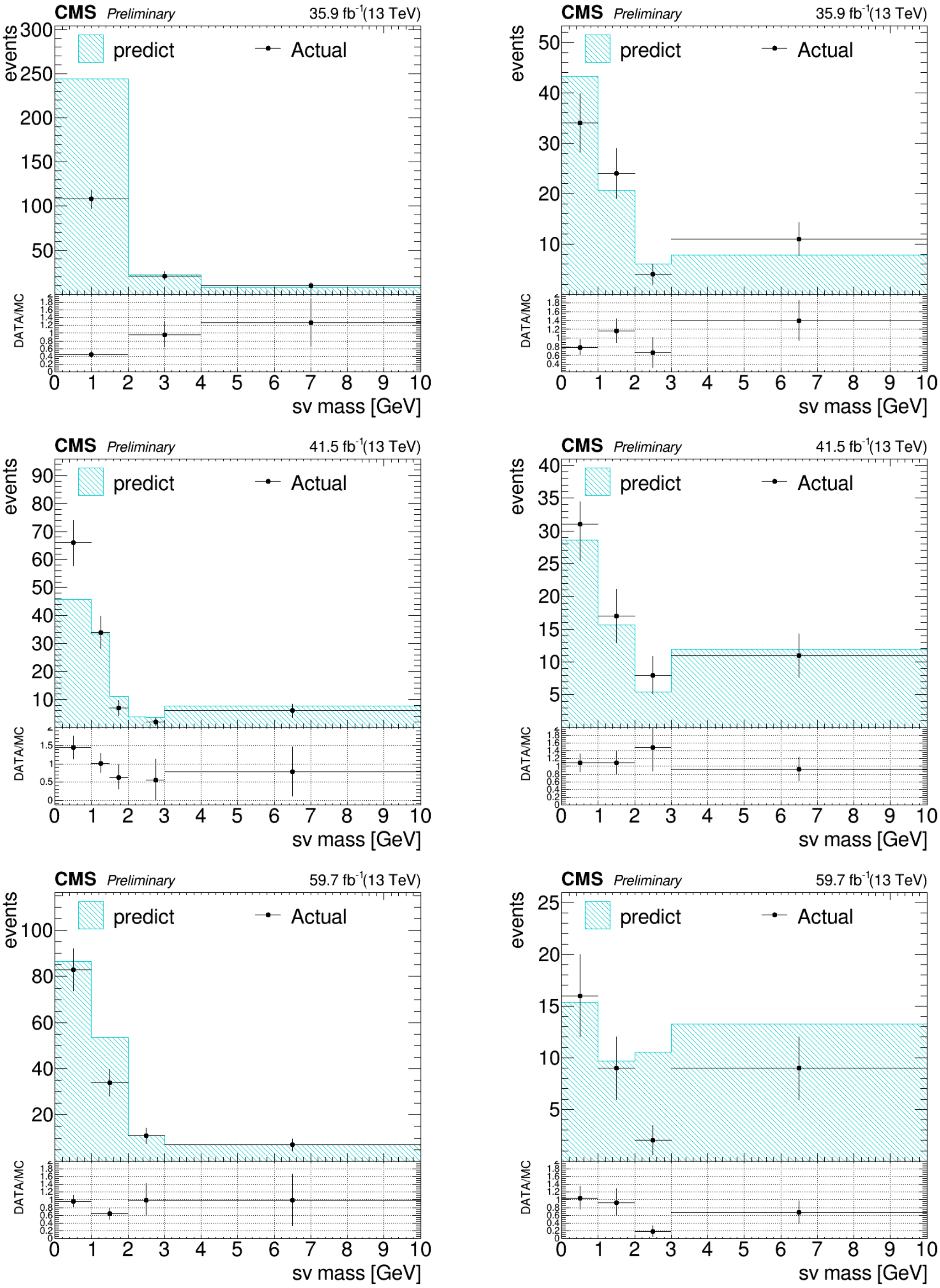

Figure 6.11: Distribution of estimated background events in region 3 as a function of the secondary vertex mass, compared to the real distribution, for eμ (left) and μe (right) in 2016 (top), 2017 (medium) and 2018 (bottom).

6.7 Secondary Vertex

The main contribution to the systematic uncertainties for the simulated signal samples comes from the secondary vertex (SV) reconstruction, detailed in section 4.4. In order to evaluate this uncertainty, a $t\bar{t}$ enriched region has been selected and the efficiency of reconstructing a SV in a b-jet has been evaluated for both data and MC. The procedure for this study can be summarised as follows:

- $t\bar{t}$ enriched region selections
    - Events that pass the pre-selection cuts are taken; two leptons (one muon and one electron) are required, each of them passing the tight ID and having p_T > 30(20) GeV.
    - In order to be dominated by background events and to be sure to be far away from the signal region, we select a loose b-tagged jet with p_T > 20 GeV. A jet is considered to be tight b-tagged if its Deep Flavour discriminator [125] value is greater than 0.7489 (0.7264) in 2017 (2018), and loose if its Deep Flavour discriminator value is more than 0.0521 (0.0494) in 2017 (2018).
    - Finally, a tight jet satisfying the same requirements as that of the signal, with a p_T of 20 > GeV, is required. The data-Monte Carlo agreement of events passing the above-mentioned selection is checked as a function of tight jet p_T and η, and a good agreement is found, as shown in Figure 6.12.
- SV-tracks b-jet matching
    - The same study is repeated, adding to the above-mentioned selection the requirement of matching between the selected tight jet and the tracks forming the secondary vertex to ensure that the displaced vertex is emerged in the tight jet. As shown in Figure 6.13, there is good compatibility between data and Monte Carlo simulation as a function of tight jet p_T, η, secondary vertex mass, and 2D displacement.

We compute the efficiency of having the secondary vertex within the tight jet between the two sets of selections as a function of tight jet $p_T$and η and in three different bins of SV displacement ($0-2$ cm, $2-10$ cm, >10 cm).

Figures 6.14 and 6.15 show efficiency plots for inclusive SV displacement for the SingleMuon and SingleElectron/EGamma datasets. The efficiencies computed for three different bins of SV displacement ($0-2$ cm, $2-10$ cm, >10 cm) can be found in the appendix B.

In order to quantify the impact of this increase in efficiency, we define a scale factor as a ratio between data efficiency and MC efficiency. Figures 6.16 and 6.17 show SFs obtained for SingleMuon and SingleElectron/EGamma datasets with inclusive SV displacement, respectively.

Systematic uncertainty for each displaced vertex has been obtained by assigning the uncertainty associated with the scale factor as a systematic uncertainty. This uncertainty has been applied to Monte Carlo signal samples and it has been found to be the main impact uncertainty, with values up to 1-17 % in very SV displaced bins.

To estimate the systematic uncertainty due to the tracking requirements of the inclusive vertex finder algorithm, we measure the per-vertex efficiencies of the tracking requirements as functions of the number of prompt tracks and displaced tracks, using events $t\bar{t}$ enriched region. The efficiencies obtained in data are found to be consistent with the efficiencies obtained in MC simulations. Therefore, no corresponding systematic uncertainty is assigned.

6.8 Summary of Systematic Uncertainties

The uncertainties described above are treated as the result of analysis to investigate the effect on signal and background yields and on the kinematic shape of the mass distribution of the reconstructed secondary vertex.

Since we have used a data-driven method, the estimation of the background in the analysis is not affected by imperfections in the simulation of the detector response or inaccuracies in the modelling of the reconstruction. As described in Section 6.6, the uncertainty in the shape of the non-prompt background and its effect on the fake rates were modeled.

The systematic uncertainties affecting the signal yield include the uncertainties related to the physics object reconstruction with the calibration shown in sections 6.3, 6.4, and 6.7. The sections 6.1 and 6.2 discussed the other uncertainties associated with luminosity and pile-up. The uncertainty in the signal Monte Carlo cross-section modeling is presented in section 6.5. A summary of the different systematic contributions and their application schemes is shown in Table 6.7.

Source	Value	Affected sample	Type
Fake-rate estimation	10-60%	bkg.	shape
Integrated luminosity	2016, 2017, 2018 2.5%, 2.3%, 2.3%	signal	norm
Pileup Uncertainties	1-2 %	signal	shape
Lepton id. and trigger efficiency	1% per muon 1% prompt electron 2% displaced electron	signal	norm
Jet Energy Scale	1-2%	signal	shape
Jet Energy Scale	1-2%	signal	shape
Signal MC cross section	3.8%	signal	norm
Secondary vertex	1-17%	signal	norm

Table 6.7: Summary of systematic uncertainties and their effect on the estimates of the background and signal in the analysis.

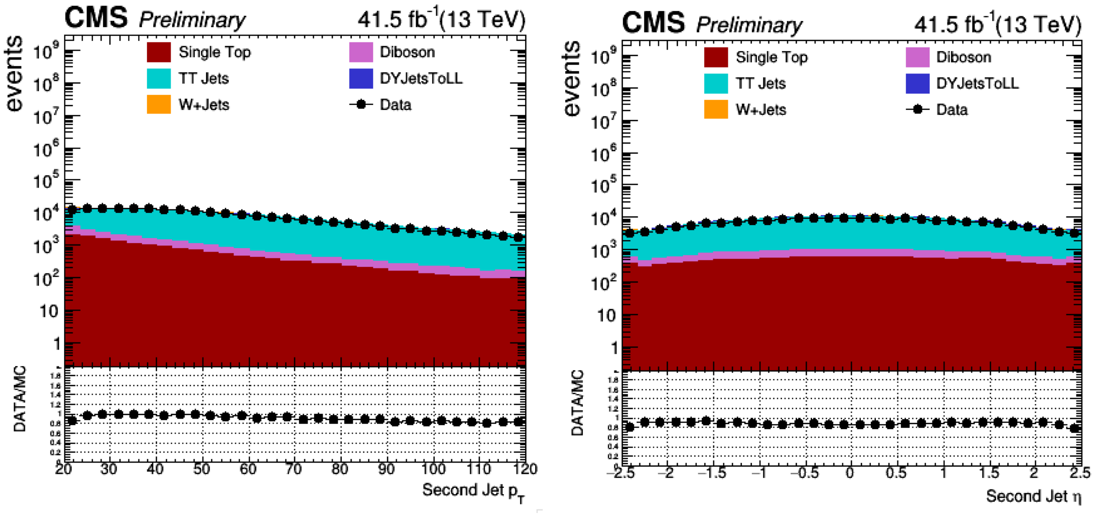

Figure 6.12: Data-Monte Carlo agreement of events passing the $t\bar{t}$ enriched region selection for tight jet p_T (left) and η (right). 2017 dataset.

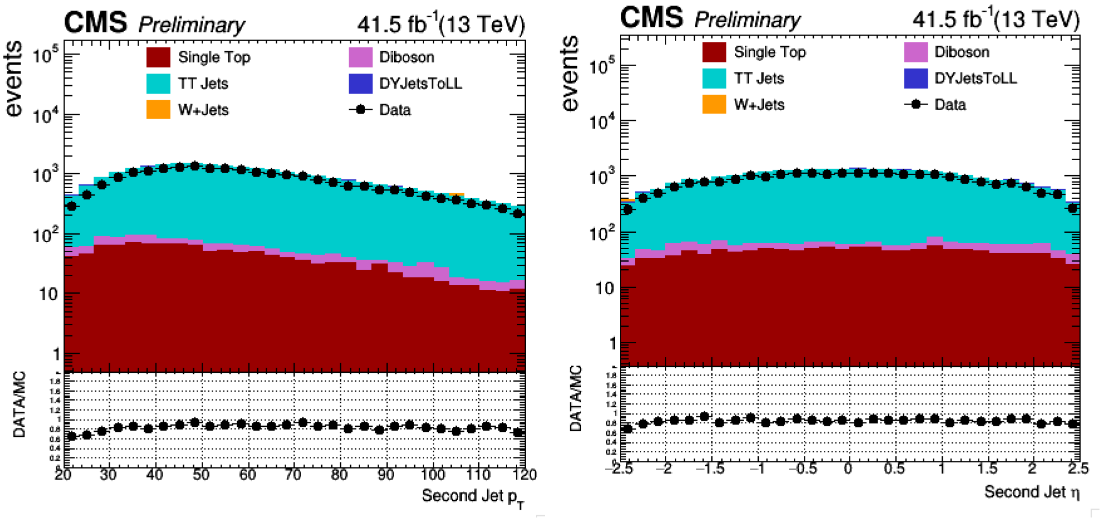

Figure 6.13: Data-Monte Carlo agreement of events passing the $t\bar{t}$ enriched region selection adding selection the requirement of matching between the selected tight jet and the tracks forming the secondary vertex for tight jet p_T (left) and η (right). 2017 dataset.

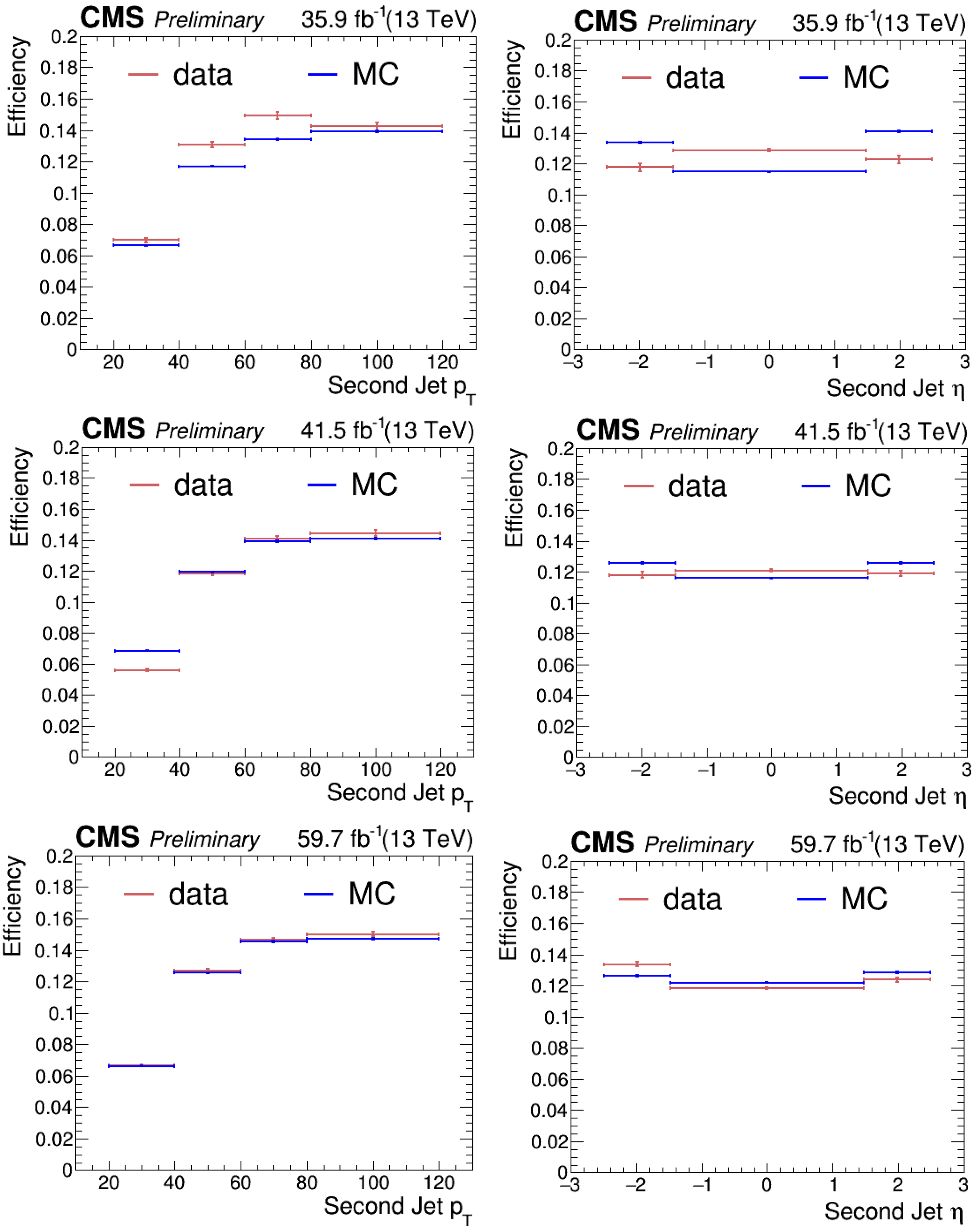

Figure 6.14: SV matching with tight jet efficiencies as a function of tight jet tight jet p_T (left) and η (right). SingleMuon 2016 dataset (top), 2017 dataset (center), 2018 dataset (bottom).

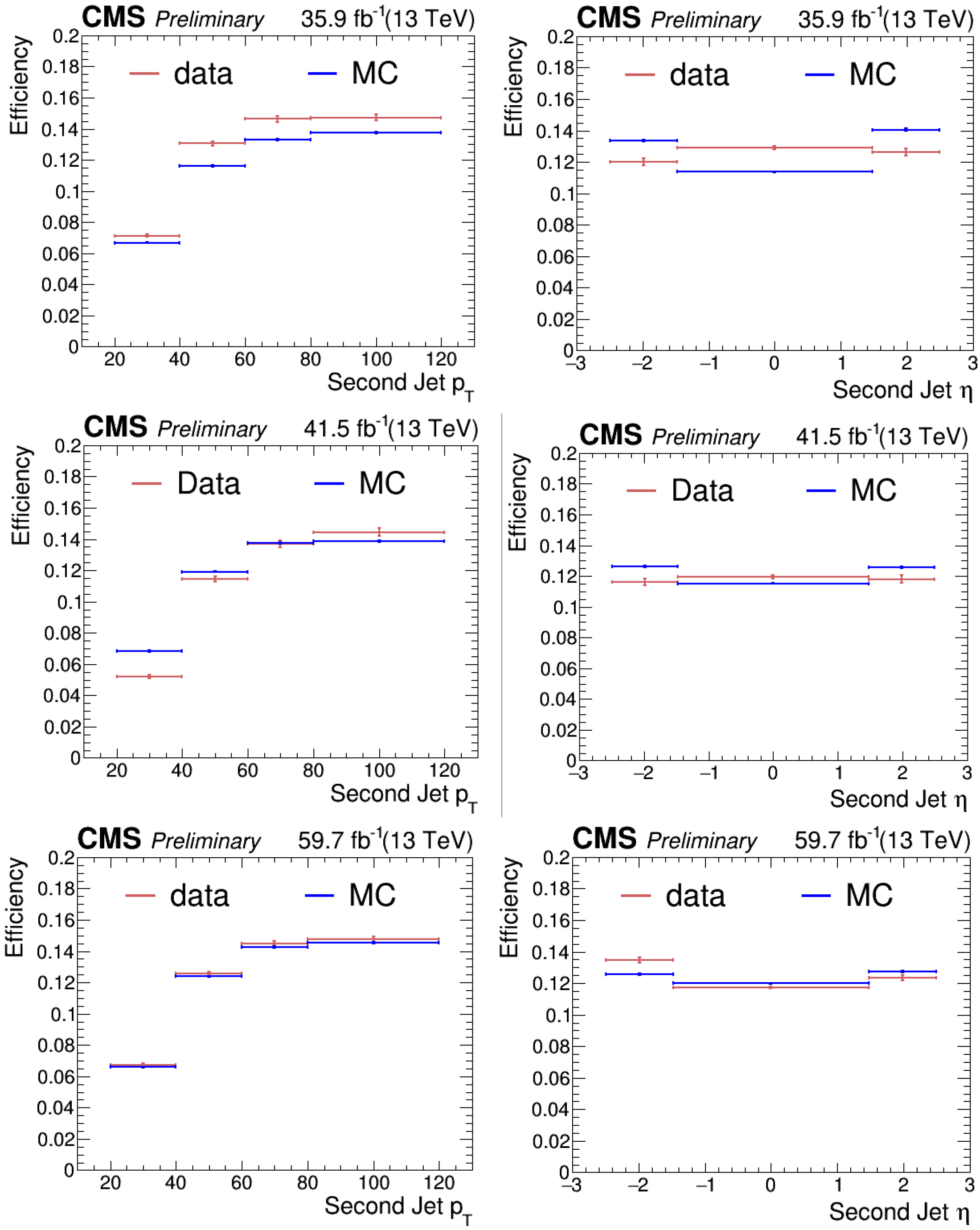

Figure 6.15: SV matching with tight jet efficiencies as a function of tight jet tight jet p_T (left) and η (right). SingleElectron-EGamma 2016 dataset (top), 2017 dataset (center), 2018 dataset (bottom).

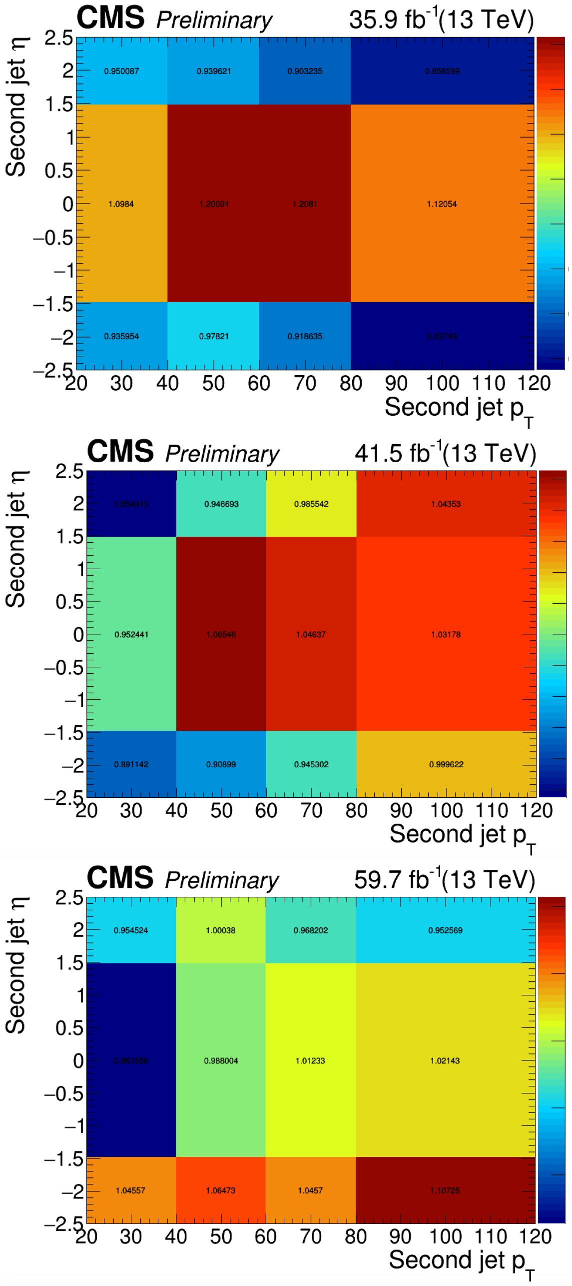

Figure 6.16: Data-MC SF as a function of tight jet p_T (left) and η (right). SingleMuon 2016 dataset (left), 2017 dataset (center), 2018 dataset (tight).

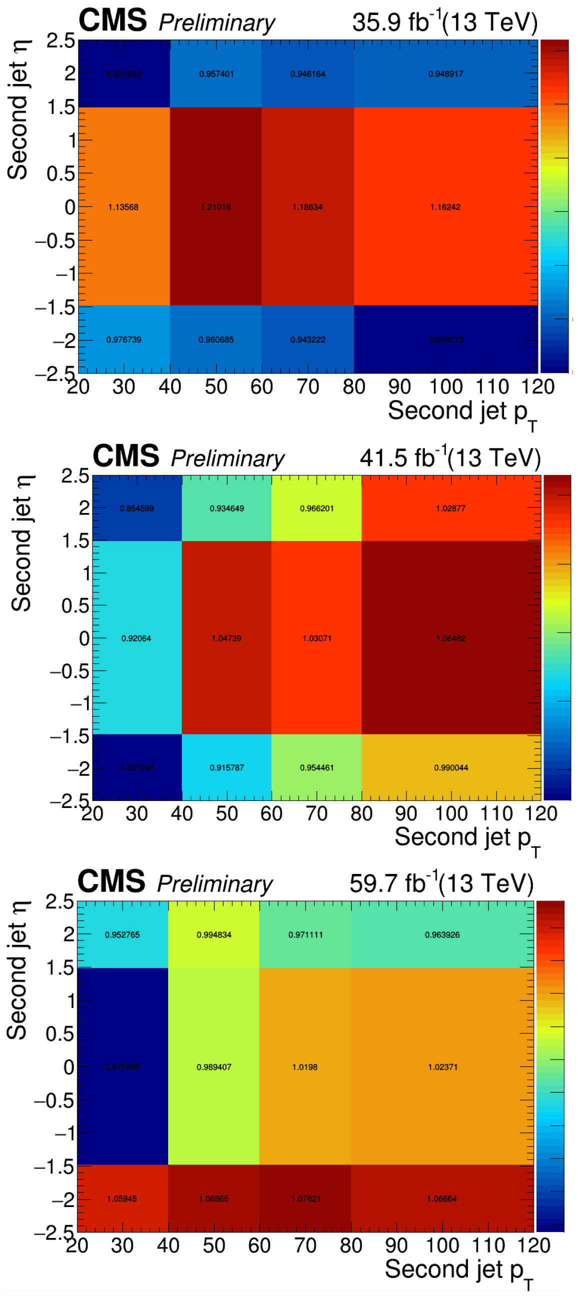

Figure 6.17: Data-MC SF as a function of tight jet p_T (left) and η (right). SingleElectron-EGamma 2016 dataset (left), 2017 dataset (center), 2018 dataset (tight).

Chapter 7

Results

The field of experimental high-energy physics requires the analysis of massive data sets. Statistical methods are extensively used at every stage of data analysis in order to successfully analyse data. First, events (for example, pp collision events) are collected, and a set of properties such as particle momentum, number of muons per event, and jet energy are measured. The observed distribution of these properties can then be compared with the theoretical predictions. By comparing the observed and theoretical distributions, the free parameters of the theory under scrutiny can be estimated. This comparison allows us to assess the level of compatibility between the theory and the observed data. However, a precise evaluation of the convention requires that the uncertainty of parameter estimates be measured in terms of probability.

In this chapter, the expected limits of an un-blinded run2 analysis is presented. Template-based shape analysis is performed using the secondary vertex mass distributions of the HNL candidate. The research result is interpreted using special statistical techniques wherein the profile likelihood ratio is used as a test statistic in combination with asymptotic approximation and the CLs criterion.

7.1 The likelihood function

To perform statistical analysis, the likelihood function is defined as the probability density function (PDF) that characterizes the set of experimental observations that were considered in the analysis, taking into account the model parameters. A nuisance parameter, θ_i is assigned to each independent source of the systematic uncertainty described in Chapter 6, and the complete set is denoted as θ. These parameters are not of direct relevance to the analysis, but must be taken into account in order to properly extract the results. In fact, the uncertainty of their determination would be expressed in the model's parameters of interest. The $p_i(\tilde{\theta}_i|\theta_i)$ associated with each nuisance parameter is assumed to account for the likelihood of calculating the θ_i value of the parameter i-th, given its true value of θ_i. The PDF is referred to as $p(\tilde{\theta}|\theta)$ for all nuisance parameters. The expected background yields (b) and the expected signal yield (s) are functions of the nuisance parameters θ. Thus, the likelihood function can thus be defined as:

$$L(data|\mu,\theta) = \prod_c L_c(data|\mu \cdot (\theta) + b(\theta)) \cdot \prod_i p_i(\tilde{\theta}_i|\theta_i) \tag{7.1}$$

The parameter μ is the signal strength modifier, and "data" represents either the observed data or values from pseudo-datasets, i.e., pseudo-random numbers sampled by a certain hypothesis of the predicted distributions provided by the probability function. The first product in equation 7.1 runs over all the channels considered in the analysis, i.e., the eight configurations obtained from the different final states of ($\mu^\pm\mu^\mp$, $\mu^\pm\mu^\pm$, $e^\pm e^\mp$, $e^\pm e^\pm$, $\mu^\pm e^\mp$, $\mu^\pm e^\pm$, $e^\pm\mu^\mp$ and $e^\pm\mu^\pm$), and the three data-taking years (2016, 2017, 2018). The L_c function is the PDF of events that are given by the Poisson probability product for binned distributions such as those used in the presented analysis.

for every bin j considered to observe n_j events:

$$L_c(data|\mu \cdot (\theta) + b(\theta)) = \prod_j \frac{(\mu \cdot s_j(\theta) + b_j(\theta))^{nj}}{n_j!} e^{-(\mu \cdot s_j(\theta) + b_j(\theta))} \tag{7.2}$$

The PDF associated with each nuisance parameter X assumes a different functional profile according to the type of systemic uncertainty described in Chapter 6. Normalization uncertainties are associated with normal-log PDFs. The shape uncertainty PDFs vary according to the different sources of uncertainty and are modeled as alternative distributions of the expected secondary veretx mass distribution for each dedicated shape variation.

7.2 Testing of hypothesis

After the likelihood function is defined, the observed results can be used to evaluate various hypotheses. From a statistical point of view, two hypotheses can be considered: the first is the null hypothesis (H_0) and the second is the alternate hypothesis (H_1). Hypothesis testing is based on creating a test statistic, an observed data function that is derived from the likelihood function and encodes information about the expected signal, background, and uncertainties. The test statistic is a random variable that must be defined in such a way as to have different distributions under the two hypotheses considered, H_0 and H_1, in order to discriminate between them. The test statistic is usually constructed as a ratio of two likelihood functions, one evaluated for the observed data set under hypothesis H_0 and the other under H_1. The expected distributions followed by the test statistic under the two hypotheses are produced by generating pseudo-datasets from the PDFs used in the likelihood function. The observed data is used to evaluate the test statistic, and its value is compared to the expected distributions to quantify the data's compatibility with the alternative hypothesis.

7.2.1 Excess quantification

The following test statistics are used to measure the statistical meaning of an excess over the background expectation:

$$q_0 = -2\ln\frac{L(data|0,\hat{\theta}_0)}{L(data|\hat{\mu},\hat{\theta})},\ with\ \hat{\mu} \geq 0 \tag{7.3}$$

The numerator is evaluated under the hypothesis of only-background (($\mu = 0$) and $\hat{\theta}_0$ is the set of values of the nuisance parameters that maximizes it under this null hypothesis. Under the hypothesis of alternative signal + background, the denominator is evaluated, and the $\hat{\mu}$ and $\hat{\theta}$ values are those that maximize the likelihood in the denominator. By this definition, q_0 is positive when there is an excess of signal ($\mu > 0$), while in the absence of an excess ($\mu = 0$), q_0 becomes 0. The significance of an excess can be quantified in terms of local p-value, defined as the probability of obtaining a value of the q_0 test statistic as large as that observed in the experimental data in the hypothesis of the background-only:

$$p_0 = P(q_0 \geq q_0^{obs}|b) \tag{7.4}$$

In other terms, p_0 characterizes the probability of a hypothesized signal being similar to that of observable data with a local context variation. The p value is generally translated by the Gaussian one-sided tail integral to the significance Z of the excess:

$$p_0 = \int_Z^{\infty} \frac{1}{\sqrt{2\pi}} e^{-\frac{x^2}{2} dx} \tag{7.5}$$

The conventional Z $= 5\sigma$ threshold for claiming a discovery corresponds to a p-value of 2.8 x 10^{-7}.

7.2.2 Upper limit

If a significant excess is not observed, an upper limit is set for the hypothesis of the considered signal. To analyse this situation, another test statistic was used, this time using the signal and background hypothesis in the numerator:

$$q_\mu = -2\ln \frac{L(data|\mu, \hat{\theta}_\mu)}{L(data|\hat{\mu}, \hat{\theta})},\ with\ 0 \leq \hat{\mu} \leq \mu \tag{7.6}$$

Where $\hat{\theta}_\mu$ maximises the numerator under the hypothesis of a signal with strength μ. $\hat{\mu}$ and $\hat{\theta}$ maximise the likelihood in the denominator, as before, and correspond to the global maximum of the likelihood. The lower constraint $0 \leq \hat{\mu}$ is needed by physics in order to provide a positive signal rate; the upper constraint $\hat{\mu} \leq \mu$ is applied to ensure a one-sided confidence interval, such that upward fluctuations in the data are not considered as evidence against the hypothesis of a signal of intensity μ. Instead of generating pseudo-datasets, this description of the test statistic q_μ allows for the analytical derivation of the expected distributions of q_μ under the signal+background and background-only hypotheses in the asymptotic limit of a large number of background events[126]. In this study, exclusion limits are calculated using a modified frequentist method known as CLs[127], with the profile likelihood q_μ serving as the test statistic in the asymptotic approximation. Given an observed value of the test statistic q_μ^{obs} obtained by evaluating Equation 7.6 with the observed results, the probability that q_μ is equal to or greater than q_μ^{obs} under the signal+background and background-only hypotheses is defined as follows:

$$CL_{s+b}(\mu) = P(q_\mu \geq q_\mu^{obs} | \mu \cdot s + b) \tag{7.7}$$

$$CL_b(\mu) = P(q_\mu \geq q_\mu^{obs} | b) \tag{7.8}$$

The quantity CLs is defined as their ratio :

$$CL_s(\mu) = \frac{CL_{s+b}(\mu)}{CL_b(\mu)} \tag{7.9}$$

A signal of strength μ is excluded at a confidence level of α if CLs(μ) $< 1 - \alpha$. Usually, and also in this analysis, exclusion limits are computed for α= 95% .

7.3 Analysis Results

The observed data yields and the predicted background yields from the DNN (section 5.3.1) method for the different bins of the signal region are shown in Figures (Figures (7.3 - C.1). Additionally, the expected event yields for several HNL signal scenarios are shown as well. This thesis introduced a new technique for a data-driven method by using the DNN fake rate method. In this approach, the DNN output is interpreted as the probability that a background event will pass the tight selection. As a result, the output will be used to re-weight the control region in order to predict the background in the signal region. No indication of an excess over the SM background prediction is observed. Since no new particles have been discovered, exclusion limits are evaluated with the modified frequentist approach to CLs [128] with a binned profile likelihood test statistics using the signal region bins.

Given the predicted background yields and observed yields in all search regions, we can evaluate the exclusion of HNL signal scenarios by computing the excluded cross section for each (M_N, $\mid \mathrm{V}_{lN} \mid^2$) hypothesis. To get the proper excluded regions in the(M_N, $\mid \mathrm{V}_{lN} \mid^2$) parameter space, we need to extrapolate the estimated limits between different points in the (M_N, $\mid \mathrm{V}_{lN} \mid^2$) plane. As discussed in Section 1.2.6, varying the mass and mixing probability of the HNL affects both its production cross section as well as its kinematics and acceptance. As a result, the computed value for excluded signal strength ($\mu = \sigma_{excl}/\sigma_{theor}$) for a given ($\mathrm{M}_N$,$\mid \mathrm{V}_{lN} \mid^2$) only indicates whether that particular point is excluded ($\mu \leq 1$) or not ($\mu > 1$). So, it cannot be interpreted as an excluded cross section. Instead, we need to employ the event-by-event re-weighting method described in Section 1.2.6 to emulate HNLs of same mass and different $\mid \mathrm{V}_{lN} \mid^2$, until we find the exact $\mid \mathrm{V}_{lN} \mid^2$ value for which $\mu = 1$.

Figure 7.1 shows the exclusion limit of HNL at mass 5 GeV across various $\mid \mathrm{V}_{\mu N} \mid^2$ values, demonstrating how the excluded region for a given mass of HNL can be obtained by determining the upper and lower limit points at which $\mu = 1$. This fit is performed in the asymptotic approximation, separately for each (M_N,$\mid \mathrm{V}_{lN} \mid^2$) HNL signal scenario. The likelihood is constructed using the observed data yields, the signal yields obtained from simulated events, and the background yields predicted with the DNN method, along with nuisance parameters that encode the effect of the systematic uncertainties associated with the estimated yields, including possible effects on the shapes of the kinematic distributions. All statistical uncertainties, as well as the integrated luminosity and pileup systematic uncertainties, are treated as uncorrelated between the different data-taking years.

The exclusion limits are evaluated from a simultaneous fit of predicted signal and background events in the considered displacement regions, separately in the ee, $\mu\mu$ channels, and we use the additional eμ and μe signal regions. Figures (7.9 - 7.14) show the excluded regions of the HNL mass and the corresponding mixing parameters ($\mid V_{N\mu} \mid^2$, $\mid V_{Ne} \mid^2$, and mixed coupling $\dfrac{\mid V_\mu \cdot V_e \mid^2}{\mid V_e \mid^2 + \mid V_\mu \mid^2}$). The results are obtained by fitting the secondary vertex mass distributions for each of the three data-taking years (2016, 2017, and 2018) individually.

Figures (7.15 and 7.16) show the exclusion limits on $\mid V_{N\mu} \mid^2$, $\mid V_{Ne} \mid^2$, and mixed coupling $\dfrac{\mid V_\mu \cdot V_e \mid^2}{\mid V_e \mid^2 + \mid V_\mu \mid^2}$ as a function of M_N for Majorana and Dirac HNL respec-

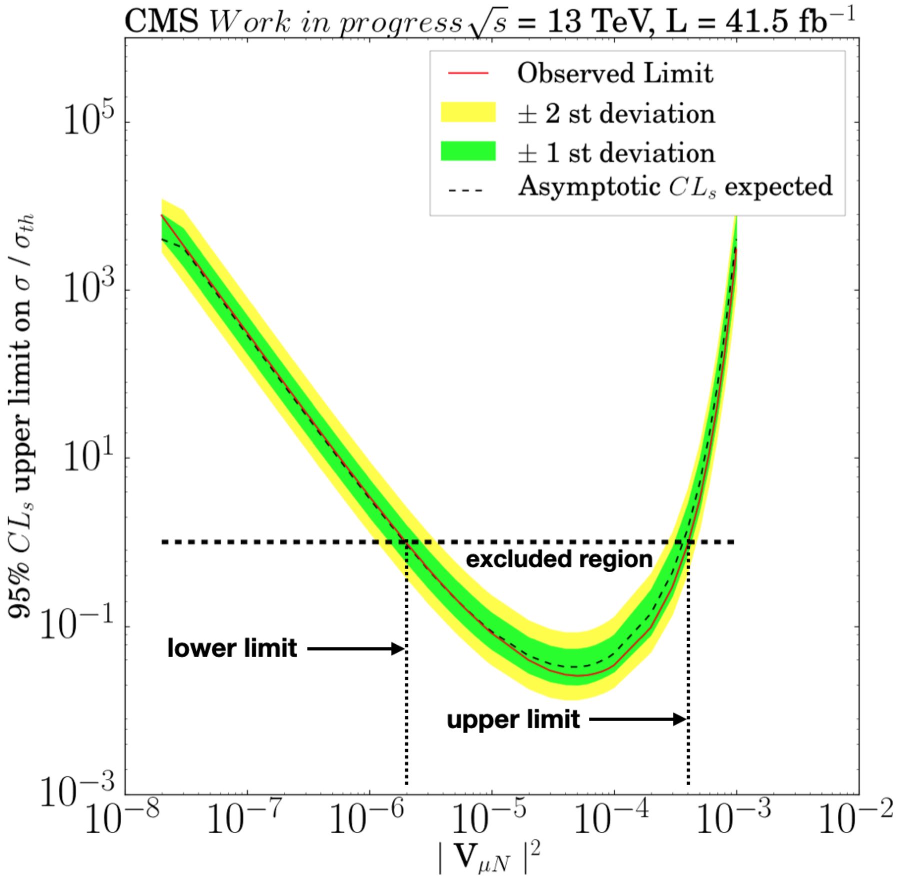

Figure 7.1: The exclusion limit of HNL at mass = 5 GeV at various $|V_{\mu N}|^2$ values.

tively, using the entire run2 data of 137 fb^{-1}. The exclusion limit result is shaped like a horizontal parabola, where the upper line indicates when the HNL is a prompt scenario and the bottom line shows when the HNL is displaced, and the area in between the two limit lines is excluded. This particular shape was obtained as a result of the equation described in Section 1.2.6. As we increase the coupling, the HNL tends to decay immediately after production, so-called prompt. In contrast, the HNL is more likely to be long-lived with lower coupling (decay far from the interaction point). In the Dirac scenario, muon (electron) couplings of $2 \times 10^{-4} (9 \times 10^{-4})$ and higher for an HNL mass of 1 GeV are excluded, as are muon (electron) couplings of $1 \times 10^{-7} (8 \times 10^{-7})$ for an HNL mass of 10 GeV. For the case of electron couplings, the limits in both scenarios improve with respect to the results of the DELPHI [129] for masses above about 3.5 GeV. In the case of muon couplings, the limits improve significantly with respect to the DELPHI [129] and CMS [[12], [50]] collaboration results for masses above about 7 GeV.

7.3.1 Systematic uncertainties impact

As mentioned in Section 7.1, systematic uncertainties are included into the fit as nuisance parameters. To determine which uncertainties have the most impact on the outcome of signal strength, the impact is determined as the $\pm$ 1σ of the post fit value of each nuisance parameter, while the rest of the parameters are set to their best fitted value. Among the many uncertainty evaluated, the fifteen that have the major effect on the post fit signal strength ($\mu = \sigma_{obs}/\sigma_{theo}$) are depicted in Figure 7.2, for 2017 analysis and the HNL signal sample of mass $M_{HNL} = 5GeV$, as an example

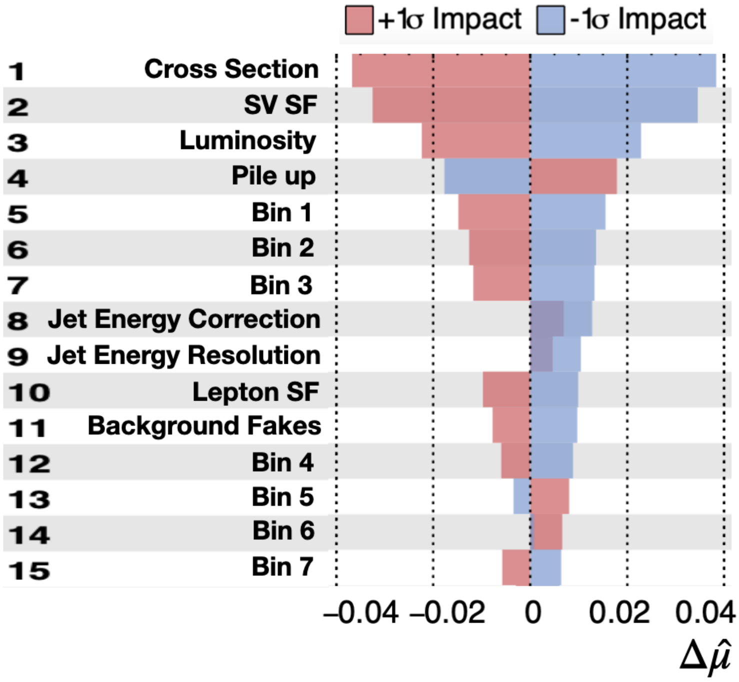

Figure 7.2: Variation at + 1σ(red) and - 1σ (blue), of the signal strength for the 15 sources of uncertainty with highest impact.

The impact bars, $\Delta\mu$, reflect the relative fluctuation of signal strength when a specific nuisance parameter varies by one standard deviation. The sign of $\Delta\mu$ indicates whether the fluctuation of signal strength is correlated or anti-correlated with the variation of the nuisance parameter. The systematic uncertainty source connected with the theoretical cross section has the biggest impact. Bin i sources provide the statistical uncertainty of the ith bin in the secondary vertex distribution used as input.

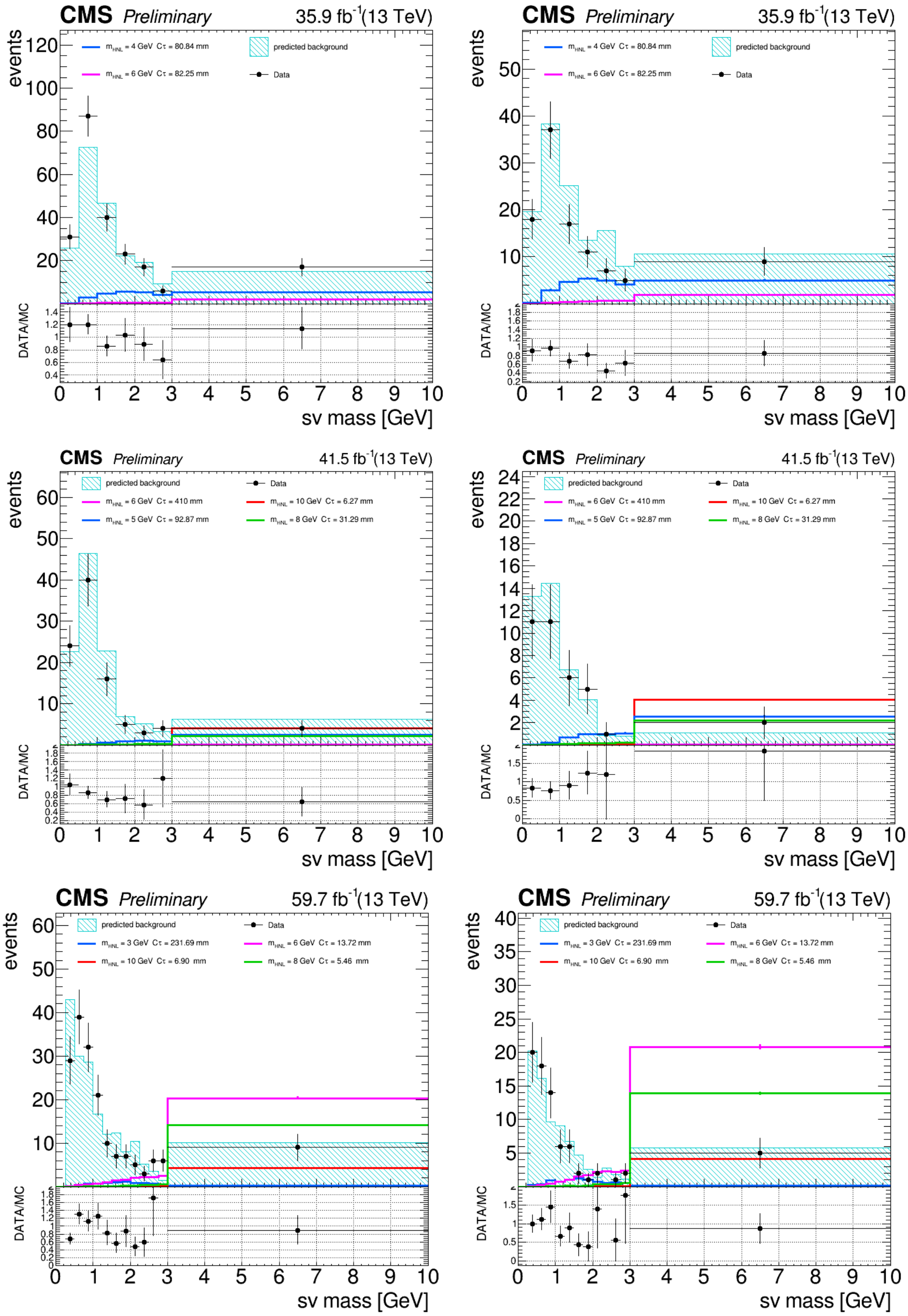

Figure 7.3: Predicted and observed event yields in the signal region for $\mu\mu$ categorises OS (left) and SS (right) selections in years 2016 (top), 2017(middle) and 2018(bottom).

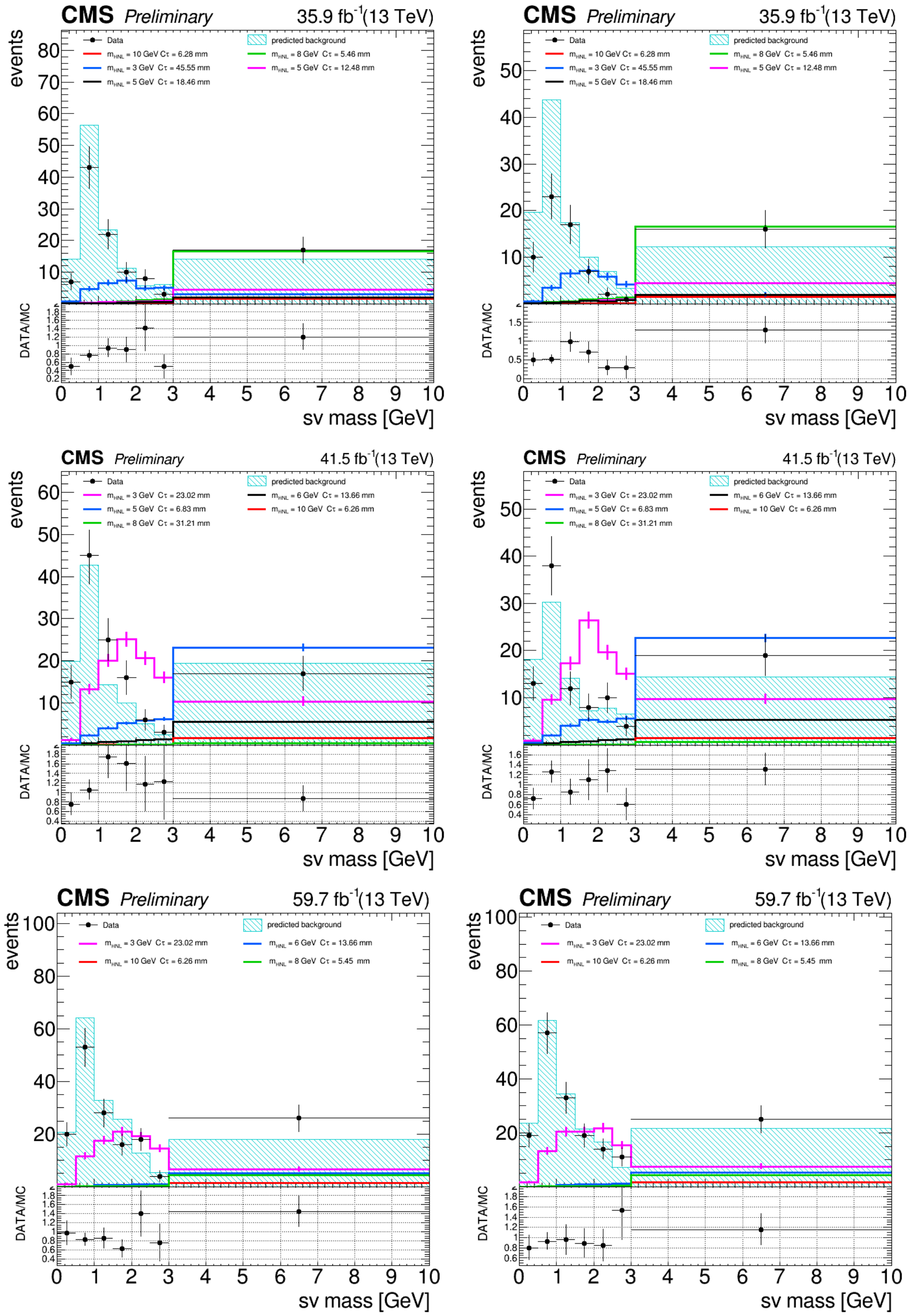

Figure 7.4: Predicted and observed event yields in the signal region for ee categorises OS (left) and SS (right) selections in years 2016 (top), 2017(middle) and 2018(bottom).

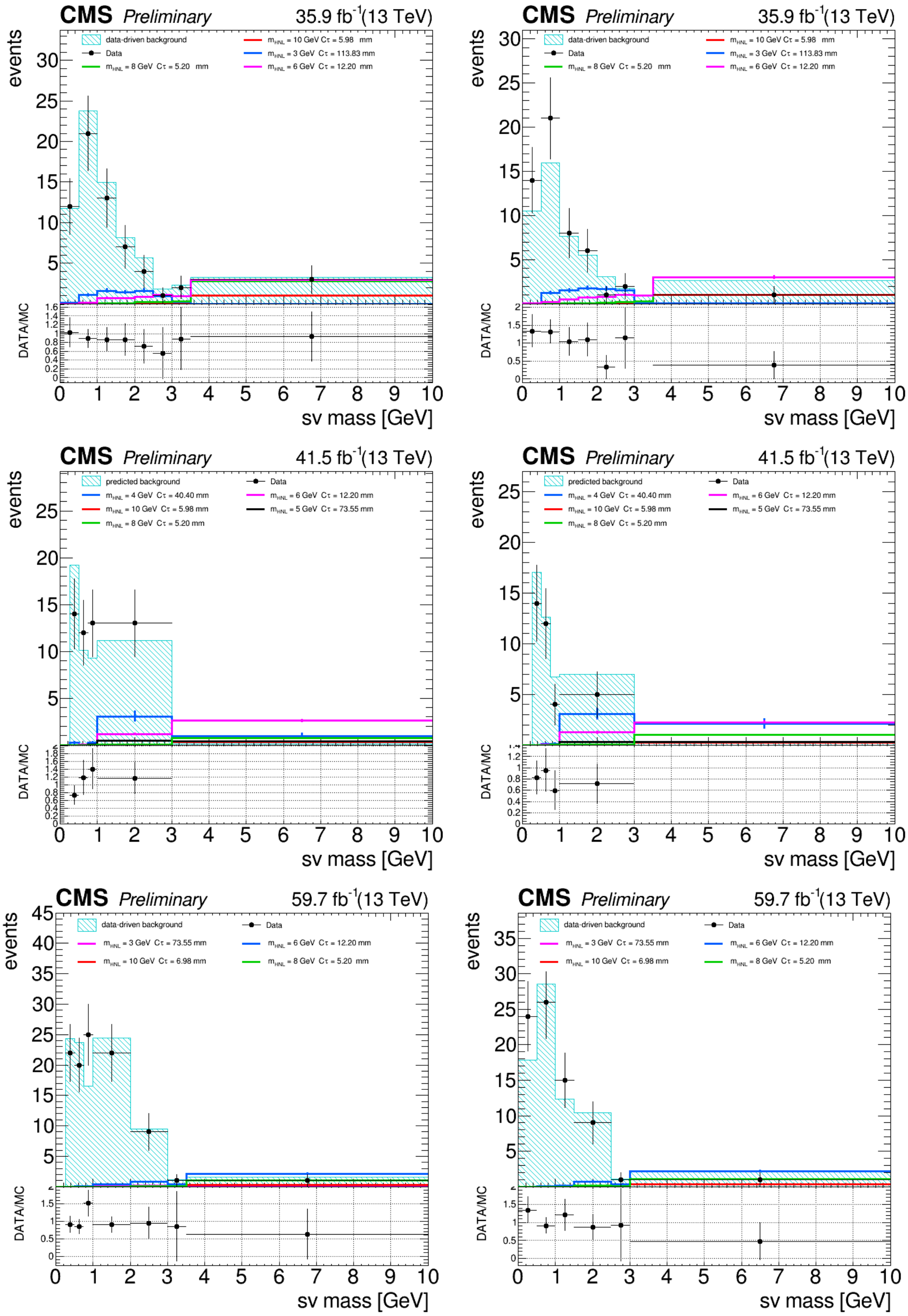

Figure 7.5: Predicted and observed event yields in the signal region for $e\mu$ categorises OS (left) and SS (right) selections in years 2016 (top), 2017(middle) and 2018(bottom).

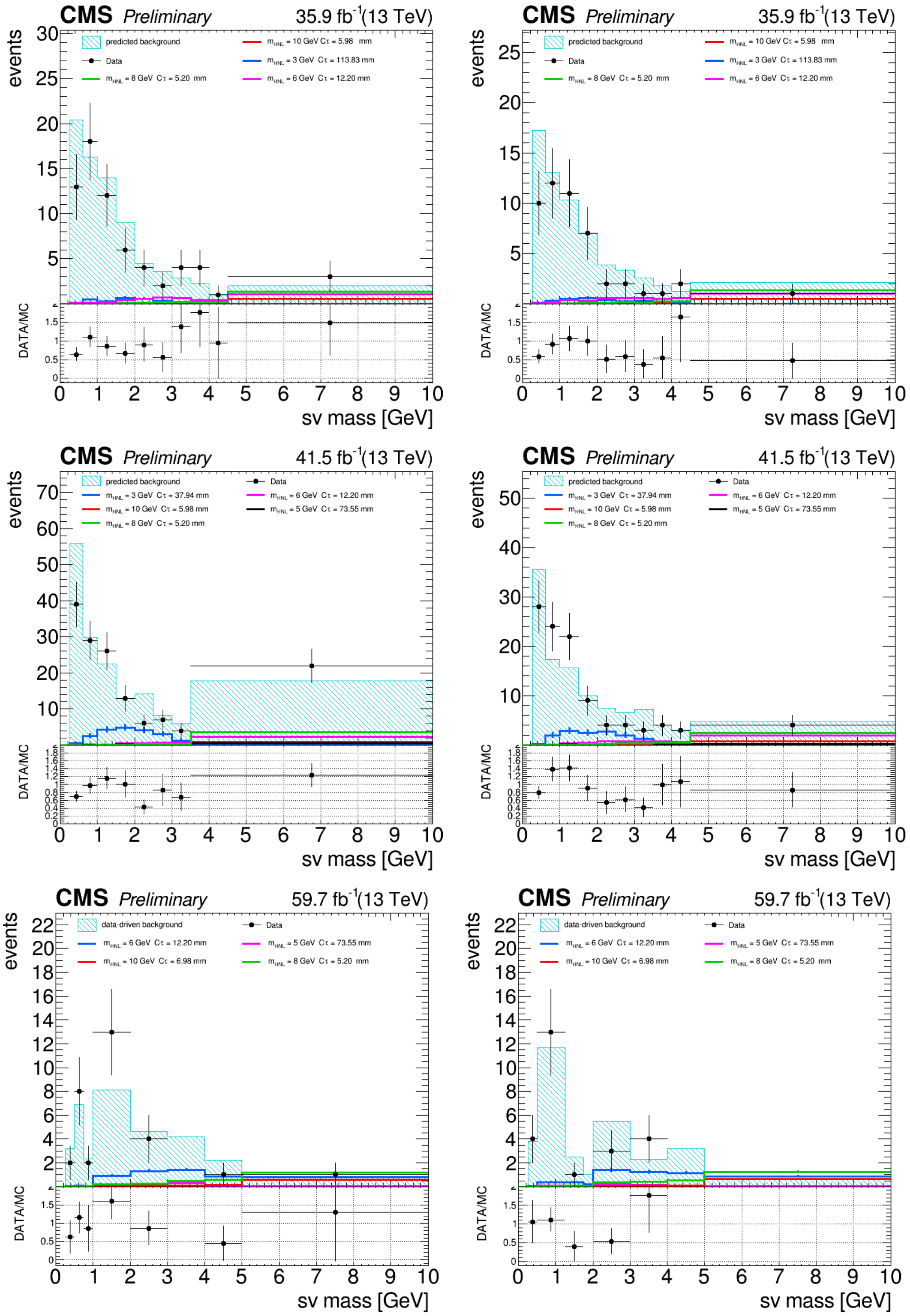

Figure 7.6: Predicted and observed event yields in the signal region for μe categorises OS (left) and SS (right) selections in years 2016 (top), 2017(middle) and 2018(bottom).

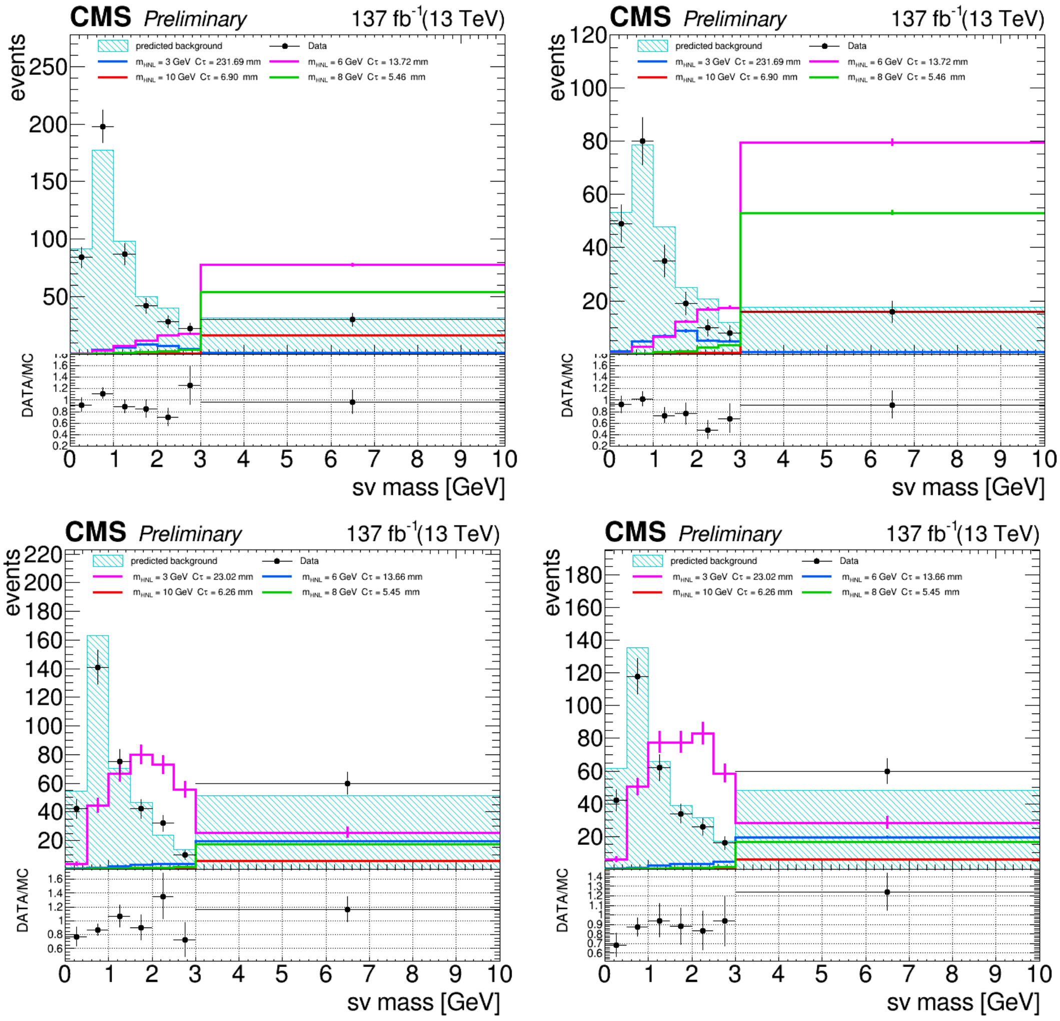

Figure 7.7: Predicted and observed event yields in the signal region for $\mu\mu$ (top) and ee(bottom) channels with categorises OS (left) and SS (right) selections for full run2.

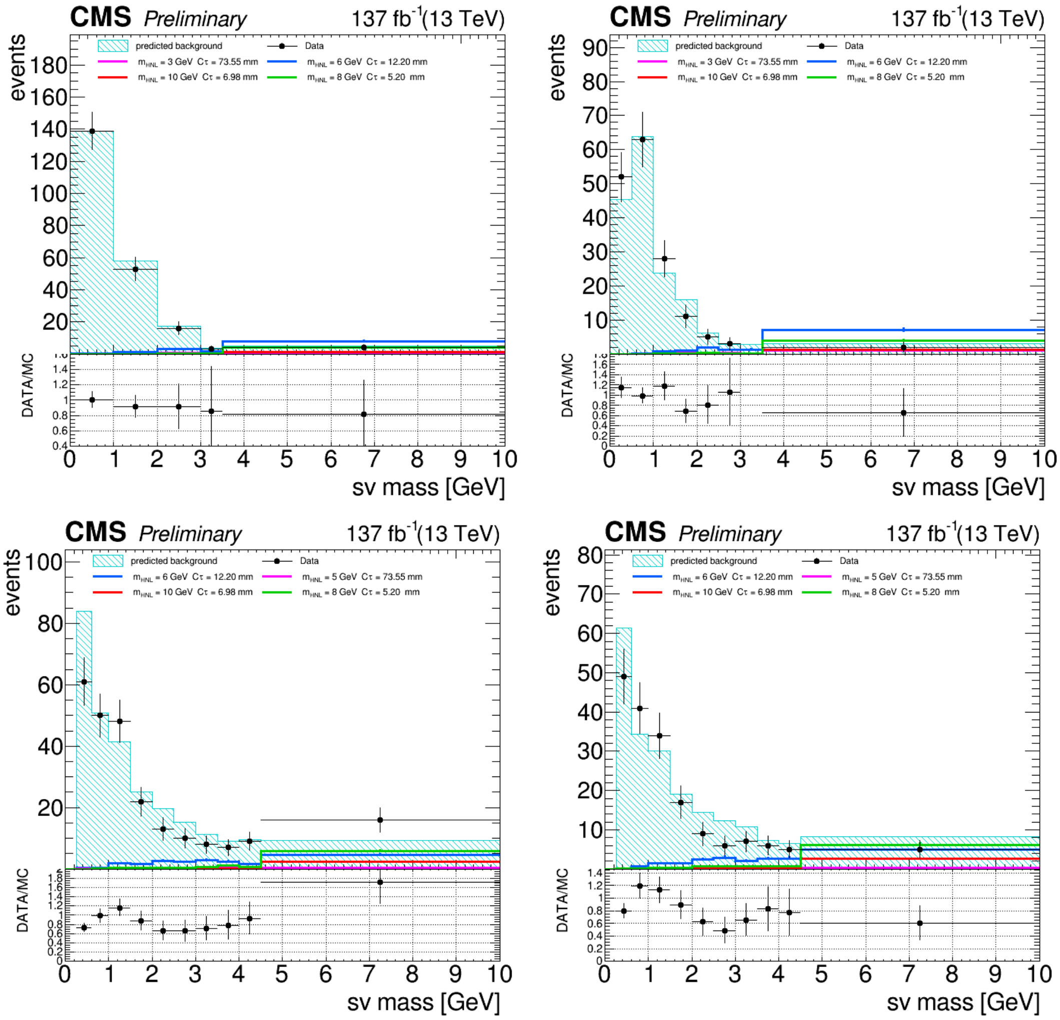

Figure 7.8: Predicted and observed event yields in the signal region for eμ (top) and μe (bottom) channels with categorises OS (left) and SS (right) selections for full run2.

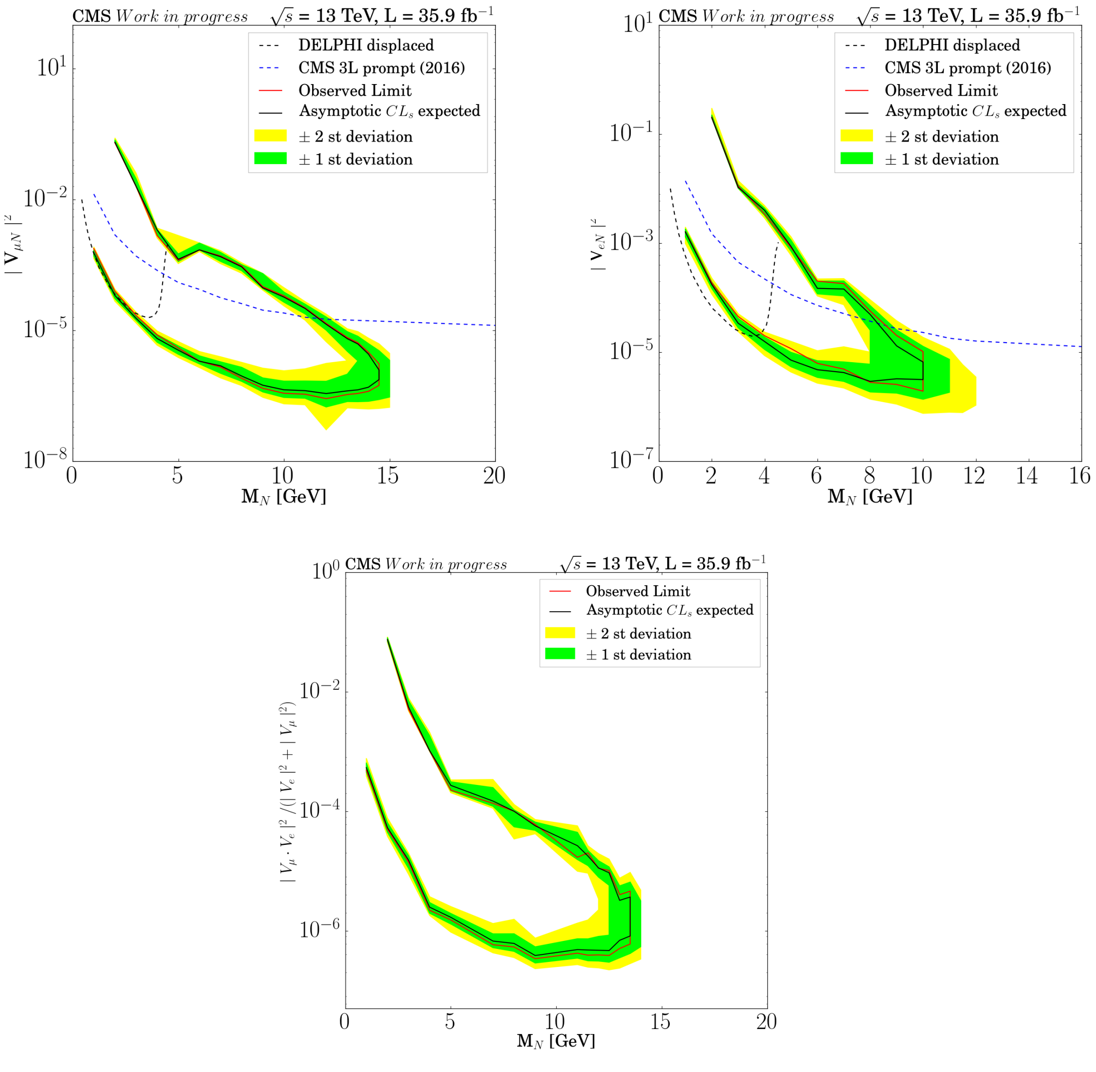

Figure 7.9: Limits on $| V_{N\mu} |^2$ (upper left), $| V_{Ne} |^2$ (upper right) and mixed coupling $\frac{| V_\mu \cdot V_e |^2}{| V_e |^2 + | V_\mu |^2}$ (below) as a function of M$_N$ for a Dirac HNL using the 2016 data set.

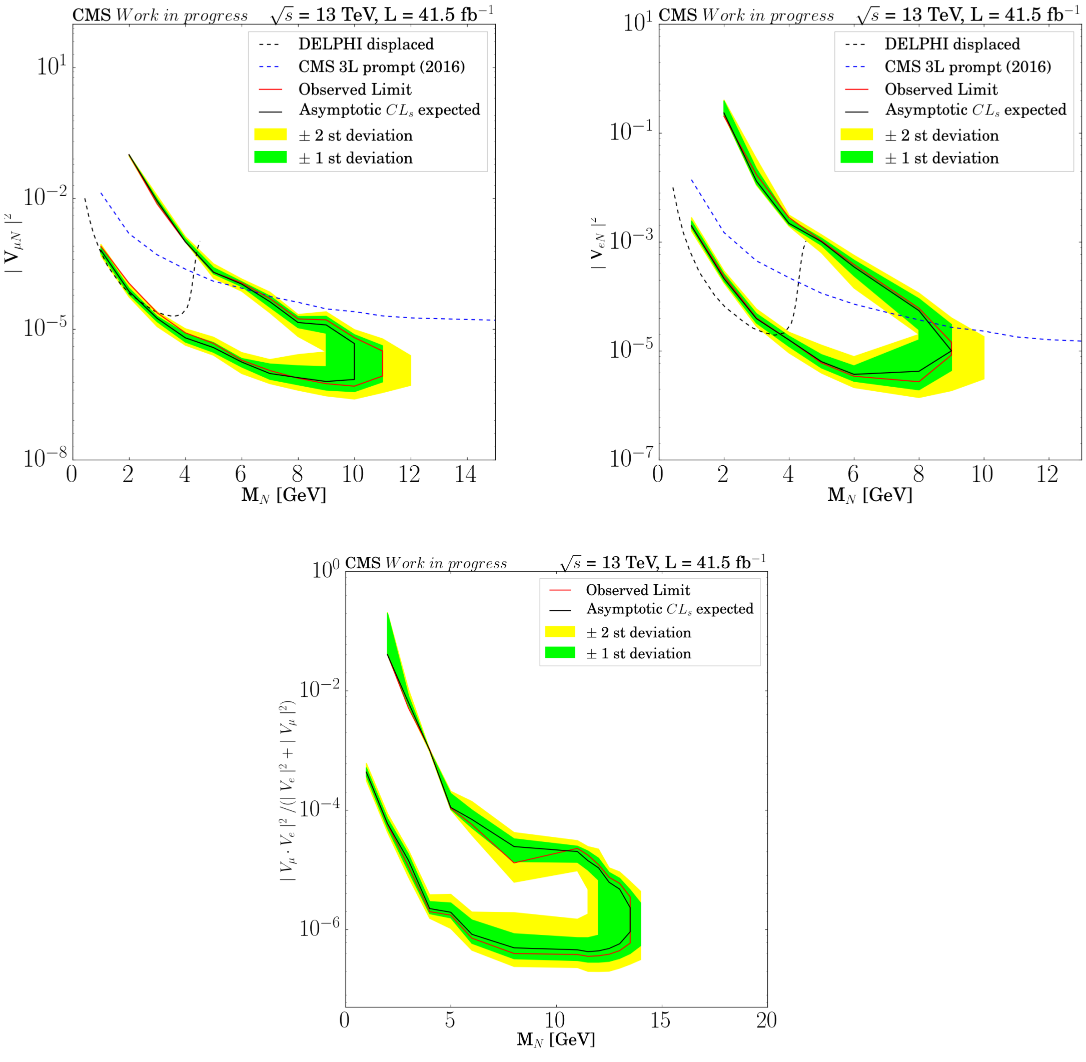

Figure 7.10: Limits on $| V_{N\mu} |^2$ (upper left), $| V_{Ne} |^2$ (upper right) and mixed coupling $\dfrac{| V_\mu \cdot V_e |^2}{| V_e |^2 + | V_\mu |^2}$ (below) as a function of M_N for a Dirac HNL using the 2017 data set.

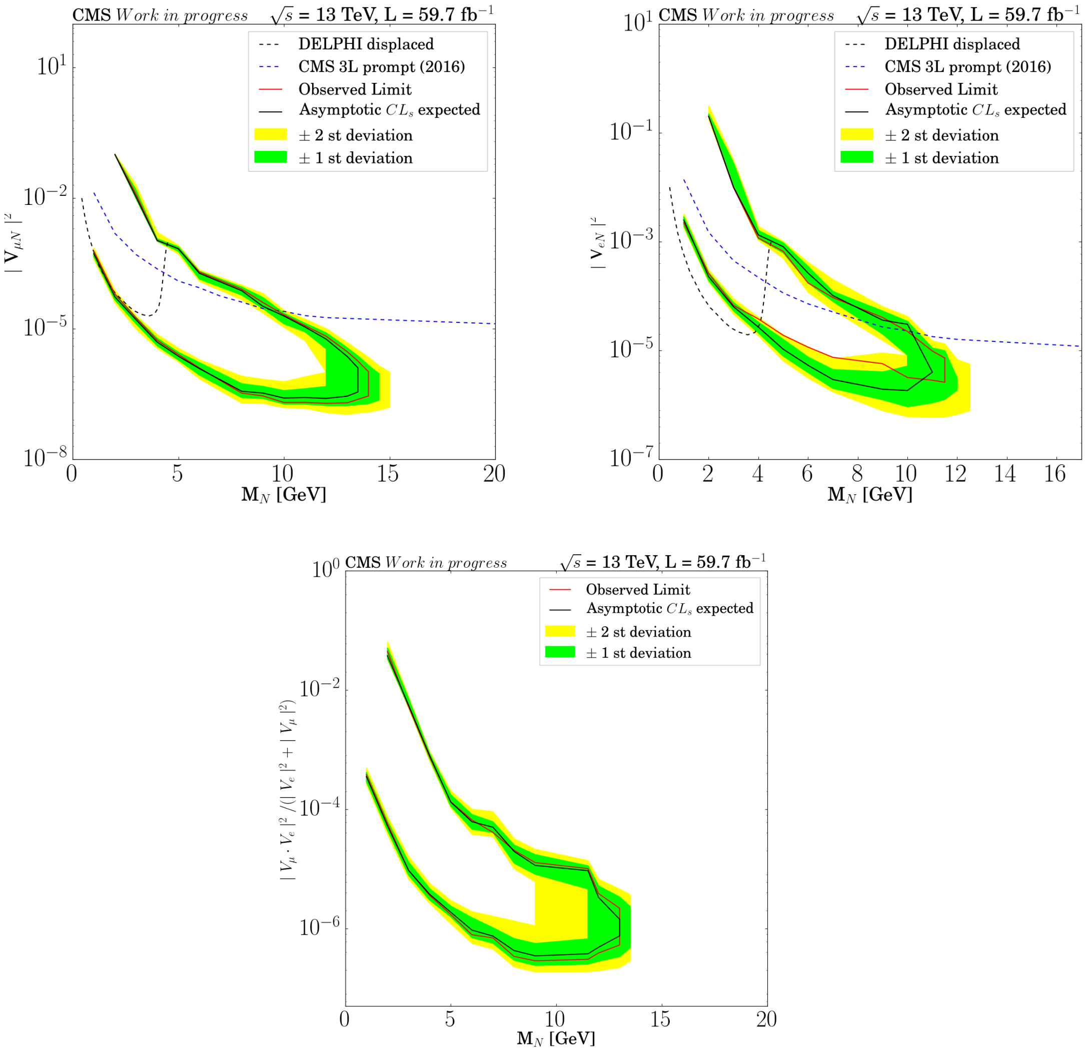

Figure 7.11: Limits on $| V_{N\mu} |^2$ (upper left), $| V_{Ne} |^2$ (upper right) and mixed coupling $\dfrac{| V_\mu \cdot V_e |^2}{| V_e |^2 + | V_\mu |^2}$ (below) as a function of M$_N$ for a Dirac HNL using the 2018 data set.

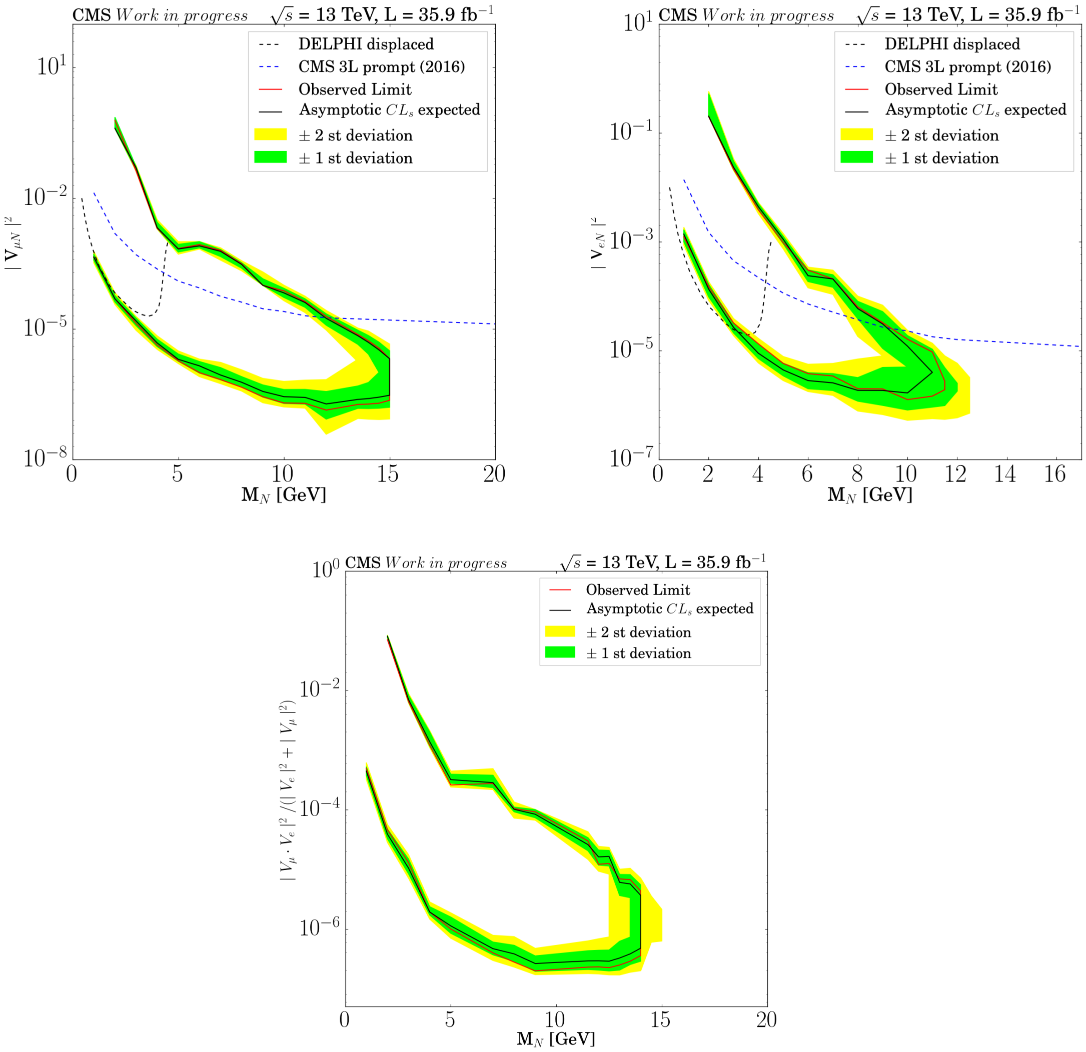

Figure 7.12: Limits on $| V_{N\mu} |^2$ (upper left), $| V_{Ne} |^2$ (upper right) and mixed coupling $\dfrac{| V_\mu \cdot V_e |^2}{| V_e |^2 + | V_\mu |^2}$ (below) as a function of M$_N$ for a Majorana HNL using the 2016 data set.

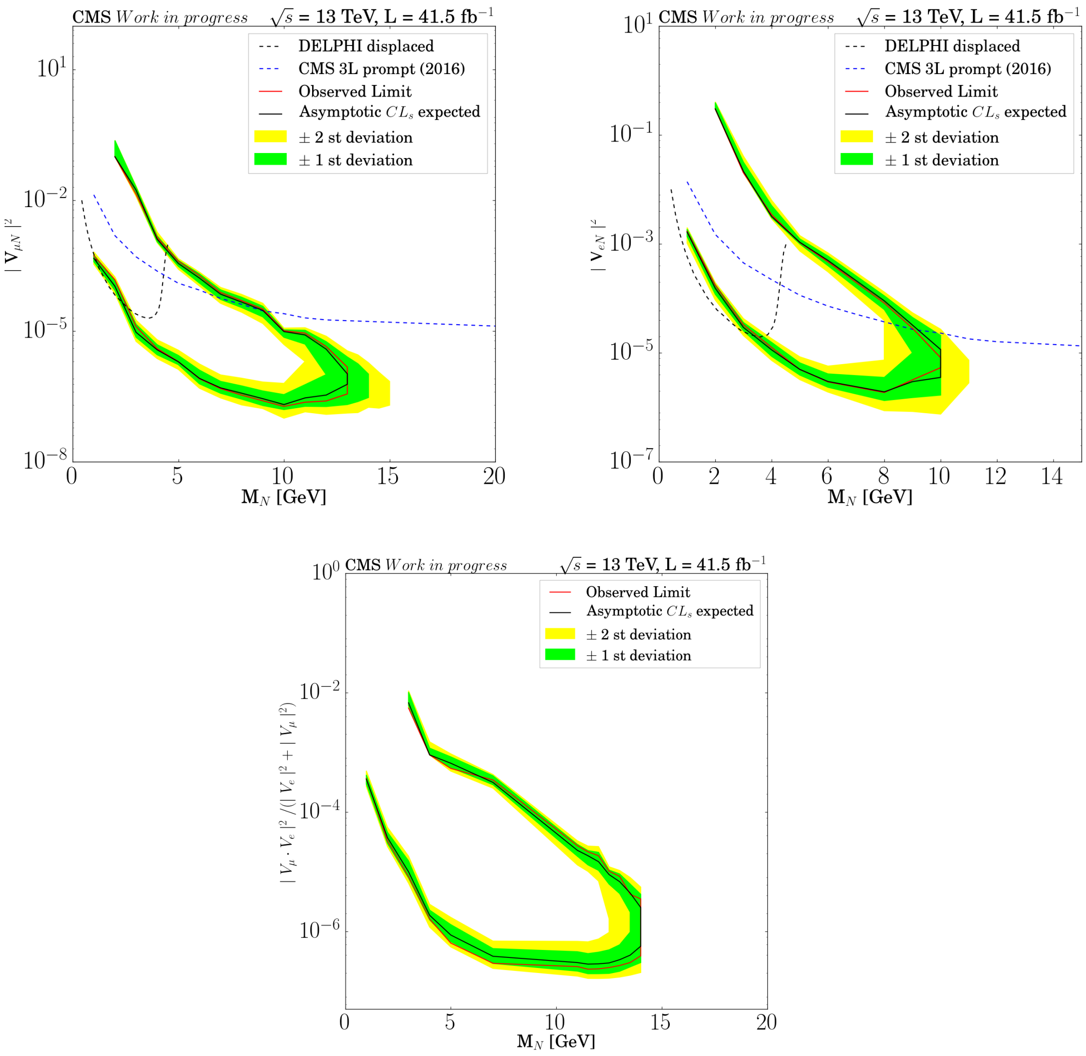

Figure 7.13: Limits on $| V_{N\mu} |^2$ (upper left), $| V_{Ne} |^2$ (upper lright) and mixed coupling $\dfrac{| V_\mu \cdot V_e |^2}{| V_e |^2 + | V_\mu |^2}$ (below) as a function of M$_N$ for a Majorana HNL using the 2017 data set.

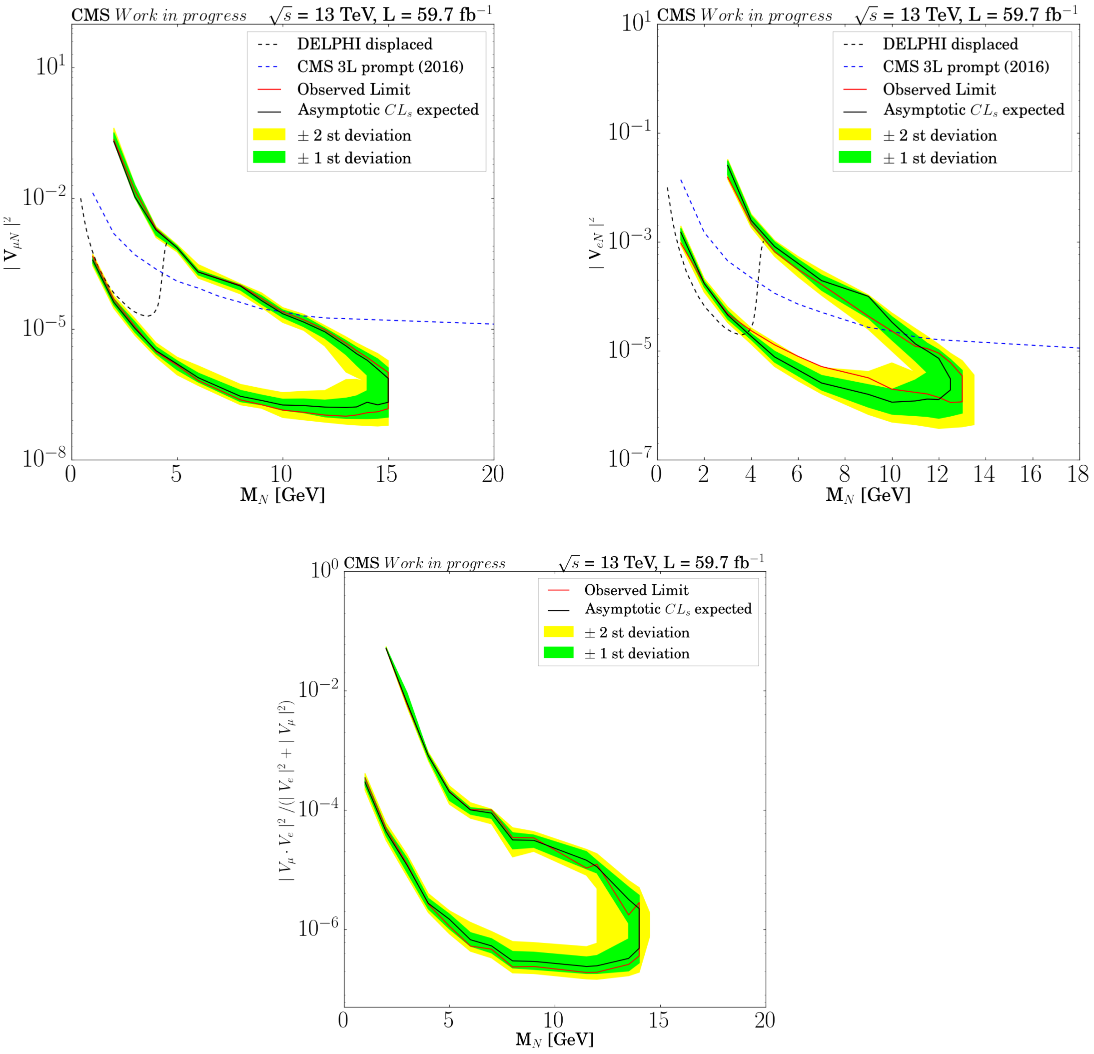

Figure 7.14: Limits on $| V_{N\mu} |^2$ (upper left), $| V_{Ne} |^2$ (upper lright) and mixed coupling $\dfrac{| V_\mu \cdot V_e |^2}{| V_e |^2 + | V_\mu |^2}$ (below) as a function of M$_N$ for a Majorana HNL using the 2018 data set.

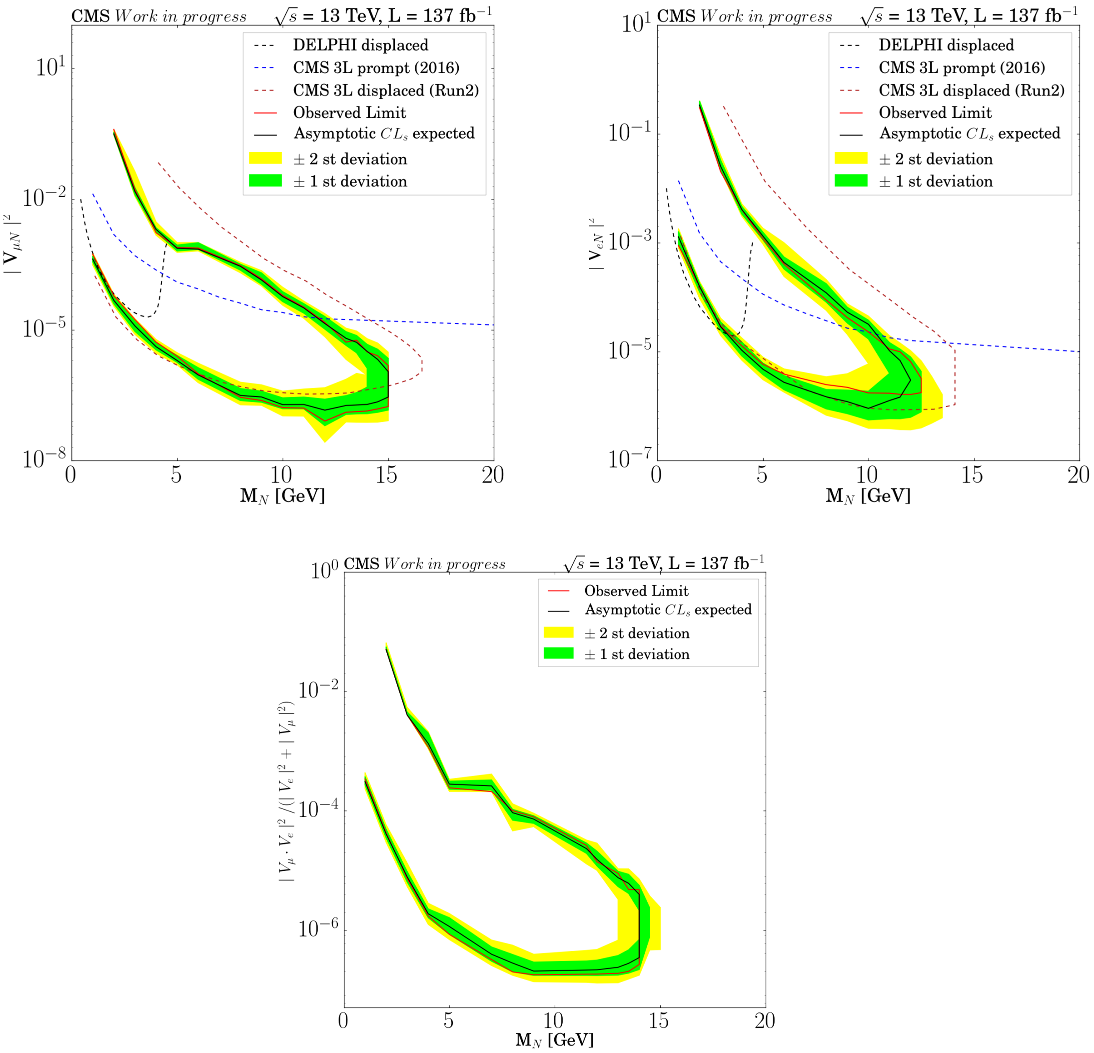

Figure 7.15: Limits on $\mid V_{N\mu} \mid^2$ (upper left), $\mid V_{Ne} \mid^2$ (upper right) and mixed coupling $\dfrac{\mid V_\mu \cdot V_e \mid^2}{\mid V_e \mid^2 + \mid V_\mu \mid^2}$ (below) as a function of M_N for a Dirac HNL using the full run2 data set (2016, 2017, 2018). Results from the Delphi [129] and the CMS [[12],[50]] Collaborations are shown for reference.

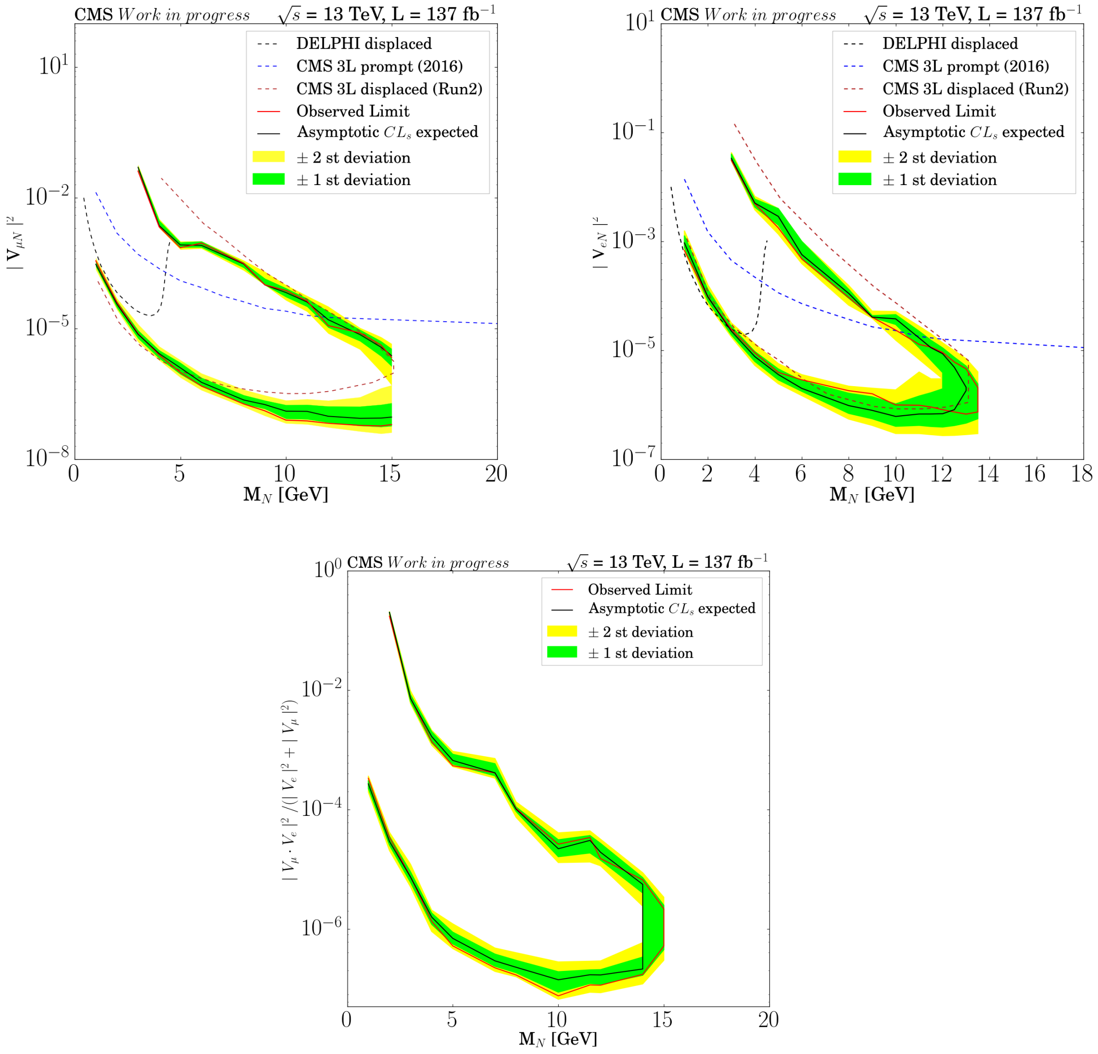

Figure 7.16: Limits on $| V_{N\mu} |^2$ (upper left), $| V_{Ne} |^2$ (upper right) and mixed coupling $\frac{| V_\mu \cdot V_e |^2}{| V_e |^2 + | V_\mu |^2}$ (below) as a function of M$_N$ for a Majorana HNL using the full run2 data set (2016, 2017, 2018). Results from the Delphi [129] and the CMS [[12],[50]] Collaborations are shown for reference.

Conclusion

A key question for experiments at the Large Hadron Collider, at CERN, is to search for signs of physics beyond the Standard Model. In this thesis we conduct a search for the hypothetical Heavy Neutral Lepton (HNL) that decay into two quarks and a lepton (μ or e) final state, with the CMS experiment. The search presented here has been performed in the theoretical framework of the νMSM model. The properties of the νMSM have been examined and a search for HNL signals with mass values below the W-boson mass has been performed using proton-proton collision data recorded by the CMS experiment. The analysed data corresponds to a data sample with an integrated luminosity of 137 fb^{-1} and was collected at a centre-of-mass energy of $\sqrt{s} = 13$ TeV. This is the first time a search has been conducted for right-handed neutrinos in the displaced dilepton channel, using the full data set collected in 2016-2018 by the CMS detector. The two key parts of the analysis are: the optimal signal selection for the search of HNL signals in the channel W $\rightarrow l_1 l_2 q\bar{q}'$; and the background estimation based on a data-driven model, using the fake rate method based on Neural Network techniques.

Optimizing the signal selection maximizes the expected discovery significance as determined by Poisson counting experimental statistics. The search is optimized for events with a high p_T prompt lepton and a displaced vertex containing a second lepton and hadrons. The data is classified into eight lepton combination categories: $\mu^\pm\mu^\mp$, $\mu^\pm\mu^\pm$, $e^\pm e^\mp$, $e^\pm e^\pm$, $\mu^\pm e^\mp$, $\mu^\pm e^\pm$, $e^\pm\mu^\mp$ and $e^\pm\mu^\pm$, where the like-sign combinations are sensitive to Majorana type HNLs. Improved signal and background separation is obtained by making use of a novel machine learning technique, called Boosted Decision Tree (BDT). Six separate BDTs are trained for the HNL search hypothesis. In each case the training for the displaced e and μ are performed separately for the different data taking years of run2 (2016, 2017 and 2018). Together with BDT classifier value, we used also the displacement of the secondary vertex and the secondary vertex mass to construct search regions.

The majority of the background events in the signal region are due to a fake or non-prompt lepton contributing to the final state, due to the specific final state topology of the signal and the relatively loose selection criteria applied for the sub-leading lepton selection. Hence a good fake background estimate is needed, for which a data-driven method is applied. A machine learning technique is used to model the fake rate background, where "fake" refers to contributions from both genuine fake leptons and from real leptons arising from non prompt decay channels. Since the leading (highest p_T) lepton in the signal finale state is essentially always prompt, the NN fake rate method is dominated by the fake contribution from the sub-leading lepton. The stability of the model is demonstrated in control regions which are similar to, but independent of, the signal region. In these regions, we find that predicted background is consistent with the observed data.

Based on the predicted background and expected signal yields, the sensitivity of the search in terms of the coupling parameter and HNL mass values was evaluated. Comparing these predictions with the observed data no significant excess is observed above the predicted background, i.e. no evidence for a signal of the production of HNL particles is observed in the search region covered by this analysis.

Hence, upper limits were set on the square of the neutrino mixing element, i.e. the couplings of the HNLs, based on the number of observed events, the predicted number of background events, and the predicted number of expected HNL signal events. The 95% confidence level limit on the cross section for heavy Neutrino production is obtained using the standard CMS HiggsCombination package, based on the CLs method. Limits are also set on $|\mathrm{V}_{lN}|^2$ as a function of M_N. The sensitivity of the CMS experiment to the mixing angle $|\mathrm{V}_{lN}|^2$ is estimated for signal samples for HNL masses of M_N = 1, 2, 3,... to 15 GeV, and improves the current state-of-the-art exclusion limits to date set by the CMS [12] and DELPHI [129] experiments. Based on the analysis made in this work, it is thus expected that the CMS experiment will publish new improved limits to $|\mathrm{V}_{lN}|^2$ in the HNL mass range from M_N = 1–15 GeV.

Finally, given the results presented in this thesis, we were excited to explore the future of HNL searches by estimating the improvement in sensitivity that may be obtained from data taking at the continuing LHC operation. This is in response to the ongoing Snowmass process in the United States, which is gathering information on what may be gleaned from present and future experiments. A study was conducted using the result that considers all final states as muons to be least sensitive to the higher pile-up expected for the High Luminosity of Large Hadron Colliders (HL-LHC). Two scenarios were considered. The first extrapolates both the signal and the background to 6 ab^{-1} (the total of the CMS plus ATLAS expected integrated luminosity). The second just extrapolates the signal to 6 ab^{-1}, reducing the expected background by a factor two to represent the possibility of future improvement in several sectors (for example, machine learning or collider technologies to achieve this).

Table C.1 in Appendix C.1 shows an improvement in the expected exclusion limits for both scenarios when compared to the results reported in this thesis and by CMS [12]. In particular, the results with snowmass scenarios appear to exclude higher masses of more than 20 GeV with much lower couplings compared to the current results, which are less than 15 GeV. The reason for this is that as the signal mass increases, the mixing angle decreases, and so do the cross sections of the signal, and thus the number of expected signal events. Therefore, higher luminosity would generally allow the analysis to exploit lower mixing angles.

PART I

Appendix

Appendix A

A.1 List of BDT input variables

Input variable	Importance
Displaced muon p_T	0.014032218
Displaced muon ϕ	0.008425623
Displaced muon $\Delta\beta$ isolation	0.022212435
Displaced muon d_{xy}	0.003975408
Displaced muon $\mathrm{d}_{xy}Sig$	0.0028935687
Displaced muon d_{xyz}	0.0025419348
Displaced muon $\mathrm{d}_{xyz}Sig$	0.0024146445
Displaced muon d_z	0.025547815
Displaced muon χ^2	0.0042688022
Secondary vertex p_T	0.027100408
Secondary vertex mass	0.051115308
Secondary vertex L_{xy}	0.34495762
Secondary vertex L_{xyz}	0.074374825
Secondary vertex L_{xyzSig}	0.0082942685
Secondary vertex L_{xySig}	0.008255164
Secondary vertex γ (energy/mass)	0.017985802
Secondary vertex χ^2	0.0041132946
Secondary vertex CNN tagger	0.034677435
Secondary vertex tracks sum($\mathrm{d}_{xy}Sig$)	0.02396912
Displaced jet p_T	0.07385733
Displaced jet ϕ	0.004706699
Displaced jet (muon energy fraction)	0.006472793
Displaced jet (neutral energy fraction)	0.013955407
Displaced jet (charged hadron energy fraction)	0.00597721
Displaced jet multiplicity (charged + neutral)	0.047057807
Δ R (displaced muon , displaced jet)	0.0060893153
Angle 2D (SV,PV)	0.02234661

Table A.1: List of BDT input variables when the displaced lepton is a muon.

Input variable	Importance
Displaced electron p_T	0.023665769
Displaced electron ϕ	0.010697081
Displaced electron d_{xy}	0.008292169
Displaced electron d_{xySig}	0.011858621
Displaced electron (energy / momentum)	0.009885857
Displaced electron nb. missing hits	0.061244935
Displaced electron (Had. / EM.) energy	0.008267433
Secondary vertex p_T	0.038330495
Secondary vertex mass	0.019122373
Secondary vertex L_{xy}	0.02946332
Secondary vertex L_{xyz}	0.014365656
Secondary vertex L_{xyzSig}	0.009649973
Secondary vertex tracks sum($d_{xy}Sig$)	0.007800893
Secondary vertex γ (energy/mass)	0.024963405
Secondary vertex β (momentum/energy)	0.018562347
Secondary vertex tracks sum charges	0.027659107
Secondary vertex CNN tagger	0.13458267
Secondary vertex number of tracks	0.015268499
Secondary vertex χ^2	0.0072744023
Displaced jet p_T	0.021103768
Displaced jet ϕ	0.010697081
Displaced jet energy	0.013542157
Displaced jet (charged hadron energy fraction)	0.010624255
Displaced jet (neutral hadron energy fraction)	0.012125179
Displaced jet (EM energy fraction)	0.0130958455
Displaced jet multiplicity (charged + neutral)	0.034254875
Δ R (displaced muon , displaced jet)	0.015724657
Angle 3D (SV,PV)	0.052743744

Table A.2: List of BDT input variables when the displaced lepton is an electron.

Appendix B

B.1 Secondary vertex efficiencies for different bins of SV displacement

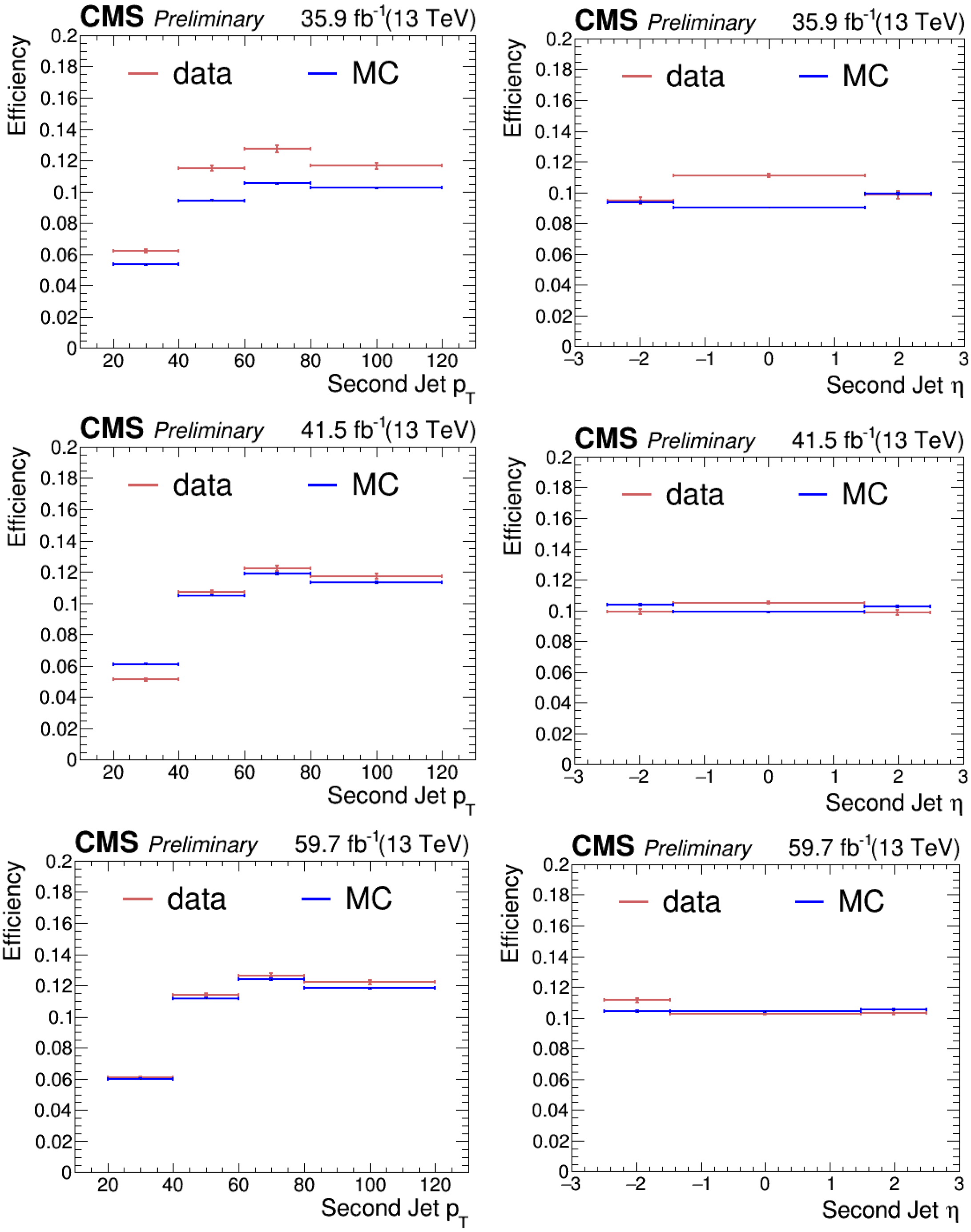

Figure B.1: SV matching with tight jet efficiencies as a function of tight jet p_T (left) and η (right) for SV displacement between $0-2$ cm. 2016 dataset (top), 2017 dataset (center), 2018 dataset (bottom).

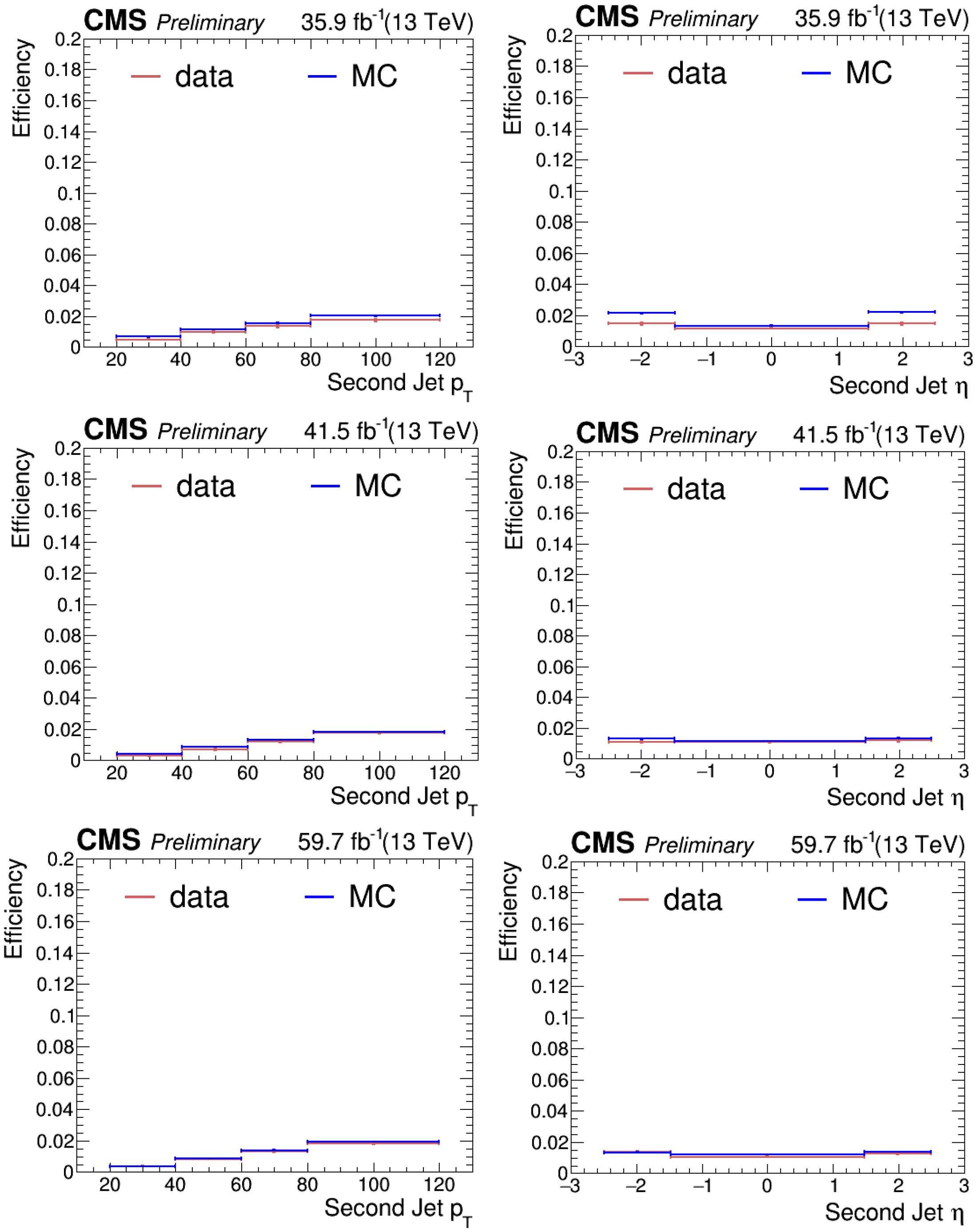

Figure B.2: SV matching with tight jet efficiencies as a function of tight jet p_T (left) and η (right) for SV displacement between $2 - 10$ cm. 2016 dataset (top), 2017 dataset (center), 2018 dataset (bottom).

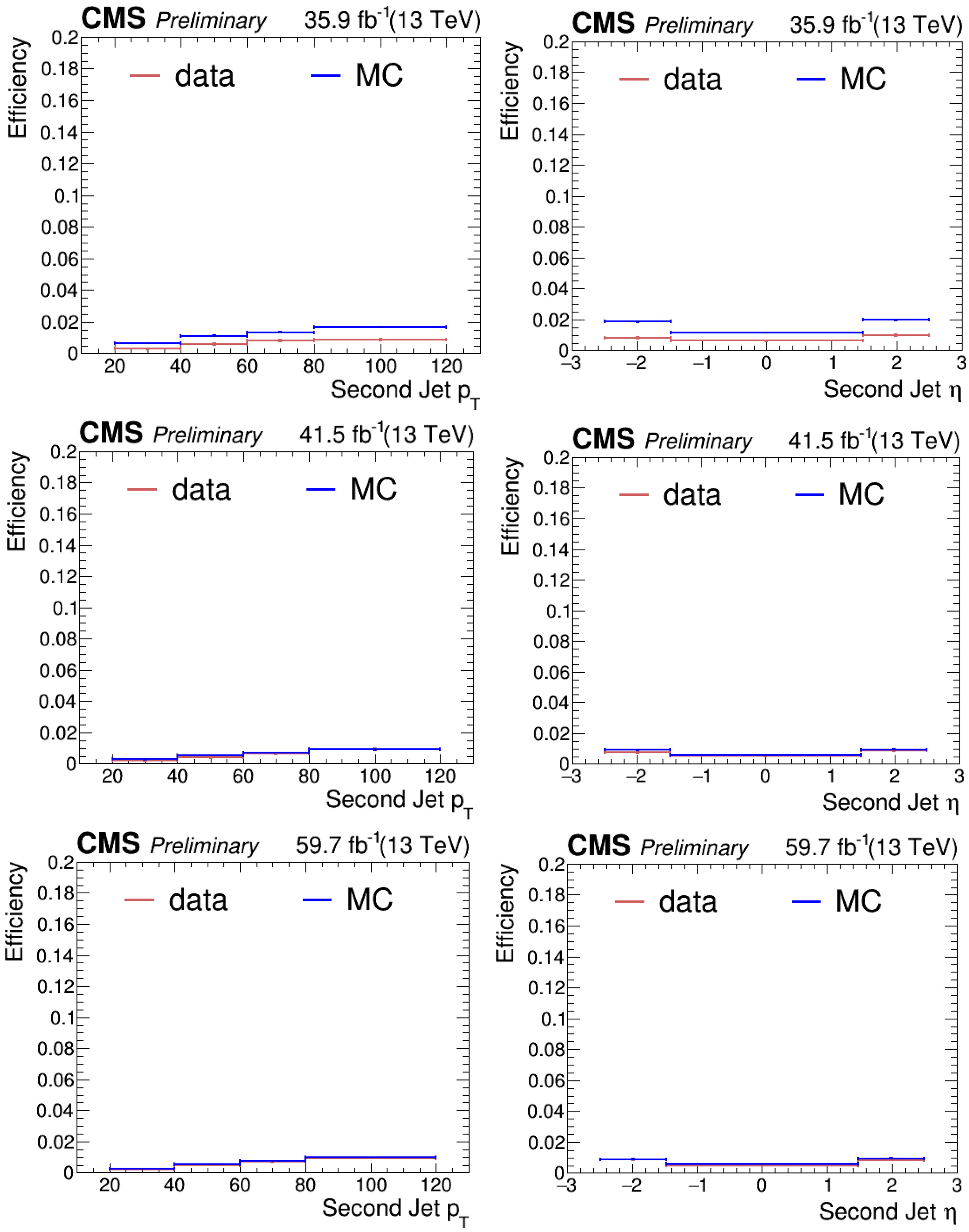

Figure B.3: SV matching with tight jet efficiencies as a function of tight jet p_T (left) and η (right) for SV displacement > 10 cm. 2016 dataset (top), 2017 dataset (center), 2018 dataset (bottom).

Appendix C

C.1 Prospects for future HNL studies

In this section, we will use the results of this study to estimate the increase in sensitivity that can be expected from data taking at the continuing LHC run. This is particularly of interest in view of the ongoing Snowmass process in the US that collects information on what can be obtained with present continuing or future new experiments and evaluates these results in the so-called P5 panel, which will produce recommendations for the US's future involvement in particle physics.

Specifically, Snowmass is a community study to discuss, establish, and propose a scientific vision for the future of particle physics. It aims to outline the most important questions in particle physics and propose potential opportunities for addressing them. The Snowmass vision will be integrated into a strategic plan for particle physics that can be implemented over a 10-year time frame. This study inspired us to use the current results, which are based on real data, to predict the extent that HNL limits can be improved with the High Luminosity operation of the LHC (HL-LHC), which is planned to start at the end of this decade and will take about 10 years of operation and is scheduled to collect 3 ab^{-1} for both ATLAS and CMS.

We perform the study for the final states with muons, which should be least sensitive to the higher pile-up expected for the HL-LHC. We began with the Majorana $\mu\mu$ channel result (see Figure 7.16), which shows a good exclusion limit at 137 fb^{-1}. As a first scenario, we extrapolated both the signal and the background in that plot to 6 ab^{-1}, i.e. the total of the CMS plus ATLAS expected integrated luminosity. Thus, we obtained an expected exclusion limit of HNL at 6 ab^{-1} (see Figure C.1 on the left), compared to CMS [50], DELPHI [129], and the analysis results presented in this thesis. Note that the improvement is not a straight-forward statistical improvement as probing lower couplings means probing longer lifetimes, and these are recorded with a reduced efficiency due to the spatial extent of the central detectors used in our analysis. The second scenario we studied is extrapolating the signal to 6 ab^{-1}, but reducing the expected background by a factor of two to represent future, potentially more sophisticated methods, e.g. in machine learning, that can be deployed to accomplish this (see Figure C.1 the right).

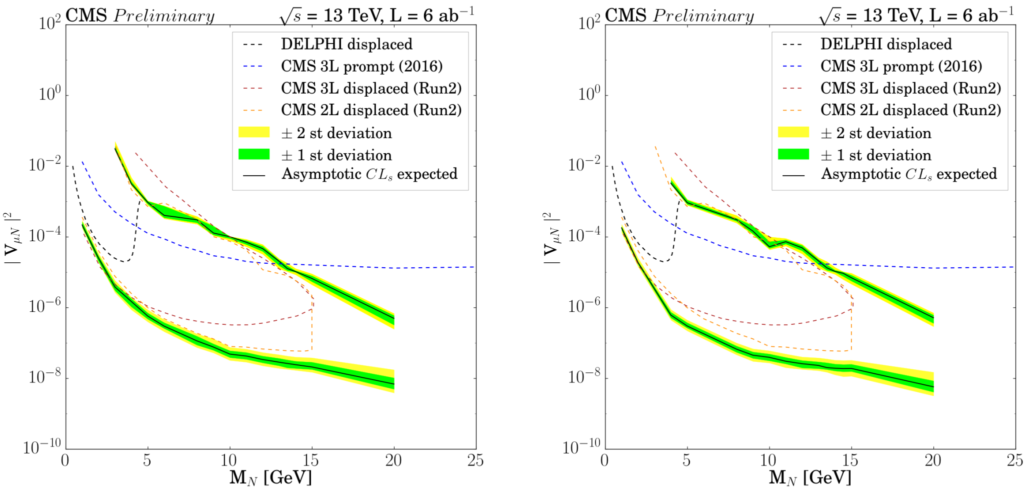

Figure C.1: Expected upper limits at 95% CL on $| V_{N\mu} |^2$ as a function of $_N$ for a Majorana HNL at two snowmass scenarios: first, both signal and background extrapolated to 6 ab^{-1} (left); second, only signal extrapolated to 6 ab^{-1} (right); whereas background to 3 ab^{-1} (right). Results from the Delphi [129] and the CMS [[12],[50]] Collaborations are shown for reference.

Table C.1 shows an improvement in the expected exclusion limits for HNL searches in both the first and second snowmass scenarios when compared to the results provided in this thesis and CMS [50], as extracted from Figure 3. In particular, the results with snowmass scenarios appear to exclude higher masses of more than 20 GeV with much lower couplings compared to the current results, which are less than 15 GeV. This is explained by the fact that as the mass of the signal increases, the

Mass M_N \ Excluded $\mid V_{N\mu} \mid^2$ value	CMS [50] result	current analysis result	Snowmass 1st scenario	Snowmass 2nd scenario
M_N = 5 GeV	1e-06	9.8e-07	5.7e-07	2.9e-07
M_N = 10 GeV	3.2e-07	7.9e-08	4.2e-08	3.9e-08
M_N = 15 GeV	5.4e-06	6.2e-08	2.1e-08	1.9e-08

Table C.1: A comparison of some excluded $\mid V_{N\mu} \mid^2$ values at various mass points of the results is presented in this thesis and by CMS [50] to the expected excluded $\mid V_{N\mu} \mid^2$ values for the first and second scenarios for snowmass.

mixing angle decreases, so does the cross section of the signal, and thus the number of expected signal events. Therefore, higher luminosity would generally allow the analysis to exploit lower mixing angles.

To summarize, this study is an attempt to go beyond the existing results, exploiting the current state-of-the-art exclusion limits defined by this analysis to give us an idea of how much we can improve the sensitivity to exclude further phase space within HNL searches. As the large datasets delivered by the LHC so far and the forthcoming runs promise a strong continuous physics output, which will extend the boundaries of knowledge at the energy frontier.

PhD Activities

Peer-reviewed journal articles with direct contribution

- CMS Collaboration, “Search for long-lived heavy neutral leptons in semi-leptonic final states”, EXO-21-011, to be publish in summer 2022.
- CMS Collaboration, “The Phase-2 Upgrade of the CMS Data Acquisition and High Level Trigger”, TDR-21-001, EPJ Web of Conferences. Vol. 251. EDP Sciences, 2021.
- CMS Collaboration, “Search for long-lived heavy neutral leptons with displaced vertices in proton-proton collisions at $\sqrt{s}=$ 13 TeV.” arXiv preprint arXiv:2201.05578 (2022).
- “The Present and Future Status of Heavy Neutral Leptons” arXiv:2203.08039 (2022).

Conferences, Workshops, and Schools

- “Searches for displaced jets at the LHC (ATLAS, CMS, LHCb)”, parallel at LHCP2022, 16-21 May 2022 (Taiwan)
- “Search for Heavy Neutral Lepton With CMS Detector Non-prompt signature”, poster at ESHEP 2018, 20 Jun-3 Jul 2018 (Italy)
- European School of High-Energy Physics (ESHEP) 2018, 20 Jun-3 Jul 2018, Maratea, Italy.
- CMS Physics Object School, Aachen, Germany, (16-20) September 2019.
- CMS Data Analysis School, CERN, (23-30) September 2020.

Awards

- **CMS Achievement Award** for continuous support to the CMS data taking as High Level Trigger (HLT) Detector On Call (DOC) expert, being one of the main players to make the excellent HLT performance in 2018 possible.

List of Figures

List of Tables

Bibliography

[1] O. KA *et al.*, “Review of particle physics,” *Chinese Physics C*, vol. 38, no. 9, pp. 1–090001, 2014.

[2] P. Hut and K. Olive, “A cosmological upper limit on the mass of heavy neutrinos,” *Physics Letters B*, vol. 87, no. 1-2, pp. 144–146, 1979.

[3] S. Boris, A. Golutvin, *et al.*, “Neutrino mass from the beta spectrum in the decay of tritium,” *Physical review letters*, vol. 58, no. 20, p. 2019, 1987.

[4] M. Gell-Mann, P. Ramond, and R. Slansky, “Complex spinors and unified theories,” in *Murray Gell-Mann: Selected Papers*, pp. 266–272, World Scientific, 2010.

[5] M. Gronau, C. N. Leung, and J. L. Rosner, “Extending limits on neutral heavy leptons,” *Physical Review D*, vol. 29, no. 11, p. 2539, 1984.

[6] P. Minkowski, “$\mu\rightarrow$ eγ at a rate of one out of 109 muon decays?,” *Physics Letters B*, vol. 67, no. 4, pp. 421–428, 1977.

[7] R. N. Mohapatra and G. Senjanović, “Neutrino mass and spontaneous parity nonconservation,” *Physical Review Letters*, vol. 44, no. 14, p. 912, 1980.

[8] M. Doi, T. Kotani, H. Nishiura, K. Okuda, and E. Takasugi, “CP violation in majorana neutrinos,” *Physics letters B*, vol. 102, no. 5, pp. 323–326, 1981.

[9] F. F. Deppisch, P. B. Dev, and A. Pilaftsis, “Neutrinos and collider physics,” *New Journal of Physics*, vol. 17, no. 7, p. 075019, 2015.

[10] C. O. Dib, C. Kim, and K. Wang, “Signatures of Dirac and Majorana sterile neutrinos in trilepton events at the LHC,” *Physical Review D*, vol. 95, no. 11, p. 115020, 2017.

[11] K. Bondarenko, A. Boyarsky, D. Gorbunov, and O. Ruchayskiy, "Phenomenology of GeV-scale heavy neutral leptons," *Journal of High Energy Physics*, vol. 2018, no. 11, pp. 1–48, 2018.

[12] A. M. Sirunyan *et al.*, "Search for heavy majorana neutrinos in same-sign dilepton channels in proton-proton collisions at $\surd$ s= 13 tev," *Journal of high energy physics*, vol. 2019, no. 1, p. 122, 2019.

[13] G. Aad, B. Abbott, *et al.*, "Search for heavy neutral leptons in decays of W bosons produced in 13 TeV pp collisions using prompt and displaced signatures with the ATLAS detector," *Journal of High Energy Physics*, vol. 2019, no. 10, pp. 1–47, 2019.

[14] L. Collaboration, "Search for heavy neutral leptons in W $\longrightarrow \mu\mu\pm$jet decays," *Eur. Phys. J. C*, vol. 81, p. 248, 2021.

[15] K. S. Hirata, T. Kajita, T. Kifune, K. Kihara, M. Nakahata, K. Nakamura, S. Ohara, Y. Oyama, N. Sato, M. Takita, *et al.*, "Observation of b 8 solar neutrinos in the kamiokande-ii detector," *Physical Review Letters*, vol. 63, no. 1, p. 16, 1989.

[16] J. N. Bahcall, "Two solar neutrino problems," *Nuclear Physics B-Proceedings Supplements*, vol. 43, no. 1-3, pp. 41–46, 1995.

[17] N. Collaboration, "P. adamson et al., First measurement of electron neutrino appearance in noνa," *Phys. Rev. Lett*, vol. 116, p. 151806, 2016.

[18] B. Kraus, Ch *et al.*, "Final results from phase ii of the Mainz neutrino mass searchin tritium beta decay," *The European Physical Journal C-Particles and Fields*, vol. 40, no. 4, pp. 447–468, 2005.

[19] F. An, J. Bai, A. Balantekin, H. Band, D. Beavis, W. Beriguete, M. Bishai, S. Blyth, K. Boddy, R. Brown, *et al.*, "Observation of electron-antineutrino disappearance at daya bay," *Physical Review Letters*, vol. 108, no. 17, p. 171803, 2012.

[20] F. Englert and R. Brout, "Broken symmetry and the mass of gauge vector mesons," *Physical Review Letters*, vol. 13, no. 9, p. 321, 1964.

[21] S. L. Glashow, "Partial-symmetries of weak interactions," *Nuclear physics*, vol. 22, no. 4, pp. 579–588, 1961.

[22] S. Weinberg, "A model of leptons," *Physical review letters*, vol. 19, no. 21, p. 1264, 1967.

[23] S. Abdus, "Weak and electromagnetic interactions, conf," *Proc. C*, vol. 680519, pp. 367–377, 1968.

[24] P. W. Higgs, "Broken symmetries and the masses of gauge bosons," *Physical Review Letters*, vol. 13, no. 16, p. 508, 1964.

[25] P. W. Higgs, "Spontaneous symmetry breakdown without massless bosons," *Physical Review*, vol. 145, no. 4, p. 1156, 1966.

[26] G. S. Guralnik, C. R. Hagen, and T. W. Kibble, "Global conservation laws and massless particles," *Physical Review Letters*, vol. 13, no. 20, p. 585, 1964.

[27] F. Halzen and A. D. Martin, "Leptons & quarks," 1984.

[28] C. Burgess and G. Moore, *The standard model: A primer.* Cambridge University Press, 2007.

[29] D. Griffiths, "Introduction to elementary particles. 2. enl. and rev," 2008.

[30] "The standard model beautiful theory." `https://www.quantumdiaries.org/2014/03/14/the-standard-model-a-beautiful-but-flawed-theory/`.

[31] E. Stueckelberg, "A new model of the point charge electron and of other elementary particles," *Nature*, vol. 144, no. 3637, pp. 118–118, 1939.

[32] K. Olive, "Review of particle physics," *Chinese Physics. C, High Energy Physics and Nuclear Physics*, vol. 40, no. FERMILAB-PUB-16-568, 2016.

[33] "Mathematical formulation of the standard model." `https://www.wikiwand.com/en/Mathematical_formulation_of_the_Standard_Model`.

[34] H. da Motta, "Chirality and neutrinos, a student first approach," in *Journal of Physics: Conference Series*, vol. 1558, p. 012014, IOP Publishing, 2020.

[35] T. Asaka and M. Shaposhnikov, "The νmsm, dark matter and baryon asymmetry of the universe," *Physics Letters B*, vol. 620, no. 1-2, pp. 17–26, 2005.

[36] "Particles in the standard model." `https://scienceblogs.com/files/startswithabang/files/2010/11/reality_standard_model2.gif`.

[37] D. Nicolò and F. Cei, "Lepton flavour violation experiments," *Advances in High Energy Physics (Online)*, vol. 2014, 2014.

[38] N. Deshpande, J. Gunion, B. Kayser, and F. Olness, "Left-right-symmetric electroweak models with triplet higgs field," *Physical Review D*, vol. 44, no. 3, p. 837, 1991.

[39] B. Gripaios, "Gauge field theory," *lecture notes*, 2013.

[40] E. Ma, "Verifiable radiative seesaw mechanism of neutrino mass and dark matter," *Physical Review D*, vol. 73, no. 7, p. 077301, 2006.

[41] M. Drewes, "The phenomenology of right handed neutrinos," *International Journal of Modern Physics E*, vol. 22, no. 08, p. 1330019, 2013.

[42] A. Boyarsky, O. Ruchayskiy, and M. Shaposhnikov, "The role of sterile neutrinos in cosmology and astrophysics," *Annual Review of Nuclear and Particle Science*, vol. 59, pp. 191–214, 2009.

[43] A. Strumia and F. Vissani, "Neutrino masses and mixings and...," *arXiv preprint hep-ph/0606054*, 2006.

[44] O. Ruchayskiy and A. Ivashko, "Experimental bounds on sterile neutrino mixing angles," *Journal of High Energy Physics*, vol. 2012, no. 6, pp. 1–27, 2012.

[45] B. Dasgupta and J. Kopp, "Sterile neutrinos," *arXiv preprint arXiv:2106.05913*, 2021.

[46] M. C. González-Garciá, A. Santamaria, and J. Valle, "Isosinglet-neutral heavy-lepton production in Z-decays and neutrino mass," *Nuclear Physics B*, vol. 342, no. 1, pp. 108–126, 1990.

[47] A. Atre, T. Han, S. Pascoli, and B. Zhang, "The Search for Heavy Majorana Neutrinos," *JHEP*, vol. 05, p. 030, 2009.

[48] D. Alva, T. Han, and R. Ruiz, "Heavy Majorana neutrinos from W γ fusion at hadron colliders," *JHEP*, vol. 02, p. 072, 2015.

[49] C. Degrande, O. Mattelaer, R. Ruiz, and J. Turner, “Fully-Automated Precision Predictions for Heavy Neutrino Production Mechanisms at Hadron Colliders,” *Phys. Rev. D*, vol. 94, p. 053002, 2016.

[50] C. Collaboration *et al.*, “Search for long-lived heavy neutral leptons with displaced vertices in proton-proton collisions at \\$\sqrt{s}$= 13 tev,” *arXiv preprint arXiv:2201.05578*, 2022.

[51] “Facts and figures about the LHC.” `https://home.cern/resources/faqs/facts-and-figures-about-lhc`.

[52] L. Evans, “and philip bryant,” *LHC Machine. JINST*, vol. 3, p. S08001, 2008.

[53] “Public CMS luminosity information.” `https://twiki.cern.ch/twiki/bin/view/CMSPublic/LumiPublicResults`.

[54] P. D. Group *et al.*, “Review of particle physics,” *The European Physical Journal C-Particles and Fields*, vol. 3, no. 1-4, pp. 1–783, 1998.

[55] E. Focardi, “Status of the CMS detector,” *Physics Procedia*, vol. 37, pp. 119–127, 2012.

[56] C. Collaboration, S. Chatrchyan, G. Hmayakyan, V. Khachatryan, A. Sirunyan, W. Adam, T. Bauer, T. Bergauer, H. Bergauer, M. Dragicevic, *et al.*, “The cms experiment at the CERN LHC,” *JInst*, vol. 3, p. S08004, 2008.

[57] “Cms spherical coordinates.” `https://wiki.physik.uzh.ch/cms/latex:example_spherical_coordinates`.

[58] “Cms tracker detector performance results..” `https://twiki.cern.ch/twiki/bin/view/CMSPublic/DPGResultsTRK`.

[59] W. Adam *et al.*, “The CMS phase-1 pixel detector upgrade,” *Journal of Instrumentation*, vol. 16, no. 02, p. P02027, 2021.

[60] I. Shvetsov, “Operational experience with the silicon strip tracker at the CMS experiment,” tech. rep., CERN-CMS-CR-2019-012., 2019.

[61] P. R. Hobson, “The lead tungstate calorimeter for CMS.” `http://people.brunel.ac.uk/~eestprh/pghep/CalorimeterCaseStudyCMS.pdf`.

[62] C. collaboration *et al.*, “The CMS hadron calorimeter project: technical design report,” *Technical Design Report CMS. CERN, Geneva*, vol. 49, 1997.

[63] A. Adair, B. Akgun, K. Ecklund, F. Geurts, W. Li, B. Michlin, B. Padley, R. Redjimi, J. Roberts, J. Zabel, *et al.*, “Performance of the CMS missing transverse momentum reconstruction in pp data at $\sqrt{}$ s= 8 tev,” *Journal of Instrumentation*, vol. 10, p. P02006, 2015.

[64] C. W. Fabjan and F. Gianotti, “Calorimetry for particle physics,” *Reviews of Modern Physics*, vol. 75, no. 4, p. 1243, 2003.

[65] M. Chadeeva and N. Lychkovskaya, “Calibration of the CMS hadron calorimeter in Run 2,” *Journal of Instrumentation*, vol. 13, no. 03, p. C03025, 2018.

[66] “The compact muon solenoid CMS.” `http://web.ethlife.ethz.ch/e/articles/sciencelife/CERNCMS.html`.

[67] “Endcap hv cable reshuffling.” `https://twiki.cern.ch/twiki/bin/view/Main/EndcapReshufflingRpc`.

[68] N. Manganelli, “Upgrades to the CMS cathode strip chambers for the HL-LHC,” *Journal of Instrumentation*, vol. 15, pp. C03047–C03047, mar 2020.

[69] “On the technique of the counter controlled cloud chamber,” *Proceedings of the Royal Society of London. Series A, Containing Papers of a Mathematical and Physical Character*, vol. 146, pp. 281–299, sep 1934.

[70] S. Chatrchyan *et al.*, “The CMS experiment at the CERN LHC,” *JINST*, vol. 3, p. S08004, 2008.

[71] R. D. Field and S. Wolfram, “A QCD model for e+ e- annihilation,” *Nuclear Physics B*, vol. 213, no. 1, pp. 65–84, 1983.

[72] C. collaboration *et al.*, “The CMS trigger system,” *arXiv preprint arXiv:1609.02366*, 2016.

[73] A. Sirunyan *et al.*, “Performance of the CMS level-1 trigger in proton-proton collisions at 13 TeV,” *Journal of Instrumentation*, vol. 15, pp. P10017–P10017, oct 2020.

[74] V. Innocente, L. Silvestris, and D. Stickland, "CMS software architecture," *Computer Physics Communications*, vol. 140, pp. 31–44, oct 2001.

[75] A. Perrotta, "Performance of the CMS high level trigger," in *Journal of Physics: Conference Series*, vol. 664, p. 082044, IOP Publishing, 2015.

[76] S. Donato, "CMS trigger performance," in *EPJ Web of Conferences*, vol. 182, p. 02037, EDP Sciences, 2018.

[77] S. Choudhury, "Performance of the high level trigger system at CMS in LHC Run-2," *IEEE Transactions on Nuclear Science*, 2021.

[78] V. Khachatryan *et al.*, "The CMS trigger system," *Journal of Instrumentation*, vol. 12, no. 1, pp. Art–No, 2017.

[79] M. Felcini, "The trigger system of the CMS experiment," *Nuclear Instruments and Methods in Physics Research Section A: Accelerators, Spectrometers, Detectors and Associated Equipment*, vol. 598, pp. 312–316, jan 2009.

[80] "Summary performance plots for 2016 data." `https://twiki.cern.ch/twiki/bin/view/CMSPublic/HLTplotsSummary2016`.

[81] "The CMS high level trigger," *The European Physical Journal C*, vol. 46, pp. 605–667, apr 2006.

[82] "Tag and probe method." `http://cms.cern.ch/iCMS/jsp/openfile.jsp?tp=draft&files=AN2009_111_v1.pdf`.

[83] A. Dominguez, "Cms technical design report for the pixel detector upgrade," tech. rep., Fermi National Accelerator Lab.(FNAL), Batavia, IL (United States), 2012.

[84] J. Mans, "Cms technical design report for the phase 1 upgrade of the hadron calorimeter," tech. rep., CMS-TDR-010, 2012.

[85] A. Colaleo, A. Safonov, A. Sharma, and M. Tytgat, "CMS technical design report for the muon endcap GEM upgrade," tech. rep., 2015.

[86] P. K. Siddireddy, "The CMS ECAL trigger and DAQ system: electronics auto-recovery and monitoring," *arXiv preprint arXiv:1806.09136*, 2018.

[87] T. A. Tobar, A Navarro and Others, “CMS drift tubes readout phase–1 upgrade,” *PoS TWEPP*, 2019.

[88] S. Agostinelli, J. Allison, and Others, “Geant4—a simulation toolkit,” *Nuclear Instruments and Methods in Physics Research Section A: Accelerators, Spectrometers, Detectors and Associated Equipment*, vol. 506, pp. 250–303, jul 2003.

[89] T. Sjöstrand, C. Ask, Stefan, and Others, “An introduction to pythia 8.2,” *Computer physics communications*, vol. 191, pp. 159–177, 2015.

[90] C. Oleari, “The powheg-box,” *arXiv preprint arXiv:1007.3893*, 2010.

[91] H. Alwall, Johan and Others, “Madgraph 5: going beyond,” *Journal of High Energy Physics*, vol. 2011, no. 6, pp. 1–40, 2011.

[92] S. Belforte and Others, “Event generator tunes obtained from underlying event and multiparton scattering measurements,” 2016.

[93] S. Belforte and Others, “Extraction and validation of a new set of CMS PYTHIA8 tunes from underlying-event measurements,” 2020.

[94] R. Placakyte, “Parton distribution functions,” *arXiv preprint arXiv:1111.5452*, 2011.

[95] R. D. Ball and Others, “Parton distributions for the lhc run ii,” *Journal of High Energy Physics*, vol. 2015, no. 4, pp. 1–148, 2015.

[96] R. D. Ball *et al.*, “Parton distributions from high-precision collider data,” *The European Physical Journal C*, vol. 77, no. 10, pp. 1–75, 2017.

[97] M. Weber, C. collaboration, *et al.*, “The CMS tracker alignment strategy,” *Nuclear Instruments and Methods in Physics Research Section A: Accelerators, Spectrometers, Detectors and Associated Equipment*, vol. 582, no. 3, pp. 795–799, 2007.

[98] G. Cerati, P. Elmer, Gravelle, *et al.*, “Speeding up particle track reconstruction in the CMS detector using a vectorized and parallelized kalman filter algorithm,” *arXiv preprint arXiv:1906.11744*, 2019.

[99] "Track reconstruction." `https://indico.cern.ch/event/93144/attachments/1101404/1571209/Sem2_Tracking.pdf`.

[100] A. M. Sirunyan *et al.*, "Particle-flow reconstruction and global event description with the CMS detector," *Journal of Instrumentation*, p. 86, 2017.

[101] "Track reconstruction." `https://twiki.cern.ch/twiki/bin/view/CMSPublic/SWGuideVertexFitterMainComponents`.

[102] A. Everett and C. Collaboration, "Muon reconstruction and identification in CMS," in *AIP Conference Proceedings*, vol. 1200, pp. 701–704, American Institute of Physics, 2010.

[103] "Reference muon id, isolation and trigger efficiencies for Run2." `https://twiki.cern.ch/twiki/bin/view/CMS/MuonReferenceEffsRun2`.

[104] J. Rembser, C. Collaboration, *et al.*, "CMS electron and photon performance at 13 TeV," in *Journal of Physics: Conference Series*, vol. 1162, p. 012008, IOP Publishing, 2019.

[105] W. Adam, R. Frühwirth, A. Strandlie, and T. Todorov, "Reconstruction of electrons with the gaussian-sum filter in the CMS tracker at the LHC," *Journal of Physics G: Nuclear and Particle Physics*, vol. 31, no. 9, p. N9, 2005.

[106] "Egamma runii recommendations." `https://twiki.cern.ch/twiki/bin/view/CMS/EgammaRunIIRecommendations`.

[107] "Jet identification for the 13 TeV data Run2." `https://twiki.cern.ch/twiki/bin/view/CMS/JetID13TeVRun2016`.

[108] C. collaboration *et al.*, "Identification of b quark jets at the CMS experiment in the LHC Run 2," 2016.

[109] R. Frühwirth, P. Vanlaer, and W. Waltenberger, "Adaptive vertex fitting," tech. rep., CERN-CMS-NOTE-2007-008, 2007.

[110] A. Botalb, M. Moinuddin, U. Al-Saggaf, and S. S. Ali, "Contrasting convolutional neural network CNN with multi-layer perceptron MLP for big data analysis," in *2018 International conference on intelligent and advanced system (ICIAS)*, pp. 1–5, IEEE, 2018.

[111] `https://keras.io/api/optimizers/adamax/`.

[112] S. S. Haykin *et al.*, "Neural networks and learning machines/simon haykin.," 2009.

[113] R. G. Mantovani, R. Cerri, and Others, "Hyper-parameter tuning of a decision tree induction algorithm," in *2016 5th Brazilian Conference on Intelligent Systems (BRACIS)*, pp. 37–42, IEEE, 2016.

[114] L.-G. Xia, "Understanding the boosted decision tree methods with the weak-learner approximation," *arXiv preprint arXiv:1811.04822*, 2018.

[115] T. Chen, "Introduction to boosted trees," *University of Washington Computer Science*, vol. 22, p. 115, 2014.

[116] T. Chen and C. Guestrin, "Xgboost: A scalable tree boosting system," in *Proceedings of the 22nd acm sigkdd international conference on knowledge discovery and data mining*, pp. 785–794, 2016.

[117] S. Hoecker, Andreas *et al.*, "TMVA-toolkit for multivariate data analysis," *arXiv preprint physics/0703039*, 2007.

[118] K. Hornik, M. Stinchcombe, and H. White, "Multilayer feedforward networks are universal approximators," *Neural networks*, vol. 2, no. 5, pp. 359–366, 1989.

[119] J. Schmidhuber, "Deep learning in neural networks: An overview," *Neural networks*, vol. 61, pp. 85–117, 2015.

[120] "Luminosity physics object group CMS." `https://twiki.cern.ch/twiki/bin/viewauth/CMS/TWikiLUM`.

[121] "Utilities for accessing pileup information for data." `https://twiki.cern.ch/twiki/bin/viewauth/CMS/PileupJSONFileforData#Pileup_JSON_F`.

[122] "Jet energy scale uncertainty sources." `https://twiki.cern.ch/twiki/bin/view/CMS/JECUncertaintySources`.

[123] "Jet energy resolution." `https://twiki.cern.ch/twiki/bin/viewauth/CMS/JetResolution`.

[124] "Sm + heavy n at nlo in QCD feynrules page." `http://feynrules.irmp.ucl.ac.be/wiki/HeavyN`.

[125] B. Sirunyan, Albert M *et al.*, "Identification of heavy-flavour jets with the CMS detector in pp collisions at 13 TeV," *Journal of Instrumentation*, vol. 13, p. P05011, 2018.

[126] G. Cowan, K. Cranmer, E. Gross, and O. Vitells, "Asymptotic formulae for likelihood-based tests of new physics," *The European Physical Journal C*, vol. 71, no. 2, pp. 1–19, 2011.

[127] A. L. Read, "Presentation of search results: the cls technique," *Journal of Physics G: Nuclear and Particle Physics*, vol. 28, no. 10, p. 2693, 2002.

[128] L. ATLASandCMSCollaborations, "Procedure for the LHC higgs boson search combination in summer 2011," tech. rep., Technical Report ATL-PHYS-PUB 2011-11, CMS NOTE 2011/005, 2011.

[129] P. Abreu, "Search for neutral heavy leptons produced in Z decays (vol 74, pg 57, 1997)," 1997.